Design of photoactivatable drug delivery systems made of lipids and porphyrins or lipid-porphyrin conjugates for the controlled release of active pharmaceutical ingredients

Julien Massiot

université PARIS-SACLAY

NNT : 2018SACLS290

Thèse de doctorat

Conception de nanomédicaments photostimulables à base de lipides et porphyrines ou de conjugués lipide-porphyrine pour la libération contrôlée de substances actives

Thèse de doctorat de l'Université Paris-Saclay
préparée à l'université Paris-Sud (Faculté de Pharmacie)

ED569 : Innovation thérapeutique : du fondamental à l'appliqué (ITFA)
Pôle: Pharmacotechnie et Physico-chimie Pharmaceutique

Thèse présentée et soutenue à Châtenay-Malabry, le 12 Octobre 2018, par

Julien MASSIOT

Composition du Jury :

Stéphanie Bonneau Maitre de conférences, Université Pierre et Marie Curie (UPMC)	Rapporteure
Vincent Sol Professeur, Université de Limoges	Rapporteur
Michel Linder Professeur, Université de Lorraine	Examinateur
Nicolas Tsapis Directeur de Recherche, Université Paris-Sud (Faculté de Pharmacie)	Président
Véronique Rosilio Professeure, Université Paris-Sud (Faculté de Pharmacie)	Directrice de thèse
Ali Makky Maitre de conférences, Université Paris-Sud (Faculté de Pharmacie)	Co-Directeur de thèse

RESUME

L'objectif des travaux de cette thèse était de développer un système de délivrance stimulus-sensible innovant permettant la libération contrôlée d'une substance anti-cancéreuse. Ce système est basé sur des vésicules lipidiques pouvant incorporer des porphyrines dans leur bicouche et une substance active hydrophile dans leur cœur aqueux. Les porphyrines permettent, une fois illuminées, de fragiliser la bicouche lipidique, assurant la libération du cargo. L'activation du phénomène de libération repose sur deux mécanismes possibles, l'un photodynamique, l'autre photothermique. Le premier génère de l'oxygène singulet qui oxyde les chaînes acyl insaturées des phospholipides. Cette oxydation aboutit à une augmentation de la perméabilité des liposomes et à la libération de leur cargo. Le second génère de la chaleur, responsable d'une plus grande fluidité de la bicouche lipidique qui favorise elle-aussi la libération.

Nous avons, dans un premier temps, effectué une sélection de phospholipides (degré d'insaturation) et de porphyrines permettant de construire le système. Une étude thermodynamique par calorimétrie différentielle à balayage, une analyse photochimique et une étude de libération de calcéine (une sonde fluorescente) ont pu être corrélées à des résultats de simulations de dynamique moléculaire. L'ensemble a mis en exergue deux observation essentielles : l'importance de la profondeur d'insertion de la porphyrine dans la bicouche lipidique et de sa proximité avec la double-liaison des phospholipides. Mais il a également montré les limites de ce système.

Nous avons alors développé deux nouvelles molécules, dérivées de phospholipides naturels auxquels ont été couplée la pheophorbide a, un dérivé de porphyrine issue de la chlorophyll a. Le choix de développer de telles molécules repose sur la possibilité d'étendre le mécanisme de libération vers une combinaison des effets photodynamique et photothermique. En effet, leurs capacités d'auto-assemblage en font des molécules idéales pour un système simple et facilement industrialisable.

Nous n'avons pas pu former d'assemblages supramoléculaires stables, mais nous avons démontré que le taux de charge en porphyrine de la matrice de liposomes pouvait être augmenté par rapport à celui de la porphyrine libre correspondante. Nous avons donc associé ces conjugués à des lipides classiques (DSPC, cholestérol) et analysé les propriétés de ces mélanges à l'interface air/eau et par des mesures de DSC. Nous avons mis en évidence les propriétés photodynamiques, mais aussi photothermiques des systèmes conçus, capables d'induire une élévation de température de 14°C. Enfin, les deux conjugués synthétisés ont montré eux-mêmes une activité photodynamique phototoxique, additionnée d'une sélectivité vis-à-vis de cellules du cancer de l'œsophage (Kyse-30) par comparaison avec une lignée saine (HET-1A). Ces nouvelles molécules offrent donc de nombreuses opportunités pour le développement de systèmes multimodaux, bio-inspirés et biodégradables, pour la délivrance d'un médicament sous l'effet de la lumière, localement, au niveau des tumeurs.

Remerciements

Ce travail de thèse s'est déroulé au sein de l'institut Galien Paris-Sud (UMR CNRS 8612), dirigé par le ***Professeur Elias Fattal****, dans l'équipe de Physico-chimie des surfaces, dirigée par le* ***Professeur Véronique Rosilio****. Je tiens donc tout d'abord à vous remercier pour l'accueil au sein de l'unité et plus particulièrement au sein de l'équipe.*

Je tiens également à remercier ***Mme Stéphanie Bonneau****, maître de conférences à l'université Pierre-Marie Curie (UPMC, Paris) ainsi que* ***M. Vincent Sol****, professeur à l'université de Limoges et directeur du laboratoire Pereine, d'avoir accepté de rapporter mes travaux de thèse.*

Je remercie ***M. Michel Linder****, professeur à l'université de Lorraine, et* ***M. Nicolas Tsapis****, directeur de recherche à l'université Paris-Sud d'avoir accepté de faire partie du jury en qualité d'examinateur.*

Je remercie profondément le ***Professeur Véronique Rosilio*** *pour avoir accepté de diriger ces travaux de thèse et pour l'accueil au sein de l'équipe : je vous suis entièrement reconnaissant pour votre soutien, votre suivi, ainsi que pour tous vos conseils pour que ma thèse se déroule dans les meilleures conditions. Au-delà de votre grande rigueur scientifique, nos échanges ont toujours été constructifs et m'ont beaucoup aidé, et ce à toutes les étapes de ma thèse. J'ai beaucoup appris pendant ces trois années sous votre encadrement, et j'ai toujours été admiratif de votre capacité à trouver les bons mots, les solutions ou encore les alternatives aux problèmes que j'ai pu rencontrer pendant ma thèse, et ce avec une grande sérénité. Vous avez su faire en sorte que tout se passe dans les meilleures conditions, et je ne vous en remercierai jamais assez !*

Bien évidemment, tout ce travail de thèse n'aurait pas été possible sans l'encadrement et la co-direction du ***Docteur Ali Makky*** *: Ali, merci pour tout ! Les mots sont durs à trouver pour exprimer toute ma gratitude envers toi. Tu m'as très vite fait confiance pour ce projet, ambitieux, passionnant et innovant. Tu as su me transmettre ta passion, tes connaissances sur le sujet, et ton énergie, pour faire en sorte que le projet soit un succès. Je te remercie pour ta grande disponibilité, tes conseils qui ont toujours été les bons, et ton optimisme qui fait que jamais je n'ai baissé les bras et que j'ai toujours cru en la réussite de ce projet, même dans les moments difficiles ! J'ai passé trois années fantastiques à travailler à tes côtés, j'ai beaucoup appris, scientifiquement mais aussi humainement, et j'ai toujours apprécié ta grande ouverture d'esprit. Je suis fier d'avoir été ton premier thésard, et je suis certains que je ne suis que le premier d'une longue liste, et que ta carrière sera longue et belle ! Merci pour tout !*

Je tiens aussi à remercier l'ensemble des membres permanents de notre équipe, ***M. Jean-Philippe Michel*** *et* ***M. David Chapron****, avec qui j'ai pu échanger, partager, et aussi travailler. Vous avez toujours été là pour moi, au sein de l'équipe, et participé à la bonne ambiance de notre équipe.*

Je remercie bien sûr mes collègues de bureau, ***Xiao****,* ***Marline*** *et* ***Islem****, avec qui j'ai tout partagé, dans le labo mais aussi en dehors ! La bonne humeur a toujours été au rendez-vous, et c'était un plaisir de partager le bureau avec vous tous les jours. Bien sûr, je n'oublie pas* ***Noémi****, ainsi que les stagiaires passés par notre équipe,* ***Marion****,* ***Arnaud****, et* ***Maroua****.*

Je remercie également les membres de l'équipe 2, et plus particulièrement ***Sylviane Lesieur****, responsable de l'équipe, pour tous ses conseils, et des discussions toujours constructives : je vous remercie pour l'accès aux différents instruments de votre équipe, pour votre confiance, et pour l'apport de vos connaissances scientifiques me permettant d'interpréter plus facilement mes résultats.*

Merci à ***Stéphanie Denis*** *pour son accompagnement lors des manipulations en salle de culture cellulaire : merci pour ta bonne humeur et tous tes conseils pour faire en sorte que tout se déroule dans les meilleures conditions. Toujours très disponible et patiente, tu as toujours pris le temps de m'expliquer chaque détail.*

Je remercie ***Juliette Vergnaud*** *pour son introduction au Western Blot qui m'aura été très utile et permis de mettre en évidence des détails important : merci pour ton temps et ton expertise précieuse sur le sujet.*

Je remercie tout particulièrement le ***Professeur Elias Fattal****, directeur de l'unité, qui a soutenu ce projet de thèse depuis le début : merci à vous pour votre accueil au sein de l'institut Galien, un institut qui transpire la science, la talent et le succès, le tout dans une ambiance chaleureuse et conviviale.*

Un grand merci à ***Athéna Kasselouri****, maître de conférences dans le laboratoire Lip(sys)^2 à la faculté de pharmacie de Châtenay-Malabry : merci de m'avoir permis l'accès à un certain nombre d'appareils, essentiels pour le bon déroulement de ma thèse. Merci pour votre accueil, et celui de votre équipe, notamment* ***Martin Souce*** *et sa bonne humeur au quotidien ! Un grand merci également à* ***Ali Tfayli*** *pour ses conseils et son expertise au niveau des lasers.*

*Merci au **Professeur Patrick Trouillas** et à **M. Florent Di Meo** de l'université de Limoges pour cette collaboration fructueuse grâce à l'apport de la simulation moléculaire, qui a permis notamment de confirmer des observations expérimentales importantes.*

*Je tiens aussi à remercier le **Professeur Jean-François Peyrat** ainsi que **Nada Ibrahim** pour l'apport de leur expertise dans le domaine de la chimie organique : merci Nada pour ta gentillesse, ta patience, et tout ce que tu as pu m'apprendre. Ces quelques mois passés à faire de la synthèse à tes côtés, avant que je vole de mes propres ailes, ont été essentiels et un tournant important dans ma thèse ! Un énorme merci !*

*Merci à **Sokunthéa Thlang** ainsi qu'à toute l'équipe de chimie du Palais de la Découverte, ou j'ai pu avoir l'opportunité d'effectuer une mission de médiation scientifique pendant les deux premières années de ma thèse. Merci à **Ludo**, **Claire**, **Véronique** et **Frédérique** pour tous vos conseils en vulgarisation et communication.*

*Merci, bien sûr, à l'ensemble des étudiants de l'institut Galien : sans vous, l'ambiance ne serait pas celle qu'elle est aujourd'hui. Sans citer tout le monde, car c'est difficile de ne pas oublier quelqu'un, je remercie tout de même **Jean-Baptiste**, **Marion**, **Corentin**, **Arnaud**, **Marie**, **Alexandre**, **Raul**, **Johanna**, **Daniele**, **Gianpiero**, et beaucoup d'autres !*

*Merci également à tous mes amis, qui m'ont suivi de près ou de loin, pendant ces trois ans ! Je pense bien évidemment à toute la team de l'**ECPM** ! Merci aussi à tous mes amis **bretons** :) Et bien sûr, merci à **Alix** et **Marius** qui étaient au plus près de l'action chaque semaine.*

*Je ne peux pas finir sans remercier ma famille, qui m'a toujours soutenue. Merci à **mes parents** : sans vous, je n'aurais jamais pu parcourir tout ce chemin ! Je vous aime et vous le savez. Mes frère et sœur : merci **Alex** et **Pauline** de toujours être la quand il faut, même avec la distance, je vous aime !*

*Enfin, s'il fallait dédier cette thèse à quelqu'un, c'est bien évidemment à la femme de ma vie : merci **Chih-Yang**, ma femme, qui me soutient tous les jours ! C'est surtout grâce à toi si je suis arrivé jusque-là ! Ton soutien a été un moteur et m'a permis de ne jamais rien lâcher. J'ai souvent eu la tête ailleurs pendant ces trois ans, perdu dans mes pensées et mes problèmes de thésard. Mais tu as toujours été là, et je ne t'en remercierai jamais assez ! Je t'aime ! Merci !*

Table of contents

List of Figures and Schemes

List of Tables

List of Appendices

Appendix I:

Appendix II: Supplementary Figures and Tables

Appendix III: Publication

Abbreviations

AMD: Age-related macular degeneration

API: Active pharmaceutical ingredient

AZOSIL: Azo-organoalkoxysilylated lipids

BChla: Bacteriochlorophyll a

BPD-MA: Benzoporphyrin derivative monoacid ring A

BVEP: 1,2-di-O-(1'Z,9'Z-octadecadienyl)-glyceryl-3-(ω-methoxy-poly(ethylene glycolate)

CHEMS: Cholesteryl hemisuccinate

Chol: Cholesterol

CLSM: Confocal laser scanning microscopy

COM: Center-of-mass

$DC_{8,9}PC$: 1,2 bis(tricosa-10,12-diynoyl)-sn-glycero-3-phosphocholine

DDS: Drug delivery systems

DLPC: 1,2-dilinoleoyl-sn-glycero-3-phosphocholine

DLS: Dynamic light scattering

DMED: Dexmedetomidine

DMPC: Dimyristoyl-phosphatidylcholine

DMPE : Dimyristoyl-phosphatidylethanolamine

DOPC: 1,2-dioleoyl-sn-glycero-3-phosphocholine

DOPE: 1,2-dioleoyl-phosphatidylethanolamine

DOTAP: 1,2-dioleoyl-3-trimethylammonium-propane

DPBS: Dulbecco's Phosphate-Buffered Saline

DPPC: 1,2-dipalmitoyl-sn-glycero-3-phosphocholine

DSC: Differential scanning calorimetry

DSPC: 1,2-distearoyl-sn-glycero-3-phosphocholine

DSPE-PEG_{2000}: 1,2-distearoyl-sn-glycero-3-phosphoethanolamine-N-[methoxy(polyethylene glycol)-2000]

DSPG: 1,2-distearoyl-sn-glycero-3-phospho-(1'-rac-glycerol)

ELTSL: Enzyme, light and temperature multi-sensitive liposome

ER: Endoplasmic reticulum

ESCC: Esophageal squamous cancer cell

ESI: Electrospray ionization

eSM: Egg sphingomyelin

FDA: Food and drug administration

FF: Force field

Fmoc-glycine (Fmoc-Gly-OH): (((9H-fluoren-9-yl)methoxy)carbonyl)glycine

GUV: Giant unilamellar vesicle

HPPH: 2-(1-hexyloxyethyl)-2-devinyl pyropheophorbide-a

HUVEC: Human Umbilical Vein Endothelial Cells

IC50: Half maximal inhibitory concentration

ISC: Intersystem crossing

LDL: Low-density lipoprotein

Lyso-PC: Lysophosphatidylcholine

MALDI-TOF: Matrix-assisted laser desorption/ionization – Time of flight

MCC: Manders' co-localization coefficient

MD: Molecular dynamics

ML: Methyl linoleate

MRI: Magnetic resonance imaging

MTG: Mitotracker-green

m-THPC: 5,10,15,20-Tetrakis(3-hydroxyphenyl)chlorin

m-THPP: 5,10,15,20-Tetrakis(3-hydroxyphenyl)porphyrin

NBD-lipid: 1,2-dipalmitoyl-sn-glycero-3-phosphoethanolamine-N-(7-nitro-2-1,3-benzoxadiazol-4-yl)

NIR: Near infra-red

NMR: Nuclear magnetic resonance spectroscopy

PAI: Photoacoustic imaging

PBC: Porphyrin bilayer cerasome

PdI: Polydispersity Index

PDT: Photodynamic therapy

PEG: Polyethylene glycol

PET: Positron-emission tomography

PGL: Porphyrin-grafted lipid

Pheo-a: Pheophorbide a

PhLPC: Pheophorbide a coupled to modified lyso-phosphatidylcholine

PhLSM: Pheophorbide a coupled to egg lyso-sphingomyelin

PL(s): Phospholipid(s)

PlasPPC: 1-alk-1′-enyl-2-palmitoyl-sn-glycero-3-phosphocholine

PLGA-PEG: Poly-(lactic acid-co-glycolic) acid–polyethylene glycol conjugate

PME: Particle-Mesh Ewald

PMIL: Photoactivatable multi-inhibitor nanoliposome

PLPC: 1-palmitoyl-2-linoleoyl-sn-glycero-3-phosphatidylcholine

POPC: 1-palmitoyl-2-oleoyl-sn-glycero-3-phosphocholine

PORSIL: Porphyrin organoalkoxysilylated lipids

PPIX: Protoporphyrin IX

PS(s): Photosensitizer(s)

PTT: Photothermal therapy

Pur-lipid: Purpurin-18 coupled to lysophosphatidylcholine

Pyro-lipid: Pyropheophorbide-a coupled to lysophosphatidylcholine

ROS: Reactive oxygen species

SA: Stearylamine

SLPC: 1-stearoyl-2-linoleoyl-sn-glycero-3-phosphocholine

SOPC: 1-stearoyl-2-oleoyl-sn-glycero-3-phosphocholine

SPECT: Single-photon emission computed tomography

SDDS: Smart drug delivery systems

TEM: Transmission electron microscopy

THF: Tetrahydrofuran

TPP: Tetraphenylporphyrin

TRITC: Tetramethylrhodamine isothiocyanate

XRR: X-ray reflectivity

Introduction

Introduction

Liposomal drug delivery systems are considered nowadays as the most successful nanomedicine application since the concept of "magic-bullet" was proposed by Paul Ehrlich in early 1900s[1]. The number of liposomal drugs on the market, however, remains low, and didn't raise as expected. Although liposomes can change the biodistribution of a drug (and thus reduce its toxicity), protect it from degradation, and favor tumor accumulation by passive targeting (*via* EPR effect[2,3]), there are still two important issues: first, the liposome circulation lifetime, and second, the rate of release of the encapsulated therapeutic molecule[4]. While the first issue is believed to be resolved by addition of hydrophilic polymer chains (such as polyethylene glycol, increasing liposome residence time from minutes to hours or days[5]) at the surface of liposomes, the release of a drug from liposomes can be improved by an exogenous stimulus.

Light is non-invasive, and its temporal, spatial and wavelength parameters are easy to modulate and to transfer to clinic. Phototriggered release of encapsulated drugs from liposomes is thus considered as a potential and interesting modality for drug delivery in a well-controlled manner[6,7].

Photosensitive liposomes can be activated upon illumination at a specific wavelength to release their cargo[8,9]. Biodegradable organic dyes that can absorb in the near infra-red region – the range of light that can penetrate deep enough into a biological tissue – are among the best candidates, once combined with liposomes, for biocompatible, and efficient light-triggered release systems. For these reasons, porphyrin and porphyrin derivatives are among the most widely used photosensitizers[10].

Indeed, porphyrin derivatives, either in their free form, or conjugated to a lipid, can be efficiently incorporated in the lipid matrix of liposomes. Depending on the structure of both the lipid membrane and porphyrin derivative, and the incorporation rate of the latter, the phototriggering mechanism can be either photochemical (photooxidative) or photophysical (photothermal) (Figure 1.0).

The first mechanism takes advantage of singlet oxygen generation which oxidizes the unsaturated acyl chains of the phospholipids, and thus, increases the permeability of the liposomes. In the second one, the energy absorbed is dissipated thermally and results in an increase of the fluidity of the lipid bilayer. Both mechanisms, thus, would promote the release of the encapsulated cargo, and these systems may offer multimodal applications. Indeed, the reactive oxygen species generated by illumination of the photosensitizer may also contribute to the therapeutic effect by direct cytotoxic effect. This additional modality of treatment is called photodynamic therapy.

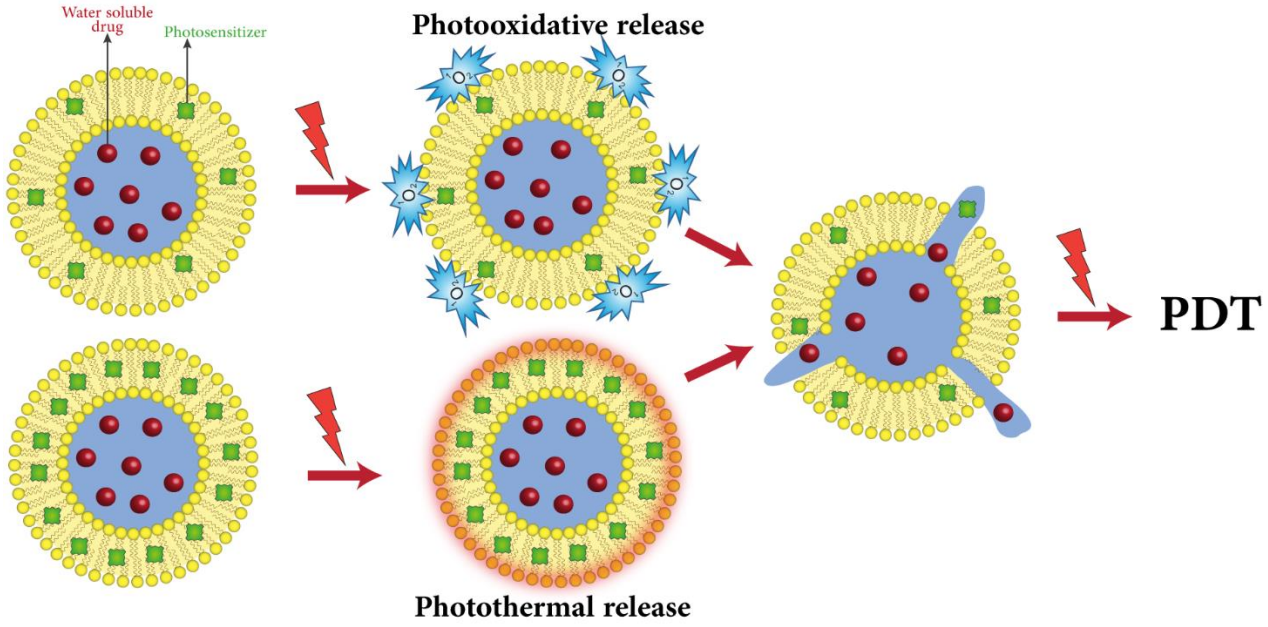

Figure 1.0. Light-triggered release mechanisms, either photooxidative based (up), or photothermal based (down). Both can lead, after a second illumination, to an additional modality: photodynamic therapy.

The main objective of this thesis was to design phototriggerable liposomes allowing drug release in a spatiotemporal manner. Our work was experimentally achieved following two strategies. The first one was based on the conception of liposomes with photooxidative-based release mechanism. The second strategy consisted in the development of liposomes with photothermal properties. We first conducted a mechanistic study in order to get deeper comprehension of the photooxidative-based release mechanism. Then, we developed two new lipid-porphyrin conjugates and studied their physico-chemical properties, phototoxic activity, and tried to find the best formulation for light-triggered release *via* a photothermal mechanism.

This thesis is divided in 4 chapters.

The **first chapter** details the state-of-the-art of phototriggerable liposomes based on the combination of lipids and porphyrin derivatives. It establishes the list of all the light-triggered release mechanisms and requirements for the development of such system. It also details the different strategies for the conjugation of porphyrin derivatives to different lipid backbones.

The **second chapter** reports on the evaluation of the influence of the hydrophobicity of free porphyrins, when embedded in lipid bilayers composed of phospholipids with different degrees of unsaturation. The purpose of this mechanistic study, correlated to molecular dynamics simulations, was to identify the important factors that must be taken into account when building phototriggerable liposomes based on a photooxidative mechanism.

The **third chapter** describes the synthesis of two new lipid-porphyrin conjugates, the assessment of their self-assembling and photooxidative properties, and their phototoxicity against esophageal squamous cancer cells.

The **fourth chapter** is dedicated to the study of possible use of these lipid-porphyrin conjugates for the conception of phototriggerable liposomes *via* a photothermal mechanism.

These chapters are followed by a general discussion on the main breakthroughs and critical points of this experimental work, and a conclusion opening towards new perspectives.

Chapter 1

State-of-the-art

1.1. Introduction

In the past few decades, the conception of nanoparticulate drug delivery systems (DDS) such as liposomes, organic and inorganic nanoparticles has become an integral part of the research for the development of an efficient anticancer therapy owing to their unique properties in increasing drug solubility, protecting fragile compounds against their degradability in the bloodstream, and reducing their side-effects thanks to better controlled biodistribution[11]. However, despite many improvements compared to free injected drugs, these drug delivery systems were still accompanied by systemic side effects due to nonspecific bio-distribution[12], and/or uncontrollable drug release from the surface of nanocarriers (burst release)[13]. To overcome these limitations, smart drug delivery systems (SDDS)[7,14–16] also known as stimuli-responsive drug delivery systems[17,18] have emerged as a promising nanotechnology compared to conventional nanomedicines, due to their unique spatiotemporal controlled activation/release mechanism[12,17,18]. Various activation modalities have been developed in the last years for triggering the release from these nanosystems and can be broadly classified into two categories, namely internal and external triggers[7,17]. While the internal stimuli are dependent on the characteristics of the targeted tissue such as pH[19], temperature[20], enzymatic expression[21] and redox potential[22], the external stimuli are independent of the biological systems since they are externally manipulated[17]. Among the different described stimuli, light appeared to be as one of the most versatile triggering methods, since (i) it is non-invasive, (ii) a wide variety of tissues can be easily irradiated endoscopically, and (iii) the light fluence, the wavelength as well as the illumination zone can be effectively tuned[23].

Although several novel smart drug delivery systems have been designed, most of them are still in development process or early clinical phases[24]. This is mostly due to their complexity, since they are composed of multiple components to provide the desired multifunctional properties[25]. In fact, the conception of SDDS presents several shortcomings, including the requirement for multistep synthesis and purification, complex toxicity studies for the multiple components and potentially heterogeneous formulations that jeopardize clinical translation as well as production at industrial scale[24,26,27]. Anselmo *et al.*[28] have excellently reviewed the list of intravenous nanoparticles systems that are either approved or currently in clinical trials and showed that the total number of FDA approved or under investigation intravenous nanoparticles do not exceed the number of 50, among which more than 50% are liposomal formulations. Indeed, compared to other drug delivery systems, liposomes have an aqueous solution core surrounded by lipid bilayers thus allowing the encapsulation of hydrophobic and hydrophilic drugs at the same time. Moreover, liposomes are made of biocompatible, biodegradable materials and can be easily produced at industrial scale, due to their simplicity and to lower investment costs compared to other nanoparticulate systems. Interestingly, the liposomes

surface can easily be functionalized with hydrophilic polymers such as PEG[5,29] and/or a specific ligand to delay clearance by the reticuloendothelial system and to reach specifically the target site[18,30,31] (Figure 1.1). In addition, the incorporation of a photoactive molecule called photosensitizer (PS) inside the bilayer allows the conception of photostimulable liposomes for cargo release.

Indeed, photosensitizers (PSs) are compounds that are usually used in photodynamic therapy (PDT) for treating several diseases including cancer and bacterial infections. These compounds are able to absorb light in visible/NIR regions and transform the light energy into the production of reactive oxygen species. When a PS is illuminated at a specific wavelength, it is temporarily brought to a highly excited singlet state, S_1 (Figure 1.1), then either goes back directly to its fundamental singlet state S_0 (through radiative transition called fluorescence), or undergoes intersystem crossing (ISC), a non-radiative transition, and reaches a lower energy excited triplet state T_1. The environmental oxygen, naturally found in triplet state ($^3O_2$), is a fluorescence quencher and thus preferably reacts with PS in its triplet state. This results in the generation of reactive oxygen species (ROS). Two kinds of reaction may occur: type I and type II which generate free radicals and singlet oxygen ($^1O_2$), respectively[32]. In type I reaction, an electron or a hydrogen atom is transferred to a neighboring molecule, and the PS triplet state can thus induce radical species formation and chain reaction. In type II reaction, a transfer of energy to oxygen ($^3O_2$) takes place, leading to the formation singlet oxygen ($^1O_2$). ROS can be used directly as cytotoxic entities as they strongly react with cell components (protein, DNA) and provoke organelles damage and cell death. This is the mechanism of photodynamic therapy (PDT)[32]. Taking advantage of the same mechanism, the production of ROS can be used as a trigger for controlled photoactivated drug release from liposomes.

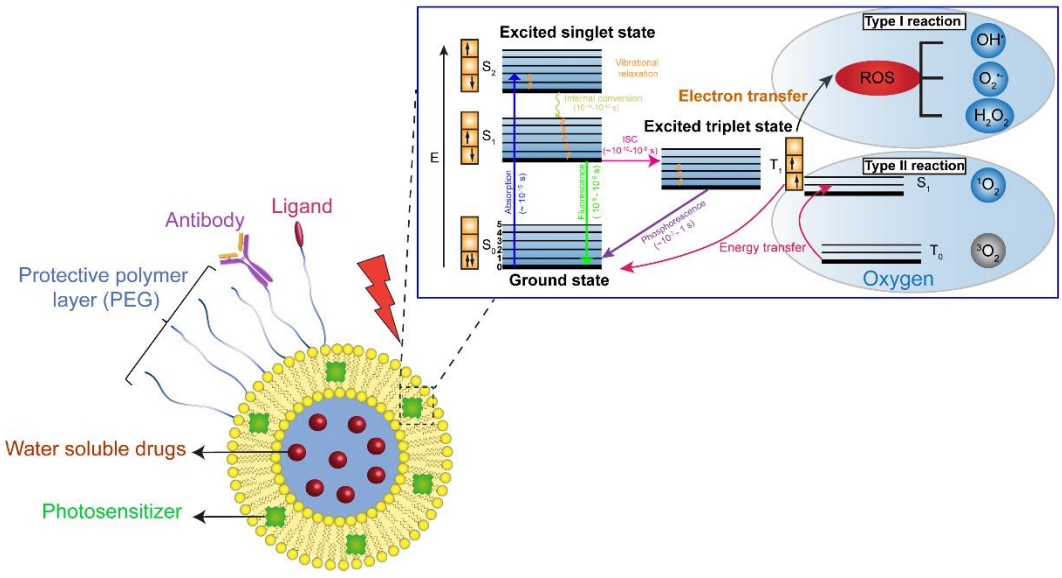

Figure 1.1. Scheme of a drug-loaded, multifunctional, phototriggerable liposomes and Jablonski diagram of an excited photosensitizer.

1.2. Phototriggering release strategies from liposome containing porphyrin derivatives

Although different classification systems were adopted for phototriggered liposomes, they can generally be divided into two main groups depending on the mechanism of interaction between the porphyrin derivatives and liposome bilayers. The first group consists in liposomes that release their cargo upon ***photochemical reaction*** between the illuminated porphyrin derivatives and the lipid bilayer. The second group of phototriggerable liposomes is based on a ***photophysical activation*** process (Figure 1.2).

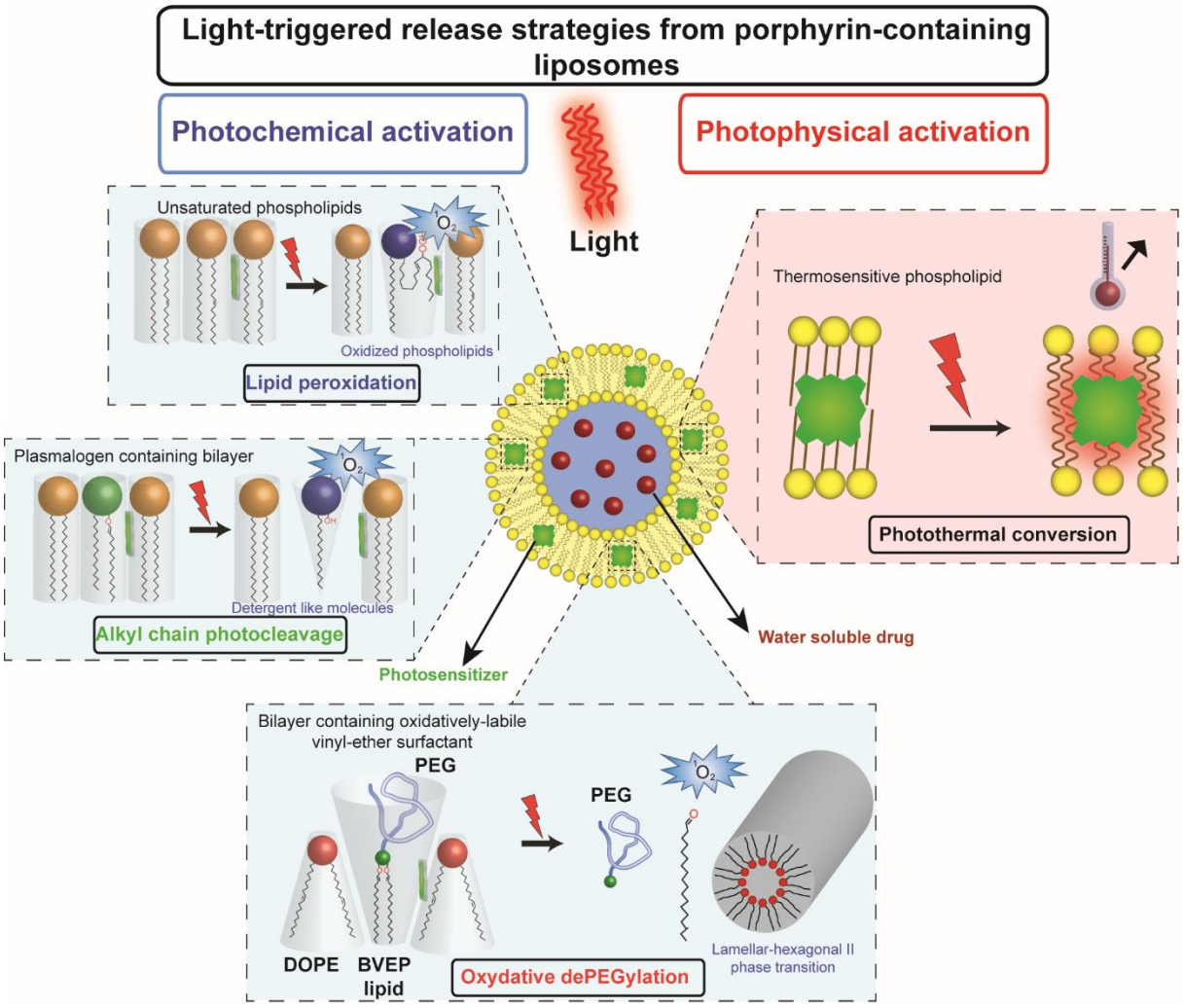

Figure 1.2. Light-triggered release modalities from porphyrin-containing liposomes.

1.2.1. Photochemical reaction for phototriggered release

The chemical reactions, which are initiated as a result of the absorption of light, are known as photochemical reactions. Indeed, the phototriggered release of encapsulated drugs from liposomes

via photochemical reaction is based on the modification of the bilayer integrity upon illumination. Several photochemical modalities have been proposed for the conception of phototriggerable liposomes which can be divided into two main groups. The first group is based on the use of chemically modified phospholipids that can be activated with UV light to experience either photoinduced crosslinking of lipids via photopolymerization mechanism or conformational change via a photoisomerization process[14]. Since these strategies do not require the presence of any photosensitizer embedded in the liposomal bilayer, they won't be discussed in this thesis. Furthermore, such modalities have been already reviewed by many authors[7–9,33–35].

The second group of light activatable liposomes consists in the photooxidation of lipid matrix upon illumination. Lipid photooxidation is one of the most common mechanism used for the conception of light-induced drug release from liposomes. This group of liposomes requires the combination of mono or polyunsaturated phospholipids with a photosensitizer that absorbs efficiently in the near infrared region (NIR) and possesses a high quantum yield of singlet oxygen. Upon illumination, the photosensitizers embedded in the lipid matrix generate reactive oxygen species (ROS), such as singlet oxygen ($^1O_2$). Singlet oxygen oxidizes the unsaturated chains of phospholipids (PLs), inducing dramatic alterations of the PL molecular organization and packing, which in turn leads to an increase in the liposomal membrane permeability[7,36]. Depending on the chemical structure of the phospholipid in the lipid matrix, the light-induced oxidation provokes different chemical modification in the phospholipids: (i) Lipid peroxidation, (ii) alkyl chain photocleavage and (iii) oxidative dePEGylation.

1.2.1.1. Lipid peroxidation

Lipid induced peroxidation can be generally described as a process under which $^1O_2$ generated by the illuminated porphyrins via type II reaction, oxidizes lipids containing carbon-carbon double bonds with oxygen insertion resulting in lipid hydroperoxides formation. This strategy requires three elements: PS, light, and a peroxidation target (usually an unsaturated phospholipid). Once the unsaturated lipid chain undergoes oxidation, the newly formed hydroperoxide (OOH)[37] destabilizes the lipid chain packing due to the conformational rearrangements[38] of oxidized phospholipids to drive hydroperoxyl groups towards polar headgroups with an increase in area per lipid[39,40] , like truncated PLs do with their carbonyl or carboxylic groups[41–43]. This results in an increase of membrane permeability which causes cargo leakage[36,44,45]. Monounsaturated, polyunsaturated phospholipids[36] and cholesterol[46] are well-known targets for oxidization by $^1O_2$. These lipids can be embedded in the liposomal bilayer at different molar ratios in order to modulate the release kinetics of the cargo. In monounsaturated phospholipid, $^1O_2$ is inserted to one of the C-atoms of the double bonds in a concerted and specific way known as "ene addition"[47]. The resulting hydroperoxides have an allylic

trans double bond[47] (Figure 1.3). Lipid hydroperoxides can also be formed following a different chemical pathway, upon their interaction with free radicals generated *via* type I reaction, in which the PS acts as free radical initiator. To understand the mechanism of oxidization of double bond by singlet oxygen, and why the double bond is a potential target for oxidization, a brief explanation about the chemistry of $^1O_2$ and its reactivity from a thermodynamic point of view is given in this chapter. The energy of $^1O_2$ is 92 kJ/mol above the ground state of triplet oxygen and exists long enough to react with non-radical, singlet state, and electron-rich compounds containing double bonds such as unsaturated phospholipids[48–50]. The lifetime of singlet oxygen ranges from 50 to 700 µs, depending on the medium in which it is formed. Also, singlet oxygen has a longer half-life in lipid membrane than in aqueous media[48], which favors its reactivity with the lipid matrix. In addition, singlet oxygen reactivity increases in direct proportion to the number of double bonds present in alkyl chains, with the following values: 1.1; 1.9; 2.9 for 18:1; 18:2 and 18:3, respectively[47].

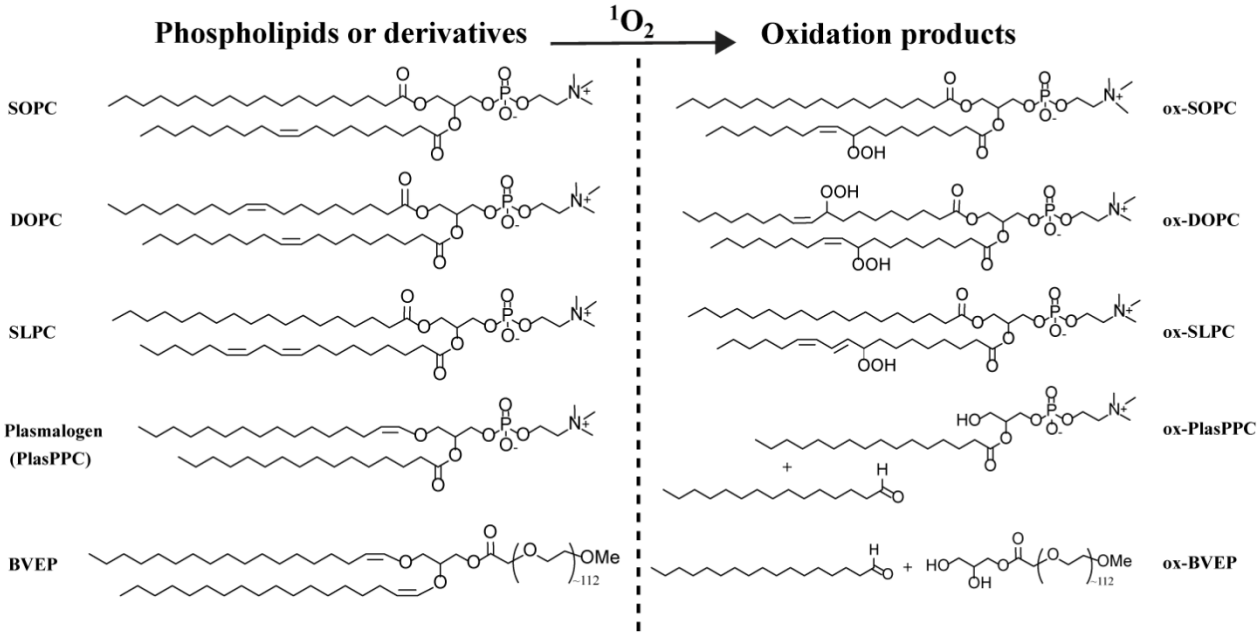

Figure 1.3. Monounsaturated and polyunsaturated phospholipids, and other lipid derivatives together with their corresponding oxidation products. (Note: only the 9-hydroperoxide is presented. While the oxidation of oleate chain produces a mixture of 9- and 10-hydroperoxides, the linoleate one generates a mixture of 9-, 10-, 12- and 13-hydroperoxides).

Many systems have been reported based on lipids peroxidation, using a large variety of porphyrin derivatives (porphyrins, chlorins, phthalocyanines, Figure 1.4, Table 1.1) and phospholipids (Figure 1.3, Table 1.1). Mojzisova et al.[36] studied the release of carboxyfluorescein from DOPC liposomes using three different chlorins: *m*-THPC (marketed as Foscan®), Chlorin-e6, and the disulfonated tetraphenyl chlorin (TPCS2a). They emphasized the fact that the deeper inserted PS in the lipid bilayer, the neutral symmetric *m*-THPC, was more likely to be efficient in unsaturated lipid

peroxidation. On the contrary, a negatively charged chlorin was less efficient, because it was localized closer to the lipid bilayer polar head groups, in a remote position relative to the phospholipid double-bonds. Pashkovskaya *et al.*[45] introduced another strategy, using egg-PC liposomes encapsulating a water-soluble PS, the trisulfonated aluminium phthalocyanine ($AlPCS_3$) in the aqueous core together with the cargo to be released. They showed that this system was less efficient for light-triggered release of hydrophilic cargos (1-aminonaphthalene-3,6,8-trisulfonic acid (ANTS) / p-xylene-bis-pyridinium bromide (DTX) pair, carboxyfluorescein, calcein and sulforhodamine B) than when the PS was embedded into the lipid bilayer, as in the case of chlorin-e6.

Rwei *et al.*[51] have recently developed near-infrared (NIR) light-triggered liposomes (Lipo-PS-TTX) to provide on-demand adjustable local anesthesia using DLPC-containing liposomes, incorporating a NIR-absorbing phthalocyanine (NIR-absorbing photosensitizer 1,4,8,11,15,18,22,25-octabutoxyphthalocyaninato-palladium(II), PdPC(OBu) and encapsulating Tedrotoxin (TTX) as a potent anesthetic agent. The efficiency of this system was demonstrated *in vitro* as well as *in vivo*. In *in vitro* experiments, authors showed that the lipids peroxidation following the illumination of Lipo-PS-TTX at 730 nm (50 mW/cm^2, 10 min) induced the release of 5.6% of TTX after the first illumination, which remained almost constant over the ensuing 2 hours. The phototriggered release of TTX was repeatable following a second illumination in the same conditions. Interestingly, there was no degradation of TTX during the light induced production of singlet oxygen in multivesicular liposomes. Moreover, the authors demonstrated the spatiotemporal control of TTX release in *in vivo* experiments. Indeed, the injection of Lipo-PS-TTX at the rat sciatic nerve induced nerve blockade lasting approximately 13 h, and this effect could be prolonged for additional ~ 3 hours upon laser illumination. In another study, the same authors increased the efficiency of a number of triggerable nerve blocks by co-delivering a second compound, dexmedetomidine (DMED) encapsulated separately in other liposome suspensions. The addition of DMED to the phototriggered system, potentiated the effect of local anesthetics due to induced local vasoconstriction[52]. Spring *et al.*[53] have developed a new photoactivatable multi-inhibitor nanoliposome (PMIL) that consists of liposomes doped with verteporfin in the lipid bilayer and encapsulating PLGA-PEG (poly-(lactic acid-co-glycolic) acid–polyethylene glycol conjugate) nanoparticles that contain a multikinase inhibitor (carbozantinib, XL 184). The PMIL illumination *in vitro* with NIR light induced the slow release of XL184 that reached 85% after 312 hours. Interestingly, the authors demonstrated that the release was mainly due to the generation of photoinduced ROS since the addition of reactive oxygen species scavenger (sodium azide) suppressed significantly the cargo release. Moreover, the intravenous injection of PMIL systems in mice triggered photodynamic damage of tumor cells and microvessels, and simultaneously initiated release of XL184 inside the tumor[53].

Table 1.1. Light-triggered release systems consisting of PS incorporated into liposomes

PS	mol%	co-excipient (mol%)	cargo	light-triggered release mechanism (wavelength / power)	References
Zn-phtalocyanine	0.002	PlasPPC : DPPC (89 : 11)	Glucose	Photocleavage (>640 nm / 80 mW/cm^2)	54
1 : Zn-phtalocyanine 2: Tin-phtalocyanine ($SnCI_2Pc(OBu)_8$)	1: 0.06 2: 0.007 3: 0.1	PlasPPC	Calcein	Photocleavage (1: >640 nm / 80 mW/cm^2 2,3: 800 nm / 300 mW, 75 min)	14
BChla	nd	DOPE : BVEP (97 : 3)	Calcein	dePEGylation 800 nm / 300 mW	8
m-THPC Chlorin-e6 TPCS2a	1	DOPC (99)	Carboxyfluorescein	Lipid peroxidation (650 nm / < 400 mW)	36
AlPcS3 Chlorin e6 $ZnPcGlyc_4$	nd	egg-PC	Calcein Carboxyfluorescein Sulforhodamince B	Lipid peroxidation (>580nm / 30 mW/cm^2)	45
Pd-phtalocyanine	0.45	DSPC : DLPC : DSPG : Chol (27.15 : 27.15 :18.1 : 27.15)	TTX	Lipid peroxidation (730 nm / 50-330 mW/cm^2)	51
Pd-phtalocyanine	0.45	DSPC : DLPC : DSPG : Chol (27.15 : 27.15 :18.1 : 27.15)	TTX/DMED	Lipid peroxidation (730 nm / 100 mW/cm^2)	52
HPPH	~10	DPPC : $DC_{8,9}PC$: $DSPE\text{-}PEG_{2000}$ (86:10:04 or 76:20:04)	Calcein	Photopolymerization (660 nm / 90 mW, 0-5 min)	55
Verteporfin	nd	DPPC : DOTAP : Chol : $DSPE\text{-}PEG_{2000}$ (58.8 : 5.9 : 29.4 : 5.9)	XL184	Lipid peroxidation hypothesis (690 nm / 100 mW/cm^2)	53
Pyropheophorbide-a conjugated to GPLGLAG –PEG_{5000}	4	DPPC : DSPC (72 : 24)	Doxorubicin HOC	Photothermal release (670 nm / 150-300 mW/cm^2)	56

Note: Semi-synthetic plasmenylcholine l-alk-1'-enyl-sn-glycero-3-phosphocholine (PlasPPC); Tin(IV)1,4,8,11,15.18,22,25-octabutoxyphthalocyanine dichloride ($SnCI_2Pc(OBu)_8$); Bchla (Bacteriochlorophyll a); PEG-lipid conjugate (BVEP); 2-[1-hexyloxyethyl]-2-devinyl pyropheophorbide-a (HPPH); Cabozantinib (XL184); 1,2 bis(tricosa-10,12-diynoyl)-sn-glycero-3-phosphocholine ($DC_{8,9}PC$), dexmedetomidine (DMED); Oxaliplatin prodrug (HOC).

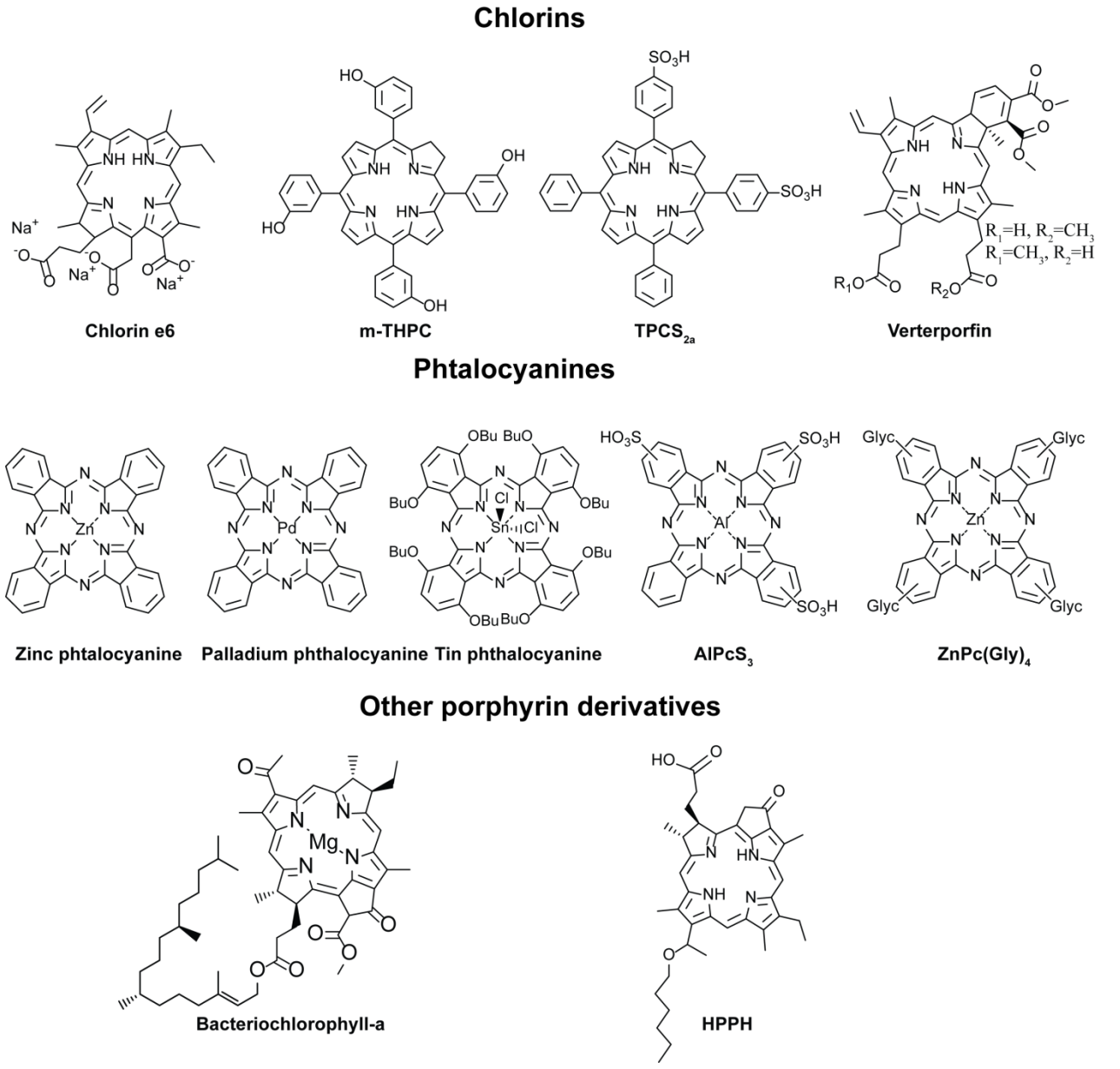

Figure 1.4. Chemical structures of some porphyrin derivatives incorporated into liposomes for phototriggerable liposomes conception.

1.2.1.2. Alkyl chains photocleavage

The photocleavage-induced controlled release of hydrophilic agents from liposomes involves the incorporation of photocleavable phospholipid such as plasmalogen with a photosensitizer into the liposomal membrane. Indeed, plasmalogens possess a labile sn-1 vinyl ether (Figure 1.3) which can be easily cleaved by the singlet oxygen produced by the activated photosensitizer[54]. The plasmalogens photocleavage provokes the loss of their amphiphilic character with concomitant destabilization in the liposome [27]. The first report on this strategy was published by Anderson *et al*. in 1992[54]. In this study, the authors demonstrated visible light-triggered release of glucose from liposomes composed

of semi-synthetic plasmalogen lipids (1-alk-1′-enyl-2-palmitoyl-sn-glycero-3-phosphocholine (PlasPPC)/1,2-dipalmitoyl-sn-glycero-3-phosphocholine (DPPC) (8:1)) with the photosensitizer zinc phthalocyanine (ZnPc) incorporated within the hydrophobic region of the membrane. Irradiation of air-saturated liposomes with visible light at 37 °C for 60 min resulted in the release of 62% of encapsulated glucose, twice the amount released in the corresponding dark control experiment.

The phototriggered efficiency of the system was later improved by the same authors by incorporating into liposomes made of 100% plasmalogens (PlsPamCho), different photosensitizers (zinc phtalocyanine, tin octabuoxyphtalocyanine or bacteriochlorophyll that absorb light between 630 and 820 nm, thus allowing content release by red and NIR light[14]. Liposomes incorporating bacteriochlorophyll-a appeared to be the most efficient system by producing 100% of calcein release within 20 minutes. The releasing rate was two order of magnitude that of liposomes made of egg-lecithin[14]. Despite the release improvement with plasmalogen-containing liposomes compared to unsaturated phospholipids, it should be noticed that such system is not specific to oxidative cleavage only, because the vinyl-ether function is also an acid-labile function[57,58]. This in turn may lead to loss in the spatiotemporal control with light. Indeed, these liposomes can release their content in the endosomal compartment after their endocytosis in a cell, which can be problematic for encapsulated active ingredients that are fragile at acidic pH.

1.2.1.3. Oxidative dePEGylation

Oxidative dePEGylation is another photoinduced cleavage approach which is based on the use of a PEG-conjugated lipid possessing a vinyl-ether linkage 1,2-di-O-(1'Z,9'Z-octadecadienyl)-glyceryl-3-(ω-methoxy-poly(ethylene glycolate)) (BVEP) that is incorporated with DOPE phospholipids to form stable liposomes[8,57,58]. Indeed, DOPE phospholipids have inverted cone shapes due to their relatively small headgroup compared to their alkyl tails. They cannot form lamellar phase on their own but are able to form inverted hexagonal phase (H_{II})[59]. However, when mixed with BVEP which has a complementary geometrical shape (cone shape), they can form stable lamellar phase. Hence, the photooxidative PEG cleavage results in the transition from the well-ordered lamellar phase of lipid bilayers, to an hexagonal phase, ending up into membrane fusion and leakage of the hydrophilic cargo[8].

1.2.1.4. Other mechanisms of photochemical membrane destabilization

Other mechanism of liposomes bilayer destabilization by activated photosensitizers have been described in the literature. One of these systems is called "POCKET" liposomes by Sine *et al.*[55]. These systems consist of DPPC liposomes containing diacetylenic phospholipid 1,2-di-(10Z,12Z-tricosadiynoyl)-sn-glycero-3-phosphocholine also known as $DC_{8,9}PC$. This phospholipid behaves differently depending on the wavelength of the used light[55]. Indeed, authors demonstrated that while the illumination at 254 nm of liposomes containing $DC_{8,9}PC$ in the absence of a PS induced photocrosslinking of the corresponding alkyl chains (photopolymerization)[60], the visible-light-mediated release (λ = 514 nm) occurred *via* a mechanism unrelated to polymerization[61]. However, the photoactivation of liposomes at both wavelengths induced efficient cargo release[62–64]. The same authors also demonstrated that $DC_{8,9}PC$ molecules may segregate together to form domains in the liposomal membrane called "Pockets" and they hypothesized that 2-(1-Hexyloxyethyl)-2-devinyl pyropheophorbide-a (HPPH) incorporated as photosensitizer would preferentially partition into the boundary regions of these domains within the lipid bilayer. It was also hypothesized that the photoactivation of HPPH caused the destabilization of pockets, resulting in defects in the liposome bilayer with concomitant calcein release that reached ~ 35% after 5 minutes of laser treatment at 660 nm[55].

1.2.2. Photophysical reaction for phototriggered release

The release induced by photophysical reaction from liposomes does not rely on any chemical change in lipid structure inside the liposomal membrane. This effect is based on the photothermal conversion of the absorbed light inducing a thermal and/or mechanical stress on the lipid membrane with subsequent cargo release[9]. Such strategy requires the use of photosensitizers that have a quenched fluorescence through concentration effect in the lipid membrane. Indeed, in this situation the absorbed photonic energy that is usually released as fluorescence and singlet oxygen is dissipated thermally through vibrational relaxation[6,65]. Such phototriggering modality is of great interest and presents several advantages compared to those based on photooxidative reaction for hypoxic tumors ablation[66]. Indeed, human solid tumors are less oxygenated than the respective normal tissues due to the imbalance between oxygen (O_2) supply and consumption[67]. This so-called tumor hypoxia leads to resistance to numerous cancer therapies including ionizing radiotherapy, anticancer chemotherapy[67] as well as the photodynamic therapy which in turn reduces the efficiency of the photooxidative release[66].

However, this phototriggering release modality is usually uncommon with free porphyrin derivatives since these latter can only be incorporated at low concentration (< 10 mol %) in the lipid bilayer. Very recently, in 2017, Zhou *et al*.[56] designed a new programmed multiresponsive nanosystem based on enzyme, light and temperature multi-sensitive liposome (ELTSL), incorporating pyropheophorbide-a linked to PEG via a heptapeptide that is cleavable by matrix metalloproteinases 2 (MMP-2), and encapsulating doxorubicin and oxaliplatin prodrug (HOC). The illumination of these drug delivery systems at 670 nm with a fluence of 300 mW/cm^2 induced a thermal increase up to 45°C with subsequent release of approximately 85 % of both cargos within 2 minutes[56].

1.2.3. Requirements for successful phototriggerable porphyrin-containing liposomes

In order to formulate successful phototriggerable porphyrin-containing liposomes, several criteria should be taken into account especially those concerning the selection of photosensitizers and phospholipids.

1.2.3.1. The choice of the photosensitizer

Several structural and photophysical properties should be taken into account for the selection of PS for the conception of phototriggerable liposomes:

- A photosensitizer should have a **high molar extinction coefficient** (**ε**, $M^{-1}.cm^{-1}$) in the near infrared region (NIR), known as the "**phototherapeutic window**" (650-850 nm). In fact, there are three main chromophores in the skin (eumelanin, hemoglobin and water) that possess several strong absorption bands in the visible region from 500-600 nm. The incident light in this region will be very highly absorbed by the skin and the penetration depth of light will be too low[68]. Porphyrins, chlorins and phthalocyanines have two major absorption bands, a strong Soret band around 400 nm, and multiple less intense Q bands of lower energy between 450-800 nm. For phototriggerable release, and in order to get deeper penetration of light, the PS excitation is achieved in the Q-bands region (Figure 1.5).
- A high **$^1O_2$ quantum yield** (**$\Phi_\Delta > 0.5$**) should be obtained after the illumination of the PS, which is necessary to induce the photooxidative release.

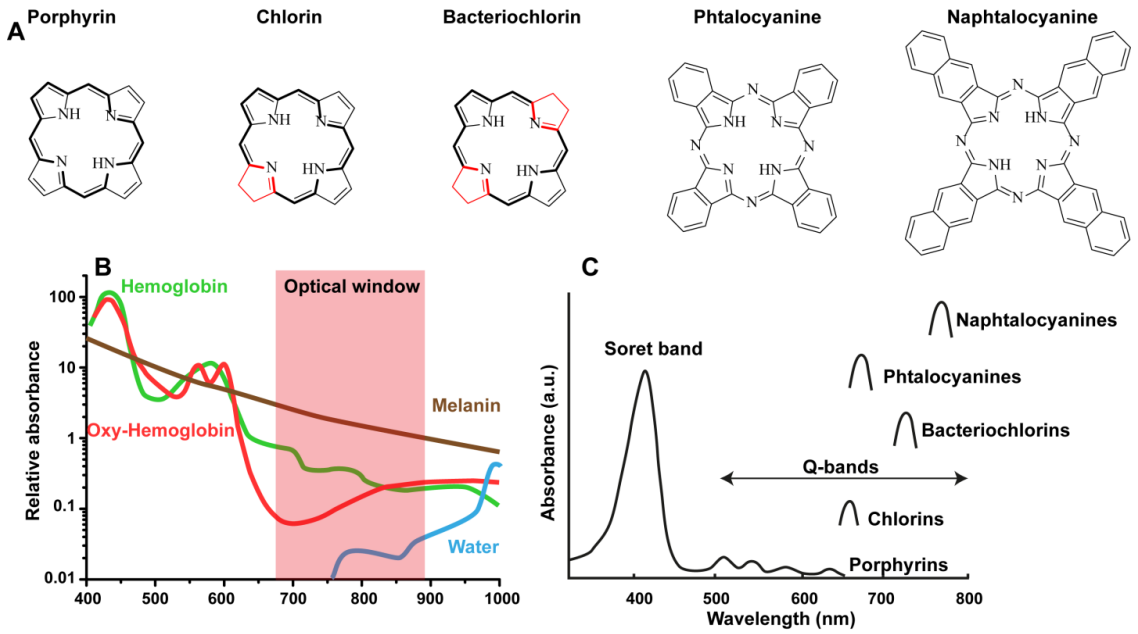

Figure 1.5. A. Chemical structures of some porphyrins derivatives. B. Relative absorbance of hemoglobin, oxy-hemoglobin, melanin and water. C. Absorption spectra of some porphyrin derivatives. The full spectrum corresponds to that of a porphyrin photosensitizer. The additional peaks correspond to the approximate position of the last Q-band of each photosensitizer (the peak intensities are not in scale).

- The **hydrophobicity** of the photosensitizer is one of the most important criteria to be taken into account. In fact, the majority of photosensitizers used in the formulation of phototriggerable liposomes are porphyrin derivatives. These compounds are hydrophobic and tend to form aggregates, which reduces their efficient singlet oxygen generation[69]. Although several liposomal delivery system containing porphyrin derivatives[70,71] have been successfully formulated and were tested either *in vitro*/*in vivo* or FDA approved[71], porphyrins incorporation into liposomal membrane is still considered as a challenging task and can only be achieved at very low percentage[72]. Furthermore, the hydrophobicity of the photosensitizers can control their partition towards blood proteins and lipoproteins[73,74] and consequently the stability of their entrapment in the lipid bilayer. The hydrophobicity of the photosensitizer may control its localization in the bilayer and thus its photooxidative permeation efficiency. In fact, it was always thought that the photopermeabilization efficiency is related to the importance of the damage in the lipid bilayer that occurs to high extent with a deeply inserted PS[36]. However, several reports have demonstrated that the efficiency of photoinduced permeabilization is more related to the asymmetric repartition of the damage in lipid bilayers[75].
- **Low dark toxicity**: to avoid any side effects after the injection of the phototriggerable liposomes.

1.2.3.2. The choice of the phospholipid

The choice of phospholipids depends mainly on the phototriggering mechanism. For example, in the case of photochemical induced release based on a photooxidative reaction, mono or polyunsaturated phospholipids should be used. Obviously, the higher the number of olefin double bonds in the alkyl chain, the more efficient the phototriggered release. However, increasing the content of unsaturated phospholipids in the lipid membrane decreases the packing order and causes an increase in membrane permeability. This in turn provokes passive leakage of the cargo. Recently, Maherani *et al.*[76] have studied the impact of liposome composition on the passive release of an hydrophilic cargo (calcein) from large unilamellar vesicles made of 1,2-dioleoyl-sn-glycero-3-phosphocholine (DOPC), 1-palmitoyl-2-oleoyl-sn-glycero-3-phosphocholine (POPC) or 1,2-palmitoyl-sn-glycero-3-phosphocholine (DPPC). DOPC liposomes exhibited the highest release rate of calcein, followed by POPC and DPPC respectively[76].

1.2.4. Limitations of free porphyrin derivative-containing liposomes for light-triggered release

The efficiency of photooxidation-induced release relies on the quantum yield of singlet oxygen of a PS present in the unsaturated lipid bilayer. Increasing concentration of the PS in the bilayer induces aggregation, which directly correlates with a decrease in singlet oxygen quantum yield[77]. Overall, photooxidation must be performed with a limited amount of PS inside the lipid bilayer (as depicted in Table 1.1), to ensure a maximum quantum yield in singlet oxygen. This limited amount of PS in the lipid bilayer often results in an incomplete cargo release. Furthermore, photosensitizers embedded into liposomes have poor entrapment stability and tend to escape from the lipid bilayer due to strong hydrophobic interactions with blood proteins and lipoporoteins[69,78,79]. PS escape from the lipid bilayer is accelerated by membrane peroxidation that makes the lipid matrix more polar, thus less suitable for PS retention.

In addition to PS loss, the passive leakage of the hydrophilic cargo is also commonly observed because the presence of unsaturated lipids in the bilayer (as shown in the Table 1.1) significantly increases membrane fluidity[46,80]. This uncontrolled release may be a problem, as it may induce severe undesired side-effects. Furthermore, passive release is against the concept of light-triggered release, since the original purpose is to deliver the encapsulated drug at the right place and right moment.

Another important limitation for controlled release from lipid vesicles is that photooxidation is a photochemical reaction, and thus a non-stoppable process. It leads to continuous leakage with time of the cargo, after the first illumination. This continuous release tends to equilibrate over time due to

the difference in osmotic pressure between the inner core and the outside environment of vesicles, or due to pore resealing.

Photooxidative release studies have mostly been conducted *in vitro*, using fluorescent probes as cargos (Table 1.1). However, one has to keep in mind that tumor tissues *in vivo* are generally in hypoxia conditions, so significant oxidation has little chance to occur[6]. Only few recent studies[53,55] have shown the potential of light-triggered release for *in vivo* applications in cancer. However, in both cases, the suggested release mechanism was not clearly demonstrated, and might not be a photooxidative-based mechanism. Thus, based on these drawbacks, the photothermal release modality from liposomes appeared to be more promising for *in vitro/in vivo* applications. However, as such modality seems to be not achievable with free inserted porphyrin derivatives in the bilayer, the synthesis of lipid-porphyrin conjugates has emerged as an efficient strategy for the conception of phototriggered liposomes with multifunctional properties.

1.3. Lipid-porphyrin conjugates: an emerging supramolecular strategy for conception of phototriggerable liposomes with multifunctional properties

Recently, a new category of supramolecular photosensitizers[10,81] based on lipid-porphyrin conjugates has emerged as promising approach for the conception of multifunctional drug delivery systems with phototriggerable release properties and rejuvenated the application of photodynamic therapy for cancer treatment[82]. Among a plethora of lipid-porphyrin conjugates described in the literature, those developed by Gang Zheng's group[10] appeared to be the most efficient compounds for the conception of multifunctional drug delivery systems[6,83]. Indeed, these compounds are able to self-assemble into liposome-like structures called porphysomes[6] that are formed of non-covalent association of 80,000 lipid-porphyrin conjugates approximately[6]. The lipid-porphyrin conjugate nanotechnology is a real benefit for light-triggered API release. Indeed, the covalently bound PS, once incorporated into the lipid bilayer, is less prompt to leave the lipid matrix through protein interactions[78], because it develops stronger intermolecular interactions with phospholipids of the bilayer than the free PS. The nanocarrier can reach the target cell with the initial amount of inserted PS in the bilayer before light-triggered release is activated. It is also a manner to improve the incorporation rate of PS into liposomes. In comparison, incorporation of free PS in the lipid matrix is limited to a certain amount (about 2.5 to 15% mol depending on the PS)[6] due to rapid aggregation. This uncontrolled aggregation directly affects optical properties of the PS, and subsequently affects the efficiency of light-triggered release.

Interestingly, porphysomes can offer the usual applications of liposomes, such as surface functionalization for targeting, aqueous core loading, as well as photodynamic therapy. The high-PS payload enables additional applications, for imaging (MRI), and for photothermal therapy (Figure 1.6). Obviously, lipid-porphyrin conjugates, self-assembled into porphysomes, or combined with other phospholipids to form high-payload liposomes, are of great interest for light-triggered release.

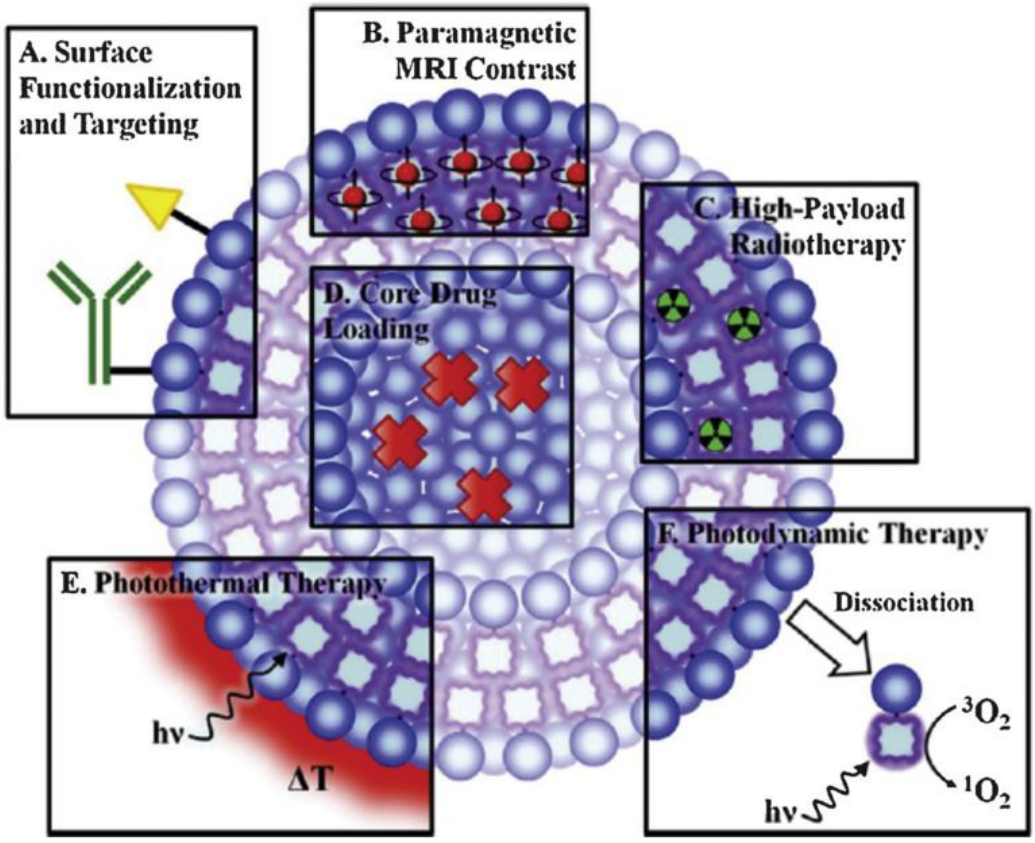

Figure 1.6. Porphysome nanotechnology multiple applications. Adapted from Huynh *et al.*[15]

Both light-triggered release mechanisms can be considered when using a lipid-porphyrin conjugate: either photochemical-based (photooxidative), or photothermal-based (photophysical-based) release. These mechanisms differ in two requirements: the amount of encapsulated PS in the lipid bilayer, and light intensity. Photooxidative-induced release depends on the molecular oxygen and the quantum yield in singlet oxygen of the PS, activated by light in a large range of fluences (2 mW/cm^2 up to several hundreds of mW/cm^2) (Table 1.1). As previously mentioned, the quantum yield of the PS is directly correlated to its aggregation state, and monomeric PS is required for efficient photodynamic effect (as depicted in Table 1.1). On the other hand, photothermal effect relies on the fluorescence quenching of encapsulated PSs. This is only possible when highly concentrated PS molecules form closely packed aggregates in the lipid bilayer due to π- π stacking of porphyrin cores[84,85]. In addition, the second requirement is the use of laser with high-power lasers density (hundreds of mW/cm^2 to

several W/cm^2)[9,86]. In the second part of this chapter, we review the different lipid-porphyrin conjugates that are described in the literature with special emphasize on those that can self-assemble into porphysomes and be applied to light-triggered release.

1.3.1. Strategies of modification of lipids by porphyrins

Several strategies have been developed for conjugation of a porphyrin derivative to the desired lipid (Figure 1.7), including:

(i) binding the porphyrin to the polar head group of the lipid,

(ii) direct modifications of the porphyrin itself, by adding hydrophobic moieties (such as cholesterol or long hydrocarbon chains) conferring lipid-like properties,

(iii) binding the porphyrin at the extremity of the alkyl chain,

(iv) full synthesis of a synthetic lipid to obtain "lipid-like"-porphyrin conjugate,

(v) binding the porphyrin along the alkyl chains of the lipid by sn-2 conjugation.

Lipid modification may have significant consequences on the properties of lipid bilayers, including their thickness, stability and molecule packing parameter. Indeed, porphyrins are large, flat and highly hydrophobic molecules, so their conjugation to a lipid will induce significant alterations of the lipid properties.

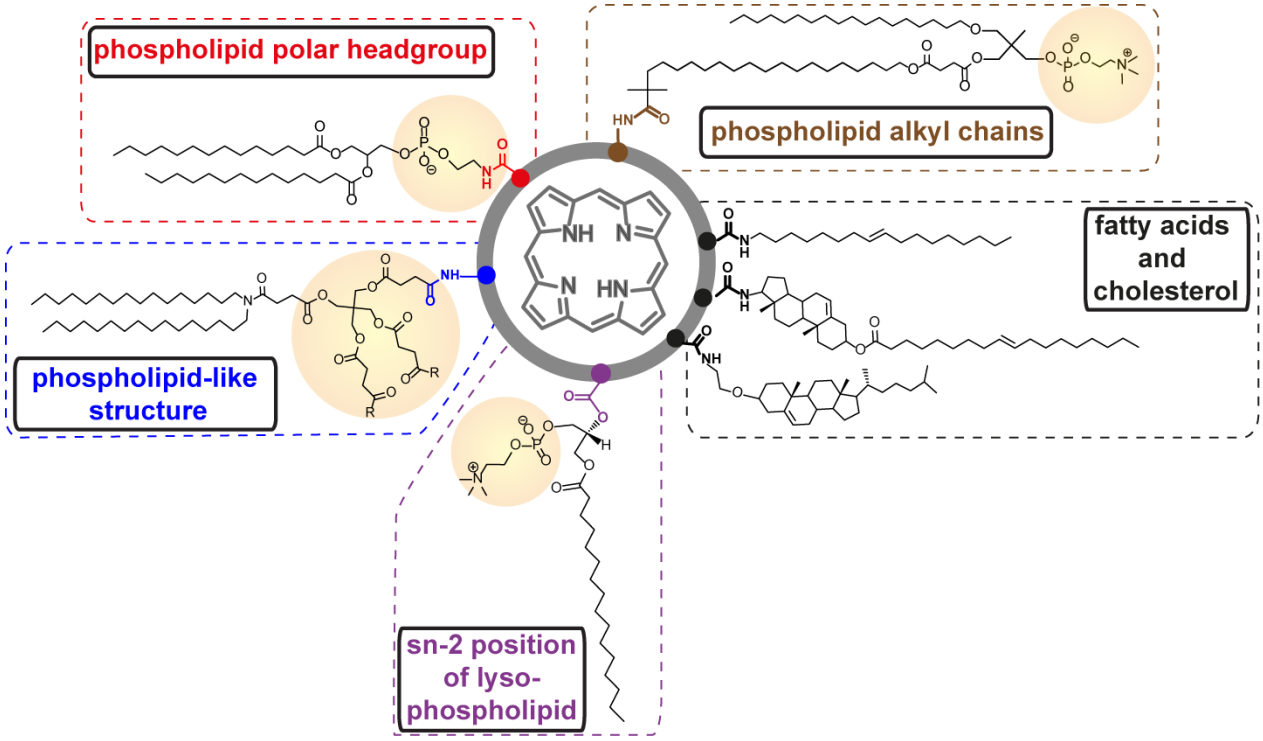

Figure 1.7. Lipid-porphyrin conjugation strategies.

1.3.1.1. At the level of the phospholipid polar head group

The most straightforward strategy for phospholipid modification is by using the free amine of phosphatidylethanolamine to conjugate molecules, such as fluorescent groups (NBD-lipid) or polyethylene glycol chain (DSPE-PEG). Riske *et al.*[87] used this strategy to develop PE-porphyrin molecules (Figure 1.8), by covalently binding protophorphyrin IX to the polar head group of dimyristoyl-phosphatidylethanolamine (DMPE), each porphyrin bearing two DMPE molecules[87]. Although this was not clearly demonstrated, self-assembling of such PE-porphyrin molecules is quite improbable, due to structural and geometrical constraints. Indeed, the amphiphilic properties of the lipid are lost, and the volume of the polar head is significantly affected by the presence of the PS: this prevents good molecular packing. Generally speaking, an increase of the polar head volume, either by hydrophobic groups like PS or hydrophilic groups (like PEG chains), results in the formation of micelles. Riske *et al.*[87] showed that up to 10 mol% PE-porphyrin could be incorporated in giant vesicles made of lipids such as POPC and DMPC, and that the PS remained exposed at the surface of the bilayer. In addition, an increase in the lipid bilayer area after irradiation was observed, due to direct peroxidation of the unsaturated POPC and subsequent hydroperoxide groups formation (Figure 1.8). However, binding the PS to the polar head of lipids may not be the best strategy, as it may disrupt the lipid bilayer integrity at high incorporation rate and may not be compatible with cargo release since the PS is not inserted in the vicinity of the lipid matrix.

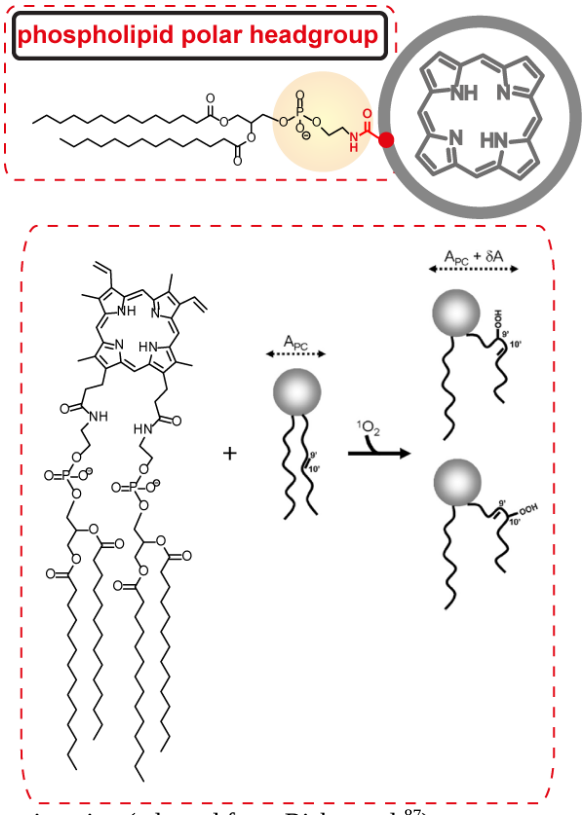

Figure 1.8. Polar head conjugation (adapted from Riske et al.[87])

1.3.1.2. Porphyrin derivatives conjugation to lipid derivatives: fatty acids and cholesterol

This coupling strategy consists in adding either one[88], or two alkyl tails[89,90] to the PS, or a cholesterol moiety (Figure 1.9).

- **Alkyl-tails conjugation**

In one application, an hexadecyl alkyl chain was conjugated to methyl-pheophorbide a (Figure 1.9 A). The conjugate showed self-assembling properties into micelles when mixed with egg-PC lipids[88]. However, those micelles were not stable and quickly aggregated[88]. Temizel *et al.*[89] functionalized protoporphyrin IX with two oleylamine chains (Figure 1.9 B) to generate the lipophilic conjugate PPIX-Ole[89]. This latter could be efficiently incorporated into a DOPC lipid bilayer (10 mol%) and showed higher photodynamic activity *in vitro* compared to free PPIX due to its higher internalization into cells[89]. Similarly, Nathan *et al.*[90] proposed a strategy in which 5-(4-carboxyphenyl)-10,15,20-triphenylporphyrin was covalently bound to the polar head group of a didodecyl-L-glutamide derived lipid (Figure 1.9 E). This (1:1)–lipid:PS conjugate was successfully incorporated in egg-PC or DPPC liposomes with an incorporation rate of 10 mol%. Taken together, grafting one or two alkyl chains on the porphyrin moiety shows limitations, in terms of liposome formulation, and doesn't show significant improvement compared to free porphyrins.

- **Cholesterol moiety conjugation**

Cholesterol, the most commonly found sterol in mammalians membrane, cannot form bilayer on its own[91,92]. However, due to its amphiphilic properties, cholesterol orients along the lipid bilayer normal, inserting its hydrophobic backbone into the hydrocarbon region while maintaining contact between its OH group and the polar headgroup region[93]. In addition, the OH group can be conjugated via esterification reaction to a porphyrin derivative possessing a carboxylic group. Nikolaeva *et al.*, showed that the conjugation of chlorin-*e*6 to cholesterol moiety (Figure 1.9 C) allowed the incorporation of the conjugates into egg-PC vesicles (about 2 mol%) by exposing the porphyrin core outwards the lipid bilayer[94]. The same group synthesized another form of chlorin-cholesterol conjugates (Figure 1.9 A), by covalent binding of methyl pheophorbide-a derivatives[88]. Interestingly, once mixed to egg-PC at different ratios, those conjugates could form micelles, with significant red-shift of the Q-band (from 667 nm to 710 nm), indicating stacking of the PS in the assemblies. However, these micelle-like structures were not stable and quickly formed aggregates, making impossible additional drug encapsulation and light-triggered release. Zheng *et al.*[95] showed that cholesteryl oleate, once conjugated to pyro-pheophorbide a (Figure 1.9 D), could be used as an anchor in the lipid matrix

core of LDL[95,96]. This strategy was efficient for better membrane or lipid matrix incorporation, but it was not investigated for cargo release from liposomal formulations.

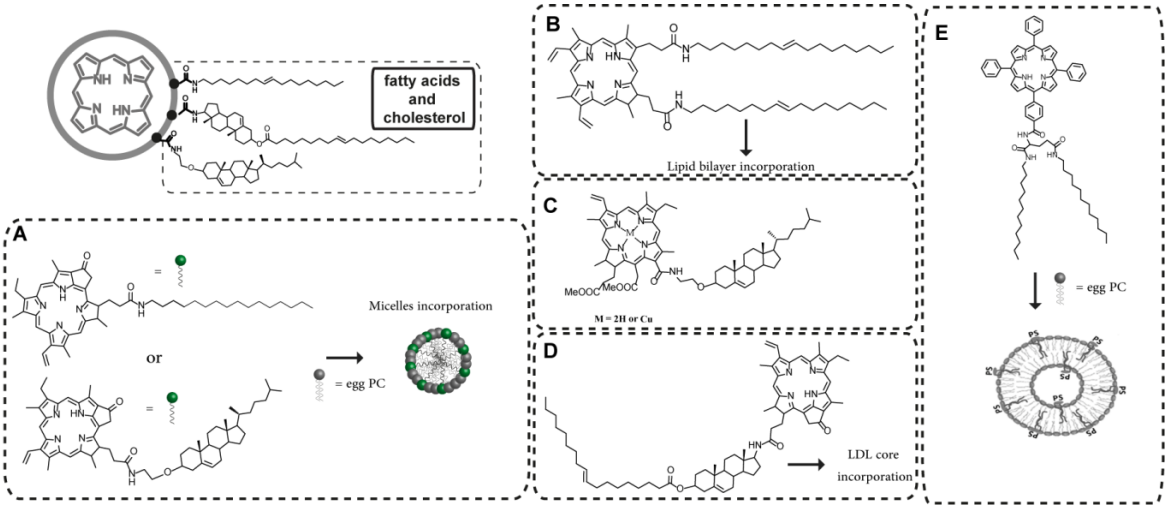

Figure 1.9. Lipid like structures, including A (Ponomarev et al.[88]) – B (Temizel et al.[89]) – C (Nikolaeva et al.[94]) – D (Zheng et al.[95]) – E (adapted from Nathan et al.[90])

1.3.1.3. Porphyrin derivatives conjugation to lipid derivatives: Alkyl chains of phospholipids

Another strategy for covalently linking the PS to the lipids is to use the end of one of the alkyl chains of a phospholipid. The lipid-porphyrin conjugate developed using this strategy by Tsuchida's group[97–99] was a single tetraphenylporphyrin (TPP-($C_{18}OH)_4$) bearing four copies of a synthetic trimethylolethane-derived phospholipid (Figure 1.10 A). A six-step reaction was required to obtain this (4:1)–lipid:porphyrin conjugate. The purpose of the modification was to stabilize the porphyrin molecule from any motion, by placing it at a 90° angle against the four phospholipid acyl chains. This molecule was able to self-assemble, once dispersed in water, into liposome-like vesicles (Figure 1.10 A), with a much thicker bilayer (10 nm), compared to a common phospholipid bilayer (4 nm)[100,101]. The increase in thickness was due to the trimethylolethane group between the polar head and the two acyl-chain (C18 and C20) of the phospholipid, as well as to the porphyrin itself, giving an overall molecule thickness of 4.6 nm. This elongated form of the phospholipid made impossible high curvature in the lipid bilayer, preventing smaller vesicles to form and membrane fusion to occur between two vesicles. The obtained vesicles thus exhibited good stability. The close vicinity of porphyrin molecules in the middle of the bilayer favored edge-to-edge arrangement, characteristic of J-aggregates, like those of bacteriochlorophyll in the chlorosomes of green bacteria[102,103]. These nano-

objects, each one containing approximately 23,000 porphyrin molecules, were originally developed as possible blood substitute for oxygen transportation, but also hold promising applications as drug delivery systems and fluorescent probes. However, the synthetic pathway is too complex for scale up processes and their phototriggering release ability is not yet studied.

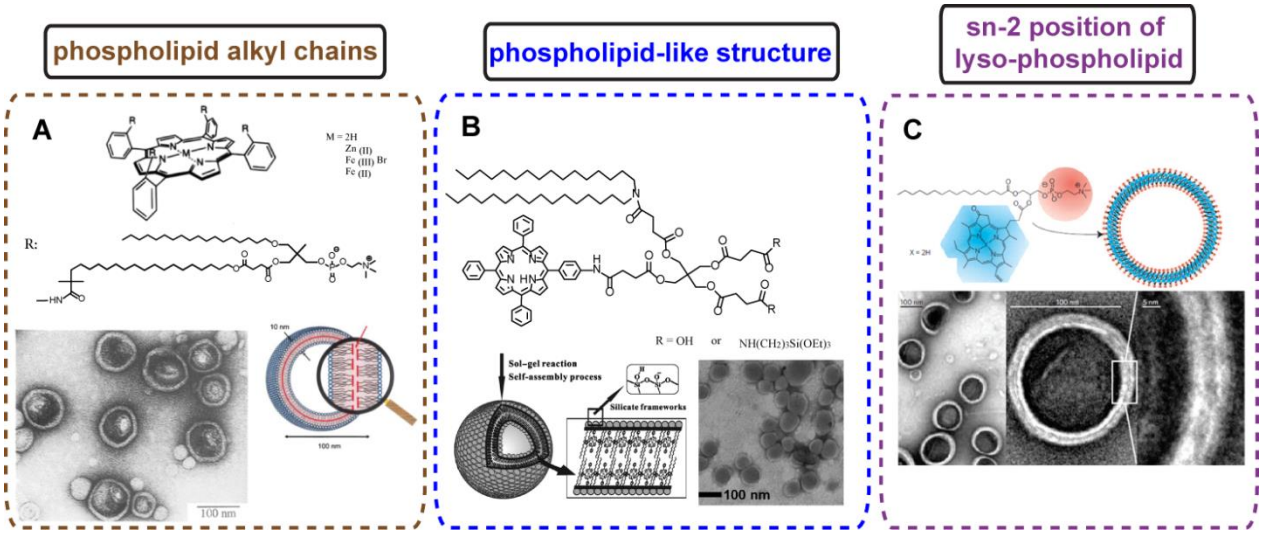

Figure 1.10. Different conjugation methods of photosensitizers to phospholipid derivatives. A. (adapted from Komatsu *et al.*[99]) – B (adapted from Liang *et al.*[104]) – C (adapted from Lovell *et al.*[6])

1.3.1.4. Porphyrin derivatives conjugation to phospholipid-like structures

One possible strategy also consists in the full synthesis of lipid-like structures, binding to the porphyrin moiety. Liang *et al.*[104,105] developed new lipid-porphyrin-like conjugates (PORSILs) based on organoalkoxysilylated lipids. Each lipid-like molecule contained two triethoxysilyl groups as a polar head (Figure 1.10 B), two hydrophobic chains (C16) parallel to the porphyrin moiety (5,10,15,20-tetraphenylporphyrin), and required a six-step synthesis. PORSIL lipids can self-assemble into hybrid organic-inorganic vesicle like structures (Figure 1.10 B), named porphyrin bilayer cerasomes (PBC). They are able to retain hydrophilic cargo such as calcein. These high porphyrin-content vesicles not only retain the PS fluorescence, but also improve singlet oxygen generation. This is explained by the high porosity of such nanoparticles, preventing quenching of the PS in the unwell packed PORSIL bilayer. Cerasomes showed high stability even in the presence of a detergent. Such high stability may prevent a possible light-triggered release by illumination of embedded PS. Only a very significant membrane disruption can enable cargo release, as shown in a similar study using the UV-activatable azo-organoalkoxysilylated lipids (AZOSIL)[105]. Although cerasomes are promising systems, their biocompatibility is still under investigation, and they were toxic (0.2 mg/mL) on HUVECs cells[106]. Recently, the authors reported many improvements in terms

of cerasome toxicity by the development of silica free porphyrin-grafted lipids (PGL), that also showed similar self-assembling properties[107].

1.3.1.5. Porphyrin derivatives conjugation to sn-2 position of lyso-phospholipids

Based on the two previous examples, it is now clear that the position of the hydrophobic PS on the lipid molecule is crucial for the formation of a stable lipid bilayer: when a PS is close to the hydrophobic alkyl chain, the conjugate inserts more easily in the phospholipid bilayer than when the PS is bound to the polar head. However, the right strategy for lipid-porphyrin conjugate in order to ensure both cargo stable encapsulation and light-triggered release still remains unclear. Furthermore, the two previous examples both involve TPP-core porphyrin, which lacks of efficient absorbance properties in the 650-800 nm therapeutic window (the Q-band at 650 nm has a very weak extinction coefficient). This significantly reduces their chances for clinical application. In 2011, Lovell *et al.*[6] demonstrated the successful conjugation of the chlorophyll-based pyropheophorbide a to the sn-2 position of lysophosphatidylcholine (16:0 Lyso-PC)[6] through a single step esterification reaction (Figure 1.10 C). The obtained porphyrin-phospholipid conjugates (also named pyro-lipid) were able to self-assemble into stable liposome-like vesicles (porphysomes), stabilized by the incorporation of 5 mol % of DSPE-PEG_{2000}. Porphysomes contain about 80,000 highly packed porphyrins and show tremendous possible applications for photothermal therapy (PTT)[6,66,108], photoacoustic imaging[6], PET imaging[109], fluorescence imaging, and photodynamic therapy. These two latter applications can only be achieved after porphysomes dissociation into monomers. More particularly, they offer a new modality for light-triggered liposomal release[46,78,80,110–112]. Once self-assembled into vesicles, the well-ordered and densely packed porphyrin molecules exhibit a high fluorescence quenching. Due to this self-quenching, the absorbed energy, usually released in the form of fluorescence and singlet oxygen, is this time released as heat. In addition, due to the high porphyrin content, the amount of light-energy absorbed by one porphysome is so important that thermal release is similar to that of gold nanoparticles[6]. This makes porphysomes a potent tool for PTT and the first organic, bio-based, biodegradable particle in the group of photothermal nanoparticles. Depending on the concentration, the chemical structure of the conjugated porphyrin as well as on the lipid composition of liposomes, different functionalities can be finely tuned[23]. Subsequently, the phototriggered release mechanism can be either photooxidative or photothermal.

1.3.2. Lipid-porphyrin conjugates for light-triggered release applications

Most of the reported studies on porphysomes were achieved using pyro-lipids. However, due to mismatch between the length of the alkyl chain in sn-1 position and the adjacent porphyrin, several formulations have been tried in order to obtain stable liposomes. In fact, Lovell *et al.* have demonstrated that at least 30 mol% of cholesterol should be added to pure pyro-lipid porphysomes in order to form stable vesicles that retain their cargo[6]. The amount of cholesterol required for stable doxorubicin entrapment was even higher (50 mol%), due to the tendency of doxorubicin to precipitate into elongated fibrils when encapsulated into liposomes, forcing vesicles to transit from spherical to elongate ellipsoid shape.

In more recent applications (Table 1.2), liposomes were prepared by combining lower amount of pyro-lipid (2 mol%) with high transition temperature lipids, such as 1,2-distearoyl-sn-glycero-3-phosphocholine (DSPC), together with cholesterol (40 mol%) and DSPE-PEG_{2000} (5 mol%)[111]. Low-content pyro-lipid-containing liposomes enabled phototriggered release of doxorubicin (Figure 1.11 A) within minutes, in physiological conditions (50 % serum, at 37 °C)[111]. Although *in vivo* observations underlined a slight rise in temperature on the tumor site[111], the release mechanism was identified as photooxidative-based, due to cholesterol oxidation species detected after illumination[46].

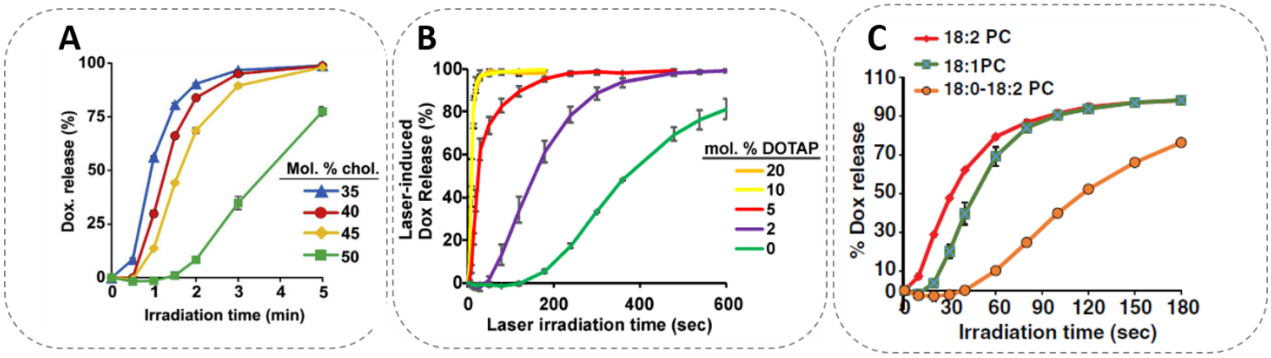

Figure 1.11. Doxorubicin release from DSPC formulations containing 2 mol% of pyro-lipid (A – adapted from Luo *et al.*[111]), 2 mol% of pyro-lipid with increasing amounts of DOTAP-lipid (B – adapted from Luo *et al.*[80]) or 0.1 mol% of pyro-lipid with 5 mol% of either DLPC, DOPC or SLPC lipids (C – adapted from Luo *et al.*[46])

In another study, in 2017, Luo *et al.*[80] demonstrated that decreasing the rigidity of the lipid membrane induced improved photooxidative-based release. This was done by replacing 20 mol% of DSPC by an unsaturated lipid, DOTAP (1,2-dioleoyl-3-trimethylammonium-propane) in the previous formulation (Figure 1.11 B)[80]. The authors could identify oxidized DOTAP species after liposomes illumination, demonstrating that phototriggered release was photooxidatively driven. Similarly, the photoinduced release could be optimized when different unsaturated lipids were used, such as

18:1(*cis*) PC (DOPC), 18:2(*cis*) PC (DLPC), or 18:0-18:2 PC (SLPC), at lower amount of pyro-lipid[46]. Only 0.1 mol% was required for efficient release within seconds in the same conditions (Figure 1.11 C).

In order to overcome the mismatch problem encountered with pyro-lipids, a new type of phospholipid-porphyrin conjugate was developed by Lovell *et al.* with the conjugation of lysophosphatidylcholine (Lyso-PC) to 2-(1-hexyloxyethyl)-2-devinyl pyropheophorbide-a (HPPH)[78]. HPPH is a photosensitizer which is already used in advanced clinical trials for several types of cancer, (esophageal, non-small lung, head and neck cancers[55]). It possesses an additional 6-carbon alkyl chain which aligns with the C16 alkyl chain of the covalently bound Lyso-PC (Figure 1.12 A). Molecular dynamics simulations confirmed the slightly enhanced stability of the HPPH-lipid bilayer, due to a better alignment of the lipid chains, and the formation of a slightly thicker bilayer compared to the pyro-lipid bilayer[78]. Additionally, successful cargo retain was observed when porphysomes were formed with 100% of HPPH-lipid, without addition of cholesterol.

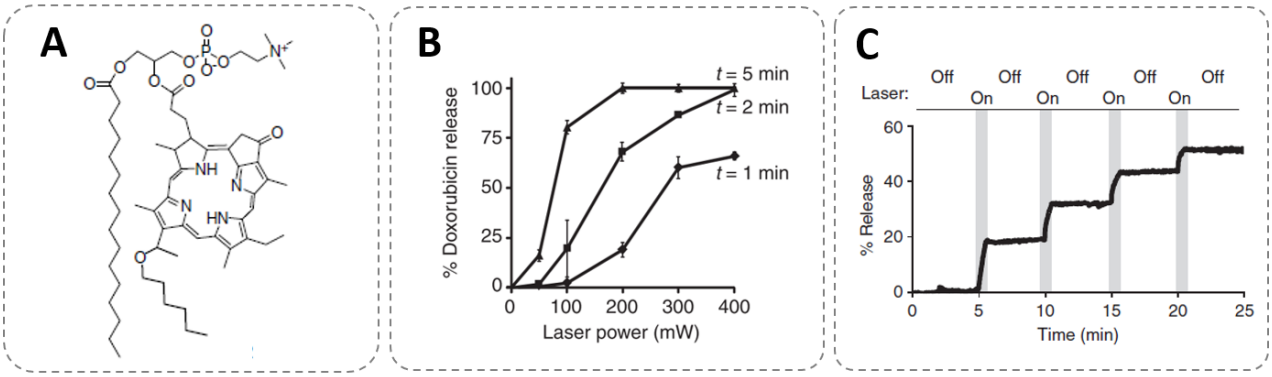

Figure 1.12. (A) HPPH-lipid structure (adapted from Carter *et al.*[78]). Doxorubicin release (B – adapted from Carter *et al.*[78]) or Calcein ON-OFF release (C – adapted from Carter *et al.*[78]) from DSPC liposomes containing 10 mol% of HPPH-lipid.

Photothermal-induced release of doxorubicin was possible within minutes (Figure 1.12 B) with liposomes composed of 10 mol% of HPPH-lipid combined with DSPC (50 mol%), cholesterol (35 mol%) and DSPE-PEG_{2000} (5 mol%). In addition, authors successfully showed the possible ON-OFF calcein release (Figure 1.12 C) which supports the photothermal-based release, although no bulk solution temperature increase was observed. Furthermore, the PS leakage due to interaction with proteins of serum was prevented due to covalently bond PS to phospholipid.

Table 1.2. Lipid-porphyrin conjugates for light-triggered release

	mol%	Co-excipient (mol%)	Cargo	Light-triggered release mechanism (wavelength / power)	References
Pyro-lipid	95	DSPE-PEG_{2000} (5)	/	/	6
	70	egg-PC : chol (18 : 12)	Fluorescent probes : Carboxyfluorescein 10 kDa Texas Red 155 kDa TRITC-dextran	Hypothesis: thermal (405 nm, 210 µW/µm^2)	110
	45	DSPE-PEG_{2000} : chol (5 : 50)	Doxorubicin	/	6
	2 to 15	1- DSPC-DSPE-PEG_{2000}-chol (48 : 5 : 45) 2- SPM : chol (53:2:45)	IRT	ON-OFF release (665 nm, ~310 mW/cm^2)	112
	2	DSPC- DSPE-PEG_{2000}-chol (53 : 5 : 40)	Doxorubicin	Cholesterol oxidation (665 nm, ~310 mW/cm^2)	111
	2	DSPC : DOTAP : chol (38 : 20 : 40)	Doxorubicin	DOTAP photooxidation (665 nm, 250 mW/cm^2)	80
	0.1 to 1	DSPC : DOPC : chol (54.9 : 5 : 40)	Doxorubicin	DOPC photooxidation (665 nm, ~310 mW/cm^2)	46
HPPH-lipid	95	DSPE-PEG_{2000} (5)	Calcein	/	78
	5 to 40	DSPC : DSPE-PEG_{2000} : chol (55 : 5 : 35)	Calcein	Photothermal (ON-OFF) (658 nm, 240 mW/cm^2)	78
	10	DSPC : DSPE-PEG_{2000} : chol (50 : 5 : 35)	Doxorubicin	Photothermal (658 nm, 200 mW/cm^2)	78
	2 to 5	DSPC : DSPE-PEG_{2000} : chol (45 : 5 : 45)	Doxorubicin	passive release (leaky liposomes without illumination)	113
Pur-lipid	2	DSPC : DOPC : DSPE-PEG_{2000} : chol (33 : 10 : 5 :50)	Basic orange / calcein	DOPC photooxidation (690 nm, 125 / 200 mW/cm^2)	114

Note: cholesterol (chol); Tetramethylrhodamine isothiocyanate–Dextran (TRITC-dextran); irinotecan hydrochloride (IRT), Purpurin-18-Lyso-PC conjugate (Pur-lipid)

1.3.3. Lipid-porphyrin conjugates: additional applications

As the most promising conjugation strategy for lipid-porphyrin conjugates remains sn-2 position conjugation, similar strategy was used in order to covalently bind other types of porphyrin derivatives (Figure 1.13 A). In 2018, Purpurin-18[114] was covalently bound to Lyso-PC (Pur-lipid) and showed comparable results in terms of light-triggered release, for both fluorescent probes and anticancer therapeutic agent such as doxorubicin (Table 1.2). In addition, different liposomal formulations encapsulating separately different cargos enabled selective cargo release depending on the wavelength of the laser. Rizvi *et al.* developed, in 2018, a verteporfin-lipid (LPC-BPD) conjugate[115] using the same route as previously described (Figure 1.13 B), by covalently binding the PS to Lyso-PC through Steglish esterification, taking advantage of the carboxylic group of verteporfin. Verteporfin is a mixture of two regioisomers, so LPC-BPD is also a mixture. However, they emphasized that verteporfin in free form localized specifically in endoplasmic reticulum (ER) and mitochondria whereas LPC-BPD accumulated more into lysosomes.

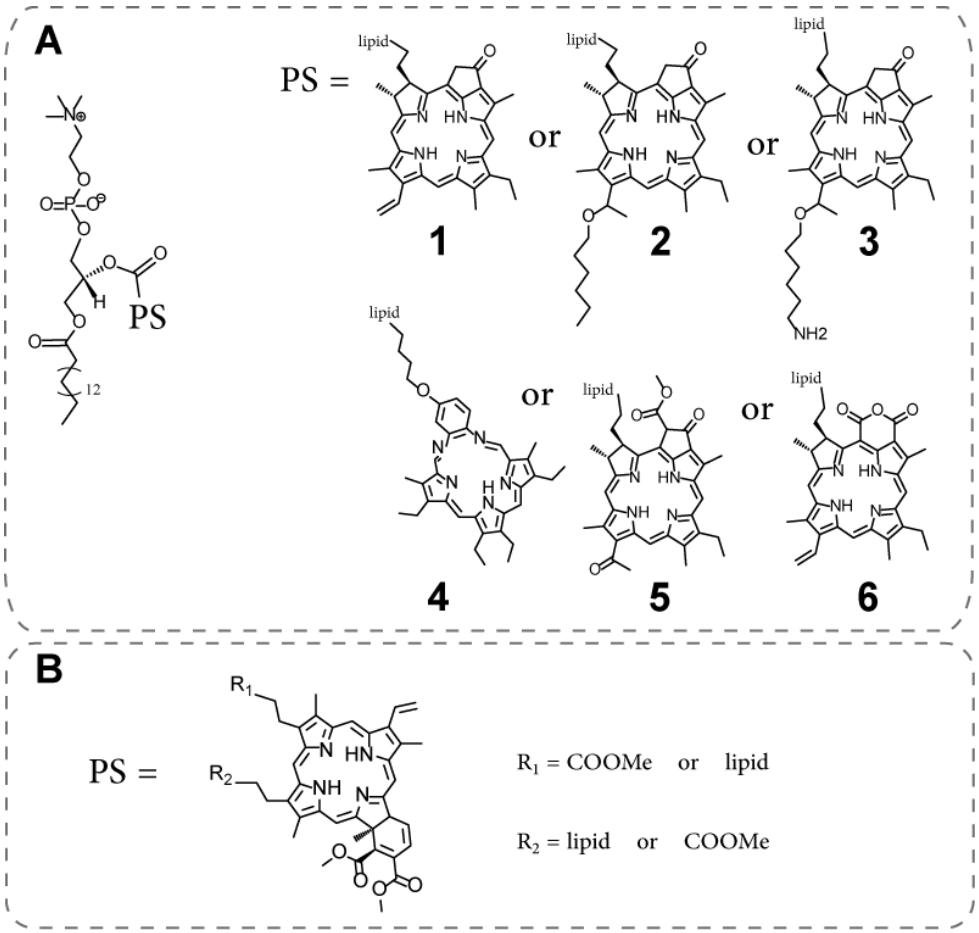

Figure 1.13. A. Lipid-porphyrin conjugates (1. pyropheophorbide a[6], 2. HPPH[78], 3. NH_2-HPPH[116], 4. Texaphyrin[117], 5. Bacteriochlorophyll a[6], 6. Purpurin[114]) – B. Verteporfin-lipid conjugate, LPC-BPD[115].

Adding to the aforementioned applications, porphysomes pave the way for several medical applications such as theranostics as a single molecule can simultaneously be used for its therapeutics properties, and as a diagnostic agent. Indeed, the porphyrin ring offers the possibility to host metals for different properties and additional applications. While pyro-lipid, self-assembled into porphysomes, has shown potential for photoacoustic imaging[6], addition of copper makes PET imaging applications possible. Manganese (Mn), a paramagnetic contrast agent commonly used for magnetic resonance imaging (MRI), has already shown promising results when chelated to pyro-lipid formulated into liposomes[118]. The introduction of an amine group at the extremity of HPPH-lipid C6-lipid chain promotes more water molecules to penetrate into the bilayer[116] and has shown enhanced MR signal. Another strategy has been adopted for the improvement of MRI which consisted on the conjugation of a pentaaza Schiff base macrocycle with 5-coordination pocket named texaphyrin to Lyso-PC[117]. This offers stronger coordination with the metal compared with traditional porphyrins and leads to improved stability and relaxivity of Mn-based MRI agents[117]. In addition, this strategy was applied to 17 different metals, and makes metal-texaphyrin-lipid self-assemblies potential tools for numerous applications, such as radiotherapy, radiosensitization, PET and SPECT imaging, MRI, photodynamic therapy, and fluorescence imaging[117].

1.4. Conclusion

Lipid-porphyrin conjugate technology have shown a wide range of applications, especially for the development of multimodal drug delivery systems, as it enables to combine light-trigger release of an encapsulated drug, imaging, and intrinsic PDT properties of the PS. However, none of these systems are yet clinically approved. Moreover, while these technologies showed a versatility in the phototriggering release several limitations can be underlined.

The encapsulated hydrophilic molecules (either fluorescent probes, or therapeutic molecules) are mostly comprised in the range of small molecules (250 – 650 g/mol), and to our best of knowledge only one study was done on the release of larger molecules, from giant unilamellar vesicles. Macromolecules delivery in a well-controlled manner is of a great importance to ensure endosomal escape and delivery into the cytoplasm.

Furthermore, it should be noted that in most of the cited works, little attention was given to the stability of the encapsulated molecules. Indeed, the amount of ROS that can be generated by the PS during light-triggered release can have a direct impact on the encapsulated cargo structure, and function. For example, fluorescein-based fluorescent probes are known to be very sensitive to oxidation, leading to fluorescence signal decay[119,120]. However, none of the studies investigated in this direction.

Also, the mechanism of photoinduced liposomes permeabilization needs further investigation in order to find the optimal liposome composition. As previously mentioned, phototriggered release from liposomes containing porphyrin derivatives *via* a photothermal conversion mechanism, requires the use of high concentration of photosensitizers with quenched fluorescence. However, these compounds, as other dyes, are subject to photobleaching, reducing their photothermal conversion efficiency. Additionally, the excited states of the closely packed porphyrin derivatives may promote the formation of reactive oxygen species which reduces the control of the release mechanism in a spatiotemporal manner. Finally, it should be pointed out that most of the described lipid-porphyrin conjugation required several steps of chemical synthesis with low yields. Thus, further investigation should be done in order to improve the synthetic protocols, for minimizing costs and facilitating clinical translation.

Chapter 2

Impact of lipid composition and photosensitizer hydrophobicity on the efficiency of light-triggered liposomal release

2.1. Introduction

Phototriggerable liposomes are nanocarriers that can be activated upon illumination at a specific wavelength to release their cargo[8,9]. Composed of biocompatible molecules, *i.e.*, phospholipids (PLs), these systems provide efficient drug loading capacity, and are able to release their drug payload in a spatial, temporal, and dose controlled way[6,46].

Among the previously mentioned light-triggered release modalities, in chapter 1, photothermal and photooxidation methods appear as the most advantageous ones, due to the use of some photoactive molecules that efficiently absorb in the Near Infrared Region (NIR), known as the "phototherapeutic window"[6]. Due to this absorption feature, these molecules allow using deeper light penetration into tissues. In photooxidative liposomes, they can be embedded in a matrix constituted of PLs with monounsaturated or polyunsaturated fatty acyl chains[36].

So far, a few studies, including molecular dynamic (MD) simulations, have highlighted the importance of the localization and orientation of PSs in lipid bilayers of liposomes in the efficiency of light-triggered drug delivery systems[78,121–123]. This theoretical approach elucidated the role of PS charge state[122] or the presence of PEG (polyethylene glycol) inside lipid bilayers[121]. For instance, hematorporphyrins were shown to reside in the phospholipid headgroup region of POPC in close contact with carbonyl groups, highlighting the importance of charge state. By combining MD simulations with fluorescence quenching analysis, Dzieciuch *et al.*[121] reported that *p*-THPP partitioned in PEGylated liposomes in two preferred locations, either close to the center of the bilayer or wrapped within the PEG chains. Interestingly, liposomes made of coupled porphyrin-phospholipid were prepared, exhibiting new stable bilayers[78].

In this work, three promising PSs were selected and used at low molar percentage (2.5 mol%) to avoid both overestimation of release efficiency due to liposomal formulation instabilities[6], and PS aggregation which may significantly alter singlet oxygen quantum yields[124,125]. *m*-THPP is the porphyrin derivative of a commercial chlorin, *m*-THPC, which is approved in the European Union for head and neck tumors under the name of Foscan® [126] (Figure 2.1 A-C). Verteporfin is a benzochlorin derivative monoacid ring A (BPD-MA), which is composed of an equal mixture of two regioisomers (C and D), each of which consisting of a pair of enantiomers. Verteporfin is clinically approved by the Food and Drug Administration (FDA) as liposomal formulation (trade name Visudyne®) for age-related macular degeneration (AMD)[127], and it exhibits efficient capacity for phototriggered drug release from liposomes[53]. Pheophorbide a is a chlorophyll catabolite that has

shown potential efficiency in photodynamic therapy (PDT) for the treatment of different cancers *in vitro*[128,129] causing lipid peroxidation in the mitochondrial membrane[130].

The aim of this work was to investigate the efficiency of these three PSs on photoinduced membrane permeation using low irradiance rate (*i.e.*, 2 mW/cm^2), which is usually used for *in vitro* PDT experiments[131–133]. We intended to establish the relationship between a well-defined lipid bilayer composition and the photoinduced drug release capacity of these PSs. Molecular dynamics (MD) simulations provided atomic rationalization of insertion of the three PSs into bilayers with different compositions. This supported understanding of photoreaction, photooxidation, and thermotropic effects.

2.2. Materials and Methods

2.2.1. Chemicals

Verteporfin (≥ 94%, Mw = 718.79 g/mol), pheophorbide a (≥ 90%, Mw = 592.68 g/mol), methyl linoleate (≥ 99%, Mw = 294.47 g/mol), calcein (Mw = 622.53 g/mol) HEPES (99.5% pure, Mw = 238.31 g/mol), sodium chloride (NaCl, 99% pure, Mw = 58.44 g/mol), ammonium molybdate (VI) tetrahydrate (81-83%, Mw = 1235.86 g/mol), L-ascorbic acid (99%, Mw = 176.12 g/mol), 0.65 mM phosphorus standard solution and hydrogen peroxide (30 wt %) were purchased from Sigma (St. Louis, MI., USA). *m*-THPP was a gift of Dr Philippe Maillard (Institut Curie, France)[134].

The 1-stearoyl-2-oleoyl-sn-glycero-3-phosphocholine (SOPC, Mw = 788.14 g/mol), 1,2-dioleoyl-*sn*-glycero-3-phosphocholine (DOPC, Mw = 786.11 g/mol) and 1-stearoyl-2-linoleoyl-*sn*-glycero-3-phosphocholine (SLPC, Mw= 786.11 g/mol) PLs were purchased from Avanti Polar Lipids (Alabaster, AL., USA). They were 99% pure and were used without any further purification. Chloroform, methanol, and tetrahydrofurane (99% pure) were analytical-grade reagents provided by Merck (Germany). The ultrapure water used in all experiments was produced by a Millipore Milli-Q® Direct 8 water purification system with a resistivity of 18.2 MΩ.cm. The chemical structures of the studied PSs and PLs are shown in Figure 2.1

2.2.2. Light source

The light irradiation experiments were carried out by means of a homemade lamp composed of 4 Philips TL fluorescent tubes covered by a flat diffusing glass plate and fitted with an orange filter (λ ~ 520–680 nm with a λ_{max} = 590 nm) at a 2 J/cm^2 fluence (Figure S2.1). The illumination duration (14 min) was kept constant for all experiments, and the samples were illuminated from the bottom of the glass vials (V = 5 mL, S = 5.5 cm^2).

2.2.3. Vesicle suspension preparation

Porphyrin-containing liposomes were prepared by the conventional thin lipid film hydration method[135] followed by vesicle suspension extrusion. In brief, PL/PS couples were solubilized in (9:1 v/v) chloroform:methanol mixtures at a 97.5/2.5 (mol%). After evaporation of the solvent under vacuum at 45°C, the dry film was hydrated with 1 mL of either HEPES buffer (10 mM HEPES, 150 mM NaCl, pH 7.4, corresponding to ~ 285 mOsmol) or calcein solution (40 mM calcein, 10 mM HEPES, pH 7.4, ~ 285 mOsmol). The final lipid concentration was 10 mM. The osmotic pressure of the solutions was measured using a Loser osmometer (Camlab, Cambridge, UK). The mixture was then vortexed and extruded 19 times through a 200 nm pore-sized polycarbonate membrane, at room

temperature. The hydrodynamic diameter was measured by dynamic light scattering (DLS). The PS incorporation percentage was determined by UV-visible absorption, after liposome disruption with a HEPES buffer/methanol/THF (0.2:0.8:1 mL) mixture. The PS content was controlled by measuring absorbance at a specific wavelength (*m*-THPP: 417 nm, verteporfin: 689 nm, and pheophorbide a: 667 nm) using a CARY 100 Bio UV–visible spectrophotometer (Varian, USA). By comparison with standards at specific concentrations, the PS incorporation efficiency (*i.e.*, % of PS inserted into the liposome bilayer with regards to its initial amount in the chloroform-methanol solution) was determined by measuring the absorbance of each liposomal sample after their rupture in a methanol/THF mixture. The molecular state of PS in the liposome bilayer was investigated by UV-Vis spectroscopy. As deduced from the absorption spectra, the PSs were not aggregated when incorporated into the lipid matrices.

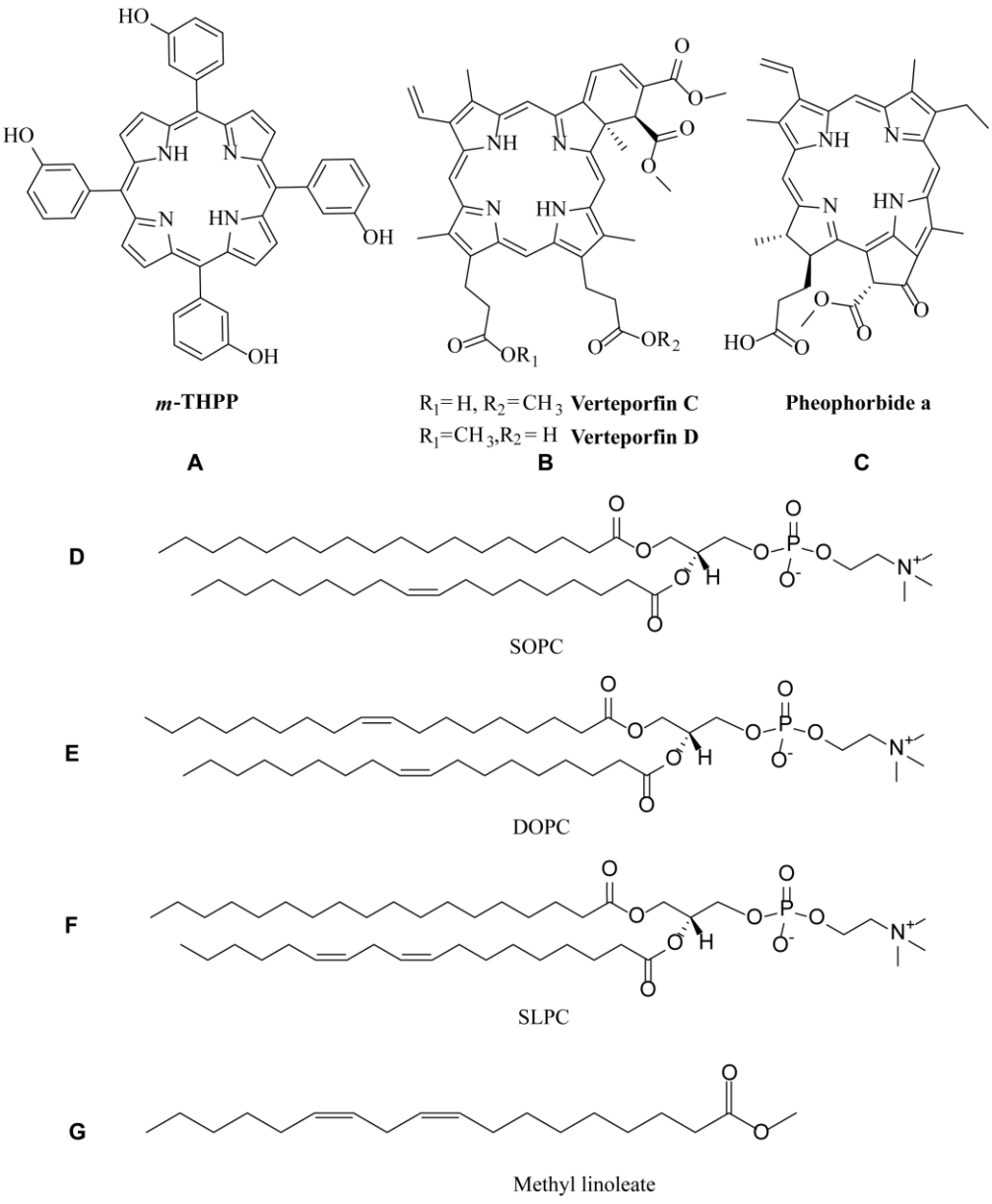

Figure 2.1. Chemical structures of the photosensitizers (A, B, C), phospholipids and methyl linoleate (D, E, F, G).

2.2.4. Dynamic light scattering (DLS) and zeta potential measurements

All DLS measurements were carried out on SOPC liposomes at 1 mM of lipid concentration with a Zetasizer (Nano ZS90, Malvern). For the ζ-potential measurements, liposomes (without calcein) at a lipid concentration of 10 mM were prepared in 5 mM HEPES buffer with low ionic strength (5 mM NaCl) and diluted to 1 mM of lipids in the same buffer just before measurements. All measurements were carried out at 25°C.

2.2.5. Differential scanning calorimetry (DSC)

DSC measurements were carried out using a DSC Diamond Perkin-Elmer apparatus. To ensure that thermal equilibrium was reached, four successive heating/cooling scans were recorded between -10°C and 15°C at a scan rates of 5°C/min (for the first two cycles), 2°C/min and 1°C/min with an empty pan as a reference. Each scan was preceded by a 2 min isotherm recording at the initial temperature to allow the samples to set thermal equilibrium. The same thermal events were observed for all scans and all the observed transitions were reversible and reproducible. The samples (multilamellar suspensions) used for the DSC measurements were prepared by rehydration of either pure SOPC thin films (5 mg) or SOPC:PS (97.5:2.5 mol%) with 45 µL of HEPES buffer. Analyses were performed in duplicate by placing the samples (~ 15 mg) in hermetically sealed aluminum pans. To monitor the effect of illumination on the PL thermal behavior, 50 µL of lamellar suspensions (5 mg of SOPC) were illuminated with orange light at a fluence of 2 J/cm^2 for 14 min before starting the thermal measurements. The calibration was carried out with pure cyclohexane (> 99.9% purity, 6.7 °C melting temperature)[136]. Data were collected and processed using Pyris thermal analysis software (version 9.1). The PL transition onset temperatures (T_{on}) were determined from the intercept of the baseline with the tangent to the left side of the peak, while offset temperatures were deduced from the extrapolation to zero heating rate from scans performed at 1°C min^{-1}, 2°C min^{-1} and 5°C min^{-1}. Enthalpy variations (ΔH) were calculated by integrating the area under the transition peaks. The transition enthalpies were determined from the areas under the curve.

$$\Delta H = \int Cp.dT \text{ (eq. 1)}$$

2.2.6. Lipid oxidation monitoring by conjugated diene formation

The formation of conjugated dienes arising from the peroxidation of methyl linoleate (ML) following illumination was monitored by measuring the UV absorbance using a molar extinction coefficient of 27 000 $M^{-1}.cm^{-1}$ at 234 nm in ethanol[137,138]. In order to investigate the impact of the environment on the oxidation efficiency of the various PSs, the measurements were performed either in ethanol or in liposome suspensions at different ML concentrations. In ethanol solutions, ML at concentrations varying from 0 to 5 mM was dissolved in 5 mL of ethanol with 5 µM PS. In the experiments conducted in liposomes, 10, 20 or 30 mol% ML were added to the initial PL:PS mixture in chloroform:methanol (9:1; v/v). All samples were irradiated for 14 min at 2 J/cm^2 (~ 2 mW/cm^2) and the absorption spectra were directly collected from 220 to 300 nm using the CARY 100 Bio UV–visible spectrophotometer. The increase in absorbance at 234 nm was evaluated by subtracting the spectrum of non-irradiated samples from that of irradiated ones.

The quantum yield of the formed conjugated dienes ($\Phi_{conjugated\ dienes}$) was determined according to the following equation:

$$\Phi_{conjugated\ dienes} = \frac{C_{conjugated\ dienes} \times V}{n_{absorbed\ photons} \times t} \quad \text{(eq. 2)}$$

where $C_{conjugated\ dienes}$ is the concentration of formed conjugated dienes determined from the absorption spectra; V is the volume of the irradiated solution; $n_{absorbed\ photons}$ is the total number of absorbed photons per second; and t is the illumination duration.

The $n_{absorbed\ photons}$ can be calculated according to Mojzisova *et al.*[36] as follows:

$$n_{absorbed\ photons} = \frac{s}{N_A} \sum_{\lambda} \frac{LI_{\lambda}}{E_{\lambda}} \times (1 - 10^{-Abs_{\lambda}}) \quad \text{(eq. 3)}$$

where s is the surface of the illuminated sample (because the sample container is much smaller than that of the used lamp); N_A is the Avogadro's number; LI_{λ} is the light irradiance (W/m^2) at each elemental wavelength; E_{λ} is the energy (joules) of one photon at the irradiation wavelength; and Abs_{λ} is the absorbance of the illuminated solution at each wavelength. For the determination of the LI_{λ}, the spectral irradiance of the lamp was measured using an Ocean Optics Red Tide UV-Vis spectrophotometer. It is noteworthy that no photobleaching of PSs was observed in ethanol after 14 min of illumination, whereas for the liposome-embedded PSs there was a slight photobleaching, which did not exceed 5%. To correct the photobleaching of PSs in the calculation of

$\Phi_{conjugated\ dienes}$ in liposome conditions, the absorption spectra of the different PL-PS liposomes were recorded before and after irradiation. The amount of absorbed photons was then calculated from the mean of the two spectra.

2.2.7. Calcein loading and release from liposomes

Calcein is a water soluble fluorescent probe which is self-quenched when confined in the inner aqueous core of liposomes[76]. Its release from the core of liposomes is accompanied by an increase in its fluorescence intensity due to its dilution in the buffer. To perform calcein release experiments, the extruded calcein-loaded liposomes were purified by ultracentrifugation, with two successive 1-hour cycles at 150 000g and at 4°C, using a Beckman Coulter Optima™ LE-80K (Palo Alto, CA, USA) with a 70.1 - Ti rotor. The supernatant containing free calcein was carefully discarded and the pellet containing the liposomes was resuspended in HEPES buffer, to obtain a liposome suspension of about 10 mM in lipid. The accurate lipid concentration was determined using total phosphorus analysis[139]. In brief, liposome samples were treated with concentrated sulfuric acid at 220°C for 25 min, followed by additional 30 min of heating after adding concentrated hydrogen peroxide. After cooling down, samples were diluted with deionized water, and a complex was formed by addition of 2.5 % ammonium molybdate, immediately reduced by addition of 10 % ascorbic acid. The blue colored complex was formed by heating this solution at 100°C for 7 min, and the related absorbance was measured at 820 nm, once the solution had cooled down.

The calcein release experiments were performed on liposome suspensions diluted in HEPES buffer to 15 µM of lipids. Estimation of calcein release was done by fluorescent spectroscopy using a Perkin-Elmer LS-50B computer-controlled luminescence spectrophotometer (Massachusetts, USA) equipped with a red sensitive R6872 photomultiplier. The emission spectra were obtained before and after illumination, with excitation at $\lambda_{excitation}$ = 490 nm and emission measured at $\lambda_{emission}$ = 514 nm. The liposomes were then disrupted by addition of Triton X-100 at a final concentration of 1% (m/v), to entirely release the calcein content, the release being calculated by the following equation:

$$\%\ calcein = \left(\frac{F-F_0}{F_{det}-F_0}\right) \times 100 \quad \text{(eq. 4)}$$

where F is the fluorescence intensity after liposome illumination at different times; F_0 is the initial fluorescence intensity; and F_{det} is the fluorescence intensity of calcein after rupture of the liposomes with 1% of Triton X-100.

Photobleaching of calcein (≤10%) after illumination was taken into account in the % of released calcein. It should be noted that the kinetic profiles obtained in this work were normalized *versus* non-illuminated liposomes to take only the active release of calcein into account.

The time evolution of calcein release (%) for SOPC and DOPC vesicles were fitted with an exponential function:

$$\%_{calcein} = a + b.e^{-b.t} \qquad \text{(eq. 5)}$$

The evolution of calcein release (%) as a function of time for SLPC formulations were fitted with a sigmoidal function:

$$\%_{calcein} = a' + \frac{b'}{1+e^{(c'-t)/d'}} \qquad \text{(eq. 6)}$$

where a' and b' are the coefficients at the base and the max of the sigmoidal curve; c' represents the critical time at which the % of released calcein reaches (base+max)/2; d' is the rise rate.

2.2.8. Force field (FF) parameters

MD simulations were performed by Dr Florent di Meo and Prof. Patrick Trouillas at the INSERM UMR 850, School of Pharmacy, Limoges University. The force field (FF) parameters of the three PSs (*m*-THPP, verteporfin, pheophorbide a) were derived from GAFF[140] using the antechamber package[141]. Atomic charges were derived from RESP (Restrained fit of ElectroStatic Potential) based on calculations achieved within the density functional theory (DFT) formalism with the (*IEFPCM*)-B3LYP/cc-pVDZ method, in diethylether[142]. The DFT calculations and the atomic charge fitting were performed with the Gaussian 09, RevA[143] and RESP-v.III softwares[144], respectively. The two regioisomers, C and D, of verteporfin (Figure 2.1) were considered for MD simulations.

Lipid FFs available in the Amber16 package were used to describe the three PL types (DOPC, SLPC and SOPC). Namely, the lipid14[145] FF was used to describe DOPC, whereas the lipid11[146] and GAFFlipid[147] FFs were used to describe both SOPC and SLPC. The lipid11 FF is known to overestimate lipid order, therefore analyses of membrane structural properties must be considered with care, and structural analyses require further validation upon more accurate FFs. The "three-point" TIP3P water model[148] was used to describe water molecules.

2.2.9. Molecular dynamic (MD) simulations

Three pure DOPC, SLPC and SOPC bilayer membranes made of 72 lipids, each, were created using the membrane bilayer builder from the CHARMM-GUI server[149]. Membranes were solvated with a hydration number of 50 water molecules per one lipid molecule. Na^+ and Cl^- ions were added to match with experimental conditions (*i.e.*, [NaCl] = 0.154 M). MD simulations were carried out using both the CPU and GPU codes available in Amber16[150,151]. Particle-Mesh Ewald (PME) MD simulations were first run on the pure DOPC, SOPC and SLPC bilayer membranes that were carefully prepared as follows: minimization of the water molecule system prior to the entire system minimization; slow thermalization of water molecules up to 100 K in the (*N*,*V*,*T*) ensemble for 200 ps; thermalization of the whole system to the final temperature (298.15 K) of the entire system for 500 ps (*N*,*P*,*T*); equilibration of the density of the system for 5 ns (*N*,*P*,*T*) MD simulations; finally, production of 400 ns MD simulation. PSs were inserted into equilibrated membranes, and the system was relaxed by a short minimization, so as to prevent any steric clash artifact; 400 ns MD simulations were then carried out. The total MD simulation time for the three PSs (considering the two regioisomers - C and D - of verteporfin) with the three lipid bilayer (DOPC, SLPC and SOPC) membranes was *ca.* 6 μs. The analyses were used along the last 200 ns of the MD trajectories (series of snapshots of the molecular systems). This allowed obtaining a complete sampling of structural properties during 200 ns, after the equilibrium is reached (*i.e.*, within the first 200 ns of the MD simulation). PME MD simulations were carried out using the SHAKE algorithm and a 10 Å noncovalent interaction cut-off. The temperature was maintained using the Langevin dynamics with a collision frequency of 1 ps^{-1}. Anisotropic pressure scaling was used in which pressure relaxation time was set at 1 ps. The analyses were carried out using the cpptraj software[152].

The *z*-axis is defined as being perpendicular to the membrane surface. The depth of penetration of PSs was measured as the *z*-component of the vector originated at the center-of-mass (COM) of the lipid bilayer and that is pointing towards the PS COM. The orientation of PSs in lipid bilayer membrane was assessed as the α-angle between the *z*-axis and the normal vector to the planar ring.
Entrapment is strongly correlated to the noncovalent interactions existing between PS and lipid tails; the stronger the interaction energy E_{nc} between PS and lipid tails, the higher the entrapment efficiency. PS-PL interactions were obtained from MD simulations by calculating noncovalent interaction energies (E_{nc}) between (i) PSs and PLs, as well as (ii) PSs and lipid tails of PLs only, lipid tails being defined as the sn_1- and sn_2- chains. Both energy types were derived from the averaged sum of electrostatic and van der Waals energies per atom.

2.3. Results and discussion

2.3.1. Characterization of SOPC liposomes incorporating the three PSs

The characteristics of SOPC liposomes doped with PSs are summarized in Table 2.1 The incorporation of various PSs in the SOPC lipid bilayers did not induce any significant change in their hydrodynamic radius compared to unloaded liposomes. Whereas, the ζ-potential of SOPC vesicles doped with *m*-THPP was also not significantly modified, both verteporfin and pheophorbide a led to more negative ζ-potential values. Apparently, these PSs were not deeply inserted in the bilayer leaflets. MD simulations agreed with these observations, showing that the distance of PS COM to the membrane center increased as follows *m*-THPP < pheophorbide a < verteporfin C/D (Table 2.1). *m*-THPP has a relative hydrophobic nature, exhibiting an octanol/water partition coefficient log*P* value of 4.8 at neutral pH[153,154].

Table 2.1. Hydrodynamic Radius (nm), Polydispersity Index (PDI), ζ-Potential (mV) of vesicle suspension and PS incorporation efficiency (%). The last column corresponds to the location of the PS COM with respect to the middle of the membrane ($z = 0$) ($\langle z \rangle$), as obtained from MD simulations. For verteporfin the two values are given for the two isoforms C and D, respectively.

Composition	R (nm)	PDI	ζ-potential (mV)	PS incorporation efficiency (%)	Distance from membrane center $\langle z \rangle$ (Å)
SOPC	106 ± 4	0.09 ± 0.02	-1.7 ± 0.1	--	--
SOPC-*m*-THPP	105 ± 3	0.09 ± 0.03	-3.8 ± 0.2	84.6 ± 4.4	9.6 ± 0.8
SOPC-verteporfin	98 ± 3	0.07 ± 0.04	-19.3 ± 0.6	68.0 ± 4.3	{ 16.0 ± 0.9 18.0 ± 0.6
SOPC-Pheophorbide a	103 ± 7	0.07 ± 0.01	-18.0 ± 0.7	75.1 ± 5.2	13.2 ± 0.8

The tetrapyrrole ring of this PS is embedded relatively deep in between the lipid tails and adopts a perpendicular orientation with respect to membrane surface (α-angle of ca. 90°, Figure 2.2). In this case, van der Waals forces constitute the major contribution to E_{nc}, with a minor contribution of electrostatic interactions (Table 2.2). This agrees with previous fluorescence quenching experiments[155] showing relatively strong interactions of this compound with phospholipid tails. This location also agrees with the greater entrapment efficiency observed for *m*-THPP into SOPC bilayers (84.6 ± 4.4 %), with respect to the other two PSs (Table 2.1).

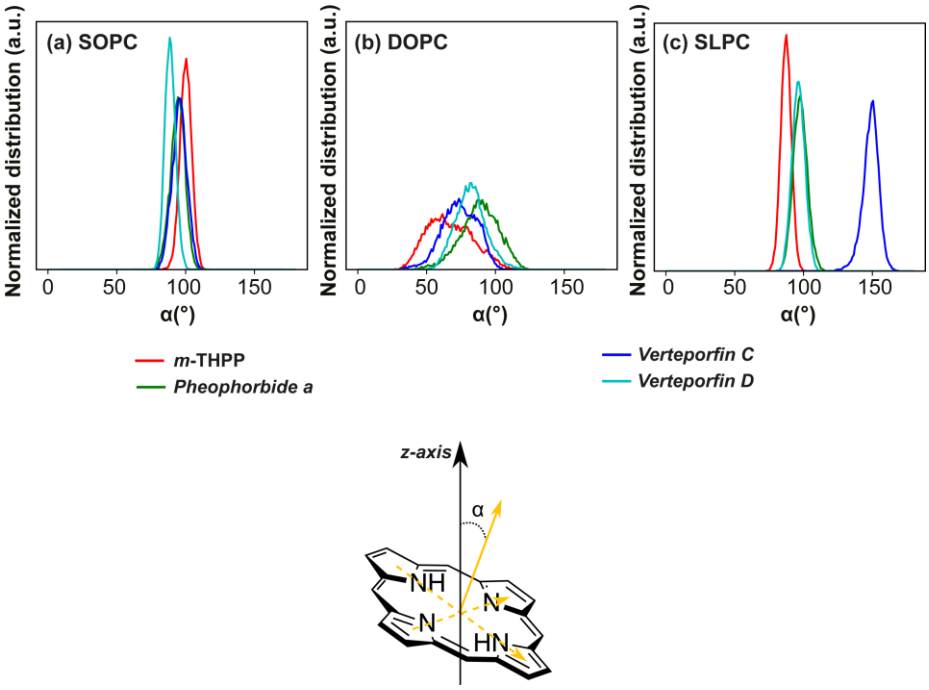

Figure 2.2. Orientation distribution of PSs in (a) SOPC, (b) DOPC and (c) SLPC. m-THPP, Pheophorbide-a, verteporfin C and D are depicted in red, green, blue and cyan, respectively.

Conversely, due to their negative charge, verteporfin and pheophorbide a appeared more anchored to the polar head region. For these two compounds, the electrostatic contribution to E_{nc} values was much greater than for *m*-THPP (Table 2.2).

Table 2.2. Electrostatic (E_{elec}, J.mol^{-1}.atom^{-1}) and van der Waals (E_{vdw}, J.mol^{-1}.atom^{-1}) contributions and standard deviations ($\sigma_{<Eelec>}$ and $\sigma_{<Evdw>}$, respectively, in J.mol^{-1}.atom^{-1}) to (A) PS-PLs and (B) PS-lipid tail E_{nc}.

A

PS	E_{elec}	$\sigma_{<Eelec>}$	E_{vdw}	$\sigma_{<Evdw>}$
***m*-THPP**	-55.6	8.4	-152.1	7.6
Pheophorbide a	-276.7	29.3	-143.6	9.2
Verteporfin C	-155.8	17.8	-165.5	8.2
Verteporfin D	-196.7	17.1	-167.3	8.0

B

PS	E_{elec}	$\sigma_{<Eelec>}$	E_{vdw}	$\sigma_{<Evdw>}$
***m*-THPP**	-3.4	2.0	-130.3	7.2
Pheophorbide a	-1.5	2.3	-117.2	8.6
Verteporfin C	1.7	1.7	-116.0	7.3
Verteporfin D	2.1	1.1	-98.0	7.1

The carboxylate moieties of verteporfin and pheophorbide a interact with the ammonium moieties of PLs (Figure 2.3), but also interestingly with water molecules. Due to the amphiphilic character of these two PSs, they are partially inserted in the bilayer, the tetrapyrrole ring being located in between the lipid chains (Figure S2.2-6), adopting an orientation perpendicular to the membrane surface (α-angle of ca. 90°, Figure 2.2). In SOPC membranes, this orientation is particularly restrained due to the relatively high order of this bilayer. This less deep insertion of verteporfin and pheophorbide a compared to *m*-THPP in turn induced larger loss of PS during liposome extrusion, as exemplified by the entrapment efficiencies compared to that of *m*-THPP (Table 2.1).

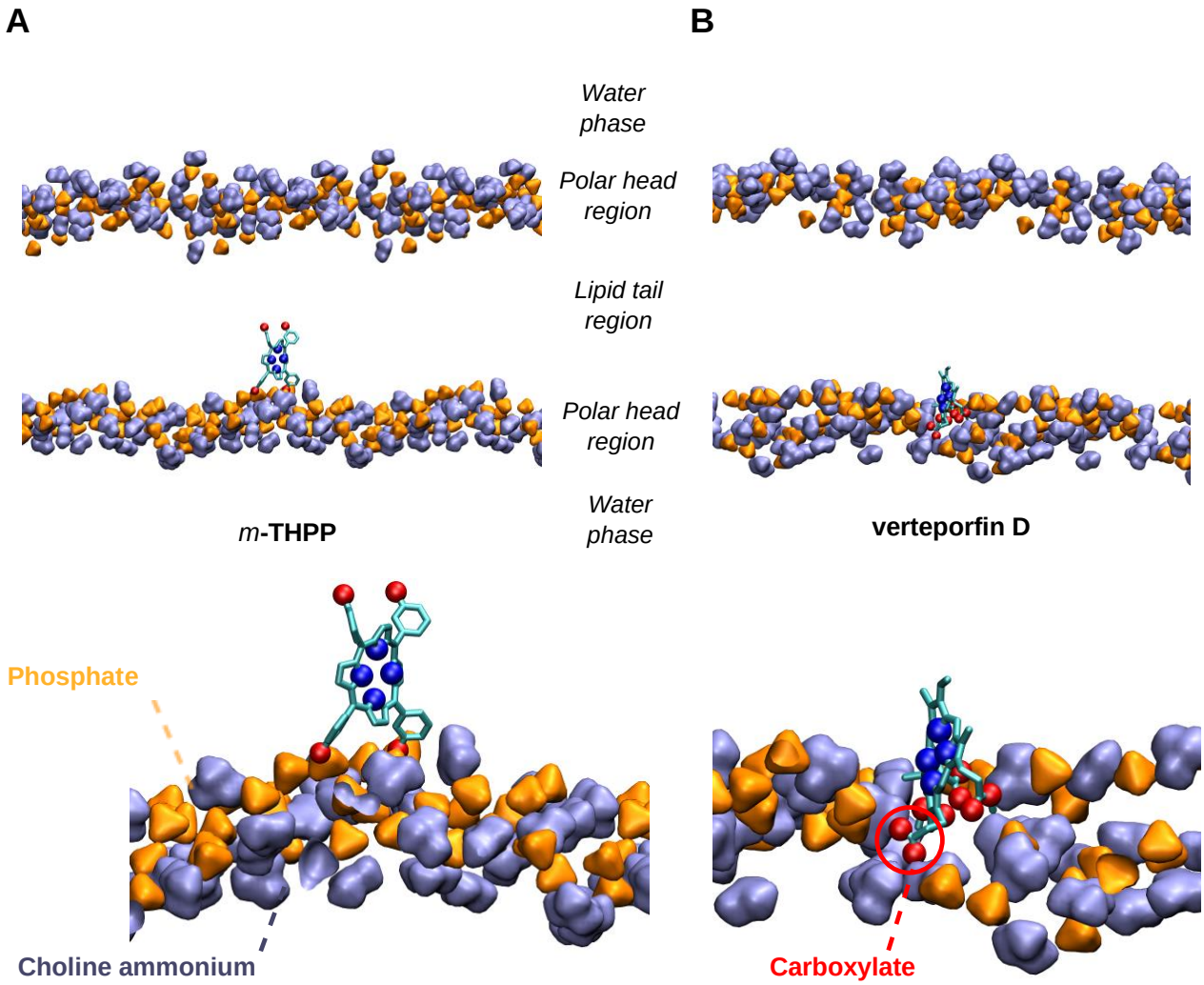

Figure 2.3. Representative snapshots (top) and zoom (bottom) of (A) *m*-THPP and (B) verteporfin D interacting with SOPC membrane. Phosphate and choline ammonium moieties are depicted in orange and ice blue, respectively. Hydrogen atoms, lipid tails and water molecules are omitted for sake of readability.

2.3.2. Impact of PS incorporation on the thermotropic behavior of phospholipid bilayers

To further investigate the incorporation of the different PSs into the lipid matrix and their ability to affect lipid bilayer properties, we have performed a calorimetric analysis on SOPC lamellar suspension without and with PSs at 2.5 mol %. The obtained DSC thermograms are shown in Figure. 2.4. The thermogram of pure SOPC exhibits a sharp endothermic peak at a T onset of ~ 6°C with ΔH of 5.8 kcal/mol, which corresponds to the main transition of pure SOPC from the gel phase (L_β) to the liquid crystalline phase (L_α)[156]. The incorporation of each PS dramatically alters the SOPC thermograms (Figure 2.4 B-D). Indeed, they all induced a decrease in the sharpness of the main transition peak and a shift toward lower transition temperatures, suggesting destabilization of the PL intermolecular cooperativity[157–160]. This alteration depends on PS chemical structures: *m*-THPP produced the strongest effect among the three PSs, inducing an intensive shift of the transition toward a (lower) T_{onset} at 1.1°C.

The presence of two peaks rather than one in the absence of *m*-THPP is attributed to its poor miscibility in the lipid bilayer at low temperature, leading to the formation of *m*-THPP-rich and -poor domains. The SOPC-pheophorbide a sample only leads to a limited T_{onset} shift; the homogenous and symmetric peak is characteristic of a good mixing with SOPC. SOPC-verteporfin systems are characterized by a broad and asymmetric peak with a T_{onset} of 3.7°C indicating partial mixing of SOPC and verteporfin. This PS might act as a substitutional impurity[161]. Despite the significant perturbation of the SOPC thermogram in the presence of the three PSs, the overall phase transition enthalpy of the different systems remained almost constant (Table 2.3).

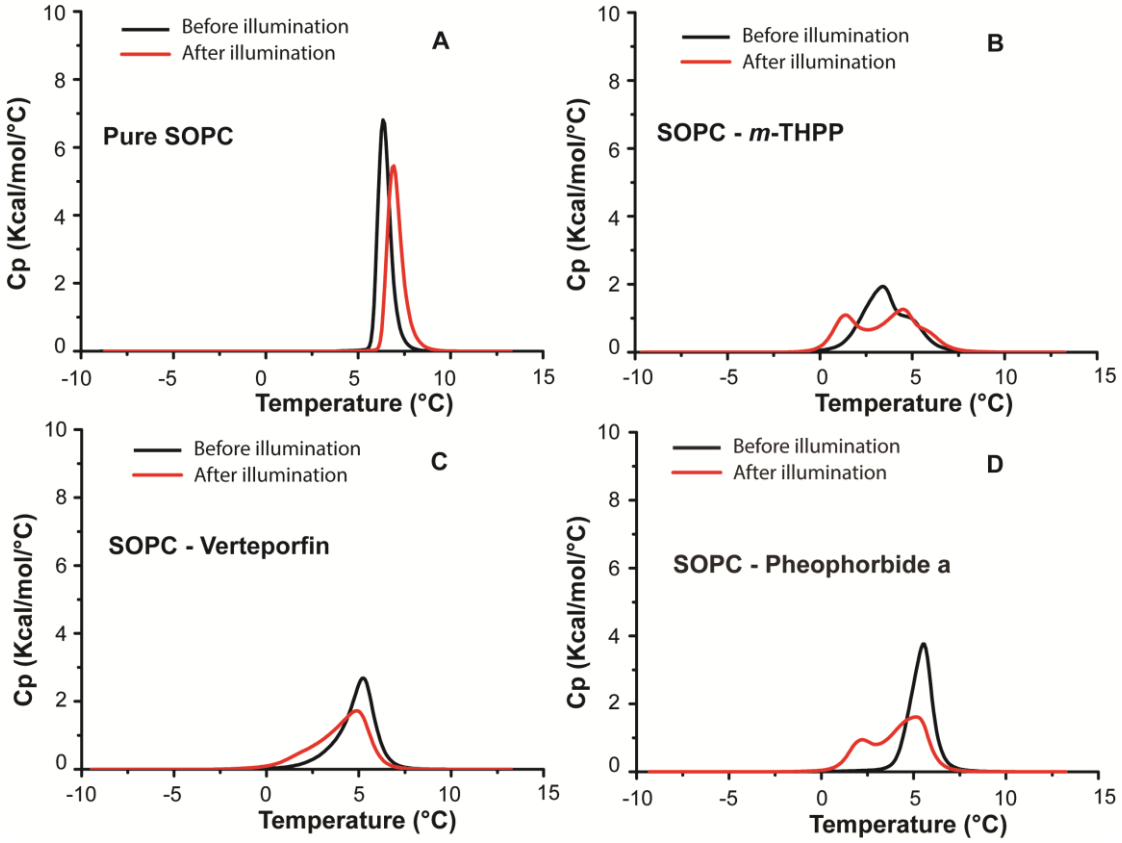

Figure 2.4. DSC heating scans of pure SOPC liposomes, SOPC-*m*-THPP, SOPC-Verteporfin and SOPC-Pheophorbide a before and after illumination.

In order to assess the thermotropic phase behavior of SOPC-PS upon illumination, DSC scans were performed after illumination of SOPC lamellar suspensions for 14 min (see Figure 2.4). After illumination of the pure SOPC, its transition temperature was almost unchanged with a slight decrease in the transition enthalpy, which remained below 7%, suggesting that the pure PL bilayers remained almost intact. Conversely, upon illumination of SOPC-PS samples, the overall shape of the thermograms was dramatically affected with a significant shift of T_{onset} towards lower temperatures, and the appearance of a second peak for both *m*-THPP and pheophorbide a. For SOPC-verteporfin sample, the peak was altered and became broader with the appearance of a shoulder at about 2°C.

Table 2.3. T_{onset} temperatures, enthalpies of pure SOPC and SOPC doped with PS before and after illumination.

	Before illumination		**After illumination**	
Composition	**T_{onset} (°C)**	**ΔH (kcal/mol)**	**T_{onset} (°C)**	**ΔH (kcal/mol)**
SOPC	5.8	5.8	6.3	5.4
SOPC - *m*-THPP	1.1	5.7	0.12	5.4
SOPC – Pheophorbide a	4.2	5.7	1.1	5.6
SOPC - Verteporfin	3.7	5.7	1.6	5.4

These results indicate the formation of new phases upon the illumination of SOPC-PS systems, which may be related to the formation of new chemical species within the lipid bilayer. Interestingly, such a behavior was previously observed by Wallgren *et al.*[162] and Makky *et al.*[43] with the incorporation of defined amounts (0 to 20 mol %) of oxidized PLs with either a carboxyl (1-palmitoyl-2-azelaoyl-sn-glycero-3-phosphocholine (PazePC)) or an aldehyde (1-palmitoyl-(9-oxononanoyl)-sn-glycero-3-phosphocholine (PoxnoPC)) group. This incorporation significantly altered the thermotropic phase behavior of DMPC[162] and SOPC[43] vesicles. Herein, *m*-THPP appeared to be the most efficient PS in creating new phases upon liposome illumination followed by pheophorbide a and verteporfin, respectively. Although the nature of the formed species upon the photosensitization reaction cannot be predicted from the DSC thermograms, these species are most probably lipid hydroperoxides. Indeed, upon illumination with adequate wavelength, the PS absorbs radiation energy, creating its singlet excited state (^{1}PS*)[163]. Porphyrin and chlorin ^{1}PS* are good candidates to intersystem crossing (ISC) processes, leading to the formation of triplet state (^{3}PS*). The ^{3}PS* then react via two different pathways – either electron/hydrogen transfer (type I reaction) or energy transfer (type II reaction) to triplet oxygen - producing free radicals or singlet oxygen, respectively[163]. The light-induced oxidation pathway highly depends upon the solubility and concentration of molecular oxygen. Nevertheless, type II reaction is usually favored in lipid bilayers, as singlet oxygen has longer half-life than in aqueous media[48]. The unsaturated alkyl chains of SOPC are substrates for singlet oxygen favoring the formation of lipid hydroperoxides.

2.3.3. Lipid peroxidation monitoring

ML is a fatty acid methyl ester that contains two unconjugated *cis* olefinic bonds (see Figure 2.1). Upon their reaction with singlet oxygen, the latter is added to one of the C-atoms of the double bonds in a concerted and specific way known as "ene addition", forming *trans* allylic hydroperoxides[37,164], only 60% of them being conjugated [71]. Since conjugated dienes and hydroperoxides are simultaneously formed, absorption measurement at 234 nm is considered as a relevant marker to quantify hydroperoxide formation[36]. The oxidation experiments of ML were performed in ethanolic solutions and on SOPC-PS liposome suspensions. Typical absorption spectra of the three PSs in ethanol ($5x10^{-6}$ M) are presented in Figure 2.5 A.

As shown in Figure 2.5 B, the characteristic absorbance of conjugated diene formation at 234 nm increased as a function of ML concentration. For all studied PSs, in ethanol and in liposomes, the concentration of conjugated dienes linearly increased as a function of ML concentration (Figure 2.5 C and D), showing that peroxidation depends on substrate availability.

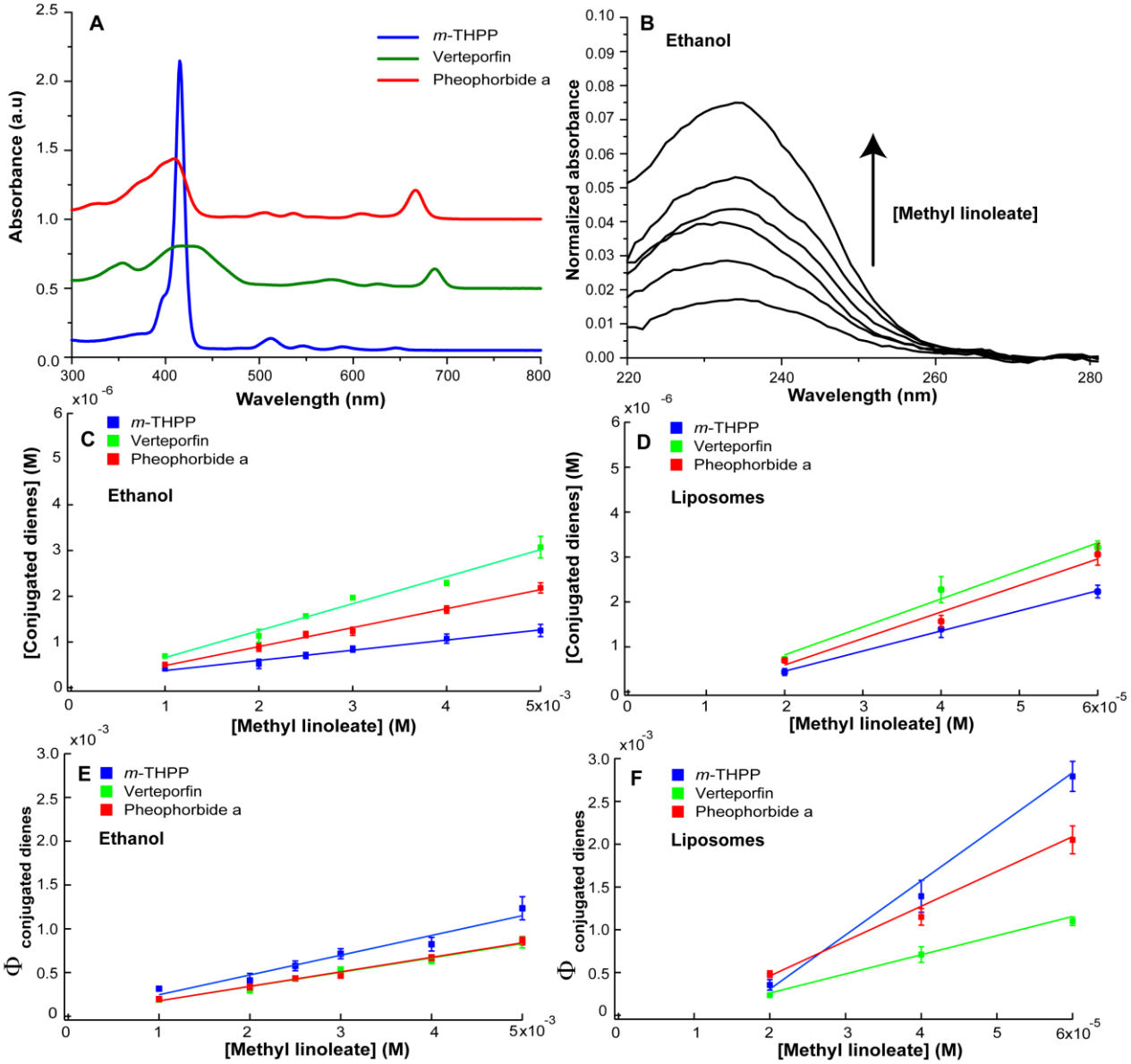

Figure 2.5. ML peroxidation monitoring in ethanol and SOPC-PS liposomes at room temperature. A. Absorption spectra of the three studied PSs at 5×10^{-6} M in ethanol. B. Typical absorption spectra of the conjugated dienes formed in ethanol upon illumination of ML in the presence of verteporfin (5×10^{-6} M) for 14 min (2J/cm^2). Concentrations and quantum yields of the formed conjugated dienes as a function of ML concentration in (C, E) ethanol and (D, F) liposomes for PSs concentration of 5×10^{-6} M.

From these linear plots, $\Phi_{\text{conjugated dienes}}$ were determined and plotted as a function of ML concentration (Figure 2.5 E and F). Interestingly, the liposomes charged with PSs exhibited different ML peroxidation efficiencies compared to those measured in ethanol. The slopes of $\Phi_{\text{conjugated dienes}}$ *versus* PS concentration in liposomes (60.90, 39.25, 21.56 M^{-1} for *m*-THPP, pheophorbide a and verteporfin, respectively) were at least two order of magnitude higher than those in ethanolic solutions (0.23, 0.17, 0.17 M^{-1} for *m*-THPP, pheophorbide a and verteporfin, respectively). Similar results were obtained by Mojzisova *et al.*[36] who studied DOPC/ML liposomes incorporating different chlorin derivatives. This was attributed to the longer lifetime of singlet oxygen in lipid membranes than in ethanol

solutions. Thus, a higher efficiency of singlet oxygen with ML unsaturation is expected in lipid membranes[165]. PS-induced oxidation efficiencies (Figure 2.5 E) were as follows: *m*-THPP > pheophorbide a > verteporfin, in agreement with DSC results (see Figure 2.4 and Table 2.3). The different behavior observed with the three PSs could thus be explained by their confinement in the lipid bilayer and the production of singlet oxygen and/or free radicals directly in the vicinity of the unsaturated chains of both PL and ML. As discussed above, *m*-THPP is incorporated deeper inside the lipid bilayer than the other two PSs, which is related to their lipophilicity, as confirmed by our MD simulations and as previously showed by Engelmann *et al.*[166]. The same authors[165] have also shown that the photodynamic efficacy of PSs is higher for those which can efficiently intercalate in between lipid tails, at a location where the excited state of a PS has higher probability to interact with dioxygen to generate singlet oxygen. In turn, singlet oxygen, generated in the hydrophobic interior, has a greater probability to react with unsaturated chains within the lipid matrix.

2.3.4. Phototriggered release of calcein from liposomes

We demonstrated with the ML oxidation experiments that the peroxidation of unsaturated chains depends on substrate availability (Figure 2.5 C-F). Peroxidation is a major driving factor for membrane permeation, which is required for phototriggered release. To investigate the effect of phospholipid unsaturation chains on the permeation efficiency, liposomes made of various unsaturated phospholipids (*i.e.*, SOPC, DOPC and SLPC) were doped with the different PSs and calcein was encapsulated into their aqueous core. Normalized kinetics release profiles upon PL-PS illumination are shown in Figure 2.6. While no leakage of the dye was observed following illumination of pure phospholipid vesicles, significant calcein release occurred in PS-containing liposomes, which increased with time. As depicted in Figure 2.6 and Table 2.4, the leakage was incomplete for all three PSs and did not exceed 40% after 6 hours in the best case, but the lipid composition of liposomes appeared to play a crucial role in controlling calcein release kinetics. Indeed, whereas for SOPC-PS and DOPC-PS the calcein leakage profiles increased exponentially with all PSs, SLPC-PS vesicles exhibited a slower release profile rate, which can be fitted by a sigmoidal function (Figure 2.6 B-D).

Table 2.4. Normalized calcein release (%) of different liposomes/PSs systems after 6 hours of illumination.

Photosensitizer	SOPC	DOPC	SLPC
m-THPP	14.1 ± 3.1	40.2 ± 6.7	12.4 ± 1.9
Pheophorbide a	28.8 ± 4.8	20.8 ± 0.8	12.7 ± 6.8
Verteporfin	33.1 ± 6.1	33.8 ± 3.8	22.8 ± 10.5

The system efficiency also seems to depend upon a PS / PL combination. Table 2.4 shows that for *m*-THPP, calcein photoinduced release was much more efficient for DOPC vesicles than for SOPC or SLPC ones. In addition, despite the low absorbance of the DOPC-*m*-THPP system in the region of the emission spectrum of the lamp (Figure S2.1), its illumination induced the highest calcein release after six hours compared to the other PL/PS combinations (Table 2.4). Conversely, for verteporfin and pheophorbide a, the phototriggered calcein release appeared to be more efficient with SOPC and DOPC than with SLPC.

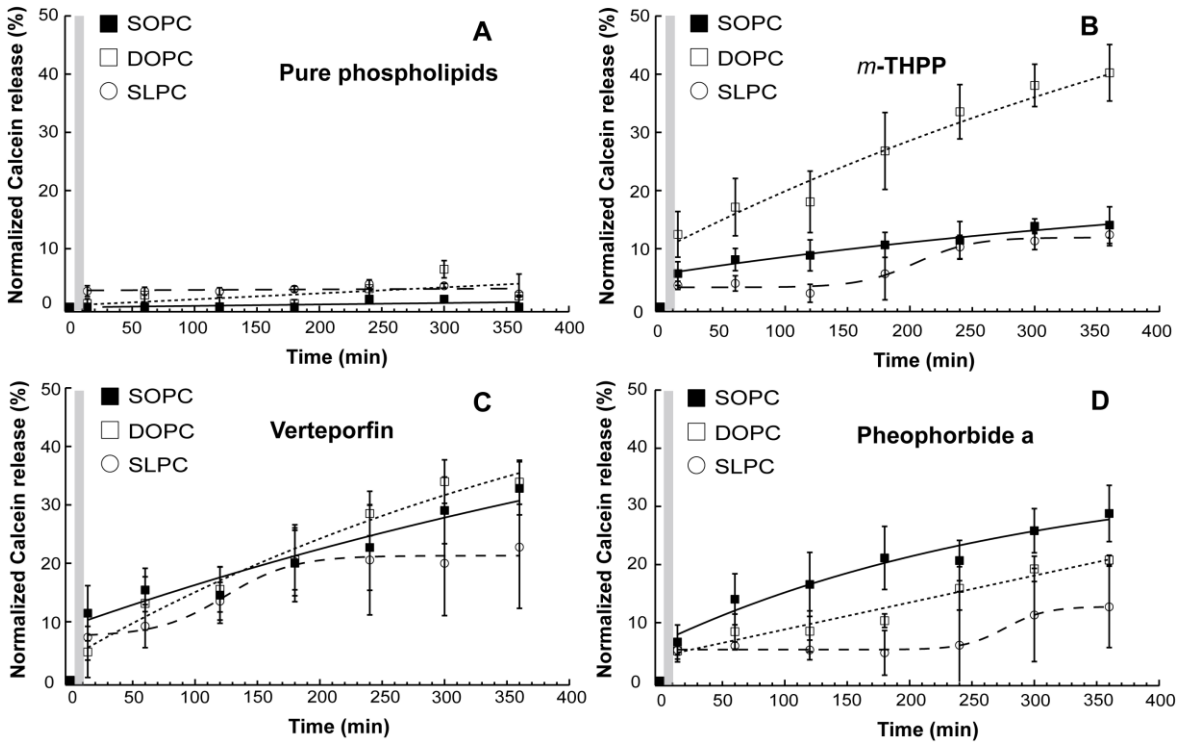

Figure 2.6. Phototriggered release of calcein as a function of time of A) pure PLs, B) PLs doped with *m*-THPP C) PLs-verteporfin and D) PLs-pheophorbide a. Solid black lines, dotted black lines and dashed black lines represent the fit of the calcein release from SOPC, DOPC and SLPC liposomes respectively. The calcein release profiles were normalized by subtraction of the percentage of calcein released from non-illuminated samples. The data at 0 min in each graph corresponds to the initial calcein release % before illumination. The gray vertical line corresponds to the duration of light exposure (14 min). The error bars are the standard deviations (n=3). All measurements were performed at room temperature.

The difference in calcein release extent between the three PL/PS combinations may be related to different permeation mechanisms. In fact, membrane oxidation leads to the formation of lipid peroxides with different structures depending on PL structure and the localization of a PS in the bilayer. PL peroxide derivatives may induce different effects on membrane properties varying from structure destabilization to liposome fusion. Hence, to get a better insight into the mechanism of phototriggered release, the size of the different liposomes was measured before and after illumination

by DLS. Our results showed that neither the size nor the distribution of the vesicles changed even after 24h of illumination (Table 2.5), ruling out the fusion hypothesis.

Table 2.5. Photosensitizers incorporation efficiency (%, n=3), mean hydrodynamic radius (nm, n =2), polydispersity index (PDI) of vesicles suspensions before and after 24 h of illumination.

		Before Illumination		After Illumination	
Liposomes composition	**PS incorporation efficiency (%)**	**R (nm)**	**PDI**	**R (nm)**	**PDI**
SOPC	--	103	0.09	103	0.04
SOPC-*m*-THPP	84.6 ± 4.4	107	0.07	107	0.06
SOPC-Verteporfin	68.0 ± 4.3	96	0.09	97	0.07
SOPC-Pheophorbide a	75.1 ± 5.2	97	0.07	97	0.07
DOPC	--	117	0.10	119	0.11
DOPC-*m*-THPP	95.3 ± 3.1	112	0.08	112	0.06
DOPC-Verteporfin	71.7 ± 5.6	111	0.07	117	0.07
DOPC-Pheophorbide a	67.6 ± 4.0	110	0.09	113	0.07
SLPC	--	107	0.09	110	0.07
SLPC-*m*-THPP	87.1 ± 3.4	105	0.02	106	0.07
SLPC-Verteporfin	59.8 ± 7.3	120	0.05	121	0.07
SLPC-Pheophorbide a	70.3 ± 4.4	120	0.17	118	0.13

Thermal destabilization of the lipid bilayers was also considered. However, the illumination induced less than 2°C increase in temperature of the liposome suspensions, and the lipids were all already in the liquid crystal phase. Furthermore, PS-unloaded vesicles illuminated in the same conditions (Figure 2.6 A) led to non-significant calcein release compared to those containing the PSs. Therefore, the mechanism of photoinduced calcein release could only be explained by the formation of a hydroperoxide group on the alkyl chain unsaturation, which altered membrane structure. As *m*-THPP is deeply inserted in the lipid bilayers, the generated singlet oxygen has higher potential to react with the alkyl chain unsaturation due to its longer diffusion path, compared to that produced by the other PSs in the proximity of polar headgroups where it is more quickly deactivated in the aqueous environment. The fact that the *m*-THPP/DOPC vesicles are more efficient than those with SOPC and SLPC could be explained by the formation of a hydroperoxide group on each alkyl chain, altering phospholipid packing. A significant area expansion would provoke higher membrane permeability compared to the SOPC and SLPC liposomes. Recently, Aoki et al.[167] have demonstrated, from surface pressure measurements combined with polarization-modulated infrared reflection absorption spectroscopy (PM-IRRAS), that the irradiation of a DOPC / erythrosin monolayer caused a significant relative surface area increase of ca. 19%[167]. Similarly, using a micropipette setup, Weber *et al.*[44] observed that the formation of PL hydroperoxides caused an increase in the excess area of GUVs of 15.6% and 19.1% for POPC and DOPC, respectively.

More recently, in 2016, Luo *et al.*[46] demonstrated that the incorporation of DOPC in liposomes accelerated the light-triggered release of doxorubicin from porphyrin-phospholipid (PoP) liposomes by one order of magnitude compared to DOPC-free liposomes[46]. By mass spectrometry, they confirmed that the light-triggered drug release was related to DOPC oxidation and revealed the formation of three DOPC oxidized species[46].

The SLPC-PS liposomes exhibited the lowest release efficiency. Such behavior was also observed by Luo *et al.*[46] who attributed it to the lower probability of singlet oxygen accessing the unsaturated bonds present on a same chain[46]. However, we found that the concentration of conjugated dienes formed in SLPC-*m*-THPP liposomes increased linearly as a function of increasing duration (Figure 2.7). This demonstrates the ability of singlet oxygen to induce SLPC diene peroxidation. Therefore, the lower efficiency of membrane permeation observed for SLPC with respect to SOPC and DOPC could only be explained by the structure of the PL-hydroperoxides formed. Indeed, Wong-Ekkabut *et al.*[38] investigated the effect of lipid peroxidation on the properties of PLPC (1-palmitoyl-2-linoleoyl-sn-glycero-3-phosphatidylcholine) lipid bilayers using MD simulations. They focused on the two main hydroperoxide products of linoleic acid: the 9-*trans*, *cis*-hydroperoxide linoleic acid (9-tc) and the 13-*trans*, *cis*-hydroperoxide linoleic acid (13-tc). According to their simulations[38], both PL-hydroperoxides at 11.1 mol% were unable to modify water permeability through PLPC bilayers. However, increasing the oxidized lipid fraction to 50 mol% in the membrane led to a higher water permeability compared to unoxidized PLPC, with an increase of two and one order of magnitude for 13-tc and 9-tc, respectively[38]. Their result suggests a relationship between water permeability of the bilayer and the position of the hydroperoxide group in the lipid bilayer, inducing a larger area expansion and a loss of lipid packing with 13-tc compared to 9-tc[38].

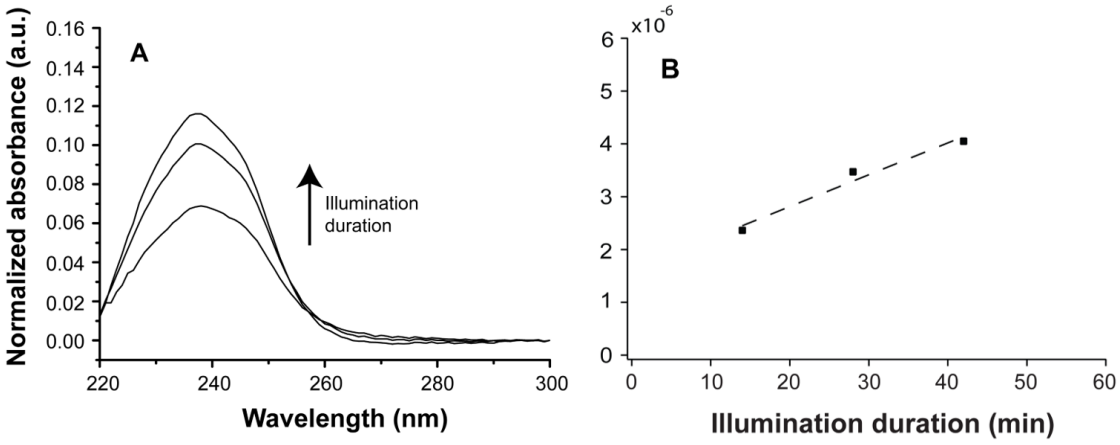

Figure 2.7. A. Typical normalized absorption changes of SLPC-*m*-THPP liposomes as a function of illumination duration. B. Concentration of formed conjugated dienes in SLPC-*m*-THPP liposomes as a function of illumination duration. The dashed line is the linear fit.

2.3.5. Molecular insights into PS efficiency

PS efficiency in membranes depends on: (i) PS intrinsic parameters (*e.g.*, photophysical, excited- and ground-state conformational properties); (ii) molecular oxygen diffusion capacity, and (iii) direct surrounding environment of the PS. The first two points are out of the scope of this work; here we evaluated PS insertion/location in various lipid bilayers with different packing order. *m*-THPP inserts significantly deeper than pheophorbide a and verteporfin into SOPC and SLPC bilayers (Table 2.6 and Figure 2.8). Similar depth of penetration and orientation are observed for the three PSs respectively, in both SOPC and SLPC bilayers (Table 2.6 and Figures S2.2 to S2.6). Conversely, in DOPC bilayers, the three PSs exhibit a similar depth of penetration (Table 2.6 and Figure 2.8) likely owing to the higher fluidity of DOPC that allows higher diffusion motions.

Table 2.6. Location of the COM with respect to the middle of the membrane (z = 0) (<z>, in Å) and related standard deviation ($\sigma_{<z>}$, in Å) for m-THPP, pheophorbide-a, verteporfin C and D in SOPC, DOPC and SLPC lipid bilayer membranes.

	SOPC		**DOPC**		**SLPC**	
	$\langle z \rangle$	$\sigma_{<z>}$	$\langle z \rangle$	$\sigma_{<z>}$	$\langle z \rangle$	$\sigma_{<z>}$
***m*-THPP**	9.6	0.8	12.2	1.7	7.6	1.0
Pheophorbide-a	13.2	0.8	11.7	1.8	15.6	1.0
Verteporfin C	16.0	0.9	11.5	1.3	20.5	0.7
Verteporfin D	18.0	0.6	11.1	1.3	14.1	0.6

DSC experiments have demonstrated that the presence of PSs in lipid bilayer membranes lead to structure destabilization. A thorough analysis of the characteristic orientation obtained, *e.g.*, with verteporfin D, highlighted disorganization of the membrane surface (Figure 2.3). Also, in the more ordered (SOPC and SLPC) lipid bilayers, the structure destabilization was suggested by the asymmetric phosphatidylcholine distributions along *z*-axis, in which the disturbance is on the side where PSs are located (Figure 2.8). However, due to the small size of the membrane model used in the MD simulations, the structural destabilization could not be quantitatively evaluated neither by the calculated area per lipid nor by lipid order profiles (*i.e.*, no significant differences were observed in the presence of PSs, see Figure S2.7 and Table S2.1).

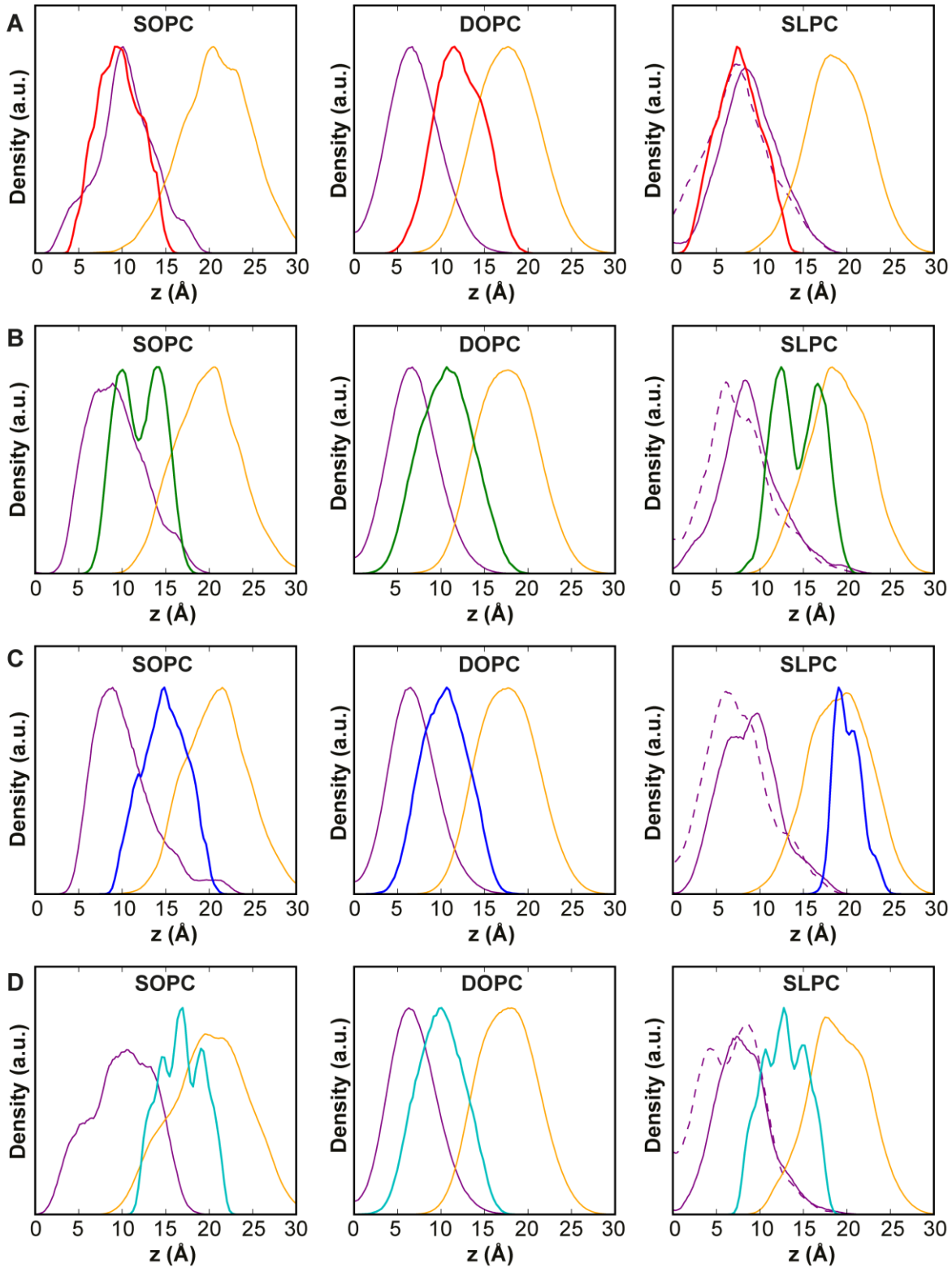

Figure 2.8. Density of (a) *m*-THPP (red), (b) Pheophorbide a (green), (c) verteporfin C (blue) and (d) verteporfin D (cyan) tetrapyrrole moieties along *z*-axis in SOPC, DOPC and SLPC. C=C double bonds as well as high-density polar head region densities (i.e., phosphatidylcholine moieties) are plotted in purple and orange, respectively. SLPC C_9=C_{10} and C_{12}=C_{13} are plotted in solid and dashed lines, respectively.

From ML peroxidation experiments, *m*-THPP appeared to be the most efficient PS in lipid peroxidation followed by pheophorbide a and verteporfin. This result agrees with their relative insertion depth in SOPC and SLPC bilayers. However, such observation was not necessarily correlated with calcein release experiments (Figure 2.6) highlighting the role of lipid environment as well as the nature of lipid peroxides produced.

It is worth noting that the tetrapyrrole planarity can be altered inside the lipid bilayers. This is known to dramatically affect photon absorption events and subsequently singlet oxygen generation. The planarity of pheophorbide a and verteporfin tetrapyrroles is more sensitive to the environment than *m*-THPP. The latter is indeed more π-conjugated and thus less flexible (Figure 2.9). DOPC allows more flexibility to the verteporfin and pheophorbide a central core leading to a broader distribution of tetrapyrrole dihedral angle. SOPC is more prone to disturb tetrapyrrole planarity owing to a slightly higher order with respect to SLPC. Lipid order is an important parameter since O_2-PS energy transfer occurs within the ^{3}PS state, in which tetrapyrrole planarity is modified with respect to the PS ground state. The present MD simulations achieved with ground state geometries underlined the different impacts of the different lipid bilayers on tetrapyrrole planarity even though no straightforward trends can be dragged out. Such investigation would require the parameterization of triplet excited state PS force fields that is out of the scope of the present study.

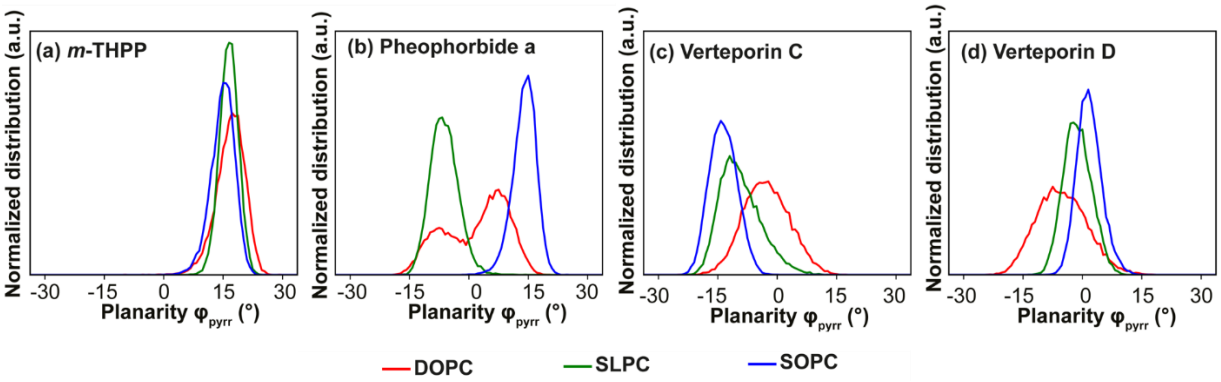

Figure 2.9. Distribution of tetrapyrrole dihedral angles.

2.4. Conclusion

In conclusion, the present work highlights the possible use of three clinically approved (or under investigation) PSs in the conception of phototriggerable liposomes. *m*-THPP/DOPC appeared to be the most efficient system, where the phototriggered release of the cargo reached approximately 40% six hours after illumination at low light fluence. Such phototriggered release would be even more efficient with encapsulated drugs having smaller molecular weight than calcein (*i.e.*, doxorubicin) and with a light source of higher irradiance.

Added to its efficiency in photopermeation drug release, *m*-THPP (or its derivative *m*-THPC which has stronger absorption coefficient at 652 nm) incorporated in DOPC liposomes would represent a promising phototriggerable system with potential dual activity (chemo- and photodynamic therapy) against relevant cancer tumors.

More particularly, our results showed that, in general, the illumination significantly altered lipid bilayer properties of the studied systems. The efficiency of membrane degradation and subsequently drug release highly depends on the PS/PL combination. Among other descriptors, the depth of PS incorporation in the lipid bilayer is a major contributor to efficiency.

Chapter 3

Synthesis and characterization of new lipid-porphyrin conjugates

3.1. Introduction

Porphyrins have received considerable attention as promising photosensitizers (PSs) for the treatment of small solid tumors by photodynamic therapy (PDT). PDT consists in the combination of a photosensitizer, oxygen and visible light at the appropriate wavelength to produce reactive oxygen species that can oxidize several vital biomolecules in cancerous cells and subsequently lead to cell death. Porfimer sodium (HpD, Photofrin®) was the earliest porphyrin derivative employed in PDT[168] and was the first PS approved by FDA in 1995 for early stage lung cancer treatment[169]. Despite its high singlet oxygen quantum yield[170] and its efficiency in the treatment of different cancers, porfimer sodium has several drawbacks including weak light absorption in the phototherapeutic window and long-term cutaneous phototoxicity[171,172]. A large variety of photosensitizers have been developed afterwards in order to minimize these drawbacks. Nevertheless, only few of them, such as temoporfin (*m*-THPC, Foscan®) and the benzoporphyrin derivative monoacid ring A (BPD-MA, verteporfin, Visudyne®) have been approved as PDT agents for the treatment of head and neck cancer[173] and age-related macular degeneration (AMD)[71], respectively.

The poor water solubility of most of these porphyrin derivatives and their tendency to aggregate under physiological conditions are key limitations to the achievement of an efficient photodynamic activity. In fact, the hydrophobic nature of most photosensitizers makes their intravenous administration a difficult task. Furthermore, the monomeric state of PSs is required to maintain their photophysical, chemical and biological properties[174]. In addition to their water solubility issue, many photosensitizers display poor tumor selectivity[175].

In order to overcome these drawbacks, several strategies have been adopted during the last years, including porphyrin glycosylation[176,177], PEGylation[178] and their incorporation into nanocarriers such as organic[23,179,180] and inorganic nanoparticles[23,181,182], and liposomes[71,82,183–185]. Among these strategies, embedding PSs in liposomal bilayers seems to be the strategy of choice for several reasons. Indeed, liposomes are composed of biocompatible, biodegradable materials and can be easily produced at industrial scale, due to their simplicity and to lower investment costs compared to other nanoparticulate systems[24,26,27]. Added to these advantages, several studies have shown the efficiency of liposomes in improving the solubility and selectivity of PSs[69,186]. Indeed, the selective accumulation of liposomes in tumors is at least partially related to the leaky tumor vasculature which allows liposomes to extravasate across the leaky tumor vessels[187]. Despite these improvements, liposomal delivery systems showed low loading efficiency of PSs within their lipid bilayers and rapid clearance of PSs from the blood due to their transfer to serum components[53,69]. Thus, the focus on PS

drug delivery has recently shifted towards the development of new nanocarriers composed of only one building block with self-assembly properties, allowing high PS payload, and facilitating their clinical translation as well as their production at industrial scale[175].

As previously described in the chapter 1, lipid-porphyrin building blocks synthesized by Gang Zheng's group[6,15] are able to self-assemble into liposome-like nanoparticles named "porphysomes" which possess multifunctional properties, including photothermal therapy (PTT), photodynamic therapy (PDT), phototriggered drug release and photoacoustic imaging (PAI)[6,15,78]. Thanks to their organic nature, porphysomes are enzymatically biodegradable and induce minimal acute toxicity during their retention in mice[6]. These lipid-porphyrin conjugates were synthesized through esterification of the sn-2 position of lysophosphatidylcholine with either pyropheophorbide a or bacteriochlorophyll a[6].

Considering these advantages, we believe there is still considerable room for the development of new lipid-porphyrin conjugates, the study of their self-assembling properties and their PDT efficiency. Thus, the aim of this work was to synthesize a new kind of lipid-porphyrin conjugates based on various lipid backbones linked to a PS via a peptide bond instead of the ester bond used in porphysomes[6,78]. To do so, two new lipid-porphyrin conjugates were synthesized by coupling Pheo-a, a photosensitizer derived from chlorophyll-a, to either chemically modified lyso-phosphatidylcholine (Lyso-PC) or egg lyso-sphingomyelin (Lyso-eSM). The physicochemical properties of these compounds and their self-assembling properties were assessed, as well as their efficiency *in vitro* on esophageal squamous cell carcinoma (ESCC) cell lines.

3.2. Material and methods

3.2.1. Chemicals

Pheophorbide a (Pheo-a, ≥ 95%, mixture of diastereomers, Mw = 592.69 g/mol) was purchased from Frontier Scientific (Logan, UT), and 6-(Fmoc-amino)hexanoic acid (≥ 98%, Mw = 353.42 g/mol) from Novabiochem (Laufelfingen, Switzerland). N,N′-Dicyclohexylcarbodiimide (DCC, ≥ 99%, Mw = 206.33 g/mol), Hexafluorophosphate Azabenzotriazole Tetramethyl Uronium (HATU, ≥ 97%, Mw = 380.23 g/mol), 4-(Dimethylamino)pyridine (DMAP, ≥ 99%, Mw = 122.17 g/mol), Dowex® 50WX8-100 ion exchange resin (hydrogen form), N,N-Diisopropylethylamine (DIPEA, 99%, Mw = 129.24 g/mol), HEPES (99.5%, Mw = 238.31 g/mol), sodium chloride (NaCl, 99%, Mw = 58.44 g/mol), Ammonium molybdate(VI) tetrahydrate (81-83%, Mw = 1235.86 g/mol), L-Ascorbic acid (99%, Mw = 176.12 g/mol), 0.65 mM Phosphorus standard solution, hydrogen peroxide (30 wt %), chloroform anhydrous (≥99%, stabilized with amylenes) and methanolic hydrogen chloride (0.5N) were provided by Sigma (St. Louis, MO, USA).

The phospholipids 1-palmitoyl-2-hydroxy-sn-glycero-3-phosphocholine (16:0 Lyso-PC, 99%, 495.63 g/mol), 1-stearoyl-2- oleoyl-sn-glycero-3-phosphocholine (SOPC, 99%, Mw = 788.14 g/mol), 1,2-distearoyl-sn-glycero-3-phosphocholine (DSPC, 99%, Mw = 790.15 g/mol), 1,2-distearoyl-sn-glycero-3-phosphoethanolamine-N-[methoxy(polyethyleneglycol)–2000]-ammonium salt (DSPE-mPEG$_{2000}$, 99%, Mw = 2805,497 g/mol) and egg sphingomyelin (Egg SM, 99%, Mw = 710.965) were purchased from Avanti Polar Lipids (Alabaster, AL). Chloroform, methanol and anhydrous N,N-dimethylformamide (DMF, 99.8% pure) were analytical-grade reagents purchased from Carlo Erba (Val de Reuil, France). The ultrapure water (γ = 72.2 mN/m at 22° C) used in all experiments was produced by a Millipore Milli-Q® Direct 8 water purification System, with a resistivity of 18.2 MΩ.cm.

3.2.2. Synthesis of compound 1

16:0 Lyso-PC (150 mg, 0.3 mmol) and Fmoc-6-Ahx-OH (212 mg, 0.6 mmol) were mixed in 5 ml of anhydrous chloroform and stirred until clear mixture was obtained. DMAP (110 mg, 0.9 mmol) and DCC (120 mg, 0.6 mmol) were added separately, in cold anhydrous chloroform. Glass beads (2 mm, previously washed with ethanol, and dried under vacuum) were added and the mixture was brought back to room temperature and sonicated for 8 hours. Temperature was kept under 25 °C. Fmoc-6-Ahx-OH (50 mg, 0.15 mmol) was added after 2, 4 and 6 hours of sonication. Once the 8 hours sonication were over, the mixture was stirred at room temperature for an additional 12 hours. It was then incubated with DOWEX (Dowex® 50WX8 hydrogen form) for 45 minutes to remove DMAP, filtered, and concentrated under vacuum until a white precipitate appeared. The 1-2 ml mixture was

then centrifuged for 5 min at 2000 *g* and the yellow liquid crude mixture was purified by chromatography on silica gel (eluted with chloroform-methanol-water 65:25:4, volume ratio; Rf = 0.35-0.4). Pure compound 1 (207 mg, white powder, yield 83 %) was dried under vacuum, lyophilized overnight, and stored at -20 °C. NMR (details in Figure S3.1): ^{1}H NMR ($CDCl_3$, 300 MHz) δ (ppm) 7.76 (d, 2H, *J* = 7.5 Hz), 7.61 (d, 2H, *J* = 7.1 Hz), 7.42 (m, 4H), 5.46 (br s, 1H), 5.23 (m, 1H), 4.38-4.10 (br m, 7H), 3.96 (m, 2H), 3.77 (br m, 2H), 3.32 (s, 9H), 3.17 (m, 2H), 2.29 (m, 4H), 1.58 (m, 6H), 1.26 (br s, 26H), 0.89 (t, 3H, *J* = 6.5 Hz); ^{13}C NMR ($CDCl_3$, 75 MHz) δ (ppm) 167.59, 165.52, 144.04, 141.26, 127.64, 127.03, 125.14, 119.93, 70.72, 66.33, 59.37,54.37,47.29, 40.81, 34.08, 31.91, 29.71 (br), 29.36 29.18, 26.11, 24.89, 22.68, 14.11. MS $(ESI)^+$ for $[C_{45}H_{72}N_2O_{10}P]^+$; calculated: 831.4925 $[M+H]^+$; observed: 831.4912.

3.2.3. Synthesis of compound 2 (PhLPC)

Compound 1 (133 mg, 0.16 mmol) was dissolved into 4 mL of DMF anhydrous, 2 mL of DIPEA and was stirred for 5 hours at room temperature to complete the full Fmoc deprotection. Pheo-a (95 mg, 0.16 mmol) and HATU (75 mg, 0.2 mmol) were combined in 4 ml of anhydrous DMF, stirred for 1 hour at room temperature under Argon, in the dark, and then added to the deprotected compound 1. The mixture was stirred in the dark at room temperature, under Argon, for 24 hours. DMF was then removed under vacuum. The crude was resuspended in minimum amount of chloroform and purified by chromatography on silica gel (eluted with chloroform-methanol-water 65:25:4, volume ratio; Rf = 0.5). Compound 2 was obtained (120 mg, dark-green powder, yield 63 %). NMR (details in Figure S3.2): ^{1}H NMR (DMSO-d_6, 400 MHz) δ (ppm) 9.34 (s, 1H), 8.93 (s, 1H), 8.80 (s, 1H), 7.86 (m, 1H), 6.40 (s, 1H), 6.15 (m, 1H), 6.03 (bd, 1H, *J* = 11.5 Hz), 5.01 (br s, 1H), 4.58 (d, 1H, *J* = 6.9 Hz), 4.19 (d, 2H, *J* = 9.3 Hz), 4.05 (br m, 3H), 3.86 (s, 3H), 3.72 (br m, 2H), 3.50 (m, 5H), 3.27 (br s, 5H), 3.13 (s, 9H), 2.91 (br m, 2H), 2.80 (s, 3H), 2.11 (br m, 6H), 1.81 (d, 3H, *J* = 6.9 Hz), 1.60 (m, 2H), 1.42 (m, 5H), 1.31 (m, 2H), 1.08 (m, 2H), 1.06-0.85 (br s, 26H), 0.706 (t, 3H, *J* = 7.1 Hz), 0.17 (s, 1H); ^{13}C NMR (DMSO-d_6, 100 MHz) δ (ppm) 189.18, 173.05, 172.52, 172.23, 171.36, 169.27, 161.90, 154.43, 150.00, 148.70, 144.57, 141.30, 137.05, 135.72, 135.10, 131.89, 128.62 (CH), 128.26, 122.80, 105.21, 104.20 (CH), 96.48 (CH), 93.70 (CH), 70.57 (CH), 65.47, 64.30, 62.60, 62.33, 58.30, 53.10 (3xCH_3), 52.62 (CH_3), 51.30 (CH), 49.41 (CH), 38.26, 33.22, 32.47, 31.12, 28.78, 28.51, 28.24, 25.71, 24.24, 24.10, 22.82 (CH_3), 21.94, 18.31, 17.13 (CH_3), 13.77 (CH_3), 11.75 (CH_3), 11.53 (CH_3), 10.36 (CH_3). MS $(MALDI\text{-}TOF)^+$ for $[C_{65}H_{96}N_6O_{12}P]^+$; calculated: 1183.48 $[M+H]^+$; observed: 1183.66; UV-Vis ($CHCl_3$:MeOH; 9:1, v:v): λ_{max}, nm (ε ($10^3.M^{-1}.cm^{-1}$) 410 (87.5), 507 (10.1), 538 (9.2), 610 (8.2), 667 (41.8).

3.2.4. Synthesis of compound 3

Egg SM (400 mg, 0.56 mmol) was dissolved in anhydrous methanolic hydrogen chloride (40 mL, 0.5 M) in a sealed vessel and stirred at 50 °C for 7 days. The crude mixture was then dried under vacuum, resuspended in minimum amount of chloroform-methanol (9:1), and purified by chromatography on silica gel (eluted with chloroform-methanol-water 65:25:4, volume ratio; Rf = 0.1). The concentrated product was then dissolved in 5 mL of methanol and stirred in the presence of Amberlite IRA-400 anion-exchange resin for two hours. The solution was then filtered. The filtrate was concentrated under vacuum and compound 3 was obtained (165 mg, white powder, yield 65 %). NMR (details in Figure S3.3): ^{1}H NMR (MeOD, 300 MHz) δ (ppm) 5.96-5.86 (m, 1H), 5.51 (dd, 1H, *J* = 15.2, 6.6 Hz), 4.33 (m, 2H), 4.08 (br m, 3H), 3.71 (br s, 2H), 3.40 (br s, 1H), 3.27 (s, 9H), 2.11 (m, 2H), 1.45 (br m, 2H), 1.30 (br s, 22H) , 0.91 (t, 3H, *J* = 6.6 Hz); ^{13}C NMR (MeOD, 75 MHz) δ (ppm) 137.29 (CH), 128.25 (CH), 70.66 (CH), 67.31, 56.92 (CH), 54.79 (3xCH_3), 33.45, 33.07, 30.80, 30.66, 30.46, 30.17, 23.74, 14.46 (CH_3); MS (ESI)$^+$ for $[C_{23}H_{50}N_2O_5P]^+$; calculated: 465.3457 $[M+H]^+$; observed: 465.3456).

3.2.5. Synthesis of compound 4 (PhLSM)

Pheo-a (160 mg, 0.27 mmol) and HATU (100 mg, 0.27 mmol) were mixed in 4 ml of anhydrous DMF and stirred for 1 hour at room temperature under Argon, in the dark. Compound 3 (115 mg, 0.25 mmol) was dissolved in anhydrous DMF with 0.5 ml of DIPEA, and then added to the Pheo a - HATU mixture, and stirred in the dark, at room temperature and under Argon for 24 hours. DMF was then removed under strong vacuum. The crude was resuspended in minimum amount of chloroform and purified by chromatography on silica gel (eluted with chloroform-methanol-ammonia 70:30:4, volume ratio; Rf = 0.3). Compound 4 was obtained (78 mg, white powder, yield 30 %). NMR (details in Figure S3.4): ^{1}H NMR (DMSO-d_6, 400 MHz) δ (ppm) 9.51 (s, 1H), 9.11 (s, 1H), 8.82 (s, 1H), 7.96 (m, 1H), 6.61 (s, 1H), 6.38 (s, 1H), 6.18 (d, 1H, *J* = 18 Hz), 6.06 (m, 1H), 5.42 (br m, 1H), 5.26 (br m, 1H), 4.53 (br s, 1H), 4.05-4.01 (br m, 3H), 3.87 (br m, 1H), 3.83 (s, 3H), 3.57 (s, 3H), 3.52 (s, 2H), 3.44-3.40 (br, m, 4H), 3.31 (s, 3H), 3.11 (s, 9H), 2.95 (s, 3H), 2.14 (br, m, 2H), 1.75 (s, 3H), 1.59-1.61 (br, m, 3H), 1.50 (s, 3H), 1.20-0.50 (br, m, 27H), 0.3 (br s, 1H); ^{13}C NMR (DMSO-d_6, 100 MHz) δ (ppm) 189.34, 173.24, 169.59, 155.52, 154.57, 145.02, 141.55, 137.23, 136.04, 135.36, 132.07, 132.01, 131.03, 130.72, 128.80, 128.41, 123.09, 105.11, 104.46, 96.57, 93.79, 69.90, 65.51, 58.42, 54.53, 53.21, 52.66, 51.42, 49.76, 31.17, 30.88, 28.69, 22.82, 21.98, 21.84, 18.38, 17.28, 13.87, 11.93, 11.66, 10.60; MS (MALDI-TOF)$^+$ for $[C_{58}H_{84}N_6O_9P]^+$; calculated: 1039.60 $[M+H]^+$; observed: 1039.58; UV-Vis ($CHCl_3$:MeOH; 9:1, v:v): λ_{max}, nm (ε (10^3.M^{-1}.cm^{-1}) 409 (89.1), 505 (12.8), 536 (11.2), 610 (10.0), 667 (40.3).

3.2.6. Surface pressure measurements

Surface pressure-molecular area isotherms (π-A) of pure components or their mixtures with DSPC were recorded using a thermostat-controlled KSV-Nima Langmuir film balance (Biolin Scientific, Finland), composed of a teflon trough (775.75 cm^2) equipped with two 145 mm Delrin barriers. Pure components or mixtures in a chloroform/methanol (9:1) solution (4.0 x 10^{16} molecules) were spread onto the aqueous buffer solution (10 mM HEPES, 150 mM NaCl, pH = 7.4). After deposition, the solvents were allowed to evaporate for 15 min before compression of the monolayer at a rate of 5.0 Å²/molecule/min. All experiments were performed at 22.1 ± 0.7°C and the results reported are mean values of at least three measurements. From the surface pressure−area data, the surface compressional moduli K of monolayers were calculated, using Eq. 7 with A the molecular area and dπ, the surface pressure change:

$$K = -A\left(\frac{d\pi}{dA}\right)_T \qquad \text{(eq. 7)}$$

The excess free energy of mixing (ΔG^{EXC}) of Pheo-a derivatives and DSPC was calculated according to Eq. 8:

$$\Delta G^{Exc} = \int_0^{\pi}(A_{12} - X_1A_1 - X_2A_2)d\pi \qquad \text{(eq. 8)}$$

where A_{12}, A_1 and A_2 are the experimental molecular areas of the binary mixture and pure compounds, respectively. X_1 and X_2 are the molar fractions of the phospholipid and the photosensitizer, respectively. ΔG^{exc} values were plotted as a function of the monolayer composition, for surface pressures of 5, 10, 15, 20, 25 and 30 $mN.m^{-1}$.

3.2.7. X-ray reflectivity experiments (XRR) at the air/buffer interface

XRR experiments were carried out at the beamline ID10B of the European Synchrotron Radiation Facility (ESRF, Grenoble). The samples were irradiated with a monochromatic synchrotron beam with an energy of 8 keV (λ = 1.55 Å). The XRR experiments were performed on monolayers of Pheo-a derivatives spread on the surface of HEPES buffer (HEPES 10 mM, KCl 150 mM, pH 7.4) and compressed to a surface pressure of 30 mN/m. The film balance was kept in a He atmosphere during the measurement to minimize the radiation damage. XRR was measured with a linear detector (Vantec-1, Bruker AXS, USA). After subtraction of the diffuse intensity background (at $\alpha_f \neq \alpha_i$), the specular reflectivity was analyzed using the Parratt formalism[188] with a genetic minimization algorithm implemented in the MOTOFIT software package[189].

3.2.8. Differential scanning calorimetry (DSC)

DSC measurements were carried out using a DSC Diamond Perkin-Elmer apparatus. Four scans of consecutive heating and cooling cycles between -10 °C and 15 °C were recorded to make sure that the thermal equilibrium was reached. Different scan rates were recorded, 5 °C/min (for the first two cycles), 2 °C/min and 1 °C/min. An empty pan was used as a reference. In addition, before each scan, a 2 min isotherm was recorded at the initial temperature to ensure that the samples were at thermal equilibrium. Multilamellar suspensions were prepared by hydration of a film made of SOPC:photosensitizer (97.5:2.5 mol%) with 45 µL of HEPES buffer (hydration rate of 90%). For each sample, a total mass of ~ 15 mg was placed in hermetically sealed aluminum pans. Samples were prepared in triplicate to check the reproducibility. To monitor the photooxidation of SOPC caused by the embedded photosensitizers, 50 µL of lamellar phase suspensions (5 mg SOPC) were illuminated for 14 min before starting the thermal measurements. Illumination was done with a homemade lamp composed of 4 Philips TL fluorescent tubes covered by a flat diffusing glass plate and fitted with an orange filter (λ ~ 520–680 nm with a λ_{max} = 590 nm) at a fluence of 2 J/cm[190]. Calibration was carried out with pure cyclohexane (> 99.9% purity, 6.7 °C melting temperature)[136]. Data were collected and processed using Pyris thermal analysis software (version 9.1). Phospholipid transition onset temperatures (T_{on}) were determined from the intercept of the baseline with the tangent to the left side of the peak.

3.2.9. Preparation and characterization of liposomes and self-assembled structures

Liposomes incorporating Pheo-a derivatives were prepared by the thin lipid film hydration method[135] followed by extrusion of the vesicles suspension. In brief, a mixture of DSPC (95 mol%), DSPE-mPEG2000 (2.5 mol%) and the studied photosensitizer (2.5 mol%) was prepared in chloroform:methanol (9:1 v/v). After removing the organic solvent under vacuum at 45 °C, the resulting film was rehydrated with 1 ml of DPBS to get a final 5 mM concentration of lipids. The mixture was vortexed and sonicated at 60 °C for 5 min. The suspension was then extruded 19 times through a 200 nm pore-sized polycarbonate membrane, while maintaining the temperature at 80 °C. The self-assembled structures were prepared following the same procedure after hydration of the lipid-porphyrin conjugate dry film with HEPES buffer. The hydrodynamic diameter and the zeta potential were measured by dynamic light scattering (DLS) (Nano ZS90, Malvern). All measurements were carried out at 25 °C. The mean diameter of the vesicles was 180 ± 10 nm, and their zeta potential was slightly negative (Table S3). The PS content in the liposome bilayers was evaluated by measuring the absorption of each liposomal sample, after disruption by addition of a methanol/THF mixture. PS loading efficiency (%) was determined as previously described in the chapter 2[190].

3.2.10. Cryo-TEM

The self-assembled structures made of lipid-porphyrin conjugates were deposited on perforated carbon-coated, copper grid (TedPella, Inc) which was immediately plunged into a liquid ethane bath cooled with liquid nitrogen (180 °C) and then mounted on a cryo holder[191]. Cryo-Transmission electron microscopy (TEM) measurements were then performed using a JEOL 2200FS (JEOL USA, Inc., Peabody, MA, U.S.A.) working under an acceleration voltage of 200 kV (Institut Curie). Electron micrographs were recorded by a CCD camera (Gatan, Evry, France).

3.2.11. Cell culture

The immortalized esophageal squamous cell line HET-1A, used as a model for normal esophageal squamous epithelium, was purchased from the American Type Culture Collection (Manassas, VA)[192]. The human esophageal squamous cell carcinoma[193] Kyse-30 was obtained from Sigma Aldrich. Cells were grown in Roswell Park Memorial Institute (RPMI) 1640 medium supplemented with 10% fetal bovine serum (FBS), 100 IU/ml penicillin and 100 µg/ml streptomycin (GIBCO, Invitrogen) in a humidified incubator with 5% CO_2 at 37 °C. Cells were passaged every three days using 0.25% trypsin/ethylenediamine tetraacetic acid (EDTA) when confluence was at 70 to 80%.

3.2.12. Cytotoxicity and phototoxicity studies

Cells were seeded into 96-well plates (4000 cells, 100 µL cell culture medium per well) and incubated overnight in the humidified incubator. On the day of experiments, free porphyrin derivatives (in DMSO) or DSPC-porphyrin derivatives liposomes (in PBS buffer) at different concentrations were added to the wells in the dark. Each well contained a final volume of 200 µl of full medium. The final porphyrin concentrations ranged from 0 to 5 µM. Cells were incubated again for 24 hours to ensure full internalization of the porphyrin derivatives. The following day, the culture medium was replaced with fresh one. Cells were then either incubated in dark for cytotoxicity tests or illuminated for 14 min for phototoxicity assessment. Cells illumination was carried out at the bottom of the culture plates with orange light in sterile conditions [35] and cells were incubated again for additional 72 hours. The cell viability was then determined by the MTT assay. Briefly, MTT was added to each well at the final concentration of 0.5 mg/mL in full medium and incubated at 37 °C with 5% CO_2 for 1h30. The medium was then removed, and the blue formazan product formed was dissolved in 200 µL DMSO. After 5 min shaking, the optical density (OD) at 570 nm of each well was measured using an ELISA plate reader (LT-5000 MS, Labtech). For each plate, each concentration was analyzed in triplicate.

3.2.13. Analysis of PSs intracellular distribution with confocal laser scanning microscopy (CLSM)

Cells (2 x 10^5 cells) were deposited on 25 mm glass cover slips housed in 6-well plates and left to grow for 24h with 5% CO_2 at 37 °C. Cells were then incubated in full RPMI medium for 24h with the appropriate treatment (free PSs in DMSO or embedded into liposomes) and then rinsed with fresh full media. Prior to imaging, cells were incubated 15 min with 200 nM of MitoTracker® Green FM (ThermoFisher scientific, Invitrogen) in DPBS at 37 °C with 5% CO_2. After washing twice with DPBS, cells were incubated for 10 min with 10 µg/mL WGA Alexa Fluor 555 (ThermoFisher scientific, Invitrogen) in DPBS at 37°C with 5% CO_2. Cells were rinsed twice with DPBS, and cover slides were transferred to the confocal microscope chamber, supplemented with full culture medium. Samples were then imaged with an inverted Leica TCS SP8 microscope gated-STED (Leica, Germany) using a HC PL APO CS2 63x/1.40 oil immersion objective lens. The instrument was equipped with a 405 nm diode for porphyrin excitation, and a WLL Laser (490 nm excitation wavelength for MitoTrackerGreen and 555 nm for AlexaFluor 555). Far red, green and red fluorescence emission were collected respectively with a 650-800 nm, a 505-550 nm and a 560-630 nm wide emission slits under a sequential mode.

The statistical co-localization analysis of the photosensitizers with mitochondria and cell membrane was performed using ImageJ statistical plugin JACoP[194]. JACoP is a commonly used tool for the calculation of colocalisation coefficient such as Manders' Co-localization Coefficient (MCC)[194]. MCC was calculated for more than 20 cells.

3.3. Results and discussion

3.3.1. Synthesis of the lipid-porphyrin conjugates

Two lipid-porphyrin conjugates with different lipid backbones were synthesized (Scheme 1). One backbone was based on sn-1-palmitoyl lysophosphatidylcholine. This lipid was modified by the introduction of 6-(Fmoc-amino)hexanoic acid via direct acylation of the secondary alcohol groups at sn-2 position using sonication in the presence of glass beads, where the reaction is believed to take place. Such procedure aims to avoid intramolecular acyl migration as demonstrated previously by Rosseto *et al.*[195,196] and Oneill *et al.*[197]. Afterwards, the amino group was deprotected and followed by attachment of Pheo-a using HATU as coupling reagent to give PhLPC (compound 2, yield 65%). The second lipid backbone, which is based on a Lyso-eSM was prepared by acidic hydrolysis of egg sphingomyelin (N-hexadecanoyl-D-erythro-sphingosylphosphorylcholine) in anhydrous methanolic hydrogen chloride at 50 °C following the same procedure as Bittman *et al.*[198]. The mild acidic hydrolysis allowed the preparation of Lyso-eSM with low extent of C-3 epimerization compared to the conventional hydrolysis methods. The Pheo-a was then coupled via peptidic coupling using the same procedure as for PhLPC, to yield compound 4 (PhLSM, yield 30%).

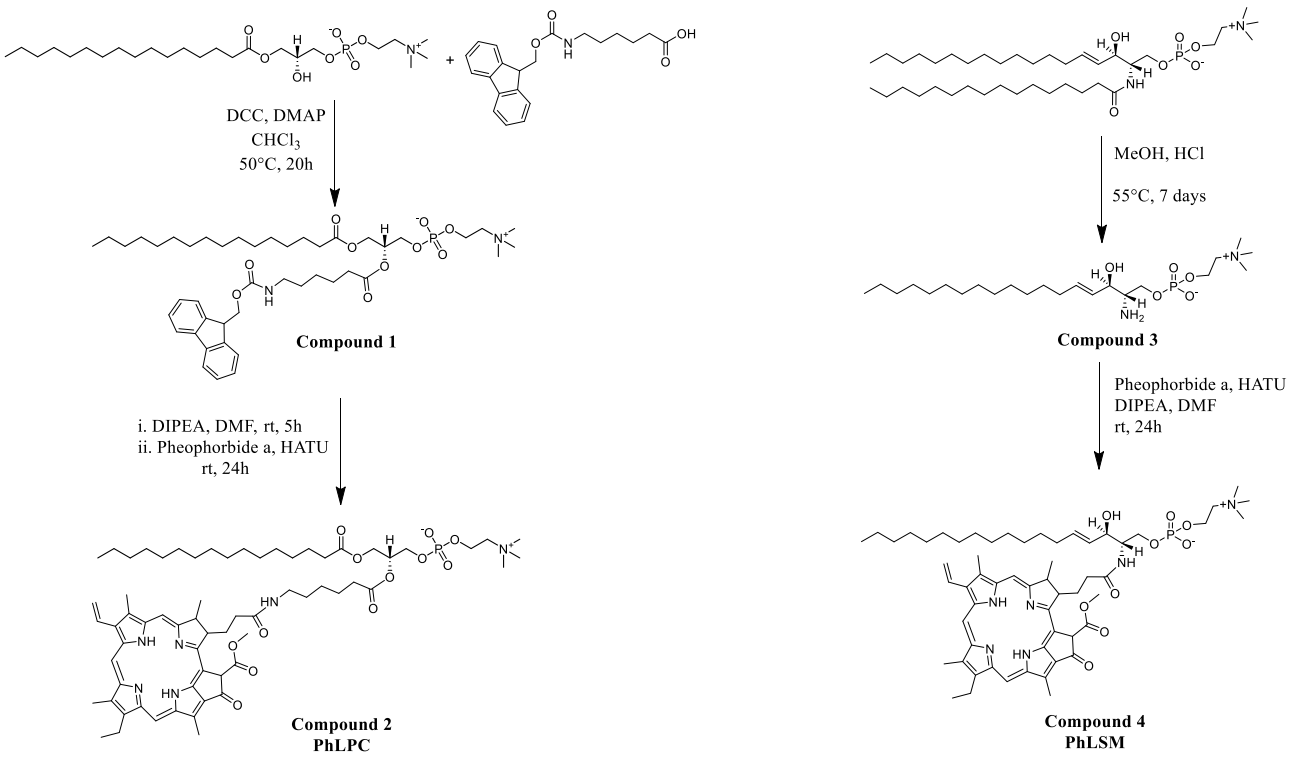

Scheme 1. Synthesis route for the lipid-porphyrin conjugates PhLPC (A) and PhLSM (B)

3.3.2. Characterization of the self-assembling and photophysical properties of the lipid-porphyrin conjugates

The ability of the synthesized compounds to self-assemble into organized structures similar to those reported for porphysomes was assessed after hydration of films made of PhLPC or PhLSM. The extruded suspensions were then analyzed by dynamic light scattering (DLS) and cryo-electron microscopy (Cryo-TEM). Interestingly, these suspensions were monodisperse (PdI < 0.2) and exhibited an average size of approximately 200 nm (Figure 3.1).

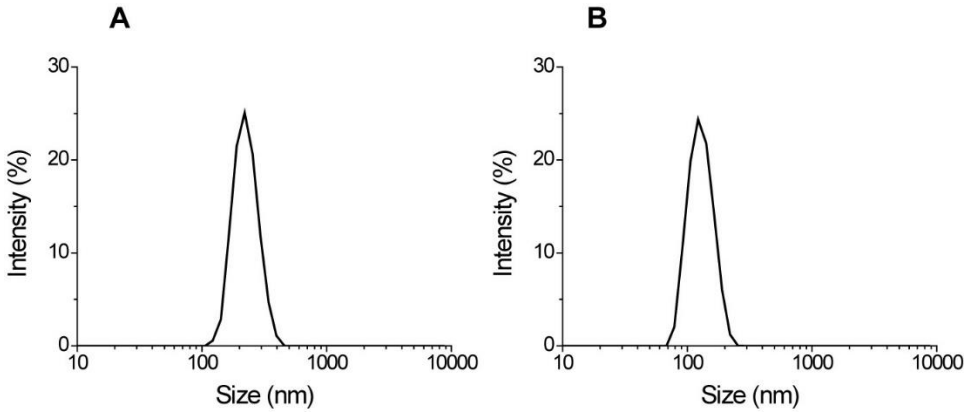

Figure 3.1. Dynamic light scattering profile of self-assembled PhLPC (A) and PhLSM (B) structures.

Cryo-TEM micrographs revealed that both lipid-porphyrin conjugates could self-assemble into liposome-like structures with a dense bilayer of lipid-porphyrin conjugates surrounding an aqueous core (Figure 3.2 C-D). The thickness of the bilayers was approximately 4-5 nm for both compounds, similar to that of ordinary phospholipid bilayers[100,101]. However, whereas self-assembled PhLPC showed spherical shape, PhLSM ones exhibited ovoid shape with undulated bilayer. The impact of PhLPC and PhLSM vesicles on their photophysical properties was studied by recording their absorption and fluorescence spectra before and after their solubilization in HEPES buffer/methanol/THF (0.2 : 0.8 : 1 mL) mixture.

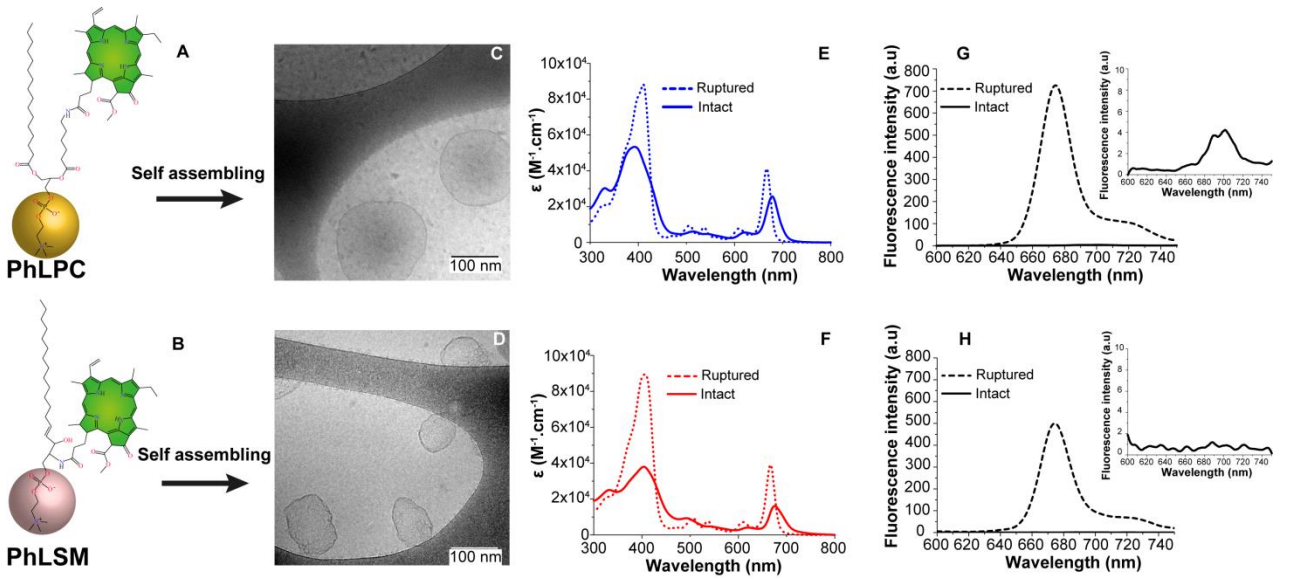

Figure 3.2. Schematic representation of (A) PhLPC and (B) PhLSM. Cryo-TEM images of self-assemblies made of pure (C) PhLPC and (D) PhLSM in HEPES buffer. Absorbance and fluorescence spectra of PhLPC (E, G) and PhLSM (F, H) vesicles, respectively before (solid line) and after (dashed line) their solubilization in HEPES/MeOH/THF (0.2, 0.8, 1 mL) mixture. The insets in (G) and (H) correspond to the quenched fluorescence spectra of PhLPC and PhLSM in buffer respectively.

As shown in Figure 3.2 and Table 3.1, lipid-porphyrin conjugates exhibited similar absorption and fluorescence spectra to that of Pheo-a in organic solvents (Figure 3.3). This result indicates that linking Pheo-a to the lipid backbones did not induce any change in the photophysical properties of the PS when the PS-lipid conjugates were in their monomeric state. Conversely, nanoassemblies of both compounds showed several interesting features. First, absorption spectra of both lipid-porphyrin vesicles revealed a broadening of porphyrin Soret and Q_{max}-bands with a significant red shift of approximately 12 nm for the latter.

Table 3.1. Soret band, Q-band and the corresponding absorption coefficient (**ε)** of monomeric (after vesicles solubilization in HEPES buffer/methanol/THF (0.2 : 0.8 : 1 mL) mixture) and aggregated forms (in HEPES buffer) of Pheo-a, PhLPC and PhLSM respectively. Values in brackets are the bandwidths (nm) at half height.

Monomers			
Compounds	**Pheo-a**	**PhLPC**	**PhLSM**
λ_{max} (Soret) [nm]	411	410	406
ε_{soret} [$M^{-1}.cm^{-1}$]	9.9 x 10^4	8.8 x 10^4	8.9 x 10^4
λ_{max} (Q) [nm]	667 (21)	667 (20)	667 (21)
ε_Q [$M^{-1}.cm^{-1}$]	3.4 x 10^4	4.1 x 10^4	3.9 x 10^4
Vesicles or aggregates			
λ_{max} (Soret) [nm]	386	392	404
ε_{soret} [$M^{-1}.cm^{-1}$]	3.1 x 10^4	5.3 x 10^4	3.8 x 10^4
λ_{max} (Q) [nm]	674 (39)	679 (30)	676 (33)
ε_Q [$M^{-1}.cm^{-1}$]	0.7 x 10^4	2.5 x 10^4	1.6 x 10^4

Compared to pure Pheo-a aggregates in buffer (Figure 3.3), the Soret and Q_{max}-band of the lipid-porphyrin vesicles were sharper, indicating that they formed more organized aggregates within their vesicular structure. The extent of the intermolecular interaction between lipid-porphyrin conjugates within the dense bilayers of the lipid-porphyrin vesicles were further analyzed by investigating their fluorescence quenching.

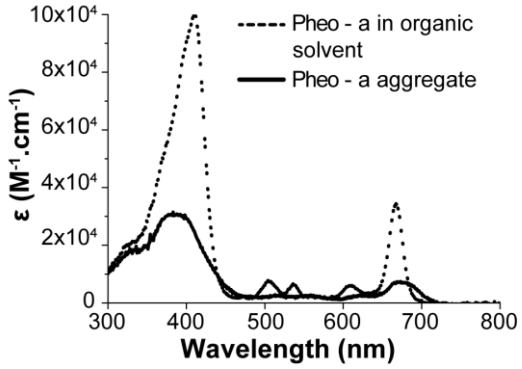

Figure 3.3. Absorbance spectra of Pheo-a aggregates in HEPES buffer (full line), or solubilized in HEPES buffer/methanol/THF (0.2 : 0.8 : 1 mL) mixture (dashed line).

As shown in the insets to Figures 3.2 G,H, the fluorescence spectra of the vesicles were extensively quenched, compared to the corresponding monomers. Interestingly, the full fluorescence intensity of lipid-porphyrin conjugates could be efficiently restored with approximately 1000-fold intensity increase, after solubilization of the lipid-porphyrin conjugates in organic solvent. Similar behavior has been described by Lovell *et al.*[6] for nanoassemblies made of pyro-lipids (pyropheophorbide-a linked to Lyso-PC via ester bond) that could be used as efficient photothermal and photoacoustic agents for tumor thermal ablation and photoacoustic imaging[6]. Taken together, the strong quenching of fluorescence emission and the red shifted absorption of the studied compounds are proof of the strong intermolecular interactions existing between chromophores within the lipid-porphyrin vesicles. However, despite these interesting properties, these vesicles were not stable and formed larger aggregates of undefined structure within few days (Figure 3.4). These results are in line with those obtained by Zheng's group[6,78] with pyro-lipids assemblies to which addition of DSPC, cholesterol and DSPE-PEG was necessary to retain efficiently an encapsulated hydrophilic cargo, and to promote higher stability of the vesicles[6,46,78].

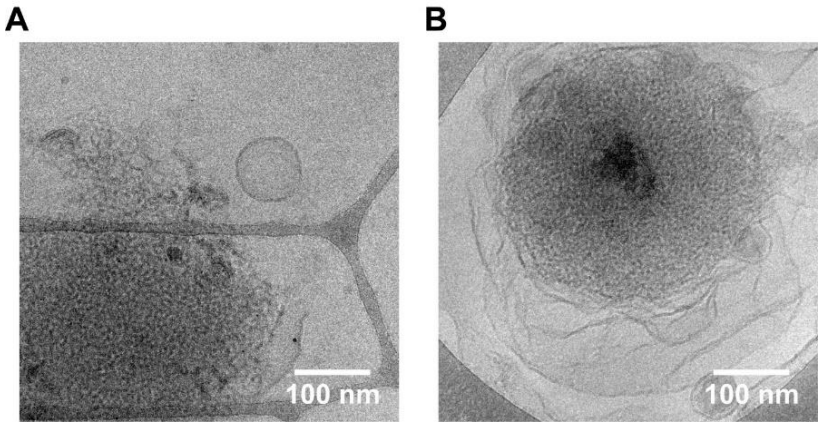

Figure 3.4. Cryo-TEM images of PhLPC (A) and PhLSM (B) aggregates.

In fact, the bilayer instability of the lipid-porphyrin conjugates can be due to the mismatch between the length of the alkyl chain in sn-1 position and the adjacent porphyrin, leading to an inadequate packing parameter for bilayer stability. The packing parameter is defined as

$$P = {}^{v}/_{a\,.\,l} \qquad \text{(eq. 9)}$$

where *v* is the hydrocarbon chain volume, *a* is the area of the polar headgroup and *l* the length of the hydrocarbon chain[199]. *P* is useful to determine the preferential organization of a surfactant at high concentration in a liquid medium. Phospholipids form bilayers because their *P* value usually lies between 0.5 and 1[199]. In the case of PhLSM, the porphyrin is grafted in the vicinity of the polar headgroup thus increasing its polar group area, and subsequently decreasing *P* to a value lower than 0.5 (conical or truncated conical shape). Conversely for PhLPC, the porphyrin is conjugated to the hydrophobic chain in sn-2, which may induce an increase in the hydrophobic volume leading to a *P* value higher than 1 (inverted conical shape)[200]. It has also been shown that when lipid molecules with complementary shapes are associated together, the value of *P* becomes additive resulting in the formation of intermediate blocks that can form a stable bilayer[200]. So, since the two studied lipid-porphyrin conjugates cannot form stable bilayers on their own, they could be mixed with unmodified phospholipids to counterbalance the effect of the length mismatch between alkyl chains.

3.3.3. Interfacial behavior of lipid-porphyrin conjugates

To further investigate the effect of the organization of the lipid-porphyrin conjugates on their self-assembling properties, we studied the interfacial behavior of the two compounds at the air-buffer interface using a Langmuir trough. The π-A isotherms for Pheo-a and the lipid-porphyrin conjugates (PhLPC and PhLSM) spread at the air-buffer interface are shown in Figure 3.5 A and the main

characteristics are summarized in Table 3.2. The data show that the three compounds formed stable monolayers and reveal interesting differences between them. The influence of the attachment of Pheo-a to the Lyso-eSM backbone or to the sn-2 aliphatic chain of Lyso-PC is readily apparent on the graph showing significant differences in isotherm shape, surface pressure and molecular area at collapse between compounds. The surface pressure corresponding to the lateral pressure in membranes or phospholipid vesicles is close to 30 mN/m[201,202]. At this surface pressure, the molecular area of Pheo-a (A_{30}) was 53 Å^2. Considering the approximate dimensions of Pheo-a as determined using the Visual Molecular Dynamics (VMD) software[203], the experimental interfacial molecular area of the PS was much smaller than that expected for a Pheo-a molecule lying flat on the surface (~ 156 Å^2). Conversely, the experimental A_{30} value for Pheo-a was in good agreement with the calculated value of the surface area of a Pheo-a molecule with carboxylic and ester groups facing the air/water interface (~ 55 Å^2). This arrangement would result from the formation of closely packed films of Pheo-a molecules, controlled by strong attractive π-π interactions between the rings of neighboring molecules.

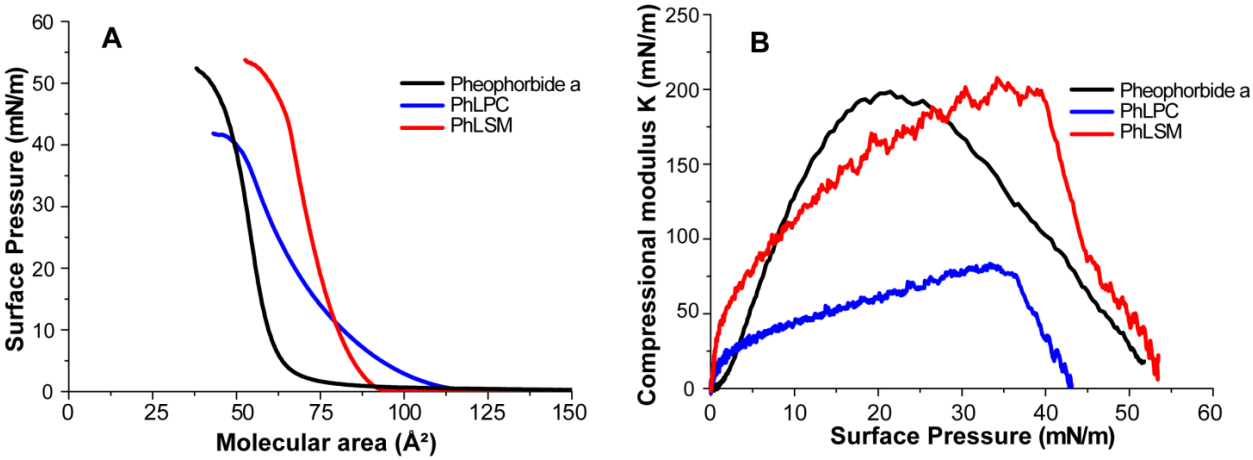

Figure 3.5. (A) π-A isotherms and the corresponding (B) compressional modulus for pure Pheo-a, PhLPC, and PhLSM spread at the air-buffer interface.

Both lipid-porphyrin conjugates formed more expanded monolayers with larger molecular areas at the surface pressure onset (A_0) for PhLPC (116 Å^2) and PhLSM (94 Å^2) compared to Pheo-a (80 Å^2). Surprisingly, while the molecular area expansion for PhLSM was maintained even at higher surface pressure, that of PhLPC at 30 mN/m was significantly reduced as compared to pure Pheo-a. In addition, while Pheo-a and PhLSM showed similar collapse surface pressure and similar π-A isotherms profile, PhLPC exhibited a completely different isotherm profile, with dissimilar shape, surface pressure and molecular area from those of the two other compounds.

Such behavior could be explained by different molecular arrangements of the studied molecules at the air/buffer interface. Apparently, grafting Pheo-a to the Lyso-SM backbone did not affect its interfacial arrangement at the air/water interface and the area expansion of its isotherm could be only explained by the presence of the PC headgroup in the vicinity of the chromophore. However, the longer C6 carbon chain linker of PhLPC, bearing the Pheo-a at its extremity would provide more flexibility to the attached chromophore to adopt distinct local orientation at different surface pressure. Indeed, the onset of the surface pressure for the PhLPC is observed at a larger molecular area (~116 $Å^2$) than the other compounds due to the presence of the acyl chain bearing Pheo-a at the interface. Upon further monolayer compression, the molecular area of PhLPC decreased significantly to reach a collapse molecular area of ~50 $Å^2$ which lies between that of Pheo-a and PhLSM. However, it should be noticed that this molecular area is smaller than that of monounsaturated phospholipids (A_c ~ 60-70 $Å^2$). Such behavior could be explained by the reorientation of the Pheo-a to align with the sn-1 C16 carbon chain with subsequent solubilization of molecules into the subphase during the compression. To gain further insight into the structural characteristics of the lipid-porphyrin conjugates, the compressibility moduli of their monolayers were calculated and plotted as a function of surface pressure. As shown in Figure 3.5 B and Table 3.2, a similar compressional modulus range is revealed for Pheo-a and PhLSM with a K_{max} value approaching ~ 200 mN/m. However, PhLPC exhibits a much lower value (~ 80 mN/m). According to Davies and Rideal[204], the values for PhLSM and Pheo-a would correspond to the liquid condensed state (100 mN/m < K_{max} < 250 mN/m) of a monolayer, while that of PhLPC would indicate a monolayer in liquid-expanded state (K_{max} < 100 mN/m). Thus, PhLPC formed a less organized monolayer than the other studied compounds.

Table 3.2. Molecular area at surface pressure onset (A_0), molecular Area (A_{30}) at 30 mN/m, molecular Area (Ac), surface Pressure (π_c) at collapse, and maximal compressional modulus K_{max} for compounds monolayers.

Monolayer composition	**A_0 ($Å^2$)**	**A_{30} ($Å^2$) at 30 mN/m**	**A_c ($Å^2$)**	**π_c (mN/m)**	**K_{max} (mN/m)**
Pheo-a	80	53	41	50.2	198.5
PhLPC	116	60	50	41.5	82.6
PhLSM	94	72	64	51.5	205.4

3.3.4. Analysis of the fine structures of Pheo-a derivatives monolayers

To get a better understanding of the fine structures perpendicular to the plane of Pheo-a derivatives monolayers, the specular X-ray reflectivity (XRR) was measured on monolayers compressed to a surface pressure of 30 mN/m. Figure 3.6 A, shows the XRR curves of Pheo-a, PhLPC and PhLSM monolayers spread onto HEPES buffer, fitted using a two-slab model. The corresponding electron density profiles (ρ) reconstructed from the best fit results (solid red lines in Figure 3.6 A) along the z-axis are also shown in Figure 3.6 B. The thickness (d), electron density (ρ) and root mean square roughness (σ) of each interface are summarized in table 3. Pheo-a exhibited total thickness $d_{pheo\text{-}a}$ of 15.7 Å. The hydrophobic core had a thickness of 9.5 Å and an electron density of 0.436 $e^- \times Å^{-3}$. Since these values are consistent with those reported for other porphyrin monolayers[205], it is plausible that Pheo-a molecules take an upright orientation with respect to the interface (Figure 3.6 C).

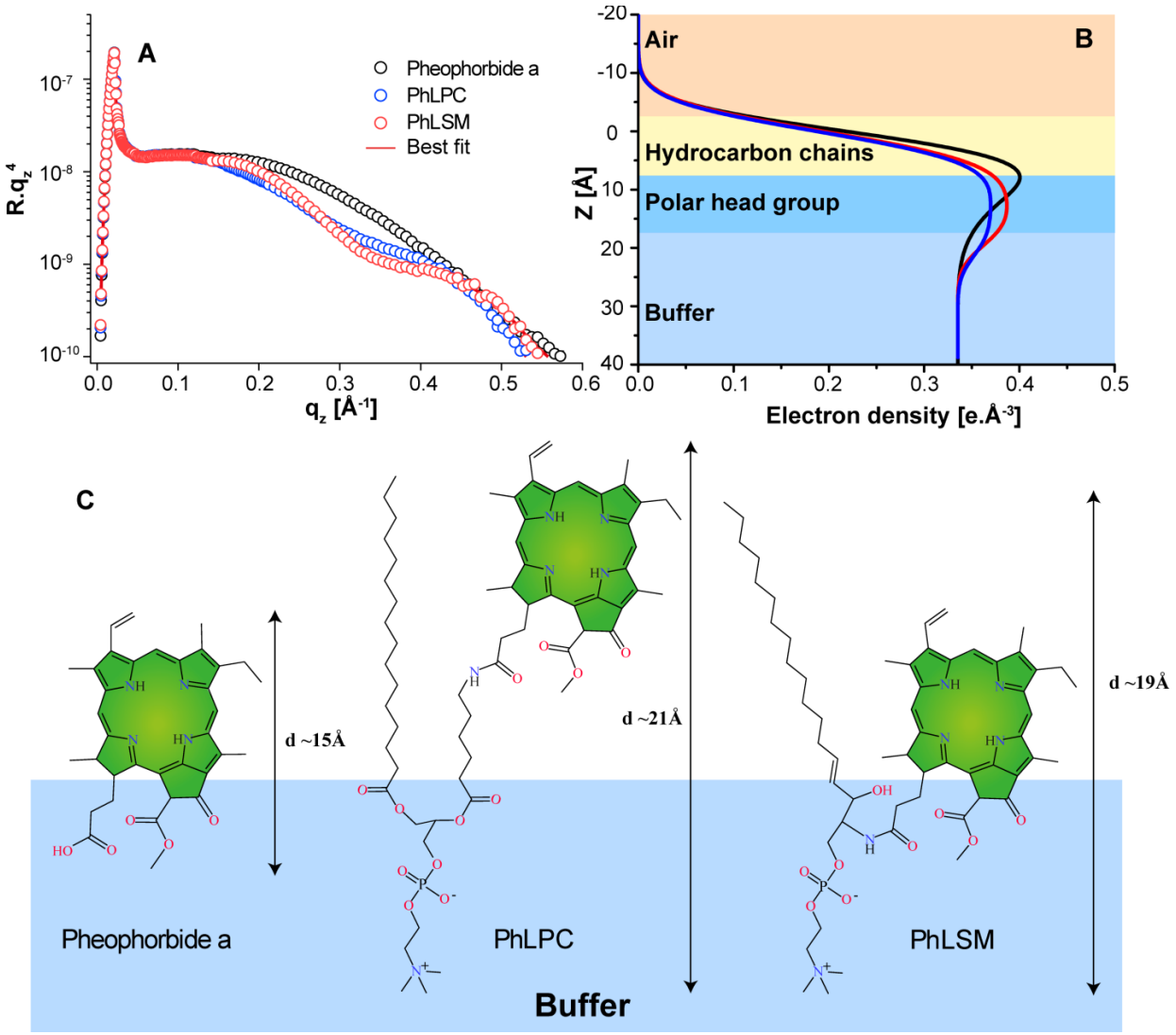

Figure 3.6. (A) XRR curves of a Pheo-a derivatives monolayers at a surface pressure of 30 mN/m. The solid lines represent the best model fits to the experimental data. The experimental errors are within the symbol size. (B) The reconstructed electron density profiles along the Z-axis. (C) Schematic representation of the orientation of Pheo-a derivatives at the air/buffer interface.

In fact, this result agrees well with the area per molecule and compression modulus determined from π-A isotherms (Figure 3.5). The thickness and electron density of the hydrophobic regions of the PhLPC monolayer are $d_{HC(PhLPC)}$ 11.6 Å and $\rho_{HC(PhLPC)}$ = 0.373 e- × $Å^{-3}$, respectively. Interestingly, the corresponding values for the PhLSM monolayer are $d_{HC(PhLSM)}$ 9.4 Å and $\rho_{HC(PhLSM)}$ of 0.391 e^- × $Å^{-3}$, respectively. The ρ_{HC} values of both compounds are higher than those reported for saturated[206,207] or monounsaturated[42] alkyl chains of phospholipids. This could suggest the presence of porphyrin core within the alkyl chains. Although the thickness of hydrophobic region of PhLPC is larger than that of PhLSM, it is notable that the total thickness of PhLPC (d_{PhLPC} = 21.5 Å) is 2 Å thicker than that of PhLSM (d_{PhLSM} = 19.5 Å). This could be explained in terms of the conformational difference of the porphyrin. In the case of PhLPC, sn-1 C16 carbon chain and porphyrins are aligned (Figure 3.6 C, middle) while such an alignment is sterically prohibited in the case of PhLSM. In order to validate the fitting quality, the average number of electrons per molecule was calculated from the fit and compared to that calculated from the chemical formula of the studied compounds. As shown in Table 3.3, there is a good agreement between the calculated number of electrons and the theoretical one for Pheo-a and PhLSM. Conversely for PhLPC, there is a significant difference between the number of electrons calculated from the molecular formula and that from the fit. This discrepancy could be interpreted by the error in PhLPC molecular area evaluation, due to its solubilization into buffer subphase.

Table 3.3. Best fit parameters for the XRR Results for Pheo-a derivatives monolayers at 30mN/m as presented in Figure 3.6.

	d (Å)	**ρ (e^- × $Å^{-3}$)**	**σ (Å)**	**Average number of e^-/molecule from the fit**	**Theoretical number of e^-/molecule**
Pheophorbide-a					
Hydrophobic core	9.5 ± 0.3	0.436 ± 0.007	4.1 ± 0.1	342	314
Hydrophilic groups	6.2 ± 0.5	0.372 ± 0.010	4.1 ± 0.5		
Buffer	∞	0.335	4.5 ± 0.6		
PhLPC					
Hydrophobic chains	11.6 ± 0.5	0.373 ± 0.001	4.4 ± 0.8	462	638
Choline headgroup	9.8 ± 0.5	0.369 ± 0.001	3.6 ± 0.5		
Buffer	∞	0.335	3.1 ± 0.1		
PhLSM					
Hydrophobic chains	9.4 ± 0.6	0.391 ± 0.001	4.3 ± 0.1	546	560
Choline headgroup	10.1 ± 0.6	0.387 ± 0.001	4.6 ± 0.8		
Buffer	∞	0.335	3.1 ± 0.1		

3.3.5. Miscibility of Pheo-a derivatives with phospholipids

We then evaluated the behavior of porphyrin derivatives when mixed with lipids in order to determine if these compounds could form stable systems when incorporated in a liposomal bilayer. To do so, we chose DSPC as phospholipid, and mixed it with increasing molar percentage of lipid-porphyrin derivatives. The recorded π-A isotherms of pure DSPC and its mixture with Pheo-a, PhLPC and PhLSM at the air/buffer interface are shown in Figure 3.7. A, B and C, respectively. Pure DSPC formed a condensed phase as previously reported[153,208]. DSPC/Pheo-a mixtures did not behave in the same manner when the molar percentage of Pheo-a increased. Indeed, the isotherms for mixtures containing up to 10 mol% Pheo-a were shifted toward larger molecular areas than that of pure DSPC, but remained still in between the isotherms of the pure components up to 30 mN/m. However, at higher surface pressures, the isotherms of DSPC/Pheo-a exhibited slight shoulders at approximately 33 mN/m, 40 mN/m and 44 mN/m for monolayers containing 2.5%, 5% and 10% of Pheo-a respectively. This behavior could be related to the solubilization of some Pheo-a in the aqueous phase. Interestingly, the isotherms for the mixtures with a Pheo-a content higher than 10% were shifted toward larger molecular areas than that of the pure Pheo-a indicating unfavorable interactions between the two components.

A similar behavior was observed for mixed DSPC/PhLSM monolayers. However, unlike DSPC/Pheo-a mixtures, the isotherms for DSPC/PhLSM monolayers exhibited shoulders at higher surface pressure (around 40 mN/m). Furthermore, the isotherms were all intercalated between those of the pure components, even at 50 mol% PhLSM, which would account for a better miscibility of DSPC with PhLSM than with the free Pheo-a.

The compression isotherms of DSPC-PhLPC mixtures exhibited sharp inflection followed by a plateau region at ~ 43 mN/m. This sharp inflection is observed at a surface pressure close to that of pure PhLPC collapse and lower than that of pure DSPC. This could be interpreted as a demixing between the two compounds, with subsequent loss of PhLPC from the monolayer in the aqueous subphase. Similar behavior has been observed by Kinnunen's group who demonstrated that addition of oxidized phospholipids to phospholipid monolayers induced phase separation and their solubilisation in the subphase, with subsequent micelles formation due to the presence of polar groups (either carbonyl or carboxylate) on the sn-2 chain[41]. In the case of PhLPC, the driving force for the phase separation would be due to the strong attractive π-π interaction between Pheo-a cores.

The isotherms of the mixtures were further analyzed in terms of compressibility modulus as shown in Figures 3.7. D-F. In fact, for the three mixtures, adding a porphyrin or a porphyrin derivative to a DSPC monolayer induced a decrease in their rigidity with a more significant decrease in the presence

of PhLPC, as expected from the low surface compressional modulus of this conjugate. In addition, compared to DSPC/Pheo-a mixtures, the sharp inflection point observed for the isotherms of PhLPC mixtures at high surface pressure (~ 40mN/m) is clearly revealed by a minimum in K at ~ 44 mN/m, close to the π_c of pure PhLPC, followed by an increase until the K values superimpose with those of pure DSPC. This is another indication of the complete expulsion of PhLPC from the monolayers at high surface pressure.

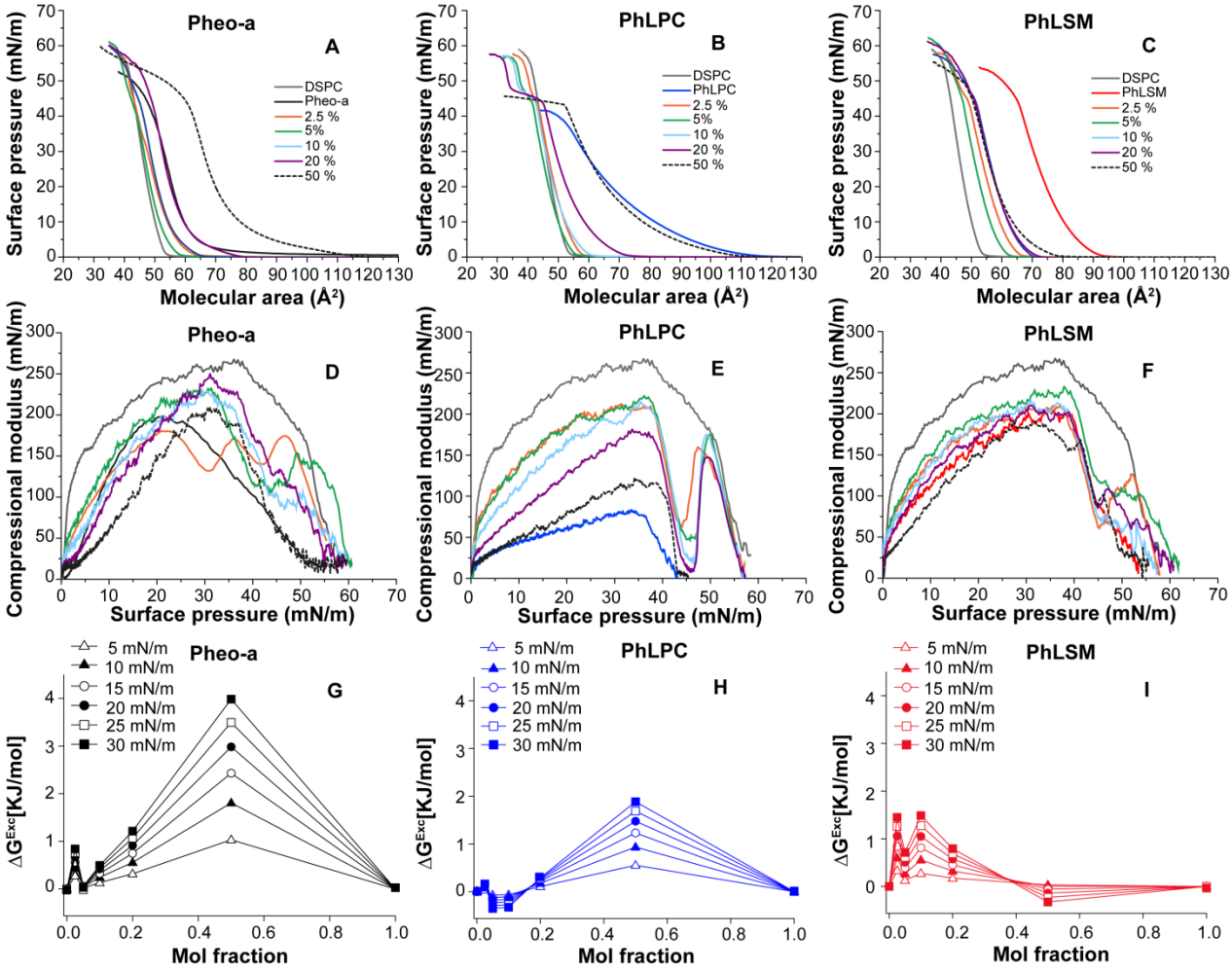

Figure 3.7. π-A isotherms of mixed monolayers of Pheo-a (A), PhLPC (B) and PhLSM (C) with DSPC at various molar %. Their corresponding compressional modulus and excess free energy of mixing (ΔG^{exc}) are shown in (D-F) and (G-I) respectively.

In order to analyze quantitatively the thermodynamics of interaction between the binary mixtures, the excess free energy of mixing (ΔG^{Exc}) was calculated up to a surface pressure of 30 mN/m. As inferred from Figures 3.7. G-I, the ΔG^{Exc} values of binary mixtures of DSPC-Pheo-a and DSPC-PhLPC at different surface pressures are positive for the various PS molar fractions denoting repulsive

interactions between DSPC and PS compounds in the mixtures. However, the situation is different for DSPC-PhLSM mixture. Indeed, this latter exhibited positive ΔG^{Exc} values up to 10% PhLSM, which then decreased down to values close to 0 at 50%. In addition, it should be stressed that ΔG^{Exc} values were the highest for DSPC-Pheo-a followed by DSPC-PhLPC and DSPC-PhLSM, thus indicating that interactions in the mixed films containing lipid-porphyrin conjugates were less repulsive than those in monolayers containing Pheo-a. Taken together, these results indicate that the three Pheo-a derivatives cannot be homogeneously mixed with DSPC and tend to segregate in the lipid monolayer.

3.3.6. The incorporation of lipid-porphyrin conjugates into liposomes

In a next step, we investigated the incorporation efficiency of Pheo-a derivatives into liposomes and evaluated their impact on their stability. DSPC liposomes doped with 2.5 mol% of DSPE-PEG_{2000} and increasing molar percentages (2.5-20 mol %) of Pheo-a derivatives were prepared and characterized. As shown in Figure S3.5, the highest Pheo-a loading rate was 5 mol%, but the liposomes increased in diameter and polydispersity. An important loss of material was also observed on the polycarbonate membrane during extrusion (Figure S3.5). A higher loading efficiency was achieved with PhLPC and PhLSM, with monodisperse vesicle suspensions and no significant material loss during extrusion.

We measured the fluorescence of DSPC liposomes incorporating the different PSs at 2.5 mol %. As depicted in Figure 3.8, the three PSs showed fluorescence quenching. The highest values were obtained for PhLSM and PhLPC. Such fluorescence quenching could be explained by the aggregation of the PSs into organized patterns in the bilayer due to their high packing density. Similar behavior has been observed by Gang Zheng's group with other lipid-porphyrin conjugates when incorporated within liposomal bilayers, and it was attributed to the formation of J-aggregates[84,102,209].

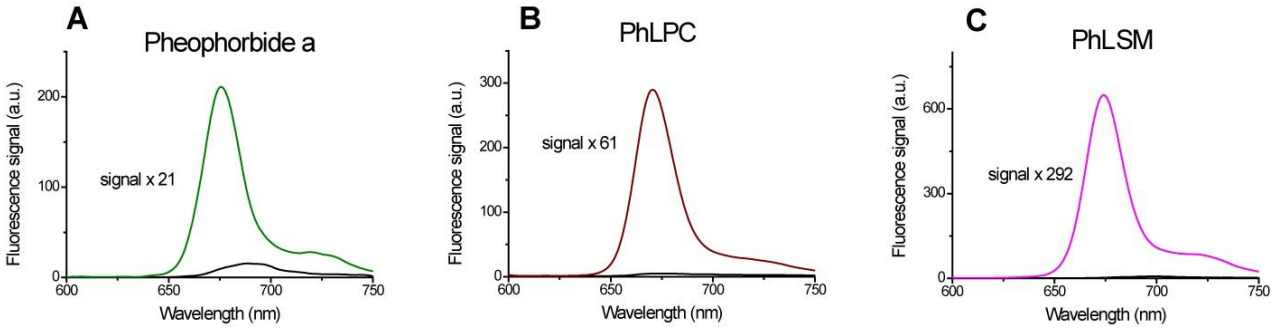

Figure 3.8. Fluorescence spectra of (A) Pheo-a, (B) PhLPC and (C) (PhLSM) incorporated at 2.5 mol% into PEGylated DSPC liposomes in HEPES buffer before (black line) and after their rupture into organic solvent (colored lines). The displayed number in each spectrum corresponds to the enhancement of PS fluorescence intensity after liposomes rupture.

3.3.7. Thermotropic behavior of phospholipid bilayers incorporating lipid-porphyrin conjugates

PS aggregation in the membrane of liposomes could be an issue for liposomal delivery of photosensitizing agents for PDT applications. Indeed, the aggregation of PSs such as Pheo-a induces a decrease in the quantum yield of triplet state (Φ_t), thus reducing the quantum yield of singlet oxygen ($^1O_2$)[77,178], which is responsible for the photodynamic activity. Therefore, in order to investigate the impact of the PSs incorporation percentage on their oxidative potential upon illumination, we performed a calorimetric analysis of SOPC lamellar suspensions incorporating different molar percentage of either PhLSM or PhLPC. SOPC was chosen in these experiments because it contains an unsaturated alkyl chain that is a good substrate for the formation of lipid hydroperoxides[190] upon interaction with singlet oxygen during the photodynamic reaction. The formation of such species can induce a phase separation within the lipid matrix that can be easily detected by DSC. Although qualitative, such method allows the determination of the optimal molar percentage of embedded PSs for efficient photodynamic activity.

First, the impact of PSs incorporation percentage on the phase behavior of the SOPC membrane was assessed. Figure 3.9 shows the heat capacity (C_p) scans for the various lamellar suspensions. Compared to pure SOPC which exhibited a sharp endothermic peak at ~6 °C, both conjugates caused a broadening of the main transition peak and a shift toward lower temperatures in a concentration-dependent manner. This suggested the destabilization of the intermolecular cooperativity of SOPC molecules. Such tendency was more pronounced for PhLSM, which could be explained by its higher disordering effect on the hydrocarbon chains of phospholipids and/or its higher incorporation efficiency than that of PhLPC.

DSC scans were also performed after illumination of the SOPC lamellar suspensions in the conditions described in the experimental section. Compared to the pure SOPC sample, the illumination of samples containing up to 2.5 mol % of either PhLPC or PhLSM induced dramatic changes in the thermograms. The main transition peaks of both SOPC-PhLPC and SOPC-PhLSM samples were broadened with a significant shift of T_{onset} towards lower temperatures and the appearance of a second peak/shoulder at lower temperature. These results indicate the formation of new phases upon illumination of the SOPC–PS systems, which could be related to the formation of new chemical species within the lipid bilayer, as demonstrated in the previous chapter[190].

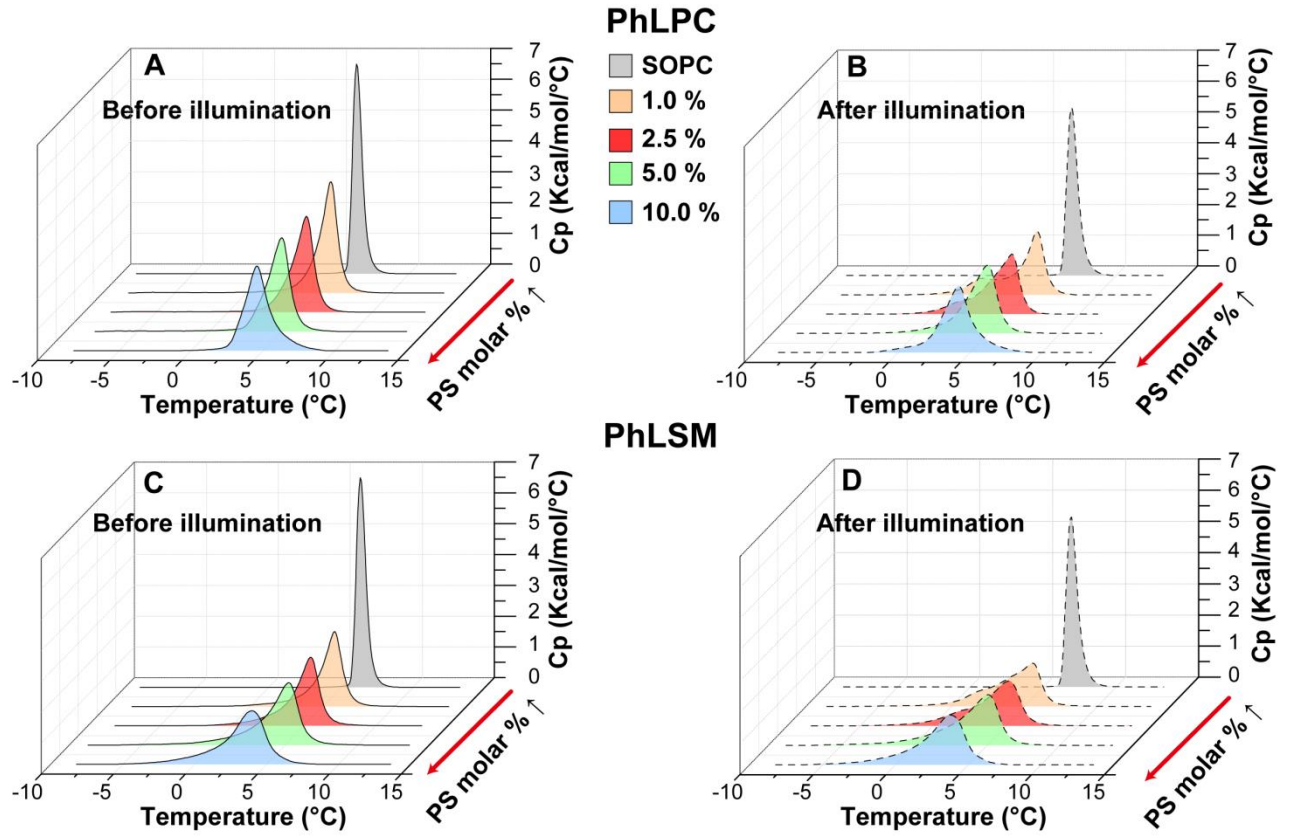

Figure 3.9. DSC heating scans for pure SOPC lamellar suspensions incorporating increasing molar percentages of PhLPC or PhLSM before (A,C) and after (B,D) illumination.

It should be noticed, however, that the impact of the illumination was more pronounced in PhLPC samples than in those of PhLSM. This could be explained by the longer spacer of PhLPC compared to PhLSM, which would allow the Pheo-a moiety to be more deeply inserted into the lipid bilayer. Hence, the singlet oxygen generated upon illumination would have greater probability to oxidize the unsaturated chains within the lipid matrix. The illumination of samples containing more than 2.5% mol of PSs did not induce a significant change (Figure 3.9, Table 3.4) in their thermal behavior, which could be due to PS aggregation in the lipid membranes. Based on the aforementioned, we formulated liposomes with only 2.5% mol of PS and their photodynamic efficiency was then evaluated *in vitro* on esophageal cell lines.

Table 3.4. T_{onset}, T_{peak} temperatures and enthalpies of SOPC doped with PhLPC, or PhLSM before and after illumination

	Before Illumination				After Illumination			
PhLPC (%)	**1**	**2.5**	**5**	**10**	**1**	**2.5**	**5**	**10**
T_{onset} (°C)	4.5	3.9	2.5	2.5	0.9	0.4	2.5	2.5
T_{peak} (°C)	5.9	5.5	5.1	4.6	5.9	5.5	5.2	4.3
ΔH (kcal/mol)	6.0	5.8	5.9	6.1	5.3	5.4	5.8	6.0
PhLSM (%)	**1**	**2.5**	**5**	**10**	**1**	**2.5**	**5**	**10**
T_{onset} (°C)	5.0	4.5	4.0	2.3	0.9	0.2	4.0	2.4
T_{peak} (°C)	5.9	5.5	5.4	4.2	5.8	5.4	5.3	4.1
ΔH (kcal/mol)	4.9	5.2	5.8	5.8	4.9	5.0	5.6	5.7

3.3.8. Phototoxicity of lipid-porphyrin conjugates in esophageal squamous cell carcinoma (ESCC) cell lines

The phototoxicity of Pheo-a derivatives (Pheo-a, PhLPC and PhLSM), free or incorporated in DSPC/DSPE-PEG_{2000} liposomes (95/2.5 mol%), was investigated on Kyse-30 and HET-1A cells. After overnight incubation with either free or incorporated PSs, the cells were illuminated for 14 min, and the phototoxicity of the three compounds was quantified by the MTT test (Figure 3.10). The cytotoxicity in darkness was found to be negligible with a survival percentage close to 100% for the three PSs in the 0.1-5 µM concentration range (Figure S3.6). As shown in Figure 3.10, free or liposomal Pheo-a exhibited a strong phototoxicity on both cell lines with a half maximal inhibitory concentration (IC50) of 0.20 and 0.15 µM, respectively (Figure 3.10, Table 3.5). These IC50 values for Pheo-a are in agreement with those previously reported by Rapozzi *et al.*[130] for other cancer cell lines.

The IC50 of the lipid-porphyrin conjugates was in all cases significantly higher than that of Pheo-a, thus indicating a decrease in Pheo-a phototoxic activity when in the form of lipid conjugates (Table 3.5). This behavior could be related to lipid-porphyrin conjugate aggregation in aqueous media, which in turn would reduce their photodynamic activity. The same explanation could be applied to these compounds when incorporated in liposome bilayers. Indeed, although the Pheo-a conjugates incorporated in liposomes maintained their photoactivity at this percentage of incorporation, as demonstrated by DSC experiments, the fluorescence intensity of embedded conjugates was partially quenched, and this effect was higher than with Pheo-a (Figure 3.8). This fluorescence quenching is explained by the aggregation of Pheo-a conjugates within the lipid bilayer because of π- π stacking of porphyrin cores.

Table 3.5. Phototoxicity (IC50, µM) of Pheo-a derivates either free or incorporated into PEGylated DSPC liposomes on HET1A and Kyse 30 cell lines.

	IC50 (µM)					
	Pheo-a		PhLPC		PhLSM	
	Free	Liposomes	Free	Liposomes	Free	Liposomes
HET-1A	0.21±0.01	0.15±0.01	2.52±0.08	2.95±0.14	> 5	2.04±0.15
Kyse-30	0.20±0.04	0.15±0.01	1.37±0.04	1.90±0.06	2.10±0.04	1.00±0.04

This in turn would cause a decrease in the quantum yield of the singlet oxygen and thus, a decrease in the photodynamic efficiency of lipid-porphyrin conjugates as compared to Pheo-a incorporated in liposomes. However, it should be noted that despite this decrease in phototoxicity for both lipid-porphyrin conjugates compared to Pheo-a, they can still be considered as strong photosensitizers with IC50 values between 1 and 2 µM for the cancerous Kyse-30 cell line. Interestingly, PhLPC and PhLSM exhibited a selective phototoxicity toward this cell line, especially when incubated with the cells in their free form. Indeed, whereas the IC50 of the free PhLPC and PhLSM were 1.4 µM and 2.1 µM in Kyse-30 cells, respectively, they were higher for HET-1A cells, with 2.5 µM and > 5µM respectively. This striking result could be explained by different cellular uptake and/or subcellular localization in cancerous cells compared to healthy ones. Indeed, several studies have shown that PSs internalization mechanism and subcellular localization are major determinants of their phototoxicity[176,210–212].

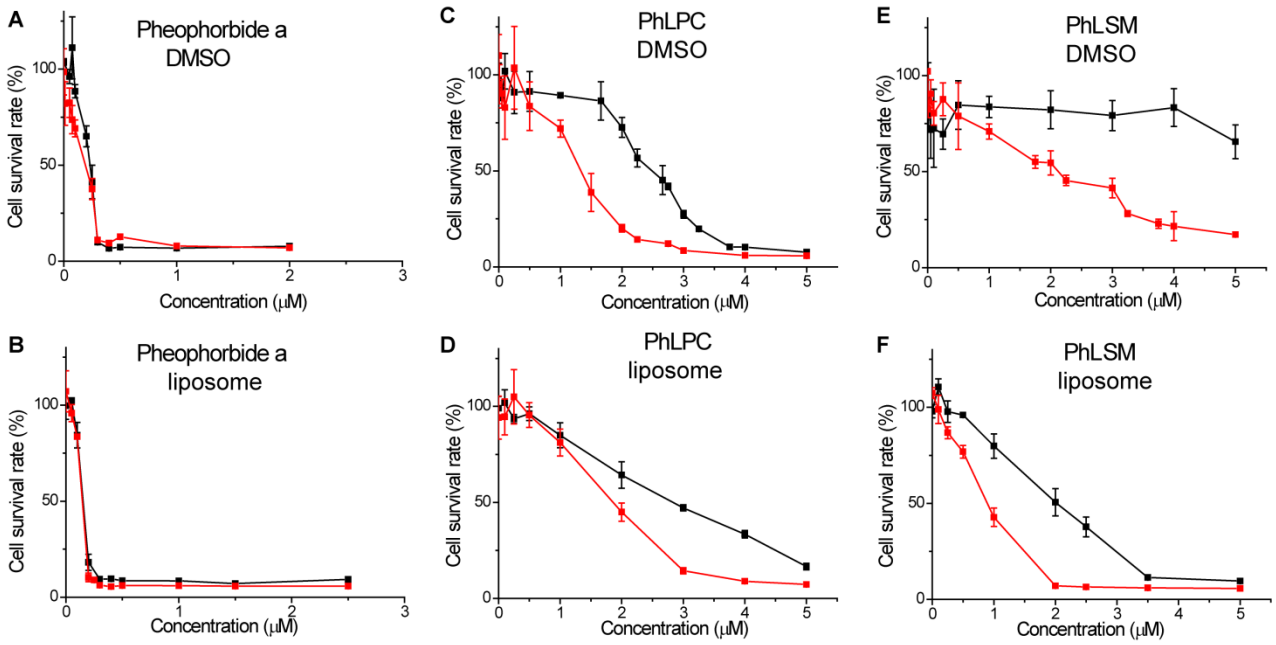

Figure 3.10. Phototoxicity HET-1A (black line) and Kyse-30 (red line) incubated with free Pheo-a (A), PhLPC (C), or PhLSM (E), or encapsulated in liposomes (B, D, F respectively).

3.3.9. Cellular uptake and subcellular localization

In order to evaluate the cellular uptake of the different PSs, as well as their subcellular distribution, we applied confocal laser scanning microscopy on HET-1A and Kyse-30 cells after overnight incubation with the studied PSs, either free or incorporated into DSPC liposomes. Figure 3.11 shows that the nucleus remained dark in all cases, and that the fluorescence signal of the three PSs was mainly inside the cytoplasm, indicating their effective internalization. The fluorescence distribution of free Pheo-a dissolved in DMSO versus liposomal formulation revealed in both cases a broadly diffused fluorescence with no obvious difference between the two cell lines. In comparison with Pheo-a, the cellular distribution of fluorescence of free lipid-porphyrin conjugates was punctuated, which could be related to PSs localization into specific intracellular compartments such as mitochondria or lysosomes. Similar tendency was observed for lipid-porphyrin conjugates embedded into liposomes.

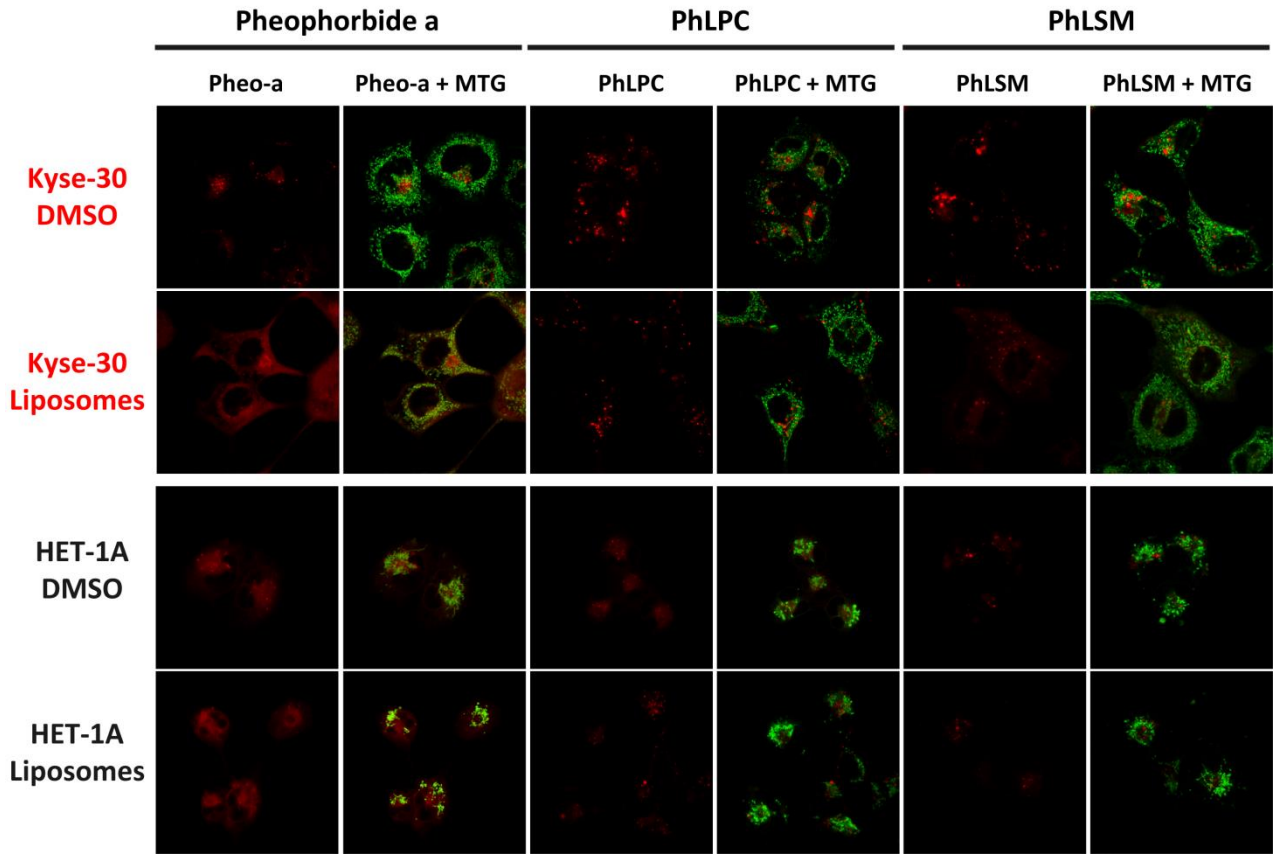

Figure 3.11. Confocal microscopy images of Kyse-30 and HET-1A cells treated with the free photosensitizers (red) dissolved in DMSO or incorporated into liposomes. The second column for each compound corresponds to the images merged with those in the presence of Mitotracker (green).

Since the pure Pheo-a and its derivatives may have higher affinity for mitochondria compared to other cell organelles[130,178], we investigated the co-localisation of the PSs with mitochondria using Mitotracker-green. The images in Figure 3.11 and their statistical analysis performed using ImageJ statistical plugin JACoP and the Manders' coefficient of co-localization (MCC), show that Pheo-a exhibited higher MCC (0.41-0.50) than the lipid-Pheo-a conjugates in both cell lines, without significant difference between Kyse-30 and HET-1A cells (Table 3.6).

Table 3.6. Manders' coefficient of co-localization (MCC) of photosensitizers with Mitotracker (green).

	MCC					
	Pheo-a		**PhLPC**		**PhLSM**	
	Free	**Liposomes**	**Free**	**Liposomes**	**Free**	**Liposomes**
HET-1A	0.41±0.06 (n=26)	0.43±0.07 (n=25)	0.24±0.09 (n=26)	0.17±0.05 (n=28)	0.14±0.03 (n=28)	0.18±0.08 (n=27)
Kyse-30	0.43±0.06 (n=22)	0.50±0.08 (n=27)	0.36±0.09 (n=26)	0.32±0.07 (n=25)	0.21±0.09 (n=26)	0.37±0.09 (n=23)

This could explain the higher photoactive efficiency of Pheo-a compared to the conjugated molecules, but also its non-selectivity towards the cancerous cell line[213,214]. The Pheo-a conjugates exhibited the lowest MCC values for HET-1A cells. Moreover, the MCC evolution of Pheo-a conjugates in both cell lines with the different formulations seemed to correlate with their IC50 values. This result would indicate the preferential affinity of PhLPC and PhLSM for the mitochondria in the cancerous cell line.

3.4. Conclusion

In this work, we have synthesized and characterized two new lipid-porphyrin conjugates which exhibit self-assembly properties. These molecules were designed in the aim to improve the photosensitizers loading efficiency in liposome bilayers and enhance PS photodynamic activity against cancerous cells. The addition of the lipid backbone exacerbated the amphipathic character of the photosensitizer, while maintaining its photodynamic activity. Both conjugates were able to self-assemble in buffer, however they were unstable and formed aggregates with unclear structure within few days. Such instability could be related to mismatch between the length of the alkyl chain in sn-1 position and the adjacent porphyrin, which would affect the lipid packing parameter. Both lipid porphyrin conjugates could be incorporated efficiently in lipid vesicles, with higher loading rates than Pheo-a. We determined the maximal molar ratio of the PS-conjugates for maintaining their

photodynamic activity. The phototoxicity of free or incorporated lipid-porphyrin conjugates was studied in two esophageal squamous cell lines. Although less photoactive than free Pheo-a, both lipid-porphyrin conjugates exhibited higher selectivity towards cancerous cells.

Interestingly, lipid-porphyrin conjugates carried by liposomes exhibited high fluorescence quenching yields. This means that upon their illumination, the absorbed photon energy could be dissipated into heat. Thus, although their photodynamic efficiency (IC50) was lower than that of Pheo-a, their self-quenching property in lipid vesicles could be taken advantage of, for use as efficient cytotoxic photothermal agents (PTT). Moreover, such systems could be used for phototriggered release of encapsulated chemotherapeutic agents. Although they were not explored in this work, these aspects will be investigated in the next chapter. Hence, liposomes containing lipid-porphyrin conjugates would present a promising photoactivatable drug delivery system with multifunctional properties (PDT, PTT and phototriggered release of an anticancerous drug) against cancer tumors.

Chapter 4

New lipid-porphyrin conjugates for the conception of phototriggerable liposomal drug delivery systems via photothermal conversion

4.1. Introduction

In PDT and in photooxidative-triggered release of a drug, PS aggregation is an issue. However, in some cases, aggregation can be desirable, as it favors non-radiative deexcitation pathways of photosensitizers, responsible for heat generation. Applications of porphyrin and porphyrin derivatives related to their photothermal properties are emerging[86,215]. They rely on two criteria: high local concentration of the PS, and light illumination with high fluences (hundreds of mW/cm^2 to several W/cm^2). Porphyrins can be specifically used for photothermal therapy (PTT), a treatment killing cells by sudden increase in heat [216,217]. Indeed, an increase of the temperature from 37°C (physiological conditions) to 42-45°C is sufficient to induce, for example, cancer cells death[218]. Photothermal effect is generally segmented into three processes depending on the temperature: when local temperature rises to 42-45°C (clinical hyperthermia), cell death is mainly caused by protein denaturation[219]. When the temperature reaches 55°C, photothermal effect induces a rapid coagulation of proteins, and results in cell death. This process is also called thermal ablation[220]. At temperatures higher than 100°C, water vaporization from the tissues induces strong dehydration[221].

Pharmaceutical formulations proposed for PTT are nowadays mainly based on the use of metal nanoparticles. These particles are efficient, but their potential toxicity is high, and their adequacy to carry drugs for additional chemotherapy is poor. Using an approach in which metal particles would be replaced by biocompatible and biodegradable porphyrin is attractive. As in photodynamic therapy, PTT using these molecules can also be used to trigger cargo release [222,223].

Porphyrins, which are hydrophobic and easily aggregate, have already shown potential as photothermal agents[86,118,219]. The main strategy for inducing sufficiently high aggregation state of these molecules in a controlled manner is to use porphyrin conjugates with self-assembling properties. Peptide conjugates[224], polymeric conjugates[225–227], and phospholipid conjugates[6,66] have indeed proven to be efficient as PTT agents. Lipid-porphyrin conjugates can self-assemble into liposome-like structures, or have to be combined with conventional lipids to form liposomes, whose aqueous core can be used to host hydrophilic drugs[6,78]. The photothermal effect can then be exerted to trigger or accelerate the release of the encapsulated drug[56,78].

We conjugated pheophorbide a (Pheo-a) to lyso-phosphatidylcholine (PhLPC) and lyso-sphingomyelin (PhLSM)[228]. The resulting lipid-porphyrin conjugates can self-assemble into liposome-like structures which were not stable in the long term. Hence, their combination with other lipid derivatives was required in order to obtain stable formulations. In this chapter, we first identified the most compatible lipids for the formulation of stable PS-loaded liposomes. The potency of these vesicles for photothermal-triggered release of a hydrophilic fluorescent probe, calcein, was evaluated, and the quantification and stability of the photothermal effect was estimated.

4.2. Material and methods

4.2.1. Chemicals

PhLPC and PhLSM were prepared as previously described[228]. Pheophorbide a (Pheo-a, ≥ 95% pure, Mw = 592.69 g/mol) was purchased from Frontier Scientific (Logan, UT). HEPES (99.5% pure, Mw = 238.31 g/mol), sodium chloride (NaCl, 99% pure, Mw = 58.44 g/mol), cholesterol (≥99% pure, Mw = 386.65 g/mol), cholesteryl hemisuccinate (CHEMS, >99% pure, Mw = 486.73 g/mol), octadecylamine (stearylamine, 97%, Mw = 269.51 g/mol), calcein (Mw = 622.53 g/mol), and Sepharose 4B, and Triton™ X-100 were purchased from Sigma (St. Louis, MO, USA).

The phospholipids 1,2-distearoyl-sn-glycero-3-phosphocholine (DSPC, 99% pure, Mw = 790.15 g/mol), 1,2-distearoyl-sn-glycero-3-phosphoethanolamine-N-[methoxy(polyethyleneglycol)–2000]-ammonium salt (DSPE-mPEG2000, 99% pure, Mw = 2805,497 g/mol) were purchased from Avanti Polar Lipids (Alabaster, AL). Chloroform and methanol were analytical-grade reagents purchased from Carlo Erba (Val-de-Reuil, France). The ultrapure water (γ = 72.2 mN/m at 22° C) used in all experiments was produced by a Millipore Milli-Q® Direct 8 water purification System, with a resistivity of 18.2 MΩ.cm.

4.2.2. Liposomes preparation and characterization

Liposomes were prepared by the thin lipid film hydration method[135] followed by extrusion of the vesicles suspension. Mixtures of lipids and the studied photosensitizer was prepared in chloroform:methanol (9:1 v/v). After removing the organic solvent under vacuum at 45°C, the resulting film was rehydrated with 1 mL of 50 mM calcein in HEPES buffer, to get a final concentration of lipids of 5 mM. The mixture was vortexed and sonicated at 60°C for 5 min. The suspension was then extruded 19 times through a 200 nm pore-sized polycarbonate membrane, while maintaining the temperature at 80°C. Liposomes were then separated from non-encapsulated free calcein by size exclusion chromatography using a home-packed column with Sepharose 4B gel. The hydrodynamic diameter was measured by dynamic light scattering (DLS) (Nano ZS90, Malvern). All measurements were carried out at 25 °C. The PS content in the liposome bilayers was evaluated by measuring absorbance at 667 nm; using a CARY 100 Bio UV–visible spectrophotometer (Varian, USA); of each liposomal sample, after disruption by addition of a methanol/THF mixture.

4.2.3. Cryo-TEM

Samples were deposited on a perforated carbon-coated copper grid (TedPella, Inc), which was immediately plunged into a liquid ethane bath cooled with liquid nitrogen (180°C) and then mounted on a cryo holder[191]. Cryo-Transmission electron microscopy (TEM) measurements were performed

using a JEOL 2200FS microscope (JEOL USA, Inc., Peabody, MA, U.S.A.) working under an acceleration voltage of 200 kV (Institut Curie, Orsay). Electron micrographs were recorded by a CCD camera (Gatan, Evry, France).

4.2.4. Surface pressure measurements

Surface pressure-surface area isotherms (π-A) of pure components or their mixtures with phospholipids were recorded using a thermostated KSV-Nima Langmuir film balance (Biolin Scientific, Finland), composed of a teflon trough (775.75 cm^2) equipped with two 145 mm-long Delrin barriers. Pure components or mixtures in a chloroform/methanol (9:1) solution (4.0 x 10^{16} molecules) were spread onto the aqueous HEPES buffer solution (10 mM HEPES, 150 mM NaCl, pH = 7.4). After deposition, the solvents were left to evaporate for 15 min before compression of the monolayer at a rate of 5.0 Å²/molecule/min. All experiments were performed at 22°C and the results reported are mean values of at least three measurements.

4.2.5. X-ray reflectivity experiments (XRR) at the air/buffer interface

XRR experiments were carried out at the beamline ID10B of the European Synchrotron Radiation Facility (ESRF, Grenoble). The samples were irradiated with a monochromatic synchrotron beam with an energy of 8 keV (λ = 1.55 Å). The XRR experiments were performed on monolayers of PhLSM:Cholesterol (50:50 mol%) mixture spread on the surface of HEPES buffer (HEPES 10 mM, KCl 150 mM, pH 7.4) and compressed to a surface pressure of 30 mN/m. The measurement was conducted before and after 10 min of illumination, with a 120 mm-diameter deep red led (spectrum 660-670 nm), with an output power of 12 W. During measurement, the film balance was kept in a He atmosphere to minimize the radiation damage. XRR was measured with a linear detector (Vantec-1, Bruker AXS, USA). After subtraction of the diffuse intensity background (at $\alpha_f \neq \alpha_i$), the specular reflectivity was analyzed using the Parratt formalism[188] with a genetic minimization algorithm implemented in the MOTOFIT software package[189].

4.2.6. Quantification of calcein release

Quantification of calcein release was done by fluorescence spectroscopy using a Perkin-Elmer LS-50B computer-controlled luminescence spectrophotometer (Massachusetts, USA) equipped with a red sensitive R6872 photomultiplier. The emission spectra were obtained before and after illumination, with excitation at λ_{exc} = 490 nm and emission measured at λ_{em} = 514 nm. The illumination of PhLSM:Cholesterol (50:50 mol%) was performed at a wavelength of 660 nm and an

estimated fluence = 80 mW/cm^2 using a laser diode. The illumination of DSPC:Chol:PhLSM (67.5:30:2.5 mol%) vesicles was performed at a wavelength of 670 nm and an output power of 25 mW (estimated fluence = 125 mW/cm^2) using a laser diode module with a laser diode driver and a temperature controller (LDM90, LDC220C, TED200C from Thorlabs Inc. Newton, New Jersey, United States). The calcein release experiments were performed on liposome suspensions diluted in HEPES buffer to 10 μM of total lipids. The liposomes were then disrupted by addition of Triton X-100 at a final concentration of 1% (m/v), to release the remaining calcein. The release was calculated using Eq. 4 (p40).

4.2.7. Evaluation of the photothermal effect

Temperature increase was measured in real-time during illumination by means of a thermocouple probe located into the middle of glass cuvette containing 1ml of the liposome suspension, under stirring. PhLSM concentration was estimated by measurement of the absorption of the suspension (ε = 8.9 x 10^4 M^{-1}.cm^{-1} and 3.9 x 10^4 M^{-1}.cm^{-1} at 667 nm, and 410 nm, respectively) [228] after disruption of the liposomes into HEPES buffer/methanol/THF (0.2:0.8:1 mL) mixture. Photothermal effect was measured for 10 minutes under illumination by a monochromatic laser at 670 nm, and an output power of 400 mW. The illuminated surface was approximately 0.5 cm^2, which gives an approximate fluence of ~800 mW/cm^2. In order to check the reproducibility of the photothermal effect, three cycles of 10 min on/10 min off illumination were carried out, and the consecutive temperature increase and decrease was measured.

4.3. Results and discussion

4.3.1. Self-assembling properties of lipid-porphyrin conjugates when mixed with other lipids

The ability of the two lipid-porphyrin conjugates to form stable liposomes-like structures, once combined with conventional lipids, was estimated based on the definition of the packing parameter[199,229,230], *P*, defined p73.

For PhLPC, the porphyrin moiety is conjugated to the hydrophobic chain in sn-2 position, which may induce an increase in the hydrophobic region (Figure 4.1 A). This produces an apparent increase in the lipid chain volume, compared to the polar head volume ($P>1$). On the contrary, for PhLSM (Figure 4.1 B), the porphyrin is grafted in the vicinity of the polar headgroup of the phospholipid and contributes to enlarge it ($P<1$). Thus, PhLPC and PhLSM would exhibit inverted conical and truncated conical shapes, respectively.

Stable lipid bilayers exist when *P* is in the range of 0.74-1[200]. Due to their molecular shape, PhLPC and PhLSM cannot form stable bilayers. The vesicles obtained quickly aggregate, as reported in the previous chapter[228]. In order to form liposomes with these molecules, it is necessary to mix them to lipids with complementary shape. Molecule pairing as depicted in Figure 4.1 was previously described by Khandelia *et al.*[92] for cholesterol and oxidized phospholipid species.

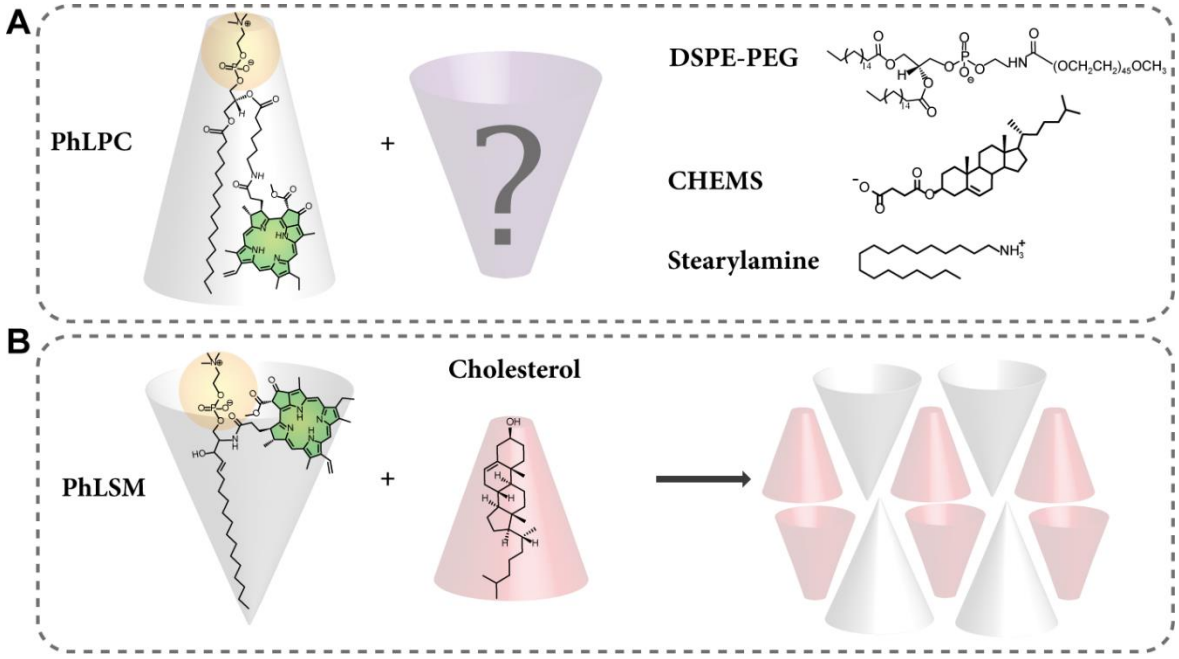

Figure 4.1. Pairing strategy of PhLPC (A) and PhLSM (B) when mixed with other lipids having complementary packing parameters.

4.3.1.1. PhLPC formulations

Two strategies were explored to form liposomes with PhLPC. In the first one, PhLPC was mixed in equimolar percentage (50:50 mol%) to DSPE-PEG_{2000}, a phospholipid modified by a long polyethylene glycol (PEG) chain. This PEGylated phospholipid is widely used in liposomal formulation in order to prolong liposome circulation time in the bloodstream[4,231–233]. However, the efficiency of this strategy depends on the molar % of the incorporated DSPE-PEG into the lipid bilayer as well as on the PEG chain length[234]. Indeed, depending on these two parameters, PEG polymer can adopt either a "mushroom" or a "brush" conformation[233,235]. Increasing the molecular weight of PEG chains extends the existence of the brush regime and lowers the mol% of DSPE-PEG at which the mushroom-to-brush transition occurs. This transition was predicted to occur at less than 4 mol % and 2 mol % for PE-PEG_{2000}[236] and PE-PEG_{5000}[237] respectively. Garbuzenko *et al*. showed that in mushroom regime (DSPE-PEG_{2000} < 4% mol), the DSPE-PEG_{2000} did not affect the additive packing parameters in the lipid bilayer and exhibited a *P* value of 1.044[238]. Conversely, in the brush regime the *P* value decreased exponentially to reach a value of 0.487 at 30 mol%[238].

Thus, based on the additivity rule of packing parameters between amphiphilic molecules with complementary molecular shapes, we investigated the ability of PhLPC to form supramolecular structures after extrusion of hydrated films made of an equimolar percentage of PhLPC and DSPE-PEG_{2000}. The DSPE-PEG_{2000}/PhLPC dispersions obtained were apparently monodisperse, with an average hydrodynamic diameter of 218 nm. However, the nano-objects observed by cryo-electron microscopy (Cryo-TEM) did not resemble to lipid vesicles (Figure 4.2 A-B). Furthermore, the calcein presumably encapsulated in these particles was lost during separation by size exclusion chromatography. This formulation was thus considered as inefficient to form vesicle-like structures. We hypothesized that at such high concentration of DSPE-$PEG_{2000,}$ the PEG chains undergo steric exclusion from the lipid bilayer surface, thus inducing a decrease in the bilayer compressibility by destabilizing its structure with subsequent micelles formation [239,240]. As PhLPC was already unstable and aggregated, DSPE-PEG_{2000} was not sufficient for stabilizing the membrane.

The second strategy was to use other lipids with voluminous ionized polar head at physiological pH. To do so, we selected two lipids: cholesteryl hemisuccinate (CHEMS, Figure 4.1 A), and stearylamine (SA, Figure 4.1 A). CHEMS is an acidic cholesterol ester (pKa~ 5.8) that self-assembles into bilayers at alkaline and neutral pH[241]. CHEMS is commonly used in combination with dioleoylphosphatidylethanolamine (DOPE) to form pH-sensitive liposomes[242,243]. Indeed, at acidic pH the negatively charged group of hemisuccinate is protonated leading to a decrease in the polar headgroup area and thus an increase in its packing parameter. Consequently, liposomes become unstable and disintegrate. Stearylamine is an alkylated ammonium molecule that is positively charged

at pH lower than 9.5 and exhibits interesting properties in the formation of stable non-containing phospholipid bilayers when mixed with equimolar percentage of cholesterol[244]. Based on these properties, and on the similarity in the geometrical shape of PhLPC and DOPE or cholesterol, mixing PhLPC with either CHEMS or SA may allow the formation of stable lipid bilayers.

After hydration with 50 mM calcein solution of a film either composed of equimolar PhLPC and CHEMS or PhLPC and SA in the presence of 2.5 mol % of DSPE-PEG_{2000}, the formulated suspensions gave monodisperse suspensions with a size of 153 nm and 217 nm, respectively, as determined by dynamic light scattering (Figure 4.2 D, F). However, in both cases, calcein could not be encapsulated in the so-formed assemblies. This indicates that these nano-assemblies were not vesicle-like structures. For CHEMS, cryo-TEM showed similar pattern as the one obtained with DSPE-PEG_{2000}, with highly condensed structures, and no apparent bilayer. Conversely, in the case of SA, the cryo-TEM pattern was significantly different, and showed obvious presence of bilayers. However, the morphology looks like open sheet-like bilayers, which would explain the impossibility to encapsulate the cargo.

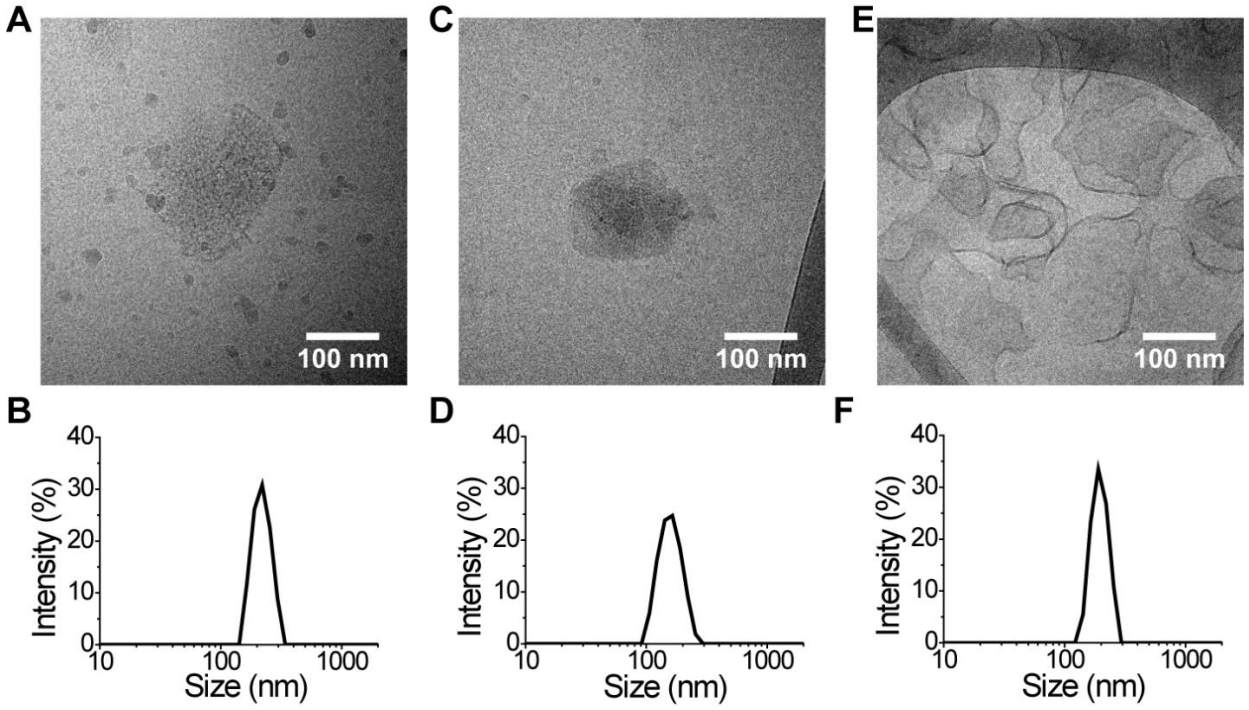

Figure 4.2. Cryo-TEM images of PhLPC formulations obtained with DSPE-$mPEG_{2000}$ (A), CHEMS (C) and Stearylamine (E), and the corresponding DLS measurements (B, D and F respectively).

4.3.1.2. PhLSM formulations

As explained above, PhLSM would exhibit a conical/truncated conical shape, due to the presence of the porphyrin moiety close to the phosphatidylcholine polar head. It must be combined with molecules that possess an inverted cone shape for complementary shape strategy. An example of cone-shape lipid is cholesterol. Cholesterol is also known to rigidify lipid bilayers and decrease their permeability.

When a film formed of equimolar PhLSM and cholesterol was hydrated with a calcein solution, successful cargo encapsulation was observed. Dynamic light scattering measurement indicated a monodisperse suspension, with an average diameter of 282 nm. Cryo-TEM revealed the presence of liposomes, however consisting of a mixture of multilamellar and unilamellar vesicles (Figure 4.3 A). When DSPE-PEG_{2000} (2.5 mol%) was added, the multilamellar population disappeared, and the average diameter decreased to 183 nm (Figure 4.3 E,F). This decrease in thickness could be related to the presence of the PEG chains that prevent stacking of bilayers, favoring formation of unilamellar vesicles (Figure 4.3 C,G). A slight increase in lipid bilayer thickness was observed on cryo-TEM images (n analyzed vesicles = 40-50): indeed, the thickness of the bilayer was ~ 4 nm in the DSPE-PEG_{2000}-free bilayer, and it increased to 4.5 nm in the presence of the polymer.

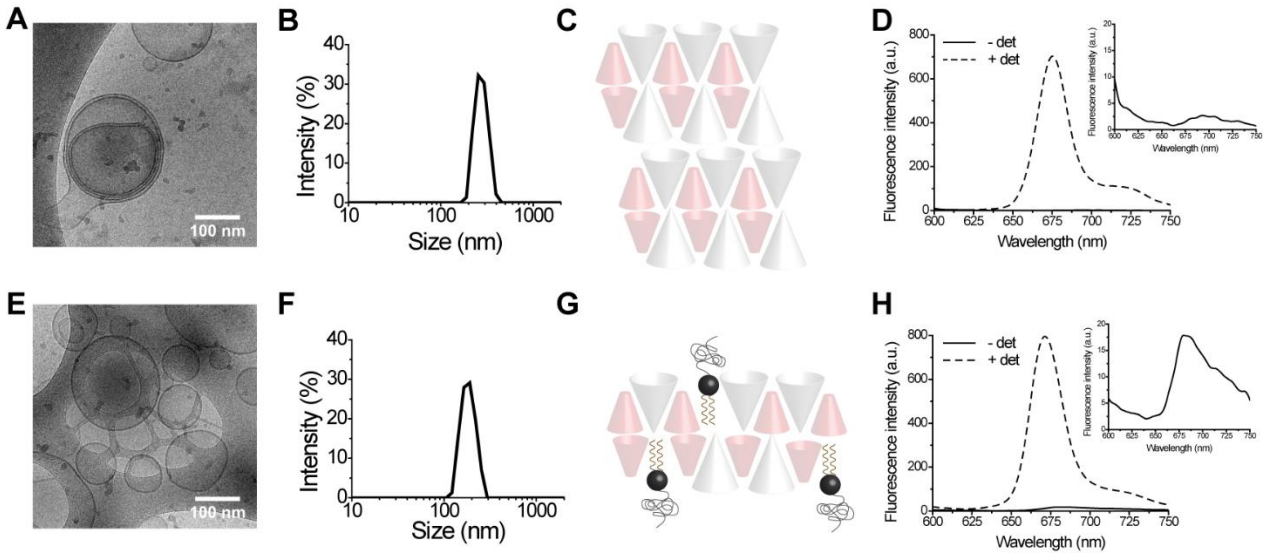

Figure 4.3. Cryo-TEM images (A and E), DLS measurements (B and F) and local bilayer organization (C and G) of PhLSM and cholesterol liposome-like structures without and with the presence of DSPE-PEG_{2000} respectively. Fluorescence spectra of PhLSM : Chol vesicles without (D) or with the presence of DSPE-PEG_{2000} (H), before (solid line) and after addition of detergent (dash line). Insets represent the quenched fluorescence of PhLSM in intact vesicles.

Based on geometrical calculation we estimated the number of lipid molecules (n) in the PhLSM:Chol formulation using the following equations[245,246]:

$$n = \frac{M_v}{M_l} \qquad \text{eq (10)}$$

Where M_v is the mean molecular weight of a vesicle, and M_l is the mean molecular weight of PhLSM:Chol (50:50 mol%, M_l = 712.47 g/mol) mixture.
M_v is given as:

$$M_v = \frac{N_A[\frac{4}{3}\pi(r_0^3 - r_i^3)]}{\upsilon} \qquad \text{eq (11)}$$

where r_0 and r_i denote the external and internal radii of the vesicle, respectively, N_A is the Avogadro's number (N_A = 6.022 x 10^{23} mol^{-1}), and υ is the partial specific volume of lipid mixture in the vesicle membrane. υ value has been previously determined to be approximately 0.985 $cm^3.g^{-1}$ for vesicles made of egg PC and cholesterol mixture[245,246]. The thickness of the bilayer was determined by cryo-TEM to be ~ 4 nm. Thus, the mean values of r_0 and r_i are 141 and 137 nm respectively. Introducing these values in the first equation, the number of lipids/vesicle could be calculated to be n = 8.33 x 10^5 lipid molecules. Assuming that PhLSM and cholesterol are homogenously distributed in 1:1 stoichiometry in all liposomes, thus the number of PhLSM per liposome is n_{PhLSM} = 4.17 x 10^5. This high incorporation rate of porphyrin derivatives in liposomal bilayer is essential for the conception of vesicles with photothermally-induced release properties. Since PhLSM could successfully form liposome-like structures in the presence or absence of DSPE-PEG, these two formulations were further investigated in terms of fluorescence quenching, cargo encapsulation, phototriggered release and photothermal conversion.
The fluorescence quenching in both of PhLSM formulations was high, however it was 5 fold higher for PhLSM:Chol compared to PhLSM:Chol:DSPE-PEG_{2000} vesicles (Table 4.1, Figure 4.3 D,H). This strong quenching suggests an aggregation of Pheo-a into highly packed patterns due to the strong π-π stacking of porphyrin cores. Such fluorescence quenching is of great interest for the conception of phototriggerable liposomes with photothermal conversion ability. Thus, due to its significantly higher fluorescence quenching properties, only the free-DSPE-PEG_{2000} formulation was kept for the rest of this work.

Table 4.1. Formulation compositions, size measured by DLS with the corresponding polydispersity index (PdI), type of structure obtained, successful encapsulation of the fluorescent probe calcein (- : no calcein was encapsulated; + : calcein was successfully encapsulated), fluorescence quenching (F_{det} / F_0, where F_0 is the fluorescence of the PS in the intact suspension, and F_{det} is the fluorescence signal after addition of 1% of Triton X-100)

Formulation composition (mol%)	Size (nm ; PdI)	Structure	Encapsulation	Fluorescence quenching
PhLPC : DSPE-PEG_{2000} (50 : 50)	218 (0.1)	undefined aggregates	-	40
PhLPC : CHEMS : DSPE-PEG_{2000} (48.75 : 48.75 : 2.5)	153 (0.1)	undefined aggregates	-	181
PhLPC : SA : DSPE-PEG_{2000} (48.75 : 48.75 :2.5)	217 (0.1)	"unfolded" bilayer	-	215
PhLSM : Chol (50 : 50)	282 (0.1)	MLV + LUV	+	572
PhLSM : Chol : DSPE-PEG_{2000} (48.75 : 48.75 :2.5)	183 (0.1)	LUV	+	93
PhLSM : DSPC : Chol : DSPE-PEG_{2000} (2.5 : 65 : 30 : 2.5)	187 (0.1)	LUV	+	330
Pheo-a : DSPC : Chol : DSPE-PEG_{2000} (2.5 : 65 : 30 : 2.5)	204 (0.1)	LUV	+	7

Abbreviations: Multilamellar vesicles (MLV), Large unilamellar vesicles (LUV)

4.3.2. Interfacial behavior of PhSLM- cholesterol mixtures

4.3.2.1. Surface pressure-area isotherms

In order to get a better insight into the miscibility of PhLSM and cholesterol, the pure compounds and their equimolar mixture were spread at the air/buffer interface, and the monolayers were compressed until collapse. The recorded π-A isotherms are shown in Figure 4.4 A. The compression isotherm of pure cholesterol shows a very steep slope, indicating the formation of a condensed monolayer with low compressibility[247,248]. As demonstrated in the chapter 3, PhLSM exhibited similar compressibility behavior to that of the free Pheo-a with formation of a more expanded monolayer due to the presence of the PC headgroup in the vicinity of the chromophore. When cholesterol was added to PhLSM in equimolar conditions, the isotherm was shifted to smaller areas compared to pure PhLSM, but its shape remained identical. To better understand the significant changes observed in the lipid-porphyrin conjugate monolayer characteristics after addition of cholesterol, the compressibility moduli of the isotherms were calculated and plotted as a function of surface pressure.

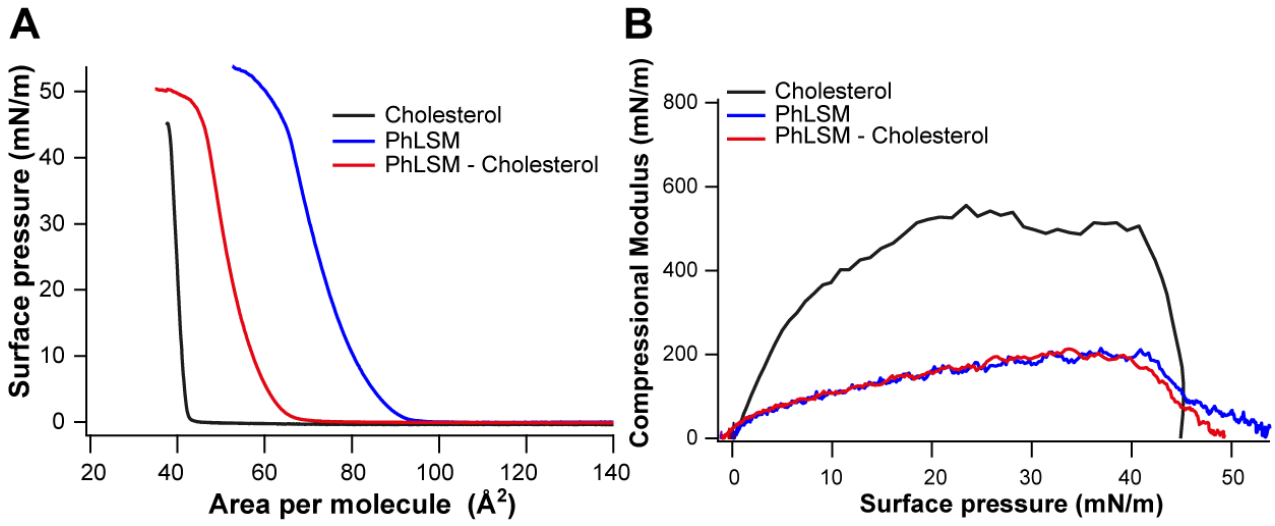

Figure 4.4. π-A isotherms(A) and compressional modulus (B) of monolayers made of pure PhLSM, pure Cholesterol or equimolar mixture of both compounds.

As shown in Figure 4.4 B, there was no significant change between monolayers made of pure PhLSM or mixed with equimolar amount of cholesterol, with a K_{max} value of about 200 mN/m, which corresponds to the liquid condensed state of a monolayer (100 mN/m < K_{max} < 250 mN/m)[204]. In order to gain more information on the stability of the mixtures, excess free energy of mixing (ΔG^{Exc}) was calculated at 30 mN/m. The ΔG^{Exc} values were negative, indicating attractive interactions between PhLSM and cholesterol (Table 4.2).

Table 4.2. Molecular area at surface pressure onset (A_0), molecular Area (A_{30}) at surface pressure of 30 mN/m, molecular Area (Ac), surface Pressure (π_c) at collapse, maximal compressional modulus K_{max} and excess free energy of mixing (ΔG^{exc}) for pure compounds and mixed monolayers.

Monolayer composition (mol%)	**A_0 (Å^2)**	**A_{30} (Å^2) at 30 mN/m**	**A_c (Å^2)**	**π_c (mN/m)**	**K_{max} (mN/m)**	**ΔG^{Exc} (J/mol)***
PhLSM	94	72	64	51.5	205	/
Cholesterol	42	39	37	45.6	555	/
PhLSM : Chol (50 : 50)	65	50	38	49.3	222	-773
DSPC : Chol (70 : 30)	52	42	35	51.1	346	/
DSPC : Chol : PhLSM (65 : 30 : 2.5)	49	40	36	46.1	412	-387

Note: * excess free energy of mixing (ΔGexc) was calculated at 30 mN/m, for mixtures of PhLSM with the corresponding lipid (or lipid mixture)

4.3.2.2. Analysis of the fine structures of the PhLSM-Cholesterol monolayer

The fine structures perpendicular to the plane of the PhLSM-cholesterol monolayer were investigated by specular X-ray reflectivity (XRR) at 30 mN/m. Figure 4.5 A shows the XRR curves of PhLSM-cholesterol and pure PhLSM monolayers spread onto HEPES buffer, fitted using a two-slab model. The corresponding electron density profiles (ρ) reconstructed from the best fit results (solid red lines in Figure 4.5 A) along the z-axis are shown in Figure 4.5 B. The thickness (d), electron density (ρ) and root mean square roughness (σ) of each interface are summarized in Table 4.3. PhLSM-Cholesterol monolayer exhibited a total thickness $d_{PhLSM\text{-}cholesterol}$ of 21.9 Å. The hydrophobic region had a thickness of 12.6 Å and an electron density of 0.392 $e^- \times Å^{-3}$. These values are higher than those obtained with the PhLSM monolayer. However, the thickness of the hydrophilic region of this mixture is reduced compared to that of pure PhLSM. This thickening of the hydrophobic region with the concomitant reduction in the thickness of the head group region could be related to a decrease in the PhLSM molecular tilt with subsequent upward shift which results in reducing the electron density of the polar region.

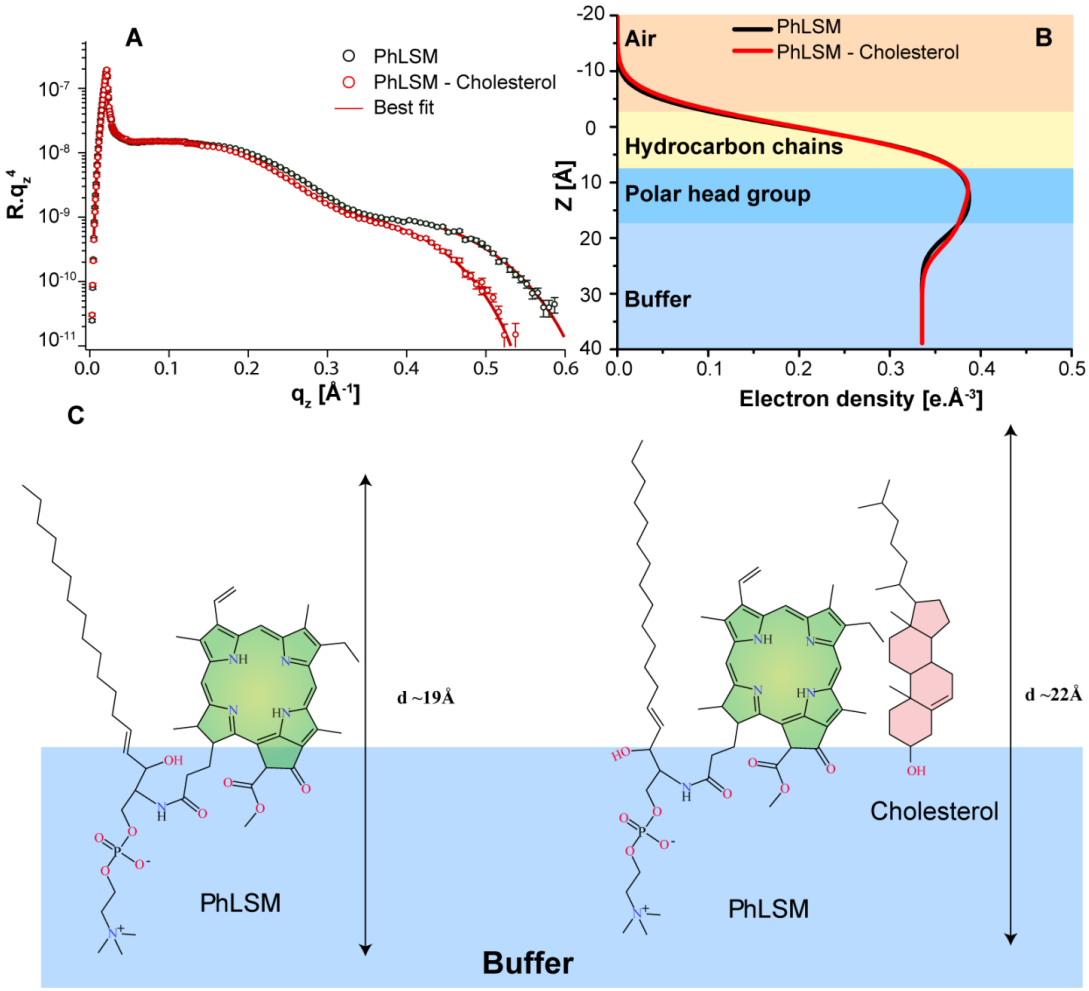

Figure 4.5. (A) XRR curves of PhLSM and PhLSM:Cholesterol equimolar mixture monolayers compressed to a surface pressure of 30 mN/m. The solid lines represent the best model fits to the experimental data. The experimental errors are within the symbol size. (B) The reconstructed electron density profiles along the Z-axis. (C) Schematic representation of the orientation of PhLSM alone, or when mixed with cholesterol at the air/buffer interface.

Table 4.3. Best fit parameters for the XRR Results for PhLSM or PhLSM-Cholesterol monolayers at 30 mN/m as presented in Figure 4.5.

	d (Å)	**ρ ($e^- \times Å^{-3}$)**	**σ (Å)**
		PhLSM*	
Hydrophobic chains	9.4 ± 0.6	0.391 ± 0.001	4.3 ± 0.1
Hydrophilic groups	10.1 ± 0.6	0.387 ± 0.001	4.6 ± 0.8
Buffer	∞	0.335	3.1 ± 0.1
		PhLSM-cholesterol	
Hydrophobic chains	12.6 ± 0.5	0.392 ± 0.003	4.8 ± 0.1
Hydrophilic groups	9.3 ± 0.6	0.375 ± 0.001	3.3 ± 0.4
Buffer	∞	0.335	3.1 ± 0.1

(*) Values for PhLSM were taken from the previous measurement in chapter 2.

4.3.3. Light-triggered release of calcein from PhLSM-lipid mixtures

4.3.3.1. Calcein-loaded Cholesterol: PhLSM (50:50) vesicles

Cholesterol:PhLSM (50:50 mol%) vesicles containing calcein were prepared. As depicted in Figure 4.6 A, 1 min illumination was sufficient to induce an increase of the calcein fluorescence signal. It may be noticed that a small shift in fluorescence emission spectra of calcein after illumination occurred (Figure 4.6 A, blue curve), which might indicate a slight degradation of the fluorescent probe[119,120] during illumination, probably due to the release of ROS by the Pheo-a moiety of PhLSM. By using Eq. 4, the total calcein release was calculated and is plotted versus time in Figure 4.6 B. A fast release step was observed during the first 15 min following illumination, with approximately 15% calcein release, but there was no more than 20% total release over a 2 hours period. During the same time period, almost no calcein release was observed from non-illuminated liposomes (about 2% after 2 hours). The passive release of the cargo from these liposomes may thus be considered as negligible. This is in agreement with the formation of a tightly packed cholesterol-PhLSM monolayer, as inferred from the results of XRR.

In order to investigate a possible ON-OFF release mechanism, several illuminations were conducted on the same sample. Interestingly, multiple phases of release were observed (Figure 4.6 C). Each 1 min illumination induced a burst release of calcein. However, after this sudden increase of fluorescence intensity, no more calcein release occurred before the following illumination. This interesting behavior could allow the design of ON-OFF triggerable systems for finely controlled release. ON-OFF behavior was reported by Carter *et al.* [78] who studied the release of calcein after illumination of liposomes made of DSPC, cholesterol, and 10 mol% of a HPPH-lipid consisting of HPPH chromophore linked to a Lyso-PC *via* an ester bond.

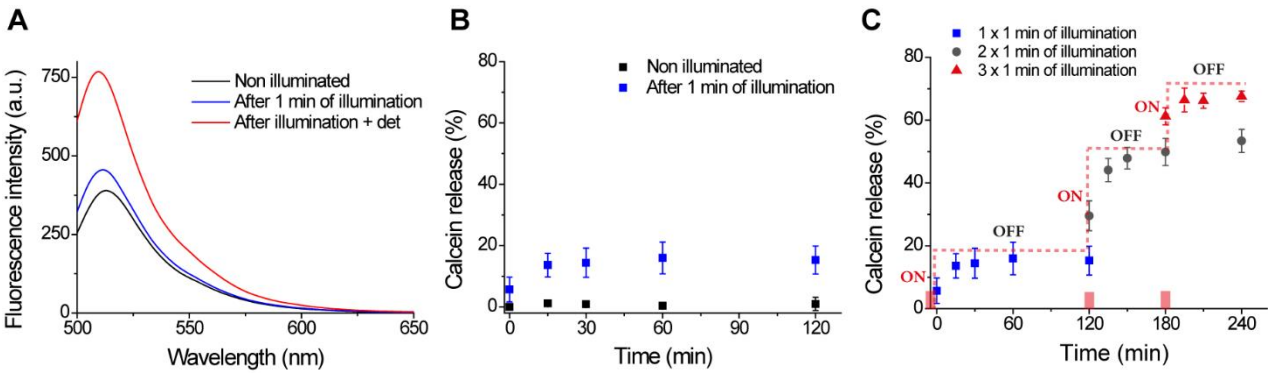

Figure 4.6. Calcein fluorescence emission spectrum (A). Calcein fluorescence in Cholesterol:PhLSM (50:50 mol%) liposomes before illumination (black) and 30 min after 1 min of illumination (blue); the red curve shows the total fluorescence after addition of 1% of Triton TX-100. Calcein release with (blue) and without (black) illumination is shown in B. Multiple illumination (C) shows an ON-OFF release process, where each illumination is shown with a red rectangle at 0, 120 and 180 min.
Error bars is the standard deviation from multiple experiments (n=3); Liposomes were illuminated with a 660 nm laser diode at an estimated fluence of 80 mW/cm^2.

4.3.3.2. PhLSM:DSPC:Chol:DSPE-PEG$_{2000}$ (2.5:65:30:2.5) liposomes

In a next step, we wanted to assess the possible phototriggered release from liposomes containing lower amount of PhLSM in combination with cholesterol. However, the low PhLSM concentration did not allow transposition of the mixed monolayer to a bilayer system, as cholesterol cannot form bilayers on its own. It was necessary to add a phospholipid and we chose DSPC, a commonly used phospholipid in approved liposomal formulations[249–251]. With two saturated stearyl chains, DSPC has a transition temperature of 55°C[252] which limits the passive drug release at physiological temperature. As shown in Figure 4.7 A, when mixed with cholesterol (30 mol%), DSPC forms a condensed monolayer with a molecular area at the surface pressure onset A_0 ~52 Å². The combination of DSPC with cholesterol allows the formation of liquid ordered phase[161] and is frequently used for liposomal drug delivery systems to reduce their passive permeability and increases their stability[253]. The π-A isotherm was slightly shifted to smaller molecular area, sign of a more condensed organization state of the monolayer. A slight increase in compressional modulus was observed (Figure 4.7 B). More importantly, excess free energy of mixing (ΔG^{Exc}) was negative (Table 4.2), indicating that PhLSM was able to mix favorably with DSPC and cholesterol. Thus, a transposition to bilayer systems such as liposomes was conceivable.

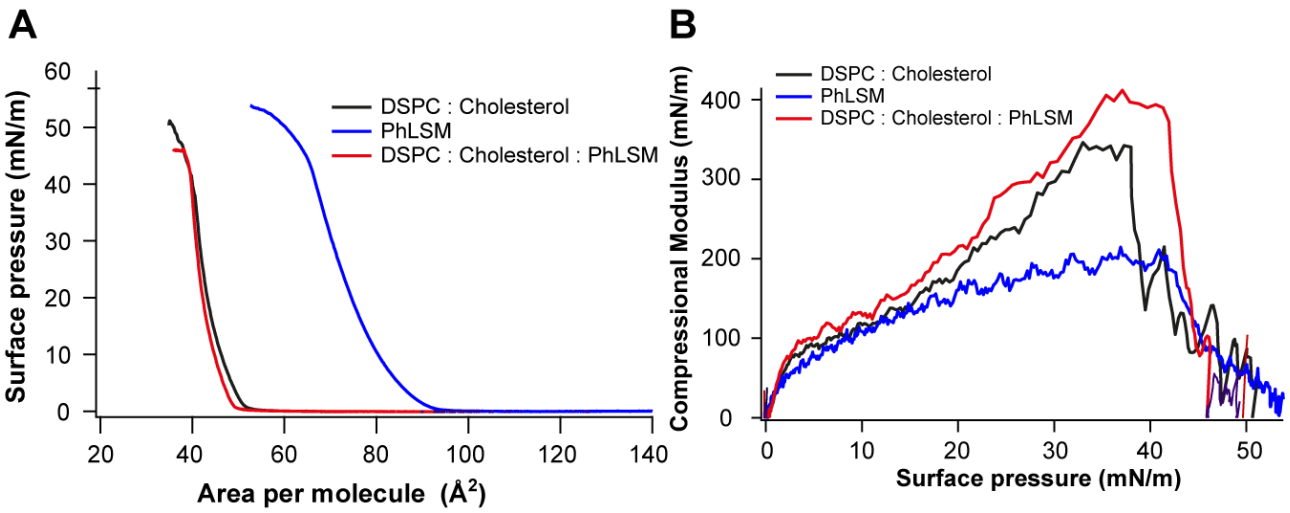

Figure 4.7. π-A isotherms(A) and compressional modulus (B) of pure PhLSM, DSPC:Cholesterol (70:30 mol%) and DSPC:Cholesterol:PhLSM (67.5:30:2.5 mol%).

Liposomes made of DSPC:Cholesterol:PhLSM:DSPE-PEG$_{2000}$ (65:30:2.5:2.5) were prepared. Encapsulation of calcein and quenching of PhLSM fluorescence were successful (Figure 4.8 A). PhLSM fluorescence increased about 300-fold after disruption by the detergent (Table 4.1). The strong quenching of PhLSM at low concentration can be explained by the propensity of the lipid-

porphyrin conjugate to segregate into the DSPC membrane, as shown in the chapter 3[228]. The liposomes were illuminated for various periods of time. After 1 min illumination, 80% of the calcein was released (Figure 4.8 B, black histograms).

Next, we evaluated the potential of this system for ON-OFF release: calcein fluorescence intensity was followed after 30 min or 1 hour following illumination. This formulation showed similar behavior to that of PhLSM:Chol liposomes. Indeed, as depicted in Figure 4.8 B, while short illumination time (from 10 to 30 s) was followed by additional calcein release after 30 min or 1h, longer illumination times (45 or 60 s) induced immediate maximum release after illumination. No further change in release occurred thereafter. This is very promising for a potential ON-OFF release system with low amount of PhLSM. In the aim to assess if this mechanism of release was specific to PhLSM or could be obtained with any other photosensitizer, we substituted PhLSM by Pheo-a in DSPC:cholesterol (67.5:30 mol%) vesicles. As shown in Figure 4.8 C, the amount of calcein released after illumination was about 25 %, independently of the duration of the illumination (black histograms). Besides, when calcein release was monitored with time after illumination, linear release was observed after 30 min and 1 hour (Figure 4.8 C, in red and blue respectively), with maximum release at 1 hour. The significant difference in triggered release between the two photosensitizers suggests a difference in release mechanism, which will be discussed below.

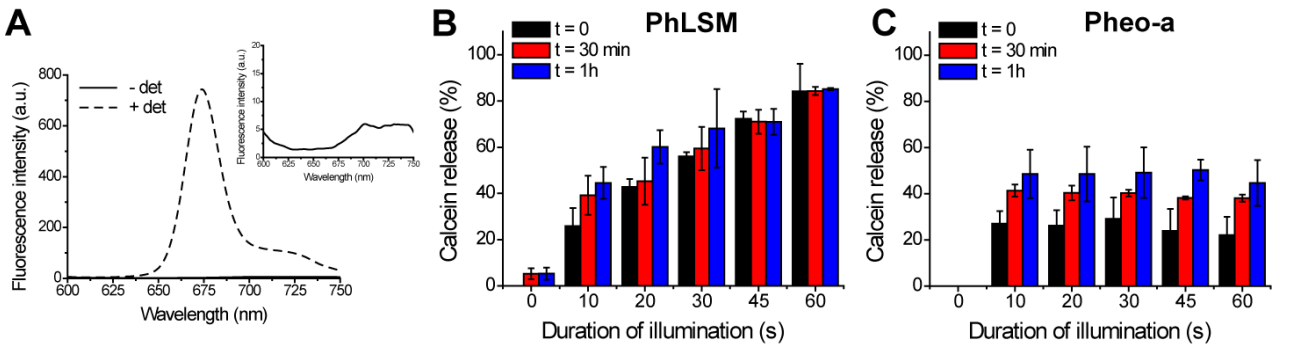

Figure 4.8. Fluorescence emission spectrum of PhLSM (A) in PhLSM:DSPC:Chol:DSPE-PEG$_{2000}$ (2.5:65:30:2.5) liposomes, before (solid line) and after (dash line) addition of 1% of Triton TX-100. The calcein release regarding the duration of illumination is shown in black for PhLSM (B) or Pheo-a (C) liposomes. Release after 30 min or 1 hour following the illumination is shown in red and blue respectively.
Liposomes were illuminated with a 670 nm laser diode at an estimated fluence of 125 mW/cm^2

4.3.4. Study of the mechanism of light-triggered release from liposomes containing PhLSM and cholesterol

In light-triggered release of a cargo from liposomes containing porphyrin derivatives, two mechanisms may occur upon illumination, either (i) a photochemical reaction which leads to the formation of ROS species that oxidize the lipid matrix, or (ii) a photophysical reaction effect which is based on the photothermal conversion of the absorbed light inducing a thermal and/or mechanical stress on the lipid membrane. In order to investigate if a photochemical reaction was responsible for the cargo release we measured the fine structures of a PhLSM:cholesterol monolayer before and after illumination. Indeed, in the liposomal formulations, no unsaturated phospholipid was incorporated in the lipid bilayer. So the only target for ROS was the double bond of the cholesterol as demonstrated by other authors[46]. If any oxidation occurred, the formation of hydroperoxide group in cholesterol molecules would alter the fine structures of the monolayer. However, as shown by the almost identical Fresnel reflectivity curves of this monolayer compressed at 30 mN/m before and after illumination (Figure 4.9), the illumination did not apparently induce any structural alteration of the lipid matrix. Hence, the release mechanism upon illumination of liposomes containing PhLSM and cholesterol was more probably due to a photothermal effect.

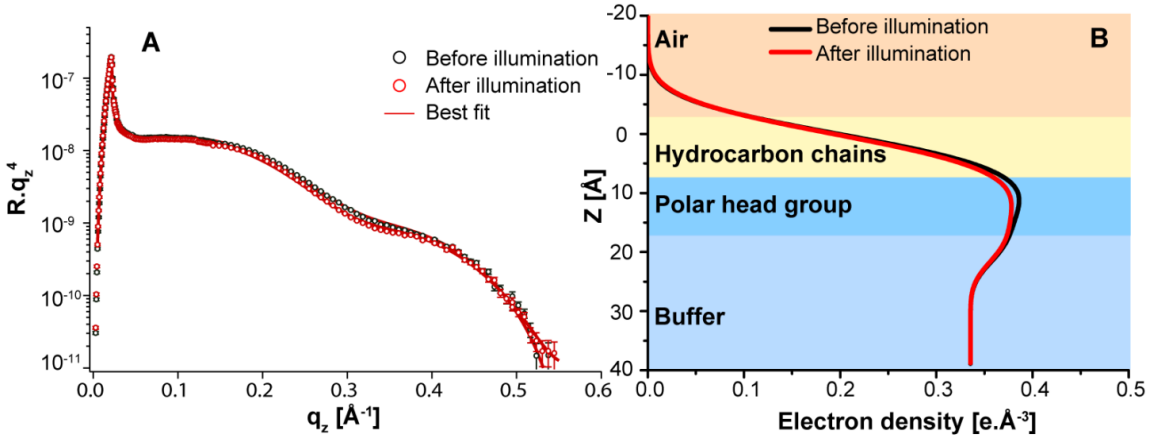

Figure 4.9. (A) XRR curves of a PhLSM:Cholesterol equimolar mixture monolayer at a surface pressure of 30 mN/m, before (black circle) and after (red circle) illumination. The solid lines represent the best model fits to the experimental data. The experimental errors are within the symbol size. (B) The reconstructed electron density profiles along the Z-axis

In order to investigate the photothermal mechanism, the increase of the temperature of different vesicle suspensions containing either the same PS concentration of PhLSM or Pheo-a was monitored during illumination using a thermocouple probe (Figure 4.10 A). Upon illumination,

PhLSM:cholesterol (50:50) vesicles induced a temperature increase of 10°C above the initial temperature (25°C). For DSPC-cholesterol-PhLSM or DSPC-cholesterol-Pheo-a, the temperature increments were 8.1°C and 1.5 °C, respectively. There is good correlation between the photothermal effect of PhLSM and light-triggered release of calcein. In addition, the results demonstrate the bilayer concentration-dependence of this relationship. For Pheo-a, the almost negligible temperature increase also agrees with the release profile of calcein. In fact, the linear release of the probe with time and the poor fluorescence quenching of Pheo-a (Table 4.1) both suggest a photooxidative-based release. PhLSM liposomes thus appear as promising systems with dual activity: photothermal therapy and light-triggered release of an encapsulated drug.

However, the stability of an organic NIR photothermal agent is crucial for biomedical applications, where longer time illuminations, or repeated illumination cycles[254] are needed. PhLSM:Cholesterol (50: 50) liposome suspensions at different concentrations were subjected to three consecutive laser illumination cycles of 10 min each, separated by a 10 min break (Figure 4.10 B). At first, the photothermal effect did not seem concentration-dependent. Indeed, independently of the concentration used ≥100µM, the maximum temperature increase was ~ 14°C. However, for low concentrations, the photothermal effect decreased after each cycle, but with higher concentration, the heating cycles were fully reproducible. This can be explained by a possible partial photobleaching of the Pheo-a moiety during illumination. This phenomenon might be attenuated in the case of higher dye concentration that prohibits the deep light penetration in the sample due to strong light absorption.

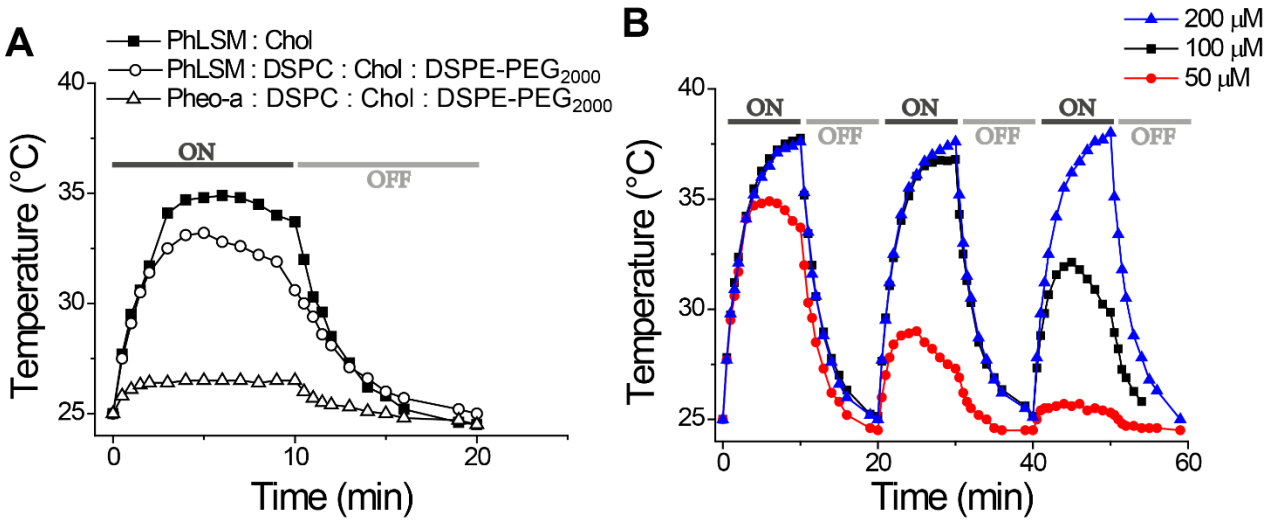

Figure 4.10. Photothermal effect of (A) PhLSM:Cholesterol (50:50 mol%), PhLSM:DSPC:Cholesterol:DSPE-PEG$_{2000}$ (2.5:65:30:2.5) and Pheo-a:DSPC:Cholesterol:DSPE-PEG$_{2000}$ (2.5:65:30:2.5) liposomes with a final concentration of 50 µM of PS. Photothermal effect of different cycles (B), at three different concentrations of PhLSM in PhLSM:Cholesterol (50:50 mol%) liposomes.
Liposomes were illuminated with a 670 nm laser diode at an estimated fluence of 800 mW/cm^2

This phenomenon has already been described by Ng *et al.*, who underlined the potential of bacteriopheophorbide-lipid dye conjugate, associated with conventional phospholipids of different transition temperatures, to promote better light propagation into samples (and tissues)[255]. In addition, the stability of photothermal cycles would enable the use of such formulations for photoacoustic imaging. Indeed, the temperature rise in the tissue induces thermoelastic expansion, and results in the emission of acoustic waves that can be detected with a ultrasound transducer[84]. As ultrasound scatters far less than light in biological environment, the photoacoustic technique provides a high-resolution imaging tool.

4.4. Conclusion

The aim of this work was to achieve phototriggerable release of an encapsulated cargo from novel liposome-like structures *via* a photothermal mechanism. To do so, we used the newly synthesized lipid-porphyrin conjugates PhLPC and PhLSM. In the previous chapter, we have demonstrated that both compounds were able to self-assemble into supramolecular structures that resemble lipid vesicles but were unstable and formed aggregates. This was attributed to the length mismatch between the alkyl chain in sn-1 position and the sn-2 adjacent porphyrins. In order to overcome this problem, we followed the pairing strategy by using lipids that exhibit complementary packing parameters. Whereas the combination of PhLPC with CHEMS or stearylamine failed to form vesicles, mixing PhLSM with cholesterol at equimolar percentage lead to the formation of stable vesicles that encapsulated efficiently calcein in their aqueous core. Interestingly, these vesicles showed phototriggered release behavior with an ON-OFF mechanism, which was attributed to their photothermal conversion. Indeed, the illumination of the vesicle suspension induced an increase in temperature of approximately 14°C.

Such phototriggerable system may offer multiple possible applications. In addition to the phototoxic photothermal effect and to light-triggered release, the stability of photothermal cycles may allow photoacoustic imaging. Encapsulation of a hydrophilic drug instead of the fluorescent probe could thus allow the development of a multifunctional drug delivery system. Finally, the fluorescence and ROS production of the PS can be restored after degradation of the drug delivery system (by internalization into cell), which increases the field of applications of such systems (light triggered release, PTT, PDT, photoacoustic imaging, fluorescence imaging).

General discussion

5. General discussion

Building an efficient photoactivatable liposomal drug delivery system relies on several factors, especially the choice of the phospholipid and photosensitizer. The photosensitizer should have strong absorbance properties in the near-IR region, a high quantum yield in singlet oxygen, well-defined hydrophobic properties, and a low toxicity in the dark. In addition, the phospholipid used for liposome formulation should possess at least one unsaturation that can be photooxidized upon PS illumination. Although several works have been reported on the impact of phospholipid oxidation on the photoinduced permeability of liposomes, to the best of our knowledge there is no previous work listing the structural and physicochemical properties of phospholipids and photosensitizers required for the formulation of effective phototriggerable liposomes.

The first objective of this thesis, as described in chapter 2, was to analyze the consequences of using different degrees of unsaturation for the phospholipids, and different degrees of hydrophobicity for porphyrin derivatives. This mechanistic study showed that, when using free porphyrin derivatives embedded into liposomes, the hydrophobicity and amphiphilic properties of the PS controlled its depth of penetration into the bilayer, and thus, its proximity to the unsaturated bond of the phospholipid to be oxidized. Independently of the singlet oxygen quantum yield, the efficacy of peroxidation relies essentially on porphyrin localization and orientation inside the lipid matrix[78,121–123]. Our experimental results have been correlated with molecular dynamics simulation. Altogether, the results confirmed the observations made by other authors, that light-triggered release based on lipid photooxidation by free porphyrins embedded in liposome walls presents several drawbacks. Indeed, we showed that the limited amount of encapsulated PS, which is essential to preserve their photophysical properties, resulted in incomplete cargo release[36,45], and that a significant passive release of the cargo occurred due to the bilayer-forming unsaturated lipids[76].

Taking into account these drawbacks, we moved towards the development of lipid-porphyrin conjugates, not only to tackle these issues, but also to develop more efficient phototriggerable liposomes. Lipid-porphyrin conjugates are one important card in the so called “all in one” strategy. These single building blocks can play the roles of drug, imaging agent, release-triggering agent, and may pave the way for the conception of new light-triggered release systems with multifunctional properties (Figure 5.1). In fact, these building blocks were first synthesized by Gang Zheng’s group who discovered the propensity of these compounds to self-assemble into liposome-like systems named “porphysomes”, possessing multifunctional properties, including photothermal therapy (PTT), photodynamic therapy (PDT), phototriggered drug release and photoacoustic imaging (PAI)[6].

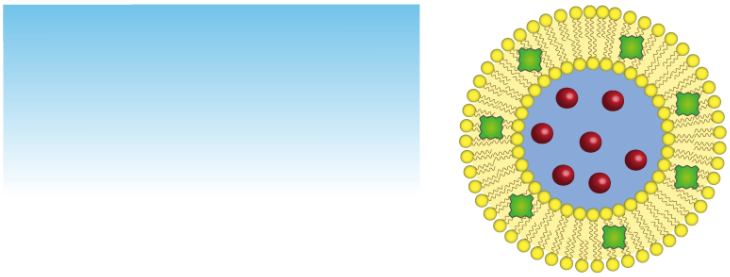

PS type :	Free porphyrin	Lipid-porphyrin conjugate
PS hydrophobicity	+++ (high) possible exchange with blood proteins	++ (amphiphilic) strong interaction with phospholipids
PS payload	- - (low) limited to 10-15 mol%	+++ (high) up to 100 mol%
Light-triggered release	PC PP	PC PP
Anti-cancer therapy	PDT PTT	PDT PTT
Transposable to clinic	already on the market	not yet on the market
Imaging	Fluorescence MRI Photoacoustic	Fluorescence PET / SPECT / MRI Photoacoustic

Figure 5.1. Comparative properties and applications of porphyrin and lipid-porphyrin conjugates embedded into liposome bilayers. Note: Photochemical (PC) and Photophysical (PP) triggered release

Additionally, when combined with phospholipids, lipid-porphyrin conjugates showed ability to release encapsulated drugs either by photooxidative-based[46,80,111] or photothermal-based mechanisms[78] depending on their molar percentage in the lipid bilayer and the nature of the bilayer-forming phospholipids. They enabled significant increase in the total PS payload inside the bilayer and prevented the leakage of the PS due to hydrophobic interactions with proteins in the blood circulation.

Inspired by the results obtained with 2-(1-hexyloxyethyl)-2-devinyl pyropheophorbide-a (HPPH)-lipid and pyropheophorbide-a (pyro)-lipid by Lovell's [78] and Zheng's groups[6] in the conception of liposomes with multifunctional properties, we designed two new lipid-porphyrin conjugates with different chemical structures (Figure 5.2). These conjugates, PhLPC and PhLSM, were synthesized by coupling pheophorbide-a (Pheo-a), to chemically modified lyso-phosphatidylcholine (Lyso-PC) and egg lyso-sphingomyelin (Lyso-eSM) respectively.

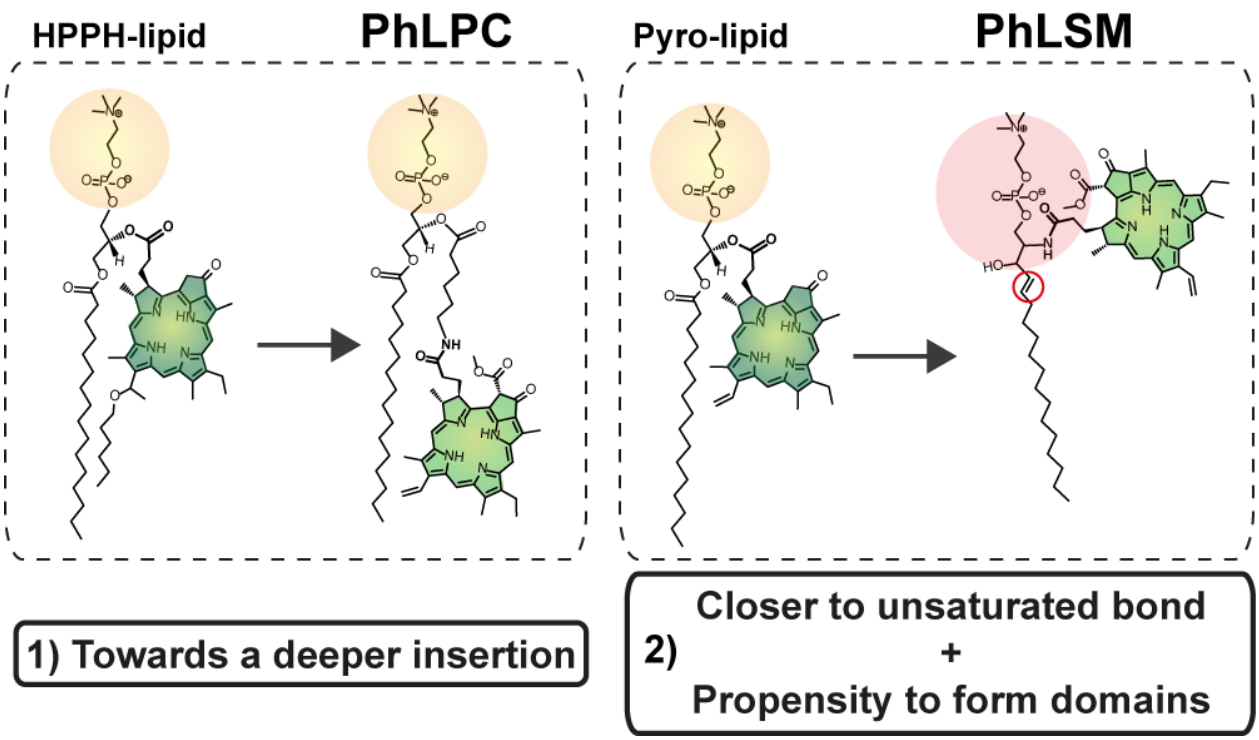

Figure 5.2. Chemical structures of the lipid-porphyrin conjugates designed in this work, compared to those synthesized by Lovell's and Zheng's groups. PhLPC promotes deeper insertion of the PS compared to HPPH-lipid, and PhLSM exhibits a double bond on the lipid chain close to the PS (unlike pyro-lipid) and high propensity to form domains.

Our motivations for the synthesis of these derivatives were threefold:

I. Firstly, to simplify the synthetic protocols as compared to those reported in the literature for other lipid-porphyrin conjugates[99,104]. Preparing in advance the lipid backbone theoretically allows any PS possessing a carboxylic group to be conjugated afterwards, *via* a simple peptide bond. Indeed, compared to other lipid-porphyrin conjugates (*i.e.*, HPPH and pyro-lipids), our strategy of synthesis allows avoiding the intramolecular acyl migration commonly observed with Steglich esterification of lysophospholipids[196]. In fact, as reported in chapter 3, two lipid backbones were prepared with yields of 83 % and 65 % respectively. Afterwards, Pheo-a was coupled to each of them. While PhLPC was produced with higher yield[6,78,256] than that reported in the literature (*i.e.*, 65 % vs 45 %), PhLSM was obtained with lower yield (~ 30%). This lower yield could be due to the limited accessibility of the amino group in the lyso-sphingomyelin to the carboxylic group of the PS. Synthesis of a lipid-porphyrin conjugate with the PS moiety close to the polar head (such as in PhLSM), could be conducted by using the same strategy as for PhLPC, and Lyso-PC could be esterified with a Fmoc-glycine with a high yield. However, we chose to use a Lyso-SM instead of the Lyso-PC (which was a novel strategy) for the following reasons:

a. The presence of a 4,5-*trans*-double bond in close vicinity (Figure 5.2) to the amino group where Pheo-a is linked may increase the light-triggered release phenomenon *via* peroxidation. In a study published in 2016, thus shortly after we started to develop PhLSM, Carter *et al*. who took part to the pioneer discovery of lipid-porphyrin conjugates, showed an increase in the release rate of irinotecan encapsulated in vesicles containing pyro-lipid (2 mol%) embedded into sphingomyelin:cholesterol (53:45 mol%) bilayers, compared to DSPC:Cholesterol:DSPE-PEG_{2000} (48:45:5 mol%) ones[112]. However, the peroxidation of the *trans* double bond in the sphingomyelin chain is still controversial in the literature. Whereas, it was reported that the *trans* double bond is six times more resistant to peroxidation than the *cis* double bond found in unsaturated phospholipids[257–259], Ayuyan *et al.* demonstrated that sphingomyelin can be easily peroxidized in GUVs containing egg-SM[260].

b. It has been demonstrated in several studies, that the sphingomyelin structure allows H-bonding at the membrane-water interface, owing to the C2 amide linkage and the C3 hydroxyl group in its backbone. This in turn could affect interactions between phospholipids and cholesterol, thus leading to the formation of tightly packed gel-like ordered domains called raft[261,262]. Following the same line of thinking, we thought that using Lyso-SM backbone would allow the formation of tightly packed PhLSM molecules that could in turn enhance its photothermal conversion efficiency.

II. Secondly, to allow deep incorporation of the PS inside the bilayer in the case of PhLPC, by the presence of a six-carbon spacer, for higher photooxidative release efficiency and limitation of PS transfer to LDL and albumin when injected in the blood stream. However, since no stable formulation could be prepared with this compound at high loading rate, such hypothesis could not be verified neither *in vitro* nor *in vivo*.

III. Thirdly, to offer more stability to the compounds when injected into the bloodstream. While in all reported lipid-porphyrin conjugates, the photosensitizers are connected to the lyso-phospholipid *via* an ester bond, we chose an amide bond. Indeed, the amide bond is more difficult to be hydrolyzed and degraded by enzymes *in vivo* than the ester bond. Moreover, amide bonds could be cleaved in specific tissues where the peptidase activity is high such as in some cancers (*i.e*., esophageal squamous-cell carcinoma, ESCC), thus allowing a selective and activatable photodynamic activity.

After successful synthesis, the self-assembling properties of both compounds were investigated (Chapter 3). Interestingly, both lipid-porphyrin conjugates were able to self-assemble into liposome-like structures. However, these assemblies were unstable and formed aggregates of undefined structures shortly after their preparation. This was explained by the mismatch between the length of the alkyl chain in sn-1 position and the adjacent porphyrin, leading to an inadequate packing parameter for bilayer stability. In addition, it should be noted that Pheo-a consists in a mixture of diastereoisomers. This may have a direct incidence on the propensity of PhLPC and PhLSM to self-assemble. Indeed, in the case of PhLPC, the modified lipid was prepared *via* direct acylation of the secondary alcohol groups at Lyso-PC sn-2 position using sonication in the presence of glass beads to avoid intramolecular acyl migration as demonstrated previously by Rosseto *et al*[196].

For PhLSM synthesis, Lyso-SM was first obtained by direct hydrolysis of egg-SM. Although this synthetic pathway is efficient (65% yield) and minimizes cost, the hydrolysis leads to two different epimers[198]. The conjugation of the Pheo-a to either lipid backbones leads thus to the formation of lipid-conjugates with 2 and 4 different diastereoisomers for PhLPC and PhLSM respectively. This can result in inefficient packing and might explain the instability of the self-assembled vesicles.

Similar behavior was observed with other lipid-porphyrin conjugates such as pyro-lipids, wherein authors found that adding high amount of cholesterol in the presence of DSPE-PEG was necessary in order to form stable formulations[6]. The authors later improved their system by synthesizing another lipid-porphyrin conjugate, HPPH-lipid, where the mismatch problem between the two lipid chains was overcome, thanks to the hexyl ether moiety of HPPH [78]. Liposomes containing 95 mol% of HPPH-lipid in the presence of DSPE-PEG_{2000} could be successfully prepared and doxorubicin-loaded liposomes were subsequently formulated with only 10 mol% of HPPH-lipid in DSPC:Chol:DSPE-PEG_{2000} (50:35:5 mol%) liposomes. However, owing to the synthesis difficulties observed with this compound and to the presence of epimers mixture of HPPH, the authors finally concluded that mixing pyro-lipid with phospholipids and cholesterol would be more relevant for an easy clinical translation[111].

In order to get a better understanding of PhLPC and PhLSM self-assembling properties, their interfacial behavior at the air-buffer interface was analyzed by surface pressure measurements. The π-A isotherms revealed the instability at the interface of PhLPC, which tends to solubilize in the subphase. This phenomenon was further confirmed by XRR measurements. While PhLSM did not show this instability, it may be explained for PhLPC, by the long six-carbon spacer bearing Pheo-a at its extremity, which could provide more flexibility to the attached chromophore to adopt distinct local orientation during lateral compression. The stability of PhLPC and PhLSM monolayers was then

examined by performing three compression–expansion cycles (Figure 5.3). The first two cycles were operated until a surface pressure of 25 mN/m was reached, and the third one until collapse. The shift towards smaller molecular area observed for PhLPC confirmed the significant loss of material in the subphase, during the consecutive compression cycles. The difference in molecular area at 25 mN/m between the first and the third cycle was 12 Å² and 1.5 Å², for PhLPC and PhLSM respectively. This accounts for the better interfacial stability of PhLSM compared to PhLPC.

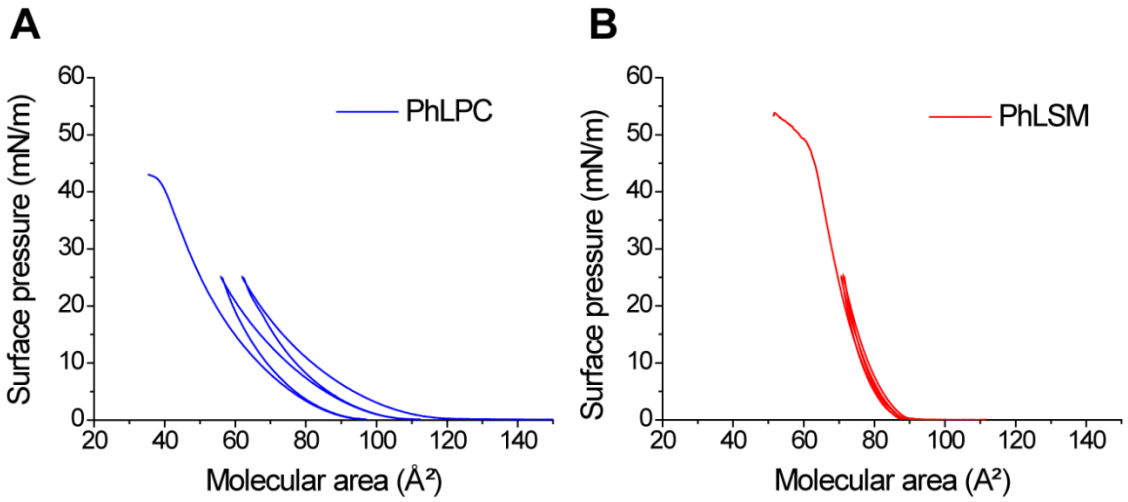

Figure 5.3. Compression-expansion cycles of (A) pure PhLPC and (B) pure PhLSM monolayers on HEPES buffer subphase at 22 °C.

Next, the photoactivity of these compounds either free or embedded into DSPC liposomes was assessed *in vitro* on esophageal squamous cell carcinoma (ESCC) cell lines. Surprisingly, both conjugates showed selectivity towards the esophageal squamous cancer cell line Kyse-30, compared with the free porphyrin which was, on the contrary, as toxic for Kyse-30 cells as for normal esophageal epithelial cells (HET-1A). This selectivity could be attributed to either a specific enzymatic cleavage of the peptide bond in lipid-porphyrin conjugates releasing the PS or to a preferential affinity of the PS for specific organelles.

In order to verify the first hypothesis, we assessed the overexpression of proteases in both esophageal cell lines (Figure 5.4). Immunoblotting analysis revealed overexpression of dipeptidyl peptidase IV (DPPIV) in Kyse-30 cell line but it was not detected in HET-1A. To ensure equal protein loading, actin, used as a positive control, was quantified in both cell lines. This result is in agreement with a published study showing a significantly high level of DPPIV in adenocarcinoma as well as in squamous cancer cells from patient with esophagus cancer[263].

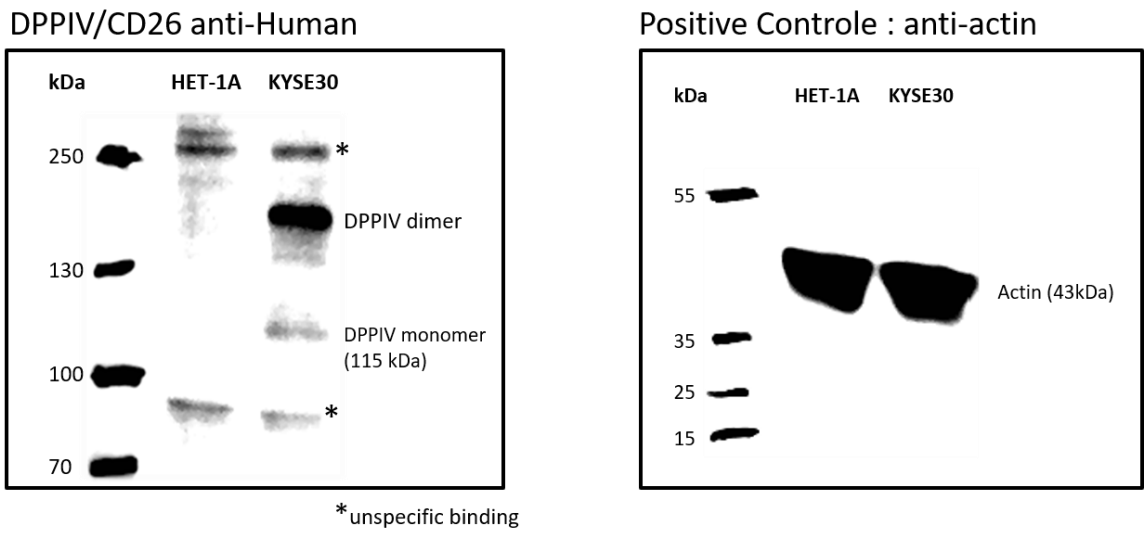

Figure 5.4. Immunoblotting for DPPIV performed on HET-1A and Kyse 30 cell lines (left). The equal loading control was performed with actin (right).

However, DPPIV was not able to selectively cleave the peptide bond between the porphyrin moiety and the Lyso-PC or Lyso-SM backbone of PhLPC or PhLSM, respectively. This is due to the fact that DPPIV requires a specific amino acid sequence, N-terminal residues with H_2N-X-Pro/Ala motifs[264]. Future perspectives in the design of lipid-porphyrin conjugates must include a specific attention to the linker between the porphyrin moiety and the lipid backbone.

We investigated the second hypothesis by studying the subcellular PS localization by means of confocal laser scanning microscopy. Our results demonstrated the preferential affinity of PhLPC and PhLSM for the mitochondria in the cancerous cell line. In fact, the conjugation of PS to a lipid backbone would affect its cellular uptake as well as its subcellular localization. Indeed, Rizvi *et al.* have shown that the conjugation of verteporfin to a Lyso-PC significantly affected its intracellular distribution after internalization[115]. Whereas free verteporfin localized specifically into endoplasmic reticulum (ER) and mitochondria, the developed verteporfin-lipid (LPC-BPD) conjugate accumulated more into lysosomes.

As both synthesized lipid-porphyrin conjugates were not able to self-assemble into stable liposome-like structures due to their apparent packing parameters, we decided to investigate their possible mixing with other lipid molecules having complementary packing parameters[92] (chapter 4). This would allow the conception of stable formulations with higher phototriggered release efficiency *via* photothermal mechanism. Since PhLPC may exhibit an inverted conical shape, its combination with conical shape molecules was assessed, to form bilayers. However, neither equimolar mixtures of

PhLPC with DSPE-PEG_{2000}, nor with cholesteryl hemisuccinate (CHEMS) resulted in the formation of bilayers. Although hydration of a film composed of equimolar PhLPC and stearylamine (SA) led to the formation of bilayers, as inferred from Cryo-TEM pictures, those did not exhibit vesicle-like structure and could not retain a cargo. Such failure could be related to either the high molar percentage of the added lipids (*i.e.,* CHEMS and DSPE-PEG) that may micellize when mixed with PhLPC or to the mismatch between compounds packing parameters. In this work, only one molar percentage of either CHEMS or DSPE-PEG was tried thus further investigation with lower incorporation rates should be done.

In the case of PhLSM, the presence of the Pheo-a moiety in the vicinity of the polar head group may result in a conical shape. Its association with cholesterol enabled to obtain vesicle-like structures, successfully encapsulating calcein, a hydrophilic fluorescent probe. This successful combination may also be due to the hydroxyl group in the SM backbone that favors intermolecular hydrogen bonding with cholesterol leading to a tight packing[265]. Interestingly, this system proved able to release the probe within one minute after illumination, by a photothermal-based mechanism. The photothermal effect of such a system resulted in a temperature increase of approximately 14°C. Assuming that the temperature of human body is 37°C, after injection of these supramolecular assemblies, the tumor tissues can thus be heated to ~ 50°C within 6 min after laser illumination. This hyperthermia would be of great benefices for cancer treatment. Indeed, it has been demonstrated that the cancer cells can be killed after heating the tumor at 42° C during 15–60 min and this duration can be shortened to 4–6 min for temperatures over 50 °C[266]. Furthermore, local hyperthermia can enhance synergistically the efficacy of conventional chemotherapy[267–269]. To the best of our knowledge, it is the first time that both photothermal effect and photothermal-induced triggered release can be obtained using a single formulation of lipid-porphyrin conjugates, while in the case of other lipid-porphyrin conjugates, the authors were forced to change the lipid composition for each application[6,78].

Combinational therapy *e.g.,* photothermal therapy and light-triggered release, has already shown promising advances, especially in the field of gold nanoparticles [270]. These latter can be roughly divided into two main categories[9]: (i) the nonresonant gold nanoparticles (GNPs) and (ii) plasmon resonant gold nanoparticles. Whereas the small size (d= 2-3 nm) of the first gold nanoparticles category allows their incorporation in the liposomal bilayer for the conception of photothermally-controlled release, the photothermal effect of these Nps can be only obtained at short wavelength (λ = 250 nm) which limits their applications for *in vivo* and clinical uses. Conversely, for plasmon resonant gold nanoparticles which have diameters in the order of tens of nanometers, their size and shape can be modified to tune their optical properties through the visible to NIR range. However, due

to their size, their association to liposomal bilayer is not an easy task and requires several steps of chemical modification in order to graft them to the lipid membrane. Furthermore, the use GNPs *in vivo* raised several concerns regarding their distribution in organs and clearance[271].

Compared to GNPs , lipid-porphyrin conjugates are organic materials, both biodegradable and biocompatible[6]. Moreover, added to their photothermal and phototriggering release properties, lipid-porphyrin conjugates may recover their photodynamic activity after PS dissociation inside the cells, thus offering unique multifunctional properties.

Conclusion and perspectives

6. Conclusion and perspectives

In this thesis, we have successfully formulated photoactivatable liposomal systems for controlled drug release based on two strategies. Whereas the first one relied on the photooxidation of phospholipids, the second one consisted in the design of liposomes releasing their cargo *via* a photothermal mechanism.

The photooxidative liposomes were composed of free porphyrin derivatives and phospholipids with different degrees of unsaturation. Our experimental study, correlated with molecular dynamics simulation has (i) shown the importance of the deep insertion of a PS in the lipid bilayer, (ii) demonstrated the higher efficiency of the system when the dye was located close to the unsaturated bond of the phospholipid, and (iii) confirmed the limitations of photooxidative-based triggered release using free porphyrin embedded in liposomes.

To achieve photothermal-triggered release of a cargo from liposomes, we synthesized two lipid-porphyrin conjugates, PhLPC and PhLSM. While both molecules could not self-assemble on their own into stable vesicle-like structures, PhLSM, once mixed with equimolar ratio of cholesterol, could form stable vesicles. These latter entrapped successfully a hydrophilic cargo and promoted its release after illumination in a controlled manner *via* a photothermal-based mechanism. Moreover, this new system exhibited an ON-OFF drug release process, with a significantly improved release rate compared to the photooxidative mechanism-based system. Illumination of the PhLSM -Chol vesicles suspension induced an increase in temperature of approximately 14°C, which makes this system also suitable for PTT applications. To the best of our knowledge, it is the first time that such a dual modality can be obtained with a single formulation, using lipid-porphyrin conjugates.

Beyond their application in the formulation of phototriggerable liposomes, PhLPC and PhLSM have brought significant improvements in the field of porphyrin derivatives, compared to the corresponding free porphyrin, but also to the already published lipid-porphyrin conjugates. Added to their easier protocol of synthesis and their good yield (Figure 6.1), both lipid-porphyrin conjugates exhibited higher selectivity towards esophageal squamous-cell carcinoma cell line. Moreover, their incorporation into DSPC liposomes showed improvement in the total payload (≥20 mol%) compared to the corresponding free Pheo-a. This work confirms the interest of lipid-porphyrin conjugates for the conception of phototriggerable liposomes with multifunctional properties.

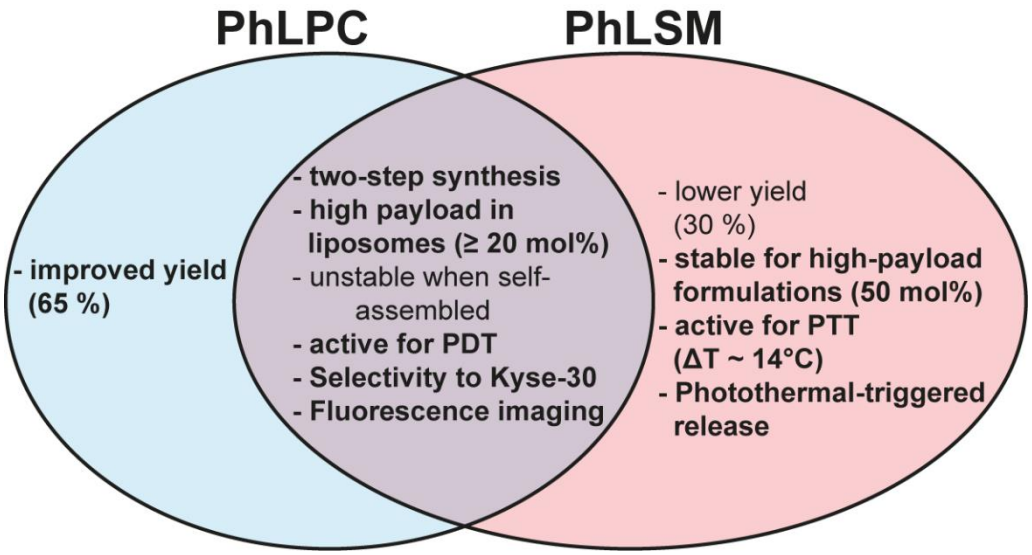

Figure 6.1. Main characteristics of PhLPC and PhLSM, with improvement compared to the free porphyrin and/or lipid-porphyrin conjugates.

Finally, future research should expand the knowledge on the behavior of the newly developed molecules:

- To obtain stable formulations with lipid-porphyrin conjugates, the packing parameter of both PhLPC and PhLSM compounds should be more precisely determined. Molecular dynamics simulations should be conducted on pure lipid-porphyrin conjugates, as well as on lipid bilayer incorporating them. They will provide important information about the localization depth of Pheo-a molecule in PhLPC and PhLSM-containing bilayers.

- Formulations including PhLSM and cholesterol should be further optimized by changing the molar percentage of cholesterol and measuring the photothermal conversion and phototriggered release efficiency. In addition, the thermotropic behavior and mechanical properties of the vesicles should be studied by differential scanning calorimetry (DSC) and AFM force-volume mode. These experiments will allow better understanding of the thermal stability of the lipid bilayer and lateral packing of the components.

- Formulations made of PhLPC were not successful for stable cargo encapsulation and light-triggered release. The current strategy focused on the pairing between PhLPC and lipids exhibiting complementary molecular shapes such as cholesteryl hemisuccinate (CHEMS) or stearylamine (SA). However, other molecules, such as BVEP, could be tried to obtain stable PhLPC formulations. Indeed, BVEP is a PEG-conjugated lipid possessing a vinyl-ether linkage which is usually employed to stabilize DOPE-containing liposomes. Since PhLPC

may exhibit similar packing parameter to DOPE, its combination with BVEP could lead to the formation of stable supramolecular assemblies.

- Once the optimal formulations are found, their stability in biological medium should be studied. In addition, the phototriggered release efficiency of an anticancerous drug such as doxorubicin should be investigated *in vitro* and *in vivo* on xenograft models of esophageal cancer.

References

(1) Vauthier, C.; Couvreur, P.; Fattal, E. *Nanomaterials : Applications in Drug Delivery*; Springer, **2013**.

(2) Matsumura, Y.; Maeda, H. A New Concept for Macromolecular Therapeutics in Cancer Chemotherapy: Mechanism of Tumoritropic Accumulation of Proteins and the Antitumor Agent Smancs. *Cancer Res.* **1986**, *46*, 6387–6392.

(3) Noguchi, Y.; Wu, J.; Duncan, R.; Strohalm, J.; Ulbrich, K.; Akaike, T.; Maeda, H. Early Phase Tumor Accumulation of Macromolecules: A Great Difference in Clearance Rate between Tumor and Normal Tissues. *Jpn. J. Cancer Res.* **1998**, *89*, 307–314.

(4) Dos Santos, N.; Allen, C.; Doppen, A.-M.; Anantha, M.; Cox, K. A. K.; Gallagher, R. C.; Karlsson, G.; Edwards, K.; Kenner, G.; Samuels, L.; et al. Influence of Poly(ethylene Glycol) Grafting Density and Polymer Length on Liposomes: Relating Plasma Circulation Lifetimes to Protein Binding. *Biochim. Biophys. Acta - Biomembr.* **2007**, *1768*, 1367–1377.

(5) Allen, T. M.; Hansen, C.; Martin, F.; Redemann, C.; Yau-Young, A. Liposomes Containing Synthetic Lipid Derivatives of Poly(ethylene Glycol) Show Prolonged Circulation Half-Lives in Vivo. *Biochim. Biophys. Acta* **1991**, *1066*, 29–36.

(6) Lovell, J. F.; Jin, C. S.; Huynh, E.; Jin, H.; Kim, C.; Rubinstein, J. L.; Chan, W. C. W.; Cao, W.; Wang, L. V.; Zheng, G. Porphysome Nanovesicles Generated by Porphyrin Bilayers for Use as Multimodal Biophotonic Contrast Agents. *Nat. Mater.* **2011**, *10*, 324–332.

(7) Puri, A. Phototriggerable Liposomes: Current Research and Future Perspectives. *Pharmaceutics* **2014**, *6*, 1–25.

(8) Shum, P.; Kim, J. M.; Thompson, D. H. Phototriggering of Liposomal Drug Delivery Systems. *Adv. Drug Deliv. Rev.* **2001**, *53*, 273–284.

(9) Leung, S. J.; Romanowski, M. Light-Activated Content Release from Liposomes. *Theranostics* **2012**, *2*, 1020–1036.

(10) Huang, H.; Song, W.; Rieffel, J.; Lovell, J. F. Emerging Applications of Porphyrins in Photomedicine. *Front. Phys.* **2015**, *3*, 1–15.

(11) Couvreur, P. Nanoparticles in Drug Delivery: Past, Present and Future. *Adv. Drug Deliv. Rev.* **2013**, *65*, 21–23.

(12) Liu, D.; Yang, F.; Xiong, F.; Gu, N. The Smart Drug Delivery System and Its Clinical Potential. *Theranostics* **2016**, *6*, 1306–1323.

(13) Couvreur, P. *Squalenoylation: A Novel Technology for Anticancer and Antibiotic Drugs with Enhanced Activity*; Lourtioz, J.-M., Lahmani, M., Dupas-Haeberlin, C., Hesto, P., Eds.; Springer International Publishing: Cham, **2016**.

(14) Thompson, D. H.; Gerasimov, O. V.; Wheeler, J. J.; Rui, Y.; Anderson, V. C. Triggerable Plasmalogen Liposomes: Improvement of System Efficiency. *Biochim. Biophys. Acta - Biomembr.* **1996**, *1279*, 25–34.

(15) Huynh, E.; Zheng, G. Porphysome Nanotechnology: A Paradigm Shift in Lipid-Based Supramolecular Structures. *Nano Today* **2014**, *9*, 212–222.

(16) Alvarez-Lorenzo, C.; Concheiro, A. Smart Drug Delivery Systems: From Fundamentals to the Clinic. *Chem. Commun.* **2014**, *50*, 7743–7765.

(17) Mura, S.; Nicolas, J.; Couvreur, P. Stimuli-Responsive Nanocarriers for Drug Delivery. *Nat. Mater.* **2013**, *12*, 991–1003.

(18) Torchilin, V. P. Multifunctional, Stimuli-Sensitive Nanoparticulate Systems for Drug Delivery. *Nat. Rev. Drug Discov.* **2014**, *13*, 813–827.

(19) Shen, Y.; Tang, H.; Radosz, M.; Van Kirk, E.; Murdoch, W. J. pH-Responsive Nanoparticles for Cancer Drug Delivery. In *Methods in molecular biology*, **2008**, *437*,183–216.

(20) Needham, D.; Dewhirst, M. W. The Development and Testing of a New Temperature-Sensitive Drug Delivery System for the Treatment of Solid Tumors. *Adv. Drug Deliv. Rev.* **2001**, *53*, 285–305.

(21) Meers, P. Enzyme-Activated Targeting of Liposomes. *Adv. Drug Deliv. Rev.* **2001**, *53*, 265–272.

(22) Graf, N.; Lippard, S. J. Redox Activation of Metal-Based Prodrugs as a Strategy for Drug Delivery. *Adv. Drug Deliv. Rev.* **2012**, *64*, 993–1004.

(23) Rajora, M. A.; Lou, J. W. H.; Zheng, G. Advancing Porphyrin's Biomedical Utility via Supramolecular Chemistry. *Chem. Soc. Rev.* **2017**, *46*, 6433–6469.

(24) Venditto, V. J.; Szoka, F. C. Cancer Nanomedicines: So Many Papers and so Few Drugs! *Adv. Drug Deliv. Rev.* **2013**, *65*, 80–88.

(25) Huynh, E.; Zheng, G. Engineering Multifunctional Nanoparticles: All-in-One versus One-for-All. *Wiley Interdiscip. Rev. Nanomedicine Nanobiotechnology* **2013**, *5*, 250–265.

(26) Hare, J. I.; Lammers, T.; Ashford, M. B.; Puri, S.; Storm, G.; Barry, S. T. Challenges and Strategies in Anti-Cancer Nanomedicine Development: An Industry Perspective. *Adv. Drug Deliv. Rev.* **2017**, *108*, 25–38.

(27) Leroux, J.-C. Drug Delivery: Too Much Complexity, Not Enough Reproducibility? *Angew. Chemie Int. Ed.* **2017**, *56*, 2–4.

(28) Anselmo, A. C.; Mitragotri, S. Nanoparticles in the Clinic. *Bioeng. Transl. Med.* **2016**, *1*, 10–29.

(29) Allen, T. M.; Hansen, C. Pharmacokinetics of Stealth versus Conventional Liposomes: Effect of Dose. *Biochim. Biophys. Acta* **1991**, *1068*, 133–141.

(30) Chitgupi, U.; Qin, Y.; Lovell, J. F. Targeted Nanomaterials for Phototherapy. *Nanotheranostics* **2017**, *1*, 38–58.

(31) Miranda, D.; Carter, K.; Luo, D.; Shao, S.; Geng, J.; Li, C.; Chitgupi, U.; Turowski, S. G.; Li, N.; Atilla-Gokcumen, G. E.; et al. Multifunctional Liposomes for Image-Guided Intratumoral Chemo-Phototherapy. *Adv. Healthc. Mater.* **2017**, *1700253*, 1-9.

(32) Castano, A. P.; Demidova, T. N.; Hamblin, M. R. Mechanisms in Photodynamic Therapy: Part One—photosensitizers, Photochemistry and Cellular Localization. *Photodiagnosis Photodyn. Ther.* **2004**, *1*, 279–293.

(33) Yavlovich, A.; Smith, B.; Gupta, K.; Blumenthal, R.; Puri, A. Light-Sensitive Lipid-Based Nanoparticles for Drug Delivery: Design Principles and Future Considerations for Biological Applications. *Mol. Membr. Biol.* **2010**, *27*, 364–381.

(34) Miranda, D.; Lovell, J. F. Mechanisms of Light-Induced Liposome Permeabilization. *Bioeng. Transl. Med.* **2016**, *1*, 267–276.

(35) Fomina, N.; Sankaranarayanan, J.; Almutairi, A. Photochemical Mechanisms of Light-Triggered Release from Nanocarriers. *Adv. Drug Deliv. Rev.* **2012**, *64*, 1005–1020.

(36) Mojzisova, H.; Bonneau, S.; Maillard, P.; Berg, K.; Brault, D. Photosensitizing Properties of Chlorins in Solution and in Membrane-Mimicking Systems. *Photochem. Photobiol. Sci.* **2009**, *8*, 778–787.

(37) E. N. Frankel. Progress in Lipid Research. *Prog. Lipid Res.* **1980**, *19*, 1–22.

(38) Wong-ekkabut, J.; Xu, Z.; Triampo, W.; Tang, I.-M.; Peter Tieleman, D.; Monticelli, L. Effect of Lipid Peroxidation on the Properties of Lipid Bilayers: A Molecular Dynamics Study. *Biophys. J.* **2007**, *93*, 4225–4236.

(39) Heuvingh, J.; Bonneau, S. Asymmetric Oxidation of Giant Vesicles Triggers Curvature-Associated Shape Transition and Permeabilization. *Biophys. J.* **2009**, *97*, 2904-2912.

(40) Mertins, O.; Bacellar, I. O. L.; Thalmann, F.; Marques, C. M.; Baptista, M. S.; Itri, R. Physical Damage on Giant Vesicles Membrane as a Result of Methylene Blue Photoirradiation. *Biophys. J.* **2014**, *106*, 162–171.

(41) Sabatini, K.; Mattila, J.; Megli, F. M.; Kinnunen, P. K. J. Characterization of Two Oxidatively Modified Phospholipids in Mixed Monolayers with DPPC. **2006**, *90*, 4488–4499.

(42) Korytowski, A.; Abuillan, W.; Makky, A.; Konovalov, O.; Tanaka, M. Impact of Lipid Oxidization on Vertical Structures and Electrostatics of Phospholipid Monolayers Revealed by Combination of Specular X - Ray Re Fl Ectivity and Grazing-Incidence X - Ray Fluorescence. *J. Phys. Chem. B* **2015**, *119*, 9787–9794.

(43) Makky, A.; Tanaka, M. Impact of Lipid Oxidization on Biophysical Properties of Model Cell Membranes. *J. Phys. Chem. B* **2015**, *119*, 5857–5863.

(44) Weber, G.; Charitat, T.; Baptista, M. S.; Uchoa, A. F.; Pavani, C.; Junqueira, H. C.; Guo, Y.; Baulin, V. A.; Itri, R.; Marques, C. M.; et al. Lipid Oxidation Induces Structural Changes in Biomimetic Membranes. *Soft Matter* **2014**, *10*, 4241-4247.

(45) Pashkovskaya, A.; Kotova, E.; Zorlu, Y.; Dumoulin, F.; Ahsen, V.; Agapov, I.; Antonenko, Y. Light-Triggered Liposomal Release: Membrane Permeabilization by Photodynamic Action. *Langmuir* **2010**, *26*, 5725–5733.

(46) Luo, D.; Li, N.; Carter, K. A.; Lin, C.; Geng, J.; Shao, S.; Huang, W.-C. C.; Qin, Y.; Atilla-Gokcumen, G. E.; Lovell, J. F.; et al. Rapid Light-Triggered Drug Release in Liposomes Containing Small Amounts of Unsaturated and Porphyrin-Phospholipids. *Small* **2016**, *12*, 3039–3047.

(47) Frankel, E. *Lipid Oxidation*; Frankel, E., Ed.; Woodhead Publishing, **2005**.

(48) Min, D. B.; Boff, J. M. Chemistry and Reaction of Singlet Oxygen in Foods. *Compr. Rev. Food Sci. Food Saf.* **2002**, *1*, 58–72.

(49) Korycka-Dahl, M. B.; Richardson, T. Activated Oxygen Species and Oxidation of Food Constituents. *C R C Crit. Rev. Food Sci. Nutr.* **1978**, *10*, 209–241.

(50) Girotti, A. W. Lipid Hydroperoxide Generation, Turnover, and Effector Action in Biological Systems. *J. Lipid Res.* **1998**, *39*, 1529–1542.

(51) Rwei, A. Y.; Lee, J.-J.; Zhan, C.; Liu, Q.; Ok, M. T.; Shankarappa, S. A.; Langer, R.; Kohane, D. S. Repeatable and Adjustable on-Demand Sciatic Nerve Block with Phototriggerable Liposomes. *Proc. Natl. Acad. Sci.* **2015**, *112*, 15719-15724.

(52) Rwei, A. Y.; Zhan, C.; Wang, B.; Kohane, D. S. Multiply Repeatable and Adjustable on-Demand Phototriggered Local Anesthesia. *J. Control. Release* **2017**, *251*, 68–74.

(53) Spring, B. Q.; Bryan Sears, R.; Zheng, L. Z.; Mai, Z.; Watanabe, R.; Sherwood, M. E.; Schoenfeld, D. A.; Pogue, B. W.; Pereira, S. P.; Villa, E.; et al. A Photoactivable Multi-Inhibitor Nanoliposome for Tumour Control and Simultaneous Inhibition of Treatment Escape Pathways. *Nat. Nanotechnol.* **2016**, *11*, 378–387.

(54) Anderson, V. C.; Thompson, D. H. Triggered Release of Hydrophilic Agents from Plasmologen Liposomes Using Visible Light or Acid. *Biochim. Biophys. Acta - Biomembr.* **1992**, *1109*, 33–42.

(55) Sine, J.; Urban, C.; Thayer, D.; Charron, H.; Valim, N.; Tata, D. B.; Schiff, R.; Blumenthal, R.; Joshi, A.; Puri, A. Photo Activation of HPPH Encapsulated in "Pocket" Liposomes Triggers Multiple Drug Release and Tumor Cell Killing in Mouse Breast Cancer Xenografts. *Int. J. Nanomedicine* **2014**, *10*, 125–145.

(56) Zhou, F.; Feng, B.; Wang, T.; Wang, D.; Meng, Q.; Zeng, J.; Zhang, Z.; Wang, S.; Yu, H.; Li, Y. Programmed Multiresponsive Vesicles for Enhanced Tumor Penetration and Combination Therapy of Triple-Negative Breast Cancer. *Adv. Funct. Mater.* **2017**, *1606530*, 1-12.

(57) Shin, J.; Shum, P.; Grey, J.; Fujiwara, S.; Malhotra, G. S.; González-Bonet, A.; Hyun, S.-H.; Moase, E.; Allen, T. M.; Thompson, D. H. Acid-Labile mPEG–Vinyl Ether–1,2-Dioleylglycerol Lipids with Tunable pH Sensitivity: Synthesis and Structural Effects on Hydrolysis Rates, DOPE Liposome Release Performance, and Pharmacokinetics. *Mol. Pharm.* **2012**, *9*, 3266–3276.

(58) Shin, J.; Shum, P.; Thompson, D. H. Acid-Triggered Release via dePEGylation of DOPE Liposomes Containing Acid-Labile Vinyl Ether PEG-Lipids. *J. Control. Release* **2003**, *91*, 187–200.

(59) Gawrisch, K.; Parsegian, V. A.; Hajduk, D. A.; Tate, M. W.; Gruner, S. M.; Fuller, N. L.; Rand, R. P. Energetics of a Hexagonal-Lamellar-Hexagonal-Phase Transition Sequence in Dioleoylphosphatidylethanolamine Membranes. *Biochemistry* **1992**, *31*, 2856–2864.

(60) Rhodes, D. G.; Blechner, S. L.; Yager, P.; Schoen, P. E. Structure of Polymerizable Lipid Bilayers. I--1,2-bis(10,12-Tricosadiynoyl)-Sn-Glycero-3-Phosphocholine, a Tubule-Forming Phosphatidylcholine. *Chem. Phys. Lipids* **1988**, *49*, 39–47.

(61) Yavlovich, A.; Viard, M.; Gupta, K.; Sine, J.; Vu, M.; Blumenthal, R.; Tata, D. B.; Puri, A. Low-Visibility Light-Intensity Laser-Triggered Release of Entrapped Calcein from 1,2-Bis (tricosa-10,12-Diynoyl)-Sn-Glycero-3-Phosphocholine Liposomes Is Mediated through a Type I Photoactivation Pathway. *Int. J. Nanomedicine* **2013**, *8*, 2575–2587.

(62) Yavlovich, A.; Singh, A.; Tarasov, S.; Capala, J.; Blumenthal, R.; Puri, A. Design of Liposomes Containing Photopolymerizable Phospholipids for Triggered Release of Contents. *J. Therm. Anal. Calorim.* **2009**, *98*, 97–104.

(63) Puri, A.; Loomis, K.; Smith, B.; Lee, J.-H.; Yavlovich, A.; Heldman, E.; Blumenthal, R. Lipid-Based Nanoparticles as Pharmaceutical Drug Carriers: From Concepts to Clinic. *Crit. Rev. Ther. Drug Carrier Syst.* **2009**, *26*, 523–580.

(64) Puri, A.; Jang, H.; Yavlovich, A.; Masood, M. A.; Veenstra, T. D.; Luna, C.; Aranda-Espinoza, H.; Nussinov, R.; Blumenthal, R. Material Properties of Matrix Lipids Determine the Conformation and Intermolecular Reactivity of Diacetylenic Phosphatidylcholine in the Lipid Bilayer. *Langmuir* **2011**, *27*, 15120–15128.

(65) Dendramis, K. A.; Chiu, D. T. Laser Photolysis of Dye-Sensitized Nanocapsules Occurs via a Photothermal Pathway. *J. Am. Chem. Soc.* **2009**, *131*, 16771–16778.

(66) Jin, C. S.; Lovell, J. F.; Chen, J.; Zheng, G. Ablation of Hypoxic Tumors with Not Photodynamic , Therapy Using a Nanostructured Porphyrin Assembly. *ACS Nano* **2013**, *7*, 2541–2550.

(67) Brown, J. M. Tumor Hypoxia in Cancer Therapy. *Methods Enzymol.* **2007**, *435*, 297-321.

(68) Weissleder, R. A Clearer Vision for in Vivo Imaging. *Nat. Biotechnol.* **2001**, *19*, 316–317.

(69) Chen, B.; Pogue, B. W.; Hasan, T. Liposomal Delivery of Photosensitising Agents. *Expert Opin. Drug Deliv.* **2005**, *2*, 477–487.

(70) Spikes, J. D. A Preliminary Comparison of the Photosensitizing Properties of Porphyrins in Aqueous Solution and Liposomal Systems. *Adv Exp Med Biol* **1983**, *160*, 181–192.

(71) Kramer, M.; Miller, J. W.; Michaud, N.; Moulton, R. S.; Hasan, T.; Flotte, T. J.; Gragoudas, E. S. Liposomal Benzoporphyrin Derivative Verteporfin Photodynamic Therapy. Selective Treatment of Choroidal Neovascularization in Monkeys. *Ophthalmology* **1996**, *103*, 427–438.

(72) Postigo, F.; Mora, M.; De Madariaga, M. A.; Nonell, S.; Sagrista, M. L. Incorporation of Hydrophobic Porphyrins into Liposomes: Characterization and Structural Requirements. *Int. J. Pharm.* **2004**, *278*, 239–254.

(73) Chauvin, B.; Iorga, B. I.; Chaminade, P.; Paul, J.-L.; Maillard, P.; Prognon, P.; Kasselouri, A. Plasma Distribution of Tetraphenylporphyrin Derivatives Relevant for Photodynamic Therapy: Importance and Limits of Hydrophobicity. *Eur. J. Pharm. Biopharm.* **2013**, *83*, 244–252.

(74) Wang, Z.-J.; Chauvin, B.; Maillard, P.; Hammerer, F.; Carez, D.; Croisy, A.; Sandré, C.; Chollet-Martin, S.; Prognon, P.; Paul, J.-L.; et al. Glycodendrimeric Phenylporphyrins as New Candidates for Retinoblastoma PDT: Blood Carriers and Photodynamic Activity in Cells. *J. Photochem. Photobiol. B.* **2012**, *115*, 16–24.

(75) Kerdous, R.; Heuvingh, J.; Bonneau, S. Photo-Dynamic Induction of Oxidative Stress within Cholesterol-Containing Membranes: Shape Transitions and Permeabilization. *Biochim. Biophys. Acta* **2011**, *1808*, 2965–2972.

(76) Maherani, B.; Arab-Tehrany, E.; Kheirolomoom, A.; Geny, D.; Linder, M. Calcein Release Behavior from Liposomal Bilayer; Influence of Physicochemical/mechanical/structural Properties of Lipids. *Biochimie* **2013**, *95*, 2018–2033.

(77) Krasnovsky, A. A.; Neverov, K. V.; Egorov, S. Y.; Roeder, B.; Levald, T. Photophysical Studies of Pheophorbide a and Pheophytin A. Phosphorescence and Photosensitized Singlet Oxygen Luminescence. *J. Photochem. Photobiol. B Biol.* **1990**, *5*, 245–254.

(78) Carter, K. A.; Shao, S.; Hoopes, M. I.; Luo, D.; Ahsan, B.; Grigoryants, V. M.; Song, W.; Huang, H.; Zhang, G.; Pandey, R. K.; et al. Porphyrin–phospholipid Liposomes Permeabilized by near-Infrared Light. *Nat. Commun.* **2014**, *5*, 1–11.

(79) Huang, H.-C.; Mallidi, S.; Liu, J.; Chiang, C.-T.; Mai, Z.; Goldschmidt, R.; Ebrahim-Zadeh, N.; Rizvi, I.; Hasan, T. Photodynamic Therapy Synergizes with Irinotecan to Overcome Compensatory Mechanisms and Improve Treatment Outcomes in Pancreatic Cancer. *Cancer Res.* **2016**, *76*, 1066–1077.

(80) Luo, D.; Geng, J.; Li, N.; Carter, K. A.; Shao, S.; Atilla-gokcumen, G. E.; Lovell, J. F. Vessel-Targeted Chemophototherapy with Cationic Porphyrin-Phospholipid Liposomes. *Mol. Cancer Ther.* **2017**, *16*, 2452–2461.
(81) Li, X.; Lee, S.; Yoon, J. Supramolecular Photosensitizers Rejuvenate Photodynamic Therapy. *Chem. Soc. Rev.* **2018**, *47*, 1174–1188.
(82) Rajora, M. A.; Ding, L.; Valic, M.; Jiang, W.; Overchuk, M.; Chen, J.; Zheng, G. Tailored Theranostic Apolipoprotein E3 Porphyrin-Lipid Nanoparticles Target Glioblastoma. *Chem. Sci.* **2017**, *8*, 5371–5384.
(83) Liu, T. W.; MacDonald, T. D.; Jin, C. S.; Gold, J. M.; Bristow, R. G.; Wilson, B. C.; Zheng, G. Inherently Multimodal Nanoparticle-Driven Tracking and Real-Time Delineation of Orthotopic Prostate Tumors and Micrometastases. *ACS Nano* **2013**, *7*, 4221–4232.
(84) Shakiba, M.; Ng, K. K.; Huynh, E.; Chan, H.; Charron, D. M.; Chen, J.; Muhanna, N.; Foster, F. S.; Wilson, B. C.; Zheng, G. Stable J-Aggregation Enabled Dual Photoacoustic and Fluorescence Nanoparticles for Intraoperative Cancer Imaging. *Nanoscale* **2016**, *8*, 12618–12625.
(85) Bolzonello, L.; Albertini, M.; Collini, E.; Di Valentin, M. Delocalized Triplet State in Porphyrin J-Aggregates Revealed by EPR Spectroscopy. *Phys. Chem. Chem. Phys.* **2017**, *19*, 27173–27177.
(86) Jung, H. S.; Verwilst, P.; Sharma, A.; Shin, J.; Sessler, J. L.; Kim, J. S. Organic Molecule-Based Photothermal Agents: An Expanding Photothermal Therapy Universe. *Chem. Soc. Rev.* **2018**, *47*, 2280–2297.
(87) Riske, K. A.; Sudbrack, T. P.; Archilha, N. L.; Uchoa, A. F.; Schroder, A. P.; Marques, C. M.; Baptista, M. S.; Itri, R. Giant Vesicles under Oxidative Stress Induced by a Membrane-Anchored Photosensitizer. *Biophys. J.* **2009**, *97*, 1362–1370.
(88) Ponomarev, G. V.; Solovieva, M. N.; Dugin, N. O.; Zavialova, M. G.; Mehtiev, A. R.; Misharin, A. Y.; Novikov, R. A.; Tkachev, Y. V.; Popenko, V. I.; Timofeev, V. P. Lipophilic Derivatives of Natural Chlorins: Synthesis, Mixed Micelles with Phospholipids, and Uptake by Cultured Cells. *Bioorganic Med. Chem.* **2013**, *21*, 5420–5427.
(89) Temizel, E.; Sagir, T.; Ayan, E.; Isik, S.; Ozturk, R. Delivery of Lipophilic Porphyrin by Liposome Vehicles: Preparation and Photodynamic Therapy Activity against Cancer Cell Lines. *Photodiagnosis Photodyn. Ther.* **2014**, *11*, 537–545.
(90) Nathan, E.; Vijayashree, K.; Harikrishna, A.; Takafuji, M.; Jintoku, H.; Ihara, H.; Rao, N. M. A Novel Photosensitizer: An L-Glutamide Lipid Conjugate with Improved Properties for Photodynamic Therapy. *Photochem. Photobiol. Sci.* **2016**, *15*, 1476–1483.
(91) Kohli, A. G.; Kierstead, P. H.; Venditto, V. J.; Walsh, C. L.; Szoka, F. C. Designer Lipids for Drug Delivery: From Heads to Tails. *J. Control. Release* **2014**, *190*, 274–287.
(92) Khandelia, H.; Loubet, B.; Olżyńska, A.; Jurkiewicz, P.; Hof, M. Pairing of Cholesterol with Oxidized Phospholipid Species in Lipid Bilayers. *Soft Matter* **2014**, *10*, 639-647.
(93) Kessel, A.; Ben-Tal, N.; May, S. Interactions of Cholesterol with Lipid Bilayers: The Preferred Configuration and Fluctuations. *Biophys. J.* **2001**, *81*, 643–658.
(94) Nikolaeva, I. A.; Misharin, A. Y.; Ponomarev, G. V.; Timofeev, V. P.; Tkachev, Y. V. Chlorin e6-Cholesterol Conjugate and Its Copper Complex. Simple Synthesis and Entrapping in Phospholipid Vesicles. *Bioorganic Med. Chem. Lett.* **2010**, *20*, 2872–2875.
(95) Zheng, G.; Li, H.; Zhang, M.; Lund-Katz, S.; Chance, B.; Glickson, J. D. Low-Density Lipoprotein Reconstituted by Pyropheophorbide Cholesteryl Oleate as Target-Specific Photosensitizer. *Bioconjug. Chem.* **2002**, *13*, 392–396.
(96) Anikeeva, N.; Sykulev, Y.; Delikatny, E. J.; Popov, A. V. Core-Based Lipid Nanoparticles as a Nanoplatform for Delivery of near-Infrared Fluorescent Imaging Agents. *Am. J. Nucl. Med. Mol. Imaging* **2014**, *4*, 507–524.
(97) Tsuchida, E.; Komatsu, T.; Arai, K.; Nishide, H. Lipid-Porphyrin Vesicles: Morphology and O2 Binding in Aqueous Medium. *J. Chem. Soc. Chem. Commun.* **1993**, *0*, 730–732.
(98) Tsuchida, E.; Komatsu, T.; Arai, K.; Yamada, K.; Nishide, H.; Fuhrhop, J. H. Self-Assembled Lipidporphyrin Bilayer Vesicles. Microstructure and Dioxygen Binding in Aqueous Medium. *Langmuir* **1995**, *11*, 1877–1884.
(99) Komatsu, T.; Moritake, M.; Nakagawa, A.; Tsuchida, E. Self-Organized Lipid-Porphyrin Bilayer Membranes in Vesicular Form: Nanostructure, Photophysical Properties, and Dioxygen Coordination. *Chem. - A Eur. J.* **2002**, *8*, 5469–5480.
(100) Lewis, B. A.; Engelman, D. M. Lipid Bilayer Thickness Varies Linearly with Acyl Chain Length in Fluid Phosphatidylcholine Vesicles. *J. Mol. Biol.* **1983**, *166*, 211–217.
(101) Nagle, J. F.; Tristram-Nagle, S. Structure of Lipid Bilayers. *Biochim. Biophys. Acta* **2000**, *1469*, 159–195.
(102) Ng, K. K.; Takada, M.; Harmatys, K.; Chen, J.; Zheng, G. Chlorosome-Inspired Synthesis of Templated Metallochlorin-Lipid Nanoassemblies for Biomedical Applications. **2016**, *10*, 4092–4101.
(103) Ogi, S.; Grzeszkiewicz, C.; Würthner, F. Pathway Complexity in the Self-Assembly of a Zinc Chlorin Model System of Natural Bacteriochlorophyll J-Aggregates. *Chem. Sci.* **2018**, *9*, 2768–2773.
(104) Liang, X.; Li, X.; Yue, X.; Dai, Z. Conjugation of Porphyrin to Nanohybrid Cerasomes for Photodynamic Diagnosis and Therapy of Cancer. *Angew. Chemie - Int. Ed.* **2011**, *50*, 11622–11627.
(105) Liang, X.; Yue, X.; Dai, Z.; Kikuchi, J. Photoresponsive Liposomal Nanohybrid Cerasomes. *Chem. Commun.* **2011**, *47*, 4751-4753.
(106) Hameed, S.; Bhattarai, P.; Dai, Z. Cerasomes and Bicelles: Hybrid Bilayered Nanostructures With Silica-Like Surface in Cancer Theranostics. *Front. Chem.* **2018**, *6*, 1–17.

(107) Liang, X.; Li, X.; Jing, L.; Yue, X.; Dai, Z. Theranostic Porphyrin Dyad Nanoparticles for Magnetic Resonance Imaging Guided Photodynamic Therapy. *Biomaterials* **2014**, *35*, 6379–6388.
(108) Jin, C. S.; Lovell, J. F.; Zheng, G. One Minute, Sub-One-Watt Photothermal Tumor Ablation Using Porphysomes, Intrinsic Multifunctional Nanovesicles. *J. Vis. Exp.* **2013**, *79*, 1-6.
(109) Liu, T. W.; MacDonald, T. D.; Shi, J.; Wilson, B. C.; Zheng, G. Intrinsically Copper-64-Labeled Organic Nanoparticles as Radiotracers. *Angew. Chemie - Int. Ed.* **2012**, *51*, 13128–13131.
(110) Huynh, E.; Lovell, J. F.; Fobel, R.; Zheng, G. Optically Controlled Pore Formation in Self-Sealing Giant Porphyrin Vesicles. *Small* **2014**, *10*, 1184–1193.
(111) Luo, D.; Carter, K. A.; Razi, A.; Geng, J.; Shao, S.; Giraldo, D.; Sunar, U.; Ortega, J.; Lovell, J. F. Doxorubicin Encapsulated in Stealth Liposomes Conferred with Light-Triggered Drug Release. *Biomaterials* **2016**, *75*, 193–202.
(112) Carter, K. A.; Luo, D.; Razi, A.; Geng, J.; Shao, S.; Ortega, J.; Lovell, J. F. Sphingomyelin Liposomes Containing Porphyrin-Phospholipid for Irinotecan Chemophototherapy. *Theranostics* **2016**, *6*, 2329–2336.
(113) Luo, D.; Carter, K. A.; Razi, A.; Geng, J.; Shao, S.; Lin, C.; Ortega, J.; Lovell, J. F. Porphyrin-Phospholipid Liposomes with Tunable Leakiness. *J. Control. Release* **2015**, *220*, 484–494.
(114) Chitgupi, U.; Shao, S.; Carter, K.; Huang, W.-C.; Lovell, J. F. Multi-Color Liposome Mixtures for Selective and Selectable Cargo Release. *Nano Lett.* **2018**, *18*, 1331–1336.
(115) Rizvi, I.; Obaid, G.; Bano, S.; Hasan, T.; Kessel, D. Photodynamic Therapy: Promoting in Vitro Efficacy of Photodynamic Therapy by Liposomal Formulations of a Photosensitizing Agent. *Lasers Surg. Med.* **2018**, *50*, 499–505.
(116) Shao, S.; Do, T. N.; Razi, A.; Chitgupi, U.; Geng, J.; Alsop, R. J.; Dzikovski, B. G.; Rheinstädter, M. C.; Ortega, J.; Karttunen, M.; et al. Design of Hydrated Porphyrin-Phospholipid Bilayers with Enhanced Magnetic Resonance Contrast. *Small* **2017**, *13*, 1–6.
(117) Keca, J. M.; Chen, J.; Overchuk, M.; Muhanna, N.; MacLaughlin, C. M.; Jin, C. S.; Foltz, W. D.; Irish, J. C.; Zheng, G. Nanotexaphyrin: One-Pot Synthesis of a Manganese Texaphyrin-Phospholipid Nanoparticle for Magnetic Resonance Imaging. *Angew. Chemie - Int. Ed.* **2016**, *55*, 6187–6191.
(118) Macdonald, T. D.; Liu, T. W.; Zheng, G. An MRI-Sensitive, Non-Photobleachable Porphysome Photothermal Agent. *Angew. Chemie - Int. Ed.* **2014**, *53*, 6956–6959.
(119) Gomes, A.; Fernandes, E.; Lima, J. L. F. C. Fluorescence Probes Used for Detection of Reactive Oxygen Species. *J. Biochem. Biophys. Methods* **2005**, *65*, 45–80.
(120) Firsov, A. M.; Kotova, E. A.; Antonenko, Y. N. Calcein Leakage as a Robust Assay for Cytochrome c/H2O2-Mediated Liposome Permeabilization. *Anal. Biochem.* **2016**, *552*, 19–23.
(121) Dzieciuch, M.; Rissanen, S.; Szydłowska, N.; Bunker, A.; Kumorek, M.; Jamróz, D.; Vattulainen, I.; Nowakowska, M.; Róg, T.; Kepczynski, M. PEGylated Liposomes as Carriers of Hydrophobic Porphyrins. *J. Phys. Chem. B* **2015**, *119*, 6646–6657.
(122) Stępniewski, M.; Kepczynski, M.; Jamróz, D.; Nowakowska, M.; Rissanen, S.; Vattulainen, I.; Róg, T. Interaction of Hematoporphyrin with Lipid Membranes. *J. Phys. Chem. B* **2012**, *116*, 4889–4897.
(123) Cordeiro, R. M. Molecular Dynamics Simulations of the Transport of Reactive Oxygen Species by Mammalian and Plant Aquaporins. *Biochim. Biophys. Acta - Gen. Subj.* **2015**, *1850*, 1786–1794.
(124) Tanielian, C.; Heinrich, G. Effect of Aggregation on the Hematoporphyrin-Sensitized Production of Singlet Molecular Oxygen. *Photochem. Photobiol.* **1995**, *61*, 131–135.
(125) Merkel, P. B.; Kearns, D. R. Radiationless Decay of Singlet Molecular Oxygen in Solution. Experimental and Theoretical Study of Electronic-to-Vibrational Energy Transfer. *J. Am. Chem. Soc.* **1972**, *94*, 7244–7253.
(126) Senge, M. O.; Brandt, J. C. Temoporfin (Foscan®, 5,10,15,20-Tetra(mhydroxyphenyl)chlorin), a Second Generation Photosensitizer. *Photochem. Photobiol.* **2011**, *87*, 1240–1296.
(127) Schmidt-Erfurth, U.; Hasan, T. Mechanisms of Action of Photodynamic Therapy with Verteporfin for the Treatment of Age-Related Macular Degeneration. *Surv. Ophthalmol.* **2000**, *45*, 195–214.
(128) Cho, M.; Park, G.-M.; Kim, S.-N.; Amna, T.; Lee, S.; Shin, W.-S. Glioblastoma-Specific Anticancer Activity of Pheophorbide a from the Edible Red Seaweed Grateloupia Elliptica. *J. Microbiol. Biotechnol.* **2014**, *24*, 346–353.
(129) Baudelet, P.-H.; Gagez, A.-L.; Bérard, J.-B.; Juin, C.; Bridiau, N.; Kaas, R.; Thiéry, V.; Cadoret, J.-P.; Picot, L. Antiproliferative Activity of Cyanophora Paradoxa Pigments in Melanoma, Breast and Lung Cancer Cells. *Mar. Drugs* **2013**, *11*, 4390–4406.
(130) Rapozzi, V.; Miculan, M.; Xodo, L. E. Evidence That Photoactivated Pheophorbide a Causes in Human Cancer Cells a Photodynamic Effect Involving Lipid Peroxidation. *Cancer Biol. Ther.* **2009**, *8*, 1318–1327.
(131) Hartl, B. A.; Hirschberg, H.; Marcu, L.; Cherry, S. R. Activating Photodynamic Therapy in Vitro with Cerenkov Radiation Generated from Yttrium-90. *J. Environ. Pathol. Toxicol. Oncol.* **2016**, *35*, 185–192.
(132) Makky, A.; Daghildjian, K.; Michel, J. P.; Maillard, P.; Rosilio, V. Assessment of the Relevance of Supported Planar Bilayers for Modeling Specific Interactions between Glycodendrimeric Porphyrins and Retinoblastoma Cells. *Biochim. Biophys. Acta - Biomembr.* **2012**, *1818*, 2831–2838.
(133) Hempstead, J.; Jones, D. P.; Ziouche, A.; Cramer, G. M.; Rizvi, I.; Arnason, S.; Hasan, T.; Celli, J. P. Low-Cost Photodynamic Therapy Devices for Global Health Settings: Characterization of Battery-Powered LED Performance and Smartphone Imaging in 3D Tumor Models. *Sci. Rep.* **2015**, *5*, 1-13.

(134) Oulmi, D.; Maillard, P.; Guerquin-Kern, J.-L.; Huel, C.; Momenteau, M. Glycoconjugated Porphyrins. 3. Synthesis of Flat Amphiphilic Mixed Meso-(Glycosylated Aryl)arylporphyrins and Mixed Meso-(Glycosylated Aryl)alkylporphyrins Bearing Some Mono- and Disaccharide Groups. *J. Org. Chem.* **1995**, *60*, 1554–1564.

(135) Bangham, A. D.; Standish, M. M.; Watkins, J. C. Diffusion of Univalent Ions across the Lamellae of Swollen Phospholipids. *J. Mol. Biol.* **1965**, *13*, 238–252.

(136) Price, D. M. Temperature Calibration of Differential Scanning Calorimeters. *J. Therm. Anal.* **1995**, *45*, 1285–1296.

(137) Chan, H. W. S.; Levett, G. Autoxidation of Methyl Linoleate. Separation and Analysis of Isomeric Mixtures of Methyl Linoleate Hydroperoxides and Methyl Hydroxylinoleates. *Lipids* **1977**, *12*, 99–104.

(138) Pryor, W. A.; Castle, L. Chemical Methods for the Detection of Lipid Hydroperoxides. *Methods Enzymol.* **1984**, *105*, 293–299.

(139) Chen, P. S.; Toribara, T. Y.; Warner, H.; Chen Jr, P. S.; Toribara, T. Y.; Warner, H. Microdetermination of Phosphorus. *Anal. Chem.* **1956**, *28*, 1756–1758.

(140) Wang, J.; Wolf, R. M.; Caldwell, J. W.; Kollman, P. A.; Case, D. A. Development and Testing of a General Amber Force Field. *J. Comput. Chem.* **2004**, *25*, 1157–1174.

(141) Wang, J.; Wang, W.; Kollman, P. A.; Case, D. A. Automatic Atom Type and Bond Type Perception in Molecular Mechanical Calculations. *J. Mol. Graph. Model.* **2006**, *25*, 247–260.

(142) Duan, Y.; Wu, C.; Chowdhury, S.; Lee, M. C.; Xiong, G.; Zhang, W.; Yang, R.; Cieplak, P.; Luo, R.; Lee, T.; et al. A Point-Charge Force Field for Molecular Mechanics Simulations of Proteins Based on Condensed-Phase Quantum Mechanical Calculations. *J. Comput. Chem.* **2003**, *24*, 1999–2012.

(143) Frisch, M. J.; Trucks, G. W.; Schlegel, H. B.; Scuseria, G. E.; Robb, M. A.; Cheeseman, J. R.; Scalmani, G.; Barone, V.; Mennucci, B.; Petersson, G. A.; et al. Gaussian 09, Revision A, Wallingford CT. *Gaussian 09, Revis. A, Wallingford CT* **2009**, *3*, 1–6.

(144) Dupradeau, F.-Y.; Pigache, A.; Zaffran, T.; Savineau, C.; Lelong, R.; Grivel, N.; Lelong, D.; Rosanski, W.; Cieplak, P. The R.E.D. Tools: Advances in RESP and ESP Charge Derivation and Force Field Library Building. *Phys. Chem. Chem. Phys.* **2010**, *12*, 7821-7839.

(145) Dickson, C. J.; Madej, B. D.; Skjevik, Å. A.; Betz, R. M.; Teigen, K.; Gould, I. R.; Walker, R. C. Lipid14: The Amber Lipid Force Field. *J. Chem. Theory Comput.* **2014**, *10*, 865–879.

(146) Skjevik, Å. A.; Madej, B. D.; Walker, R. C.; Teigen, K. LIPID11: A Modular Framework for Lipid Simulations Using Amber. *J. Phys. Chem. B* **2012**, *116*, 11124–11136.

(147) Dickson, C. J.; Rosso, L.; Betz, R. M.; Walker, R. C.; Gould, I. R. GAFFlipid: A General Amber Force Field for the Accurate Molecular Dynamics Simulation of Phospholipid. *Soft Matter* **2012**, *8*, 9617-9627.

(148) Price, D. J.; Brooks, C. L. A Modified TIP3P Water Potential for Simulation with Ewald Summation. *J. Chem. Phys.* **2004**, *121*, 10096–10103.

(149) Jo, S.; Kim, T.; Iyer, V. G.; Im, W. CHARMM-GUI: A Web-Based Graphical User Interface for CHARMM. *J. Comput. Chem.* **2008**, *29*, 1859–1865.

(150) Salomon-Ferrer, R.; Case, D. A.; Walker, R. C. An Overview of the Amber Biomolecular Simulation Package. *Wiley Interdiscip. Rev. Comput. Mol. Sci.* **2013**, *3*, 198–210.

(151) Case, D. A.; Cerutti, D. S.; Cheatham, T. E.; III; Darden, T. A.; Duke, R. E.; Giese, T. J.; Gohlke, H.; Goetz, A. W.; Greene, D.; *et al.* AMBER 2016. *Univ. California, San Fr.* **2016**.

(152) Roe, D. R.; Cheatham, T. E. PTRAJ and CPPTRAJ: Software for Processing and Analysis of Molecular Dynamics Trajectory Data. *J. Chem. Theory Comput.* **2013**, *9*, 3084–3095.

(153) Desroches, M.-C.; Kasselouri, A.; Meyniel, M.; Fontaine, P.; Goldmann, M.; Prognon, P.; Maillard, P.; Rosilio, V. Incorporation of Glycoconjugated Porphyrin Derivatives into Phospholipid Monolayers: A Screening Method for the Evaluation of Their Interaction with a Cell Membrane. *Langmuir* **2004**, *20*, 11698–11705.

(154) Čunderlíková, B.; Kaalhus, O.; Čunderlík, R.; Mateášik, A.; Moan, J.; Kongshaug, M. pH-Dependent Modification of Lipophilicity of Porphyrin-Type Photosensitizers. *Photochem. Photobiol.* **2004**, *79*, 242-247.

(155) Ibrahim, H.; Kasselouri, A.; You, C.; Maillard, P.; Rosilio, V.; Pansu, R.; Prognon, P. Meso-Tetraphenyl Porphyrin Derivatives: The Effect of Structural Modifications on Binding to DMPC Liposomes and Albumin. *J. Photochem. Photobiol. A Chem.* **2011**, *217*, 10–21.

(156) Vilcheze, C.; Mcmullen, T. P. W.; Mcelhaney, R. N.; Bittman, R. The Effect of Side-Chain Analogues of Cholesterol on the Thermotropic Phase Behavior of 1-Stearoyl-2-Oleoylphosphatidylcholine Bilayers: A Differential Scanning Calorimetric Study. *Biochim. Biophys. Acta*. **1996**, *1279*, 235–242.

(157) Manrique-Moreno, M.; Moreno, M. M.; Garidel, P.; Suwalsky, M.; Howe, J.; Brandenburg, K. The Membrane-Activity of Ibuprofen, Diclofenac, and Naproxen: A Physico-Chemical Study with Lecithin Phospholipids. *Biochim. Biophys. Acta* **2009**, *1788*, 1296–1303.

(158) Manrique-Moreno, M.; Suwalsky, M.; Villena, F.; Garidel, P. Effects of the Nonsteroidal Anti-Inflammatory Drug Naproxen on Human Erythrocytes and on Cell Membrane Molecular Models. *Biophys. Chem.* **2010**, *147*, 53–58.

(159) Manrique-Moreno, M.; Villena, F.; Sotomayor, C. P.; Edwards, A. M.; Muñoz, M. A.; Garidel, P.; Suwalsky, M. Human Cells and Cell Membrane Molecular Models Are Affected in Vitro by the Nonsteroidal Anti-Inflammatory Drug Ibuprofen. *Biochim. Biophys. Acta - Biomembr.* **2011**, *1808*, 2656–2664.

(160) Motomu Tanaka, *,†,‡, §.; Arimatti Jutila, ‡ and; Kinnunen‡, P. K. J. Static and Kinetic Investigations of the Structural Ordering of Phospholipid Membranes Doped with Azobenzene Derivative. **1998**, *102*, 5358–5362.
(161) Cevc, G. *Phospholipids Handbook*, CRC Press, New-York.; **1993**.
(162) Wallgren, M.; Beranova, L.; Pham, Q. D.; Linh, K.; Lidman, M.; Procek, J.; Cyprych, K.; Kinnunen, P. K. J.; Hof, M.; Gröbner, G. Impact of Oxidized Phospholipids on the Structural and Dynamic Organization of Phospholipid Membranes: A Combined DSC and Solid State NMR Study. *Faraday Discuss.* **2013**, *161*, 499–513.
(163) Abdel-Kader, M. H. History of Photodynamic Therapy: From Theory to Application. In *Photodynamic Therapy*; Springer Berlin Heidelberg: Berlin, Heidelberg, **2014**, 3–22.
(164) Neff, W. E.; Frankel, E. N. Quantitative Analyses of Hydroxystearate Isomers from Hydroperoxides by High Pressure Liquid Chromatography of Autoxidized and Photosensitized-Oxidized Fatty Esters. *Lipids* **1980**, *15*, 587–590.
(165) Ehrenberg, B.; Anderson, J. L.; Foote, C. S. Kinetics and Yield of Singlet Oxygen Photosensitized by Hypericin in Organic and Biological Media. *Photochem. Photobiol.* **1998**, *68*, 135–140.
(166) Engelmann, F.; Rocha, S.; Toma, H.; Araki, K.; Baptista, M. Determination of N-Octanol/water Partition and Membrane Binding of Cationic Porphyrins. *Int. J. Pharm.* **2007**, *329*, 12–18.
(167) Aoki, P. H. B.; Morato, L. F. C.; Pavinatto, F. J.; Nobre, T. M.; Constantino, C. J. L.; Oliveira, Jr., O. N. Molecular-Level Modifications Induced by Photo-Oxidation of Lipid Monolayers Interacting with Erythrosin. *Langmuir* **2016**, *32*, 3766–3773.
(168) Daniell, M. D.; Hill, J. S. A History of Photodynamic Therapy. *Aust. N. Z. J. Surg.* **1991**, *61*, 340–348.
(169) Dougherty, T. J.; Gomer, C. J.; Henderson, B. W.; Jori, G.; Kessel, D.; Korbelik, M.; Moan, J.; Peng, Q. Photodynamic Therapy. *J. Natl. Cancer Inst.* **1998**, *90*, 889–905.
(170) Ormond, A. B.; Freeman, H. S. Dye Sensitizers for Photodynamic Therapy. *Materials (Basel).* **2013**, *6*, 817–840.
(171) Bellnier, D. A.; Greco, W. R.; Loewen, G. M.; Nava, H.; Oseroff, A. R.; Dougherty, T. J. Clinical Pharmacokinetics of the PDT Photosensitizers Porfimer Sodium (Photofrin), 2-[1-Hexyloxyethyl]-2-Devinyl Pyropheophorbide-a (Photochlor) and 5-ALA-Induced Protoporphyrin IX. *Lasers Surg. Med.* **2006**, *38*, 439–444.
(172) Halperin, E. C.; Brady, L. W.; Wazer, D. E.; Perez, C. A. *Perez and Brady's Principles and Practice of Radiation Oncology*, sixth edit.; **2013**.
(173) Tan, I. B.; Dolivet, G.; Ceruse, P.; Poorten, V. Vander; Roest, G.; Rauschning, W. Temoporfin-Mediated Photodynamic Therapy in Patients with Advanced, Incurable Head and Neck Cancer: A Multicenter Study. *Head Neck* **2010**, *32*, 1597–1604.
(174) Konan, Y. N.; Gurny, R.; Allémann, E. State of the Art in the Delivery of Photosensitizers for Photodynamic Therapy. *J. Photochem. Photobiol. B.* **2002**, *66*, 89–106.
(175) Sadasivam, M.; Avci, P.; Hamblin, M. R. Self-Assembled Liposomal Nanoparticles in Photodynamic Therapy. **2013**, *193*, 118–125.
(176) Laville, I.; Pigaglio, S.; Blais, J. C.; Doz, F.; Loock, B.; Maillard, P.; Grierson, D. S.; Blais, J. Photodynamic Efficiency of Diethylene Glycol-Linked Glycoconjugated Porphyrins in Human Retinoblastoma Cells. *J. Med. Chem.* **2006**, *49*, 2558–2567.
(177) Ballut, S.; Naud-Martin, D.; Loock, B.; Maillard, P. A Strategy for the Targeting of Photosensitizers. Synthesis, Characterization, and Photobiological Property of Porphyrins Bearing Glycodendrimeric Moieties. *J. Org. Chem.* **2011**, *76*, 2010–2028.
(178) Rapozzi, V.; Zacchigna, M.; Biffi, S.; Garrovo, C.; Cateni, F.; Stebel, M.; Zorzet, S.; Bonora, G. M.; Drioli, S.; Xodo, L. E. Conjugated PDT Drug: Photosensitizing Activity and Tissue Distribution of PEGylated Pheophorbide a. *Cancer Biol. Ther.* **2010**, *10*, 471–482.
(179) Son, J.; Yang, S. M.; Yi, G.; Roh, Y. J.; Park, H.; Park, J. M.; Choi, M.-G.; Koo, H. Folate-Modified PLGA Nanoparticles for Tumor-Targeted Delivery of Pheophorbide a in Vivo. *Biochem. Biophys. Res. Commun.* **2018**, *498*, 523–528.
(180) Zhang, D.; Wu, M.; Zeng, Y.; Wu, L.; Wang, Q.; Han, X.; Liu, X.; Liu, J. Chlorin e6 Conjugated Poly(dopamine) Nanospheres as PDT/PTT Dual-Modal Therapeutic Agents for Enhanced Cancer Therapy. *ACS Appl. Mater. Interfaces* **2015**, *7*, 8176–8187.
(181) Roy, I.; Ohulchanskyy, T. Y.; Pudavar, H. E.; Bergey, E. J.; Oseroff, A. R.; Morgan, J.; Dougherty, T. J.; Prasad, P. N. Ceramic-Based Nanoparticles Entrapping Water-Insoluble Photosensitizing Anticancer Drugs: A Novel Drug−Carrier System for Photodynamic Therapy. *J. Am. Chem. Soc.* **2003**, *125*, 7860–7865.
(182) Záruba, K.; Králová, J.; Řezanka, P.; Poučková, P.; Veverková, L.; Král, V. Modified Porphyrin–brucine Conjugated to Gold Nanoparticles and Their Application in Photodynamic Therapy. *Org. Biomol. Chem.* **2010**, *8*, 3202-3206.
(183) Obaid, G.; Broekgaarden, M.; Bulin, A.-L.; Huang, H.-C.; Kuriakose, J.; Liu, J.; Hasan, T. Photonanomedicine: A Convergence of Photodynamic Therapy and Nanotechnology. *Nanoscale* **2016**, *8*, 12471–12503.
(184) Damoiseau, X.; Schuitmaker, H. J.; Lagerberg, J. W. M.; Hoebeke, M. Increase of the Photosensitizing Efficiency of the Bacteriochlorin a by Liposome-Incorporation. *J. Photochem. Photobiol. B Biol.* **2001**, *60*, 50–60.
(185) Bovis, M. J.; Woodhams, J. H.; Loizidou, M.; Scheglmann, D.; Bown, S. G.; MacRobert, A. J. Improved in Vivo Delivery of M-THPC via Pegylated Liposomes for Use in Photodynamic Therapy. *J. Control. Release* **2012**, *157*, 196–205.

(186) Derycke, A. S. L.; de Witte, P. A. M. Liposomes for Photodynamic Therapy. *Adv. Drug Deliv. Rev.* **2004**, *56*, 17–30.
(187) Jain, R. K. Delivery of Molecular Medicine to Solid Tumors: Lessons from in Vivo Imaging of Gene Expression and Function. *J. Control. Release* **2001**, *74*, 7–25.
(188) Parratt, L. G. Surface Studies of Solids by Total Reflection of X-Rays. *Phys. Rev.* **1954**, *95*, 359–369.
(189) Nelson, A.; IUCr. Co-Refinement of Multiple-Contrast neutron/X-Ray Reflectivity Data Using *MOTOFIT*. *J. Appl. Crystallogr.* **2006**, *39*, 273–276.
(190) Massiot, J.; Makky, A.; Di Meo, F.; Chapron, D.; Trouillas, P.; Rosilio, V. Impact of Lipid Composition and Photosensitizer Hydrophobicity on the Efficiency of Light-Triggered Liposomal Release. *Phys. Chem. Chem. Phys.* **2017**, *19*, 11460–11473.
(191) da Cunha, M. M. L.; Trepout, S.; Messaoudi, C.; Wu, T.-D.; Ortega, R.; Guerquin-Kern, J.-L.; Marco, S. Overview of Chemical Imaging Methods to Address Biological Questions. *Micron* **2016**, *84*, 23–36.
(192) Underwood, T. J.; Derouet, M. F.; White, M. J.; Noble, F.; Moutasim, K. A.; Smith, E.; Drew, P. A.; Thomas, G. J.; Primrose, J. N.; Blaydes, J. P. A Comparison of Primary Oesophageal Squamous Epithelial Cells with HET-1A in Organotypic Culture. *Biol. Cell* **2010**, *102*, 635–644.
(193) Shimada, Y.; Wagata, T.; Yamaguchi, N.; Tobe, T. Characterization of 21 Newly Established Esophageal Cancer Cell Lines. **1992**, *69*, 277–284.
(194) Bolte, S.; Cordelieres, F. P. A Guided Tour into Subcellular Colocalisation Analysis in Light Microscopy. *J. Microsc.* **2006**, *224*, 213–232.
(195) Rosseto, R.; Hajdu, J. Synthesis of Oligo(ethylene Glycol) Substituted Phosphatidylcholines: Secretory PLA2-Targeted Precursors of NSAID Prodrugs. *Chem. Phys. Lipids* **2010**, *163*, 110–116.
(196) Rosseto, R.; Hajdu, J. A Rapid and Efficient Method for Migration-Free Acylation of Lysophospholipids: Synthesis of Phosphatidylcholines with Sn-2-Chain-Terminal Reporter Groups. *Tetrahedron Lett.* **2005**, *46*, 2941–2944.
(197) Edward J. O'Neil; Kristy M. DiVittorio, A.; Smith*, B. D. Phosphatidylcholine-Derived Bolaamphiphiles via Click Chemistry. **2007**, *9*, 199–202.
(198) Bittman, R.; Verbicky, C. a. Methanolysis of Sphingomyelin. Toward an Epimerization-Free Methodology for the Preparation of D-Erythro-Sphingosylphosphocholine. *J. Lipid Res.* **2000**, *41*, 2089–2093.
(199) Israelachvili, J. *Intermolecular and Surface Forces*, third edition, Academic Press, Elsevier, **2011**.
(200) Kumar, V. V. Complementary Molecular Shapes and Additivity of the Packing Parameter of Lipids (chain Length/phase Preference/theory). *Biophysics (Oxf).* **1991**, *88*, 444–448.
(201) Seelig, A. Local Anesthetics and Pressure: A Comparison of Dibucaine Binding to Lipid Monolayers and Bilayers. *Biochim. Biophys. Acta* **1987**, *899*, 196–204.
(202) Fischer, H.; Gottschlich, R.; Seelig, A. Blood-Brain Barrier Permeation: Molecular Parameters Governing Passive Diffusion. *J. Membr. Biol.* **1998**, *165*, 201–211.
(203) Humphrey, W.; Dalke, A.; Schulten, K. VMD: Visual Molecular Dynamics. *J. Mol. Graph.* **1996**, *14*, 33–38.
(204) Davies, J. T.; Rideal, E. K. *Interfacial Phenomena*, Academic Press, New York **1961**.
(205) Griffith, M. J.; James, M.; Triani, G.; Wagner, P.; Wallace, G. G.; Officer, D. L. Determining the Orientation and Molecular Packing of Organic Dyes on a TiO_2 Surface Using X-Ray Reflectometry. *Langmuir* **2011**, *27*, 12944–12950.
(206) Majewski, J.; Kuhl, T. L.; Kjaer, K.; Smith, G. S. Packing of Ganglioside-Phospholipid Monolayers: An X-Ray Diffraction and Reflectivity Study. *Biophys. J.* **2001**, *81*, 2707–2715.
(207) Broniatowski, M.; Dynarowicz-Łatka, P. Search for the Molecular Mechanism of Mercury Toxicity. Study of the Mercury(II)−Surfactant Complex Formation in Langmuir Monolayers. *J. Phys. Chem. B* **2009**, *113*, 4275–4283.
(208) Ropers, M.-H.; Brezesinski, G. Lipid Ordering in Planar 2D and 3D Model Membranes. *Soft Matter* **2013**, *9*, 9440-9448.
(209) Cui, L.; Chen, J.; Zheng, G. Porphyrin Nanoparticles for Cancer Imaging and Phototherapy. *Handb. Photodyn. Ther.* **2016**, 273–293.
(210) Oliveira, C. S.; Turchiello, R.; Kowaltowski, A. J.; Indig, G. L.; Baptista, M. S. Major Determinants of Photoinduced Cell Death: Subcellular Localization versus Photosensitization Efficiency. *Free Radic. Biol. Med.* **2011**, *51*, 824–833.
(211) Thomas, A. P.; Palanikumar, L.; Jeena, M. T.; Kim, K.; Ryu, J.-H. Cancer-Mitochondria-Targeted Photodynamic Therapy with Supramolecular Assembly of HA and a Water Soluble NIR Cyanine Dye. *Chem. Sci.* **2017**, *8*, 8351–8356.
(212) Zhang, C.-J.; Hu, Q.; Feng, G.; Zhang, R.; Yuan, Y.; Lu, X.; Liu, B. Image-Guided Combination Chemotherapy and Photodynamic Therapy Using a Mitochondria-Targeted Molecular Probe with Aggregation-Induced Emission Characteristics. *Chem. Sci.* **2015**, *6*, 4580–4586.
(213) Tang, P. M.-K.; Zhang, D.-M.; Xuan, N.-H. B.; Tsui, S. K.-W.; Waye, M. M.-Y.; Kong, S.-K.; Fong, W.-P.; Fung, K.-P. Photodynamic Therapy Inhibits P-Glycoprotein Mediated Multidrug Resistance via JNK Activation in Human Hepatocellular Carcinoma Using the Photosensitizer Pheophorbide A. *Mol. Cancer* **2009**, *8*, 1-12.

(214) Lee, W.-Y.; Lim, D.-S.; Ko, S.-H.; Park, Y.-J.; Ryu, K.-S.; Ahn, M.-Y.; Kim, Y.-R.; Lee, D. W.; Cho, C.-W. Photoactivation of Pheophorbide a Induces a Mitochondrial-Mediated Apoptosis in Jurkat Leukaemia Cells. *J. Photochem. Photobiol. B Biol.* **2004**, *75*, 119–126.
(215) Wang, J.; Qiu, J. A Review of Organic Nanomaterials in Photothermal Cancer Therapy. *Cancer Res. Front.* **2016**, *2*, 67–84.
(216) Jori, G.; Spikes, J. D. Photothermal Sensitizers: Possible Use in Tumor Therapy. *J. Photochem. Photobiol. B.* **1990**, *6*, 93–101.
(217) Parrish, J. A.; Anderson, R. R.; Harrist, T.; Paul, B.; Murphy, G. F. Selective Thermal Effects with Pulsed Irradiation from Lasers: From Organ to Organelle. *J. Invest. Dermatol.* **1983**, *80*, 75-80.
(218) Zhu, X.; Feng, W.; Chang, J.; Tan, Y.-W.; Li, J.; Chen, M.; Sun, Y.; Li, F. Temperature-Feedback Upconversion Nanocomposite for Accurate Photothermal Therapy at Facile Temperature. *Nat. Commun.* **2016**, *7*, 1-10.
(219) Ng, K. K.; Zheng, G. Molecular Interactions in Organic Nanoparticles for Phototheranostic Applications. *Chem. Rev.* **2015**, *115*, 11012–11042.
(220) Diederich, C. J. Thermal Ablation and High-Temperature Thermal Therapy: Overview of Technology and Clinical Implementation. *Int. J. Hyperth.* **2005**, *21*, 745–753.
(221) Popp, J. *Handbook of Biophotonics*, volume 2.; Wiley-VCH, **2011**.
(222) Park, J.-H.; von Maltzahn, G.; Ong, L. L.; Centrone, A.; Hatton, T. A.; Ruoslahti, E.; Bhatia, S. N.; Sailor, M. J. Cooperative Nanoparticles for Tumor Detection and Photothermally Triggered Drug Delivery. *Adv. Mater.* **2010**, *22*, 880–885.
(223) You, J.; Zhang, G.; Li, C. Exceptionally High Payload of Doxorubicin in Hollow Gold Nanospheres for near-Infrared Light-Triggered Drug Release. *ACS Nano* **2010**, *4*, 1033–1041.
(224) Zou, Q.; Abbas, M.; Zhao, L.; Li, S.; Shen, G.; Yan, X. Biological Photothermal Nanodots Based on Self-Assembly of Peptide-Porphyrin Conjugates for Antitumor Therapy. *J. Am. Chem. Soc.* **2017**, *139*, 1921–1927.
(225) Guo, B.; Feng, G.; Manghnani, P. N.; Cai, X.; Liu, J.; Wu, W.; Xu, S.; Cheng, X.; Teh, C.; Liu, B. A Porphyrin-Based Conjugated Polymer for Highly Efficient In Vitro and In Vivo Photothermal Therapy. *Small* **2016**, *12*, 6243–6254.
(226) Su, S.; Ding, Y.; Li, Y.; Wu, Y.; Nie, G. Integration of Photothermal Therapy and Synergistic Chemotherapy by a Porphyrin Self-Assembled Micelle Confers Chemosensitivity in Triple-Negative Breast Cancer. *Biomaterials* **2016**, *80*, 169–178.
(227) Luo, Y.; Wu, H.; Feng, C.; Xiao, K.; Yang, X.; Liu, Q.; Lin, T. Y.; Zhang, H.; Walton, J. H.; Ajena, Y.; et al. "One-Pot" Fabrication of Highly Versatile and Biocompatible Poly(vinyl Alcohol)-Porphyrin-Based Nanotheranostics. *Theranostics* **2017**, *7*, 3901-3914.
(228) Massiot, J.; Rosilio, V.; Ibrahim, N.; Yamamoto, A.; Nicolas, V.; Konovalov, O.; Tanaka, M.; Makky, A. Synthesis and Characterization of New Lipid-Porphyrin Conjugates as Efficient and Selective Agents for Photodynamic Therapy. *Chem. Sci.* **2018**, *submitted*.
(229) Israelachvili, J. N.; Mitchell, D. J.; Ninham, B. W. Theory of Self-Assembly of Hydrocarbon Amphiphiles into Micelles and Bilayers. *J. Chem. Soc. Faraday Trans. 2* **1976**, *72*, 1525-1568.
(230) Israelachvili, J. N.; Ninham, B. W. Theory of Self-Assembly of Lipid Bilayers and Vesicles. **1977**, *470*, 185–201.
(231) Lasic, D. D.; Martin, F. J. *Stealth Liposomes*; CRC Press, **1995**.
(232) Lasic, D. D.; Papahadjopoulos, D. *Medical Applications of Liposomes*; Elsevier, **1998**.
(233) Torchilin, V. P.; Omelyanenko, V. G.; Papisov, M. I.; Bogdanov, A. A.; Trubetskoy, V. S.; Herron, J. N.; Gentry, C. A. Poly(ethylene Glycol) on the Liposome Surface: On the Mechanism of Polymer-Coated Liposome Longevity. *Biochim. Biophys. Acta - Biomembr.* **1994**, *1195*, 11–20.
(234) Allen, T. M. Stealth Liposomes: Five Years On. *J. Liposome Res.* **1992**, *2*, 289–305.
(235) Nicholas, A. R.; Scott, M. J.; Kennedy, N. I.; Jones, M. N. Effect of Grafted Polyethylene Glycol (PEG) on the Size, Encapsulation Efficiency and Permeability of Vesicles. *Biochim. Biophys. Acta - Biomembr.* **2000**, *1463*, 167–178.
(236) Nikolova, A. N.; Jones, M. N. Effect of Grafted PEG-2000 on the Size and Permeability of Vesicles. *Biochim. Biophys. Acta - Lipids Lipid Metab.* **1996**, *1304*, 120–128.
(237) Kenworthy, A. K.; Hristova, K.; Needham, D.; McIntosh, T. J. Range and Magnitude of the Steric Pressure between Bilayers Containing Phospholipids with Covalently Attached Poly(ethylene Glycol). *Biophys. J.* **1995**, *68*, 1921–1936.
(238) Garbuzenko, O.; Barenholz, Y.; Priev, A. Effect of Grafted PEG on Liposome Size and on Compressibility and Packing of Lipid Bilayer. *Chem. Phys. Lipids* **2005**, *135*, 117–129.
(239) Allen, C.; Dos Santos, N.; Gallagher, R.; Chiu, G. N. C.; Shu, Y.; Li, W. M.; Johnstone, S. A.; Janoff, A. S.; Mayer, L. D.; Webb, M. S.; et al. Controlling the Physical Behavior and Biological Performance of Liposome Formulations through Use of Surface Grafted Poly(ethylene Glycol). *Biosci. Rep.* **2002**, *22*, 225–250.
(240) Belsito, S.; Bartucci, R.; Sportelli, L. Lipid Chain Length Effect on the Phase Behaviour of PCs/PEG:2000-PEs Mixtures. A Spin Label Electron Spin Resonance and Spectrophotometric Study. *Biophys. Chem.* **2001**, *93*, 11–22.
(241) Hafez, I. M.; Cullis, P. R. Cholesteryl Hemisuccinate Exhibits pH Sensitive Polymorphic Phase Behavior. *Biochim. Biophys. Acta*. **2000**, *1463*, 107–114.

(242) Lai, M. Z.; Duzgunes, N.; Szoka, F. C. Effects of Replacement of the Hydroxyl Group of Cholesterol and Tocopherol on the Thermotropic Behavior of Phospholipid Membranes. *Biochemistry* **1985**, *24*, 1646–1653.
(243) Monteiro, L. O. F.; Malachias, Â.; Pound-Lana, G.; Magalhães-Paniago, R.; Mosqueira, V. C. F.; Oliveira, M. C.; de Barros, A. L. B.; Leite, E. A. Paclitaxel-Loaded pH-Sensitive Liposome: New Insights on Structural and Physicochemical Characterization. *Langmuir* **2018**, *34*, 5728–5737.
(244) Cui, Z. K.; Bouisse, A.; Cottenye, N.; Lafleur, M. Formation of pH-Sensitive Cationic Liposomes from a Binary Mixture of Monoalkylated Primary Amine and Cholesterol. *Langmuir* **2012**, *28*, 13668–13674.
(245) Huang, C.; Mason, J. T. Geometric Packing Constraints in Egg Phosphatidylcholine Vesicles. *Proc. Natl. Acad. Sci. U. S. A.* **1978**, *75*, 308–310.
(246) Newman, G. C.; Huang, C.-H. Structural Studies on Phosphatidylcholine-Cholesterol Mixed Vesicles. *Biochemistry* **1975**, *14*, 3363–3370.
(247) Burke, L. I.; Patil, G. S.; Panganamala, R. V; Geer, J. C.; Cornwell, D. G. Surface Areas of Naturally Occurring Lipid Classes and the Quantitative Microdetermination of Lipids. *J. Lipid Res.* **1973**, *14*, 9–15.
(248) Slotte, J. P.; Mattjus, P. Visualization of Lateral Phases in Cholesterol and Phosphatidylcholine Monolayers at the Air/water Interface — a Comparative Study with Two Different Reporter Molecules. *Biochim. Biophys. Acta - Lipids Lipid Metab.* **1995**, *1254*, 22–29.
(249) Allen, T. M.; Cullis, P. R. Liposomal Drug Delivery Systems: From Concept to Clinical Applications. *Adv. Drug Deliv. Rev.* **2013**, *65*, 36–48.
(250) Bulbake, U.; Doppalapudi, S.; Kommineni, N.; Khan, W. Liposomal Formulations in Clinical Use: An Updated Review. *Pharmaceutics* **2017**, *9*, 1-33.
(251) Li, J.; Wang, X.; Zhang, T.; Wang, C.; Huang, Z.; Luo, X.; Deng, Y. A Review on Phospholipids and Their Main Applications in Drug Delivery Systems. *Asian J. Pharm. Sci.* **2015**, *10*, 81–98.
(252) Mabrey, S.; Sturtevant, J. M. Investigation of Phase Transitions of Lipids and Lipid Mixtures by High Sensitivity Differential Scanning Calorimetry. *Proc. Natl. Acad. Sci. USA* **1976**, *73*, 3862–3866.
(253) Bozzuto, G.; Molinari, A. Liposomes as Nanomedical Devices. *Int. J. Nanomedicine* **2015**, *10*, 975-999.
(254) Guha, S.; Shaw, S. K.; Spence, G. T.; Roland, F. M.; Smith, B. D. Clean Photothermal Heating and Controlled Release From Near Infrared Dye Doped Nanoparticles Without Oxygen Photosensitization. *Langmuir* **2015**, *31*, 7826–7834.
(255) Ng, K. K.; Weersink, R. A.; Lim, L.; Wilson, B. C.; Zheng, G. Controlling Spatial Heat and Light Distribution by Using Photothermal Enhancing Auto-Regulated Liposomes (PEARLs). *Angew. Chemie - Int. Ed.* **2016**, *55*, 10003–10007.
(256) Lovell, J. F.; Jin, C. S.; Huynh, E.; MacDonald, T. D.; Cao, W.; Zheng, G. Enzymatic Regioselection for the Synthesis and Biodegradation of Porphysome Nanovesicles. *Angew. Chemie - Int. Ed.* **2012**, *51*, 2429–2433.
(257) Sargis, R. M.; Subbaiah, P. V. *Trans* Unsaturated Fatty Acids Are Less Oxidizable than *Cis* Unsaturated Fatty Acids and Protect Endogenous Lipids from Oxidation in Lipoproteins and Lipid Bilayers †. *Biochemistry* **2003**, *42*, 11533–11543.
(258) Sargis, R. M.; Subbaiah, P. V. Protection of Membrane Cholesterol by Sphingomyelin against Free Radical-Mediated Oxidation. *Free Radic. Biol. Med.* **2006**, *40*, 2092–2102.
(259) Oborina, E. M.; Yappert, M. C. Effect of Sphingomyelin versus Dipalmitoylphosphatidylcholine on the Extent of Lipid Oxidation. *Chem. Phys. Lipids* **2003**, *123*, 223–232.
(260) Ayuyan, A. G.; Cohen, F. S. Lipid Peroxides Promote Large Rafts: Effects of Excitation of Probes in Fluorescence Microscopy and Electrochemical Reactions during Vesicle Formation. *Biophys. J.* **2006**, *91*, 2172–2183.
(261) Björkbom, A.; Róg, T.; Kaszuba, K.; Kurita, M.; Yamaguchi, S.; Lönnfors, M.; Nyholm, T. K. M.; Vattulainen, I.; Katsumura, S.; Slotte, J. P. Effect of Sphingomyelin Headgroup Size on Molecular Properties and Interactions with Cholesterol. *Biophys. J.* **2010**, *99*, 3300–3308.
(262) van Duyl, B. Y.; Ganchev, D.; Chupin, V.; de Kruijff, B.; Killian, J. A. Sphingomyelin Is Much More Effective than Saturated Phosphatidylcholine in Excluding Unsaturated Phosphatidylcholine from Domains Formed with Cholesterol. *FEBS Lett.* **2003**, *547*, 101–106.
(263) Goscinski, M. A.; Suo, Z. H. E.; Nesland, J. M.; Florenes, V. A. N. N.; Giercksky, K. E.; Florenes, V. A.; Giercksky, K. E. Dipeptidyl Peptidase IV Expression in Cancer and Stromal Cells of Human Esophageal Squamous Cell Carcinomas, Adenocarcinomas and Squamous Cell Carcinoma Cell Lines. *Apmis* **2008**, *116*, 823–831.
(264) Roller, S.G., *Peptide-Based Drug Discovery: Challenges and New Therapeutics*; **2017**, *8*, 223-251
(265) Barenholz, Y. Sphingomyelin and Cholesterol: From Membrane Biophysics and Rafts to Potential Medical Applications. *Subcell. Biochem.* **2004**, *37*, 167–215.
(266) Habash, R. W. Y.; Bansal, R.; Krewski, D.; Alhafid, H. T. Thermal Therapy, Part 1: An Introduction to Thermal Therapy. *Crit. Rev. Biomed. Eng.* **2006**, *34*, 459–489.
(267) Wust, P.; Hildebrandt, B.; Sreenivasa, G.; Rau, B.; Gellermann, J.; Riess, H.; Felix, R.; Schlag, P. M. Hyperthermia in Combined Treatment of Cancer. *Lancet. Oncol.* **2002**, *3*, 487–497.
(268) Schaaf, L.; Schwab, M.; Ulmer, C.; Heine, S.; Mu rdter, T. E.; Schmid, J. O.; Sauer, G.; Aulitzky, W. E.; van der Kuip, H. Hyperthermia Synergizes with Chemotherapy by Inhibiting PARP1-Dependent DNA Replication Arrest. *Cancer Res.* **2016**, *76*, 2868–2875.

(269) Morton, J. G.; Day, E. S.; Halas, N. J.; West, J. L. Nanoshells for Photothermal Cancer Therapy. In *Methods in molecular biology*, **2010**, *624*, 101–117.
(270) Jelveh, S.; Chithrani, D. B. Gold Nanostructures as a Platform for Combinational Therapy in Future Cancer Therapeutics. *Cancers (Basel).* **2011**, *3*, 1081–1110.
(271) Soo Choi, H.; Liu, W.; Misra, P.; Tanaka, E.; Zimmer, J. P.; Itty Ipe, B.; Bawendi, M. G.; Frangioni, J. V. Renal Clearance of Quantum Dots. *Nat. Biotechnol.* **2007**, *25*, 1165–1170.

Appendix I: Immunoblotting protocol

Frozen cell pellets were lysed in cold TGH buffer (1% Triton X-100, 10% glycerol, 10 mM HEPES, pH=7.4, 150 mM NaCl) supplemented with protease inhibitor (Sigma Aldrich). After 30 min of incubation on ice, samples were centrifuge for 5 min at 10 000 rpm to remove insoluble material and the supernatant was collected. The total protein concentration was quantified using BCA protein assay kit (Thermoscientific, Pierce). 30 mg of proteins were then boiled for 10 min in presence of Laemmli buffer containing β-mercaptoethanol. SDS-PAGE was performed using precast gels (4–20% acrylamide, Biorad, France), at 150–200 V for about one hour. Proteins were then transferred to PVDF membranes. After 1 hour blocking in 5% non-fat dry milk in TBST buffer (Tris buffer saline containing 0.1% Tween) at room temperature, the membranes were incubated with either anti-human DPPIV antibody (R&D Systems, Minneapolis, MN; polyclonal Goat IgG), or with monoclonal anti-Actin antibody (clone AC-40, Sigma Aldrich, Saint Louis, MO, USA), both at a 1:1000 dilution in 5% milk in TBST, at 4°C overnight in a sealed bag. The membranes were then washed 5 times for 10 min in TBST at room temperature before incubation with the appropriate secondary antibody (donkey anti-goat and goat anti-mouse for DPPIV and Actin respectively, both diluted to 1:2000 in 5% milk in TBST); for one hour at room temperature. After washing 5 times for 10 min in TBST, the membrane was incubated 5 min with a chemiluminescent detection solution (Clarity^{TM} Western ECL substrate, BioRad). Chemiluminescent signals were analyzed using the MF ChemiBis system (Berthold, Pforzheim, Germany).

Appendix II: Supplementary Figures and Tables

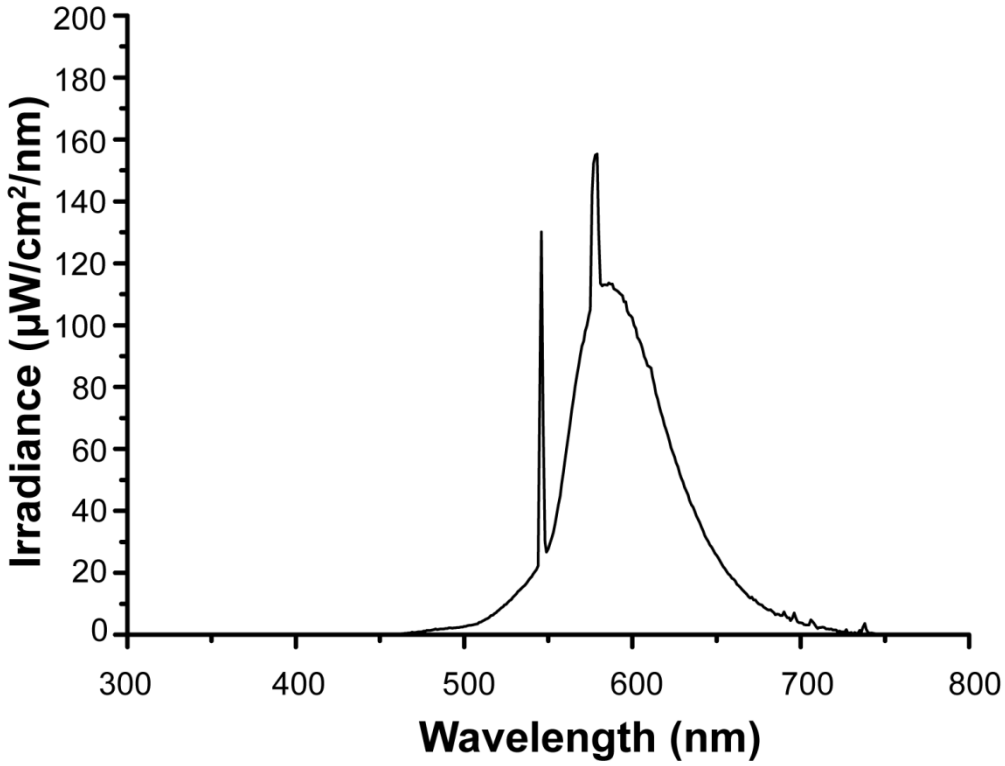

Figure S2.1. Spectral irradiance of the light source used in this study.

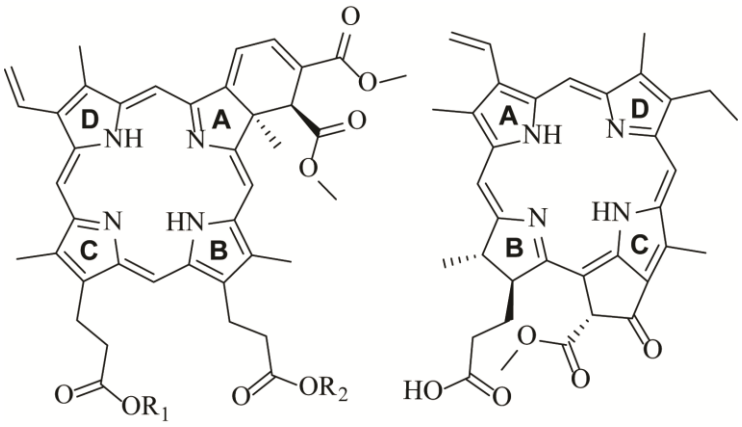

R_1=H, R_2=CH_3 **Verteporfin C**
R_1=CH_3, R_2=H **Verteporfin D**

Pheophorbide a

Figure S2.2. Pyrrol labels of verteporfin and pheophorbide-a

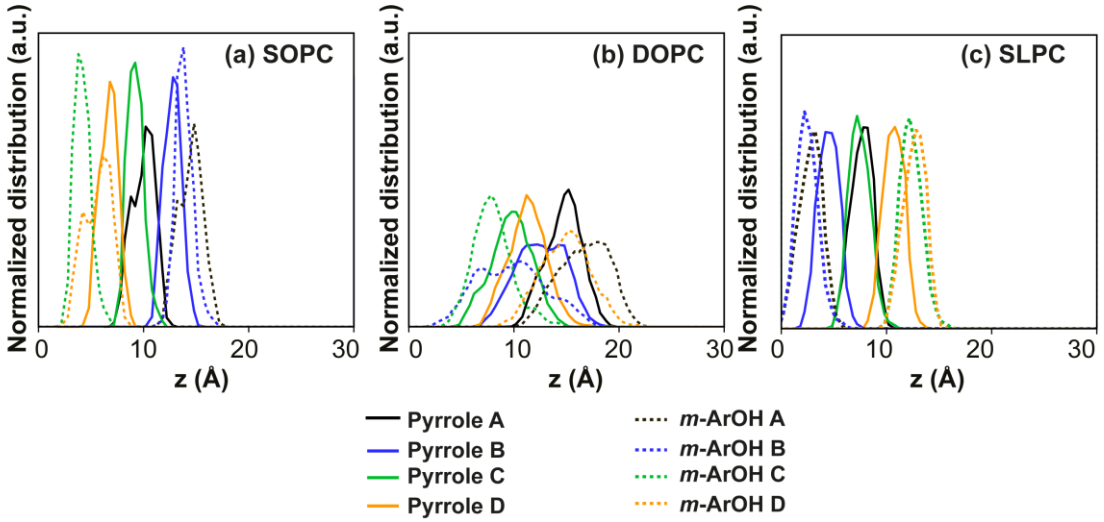

Figure S2.3. Distribution of m-THPP moiety positions along z-axis in (a) SOPC, (b) DOPC and (c) SLPC.

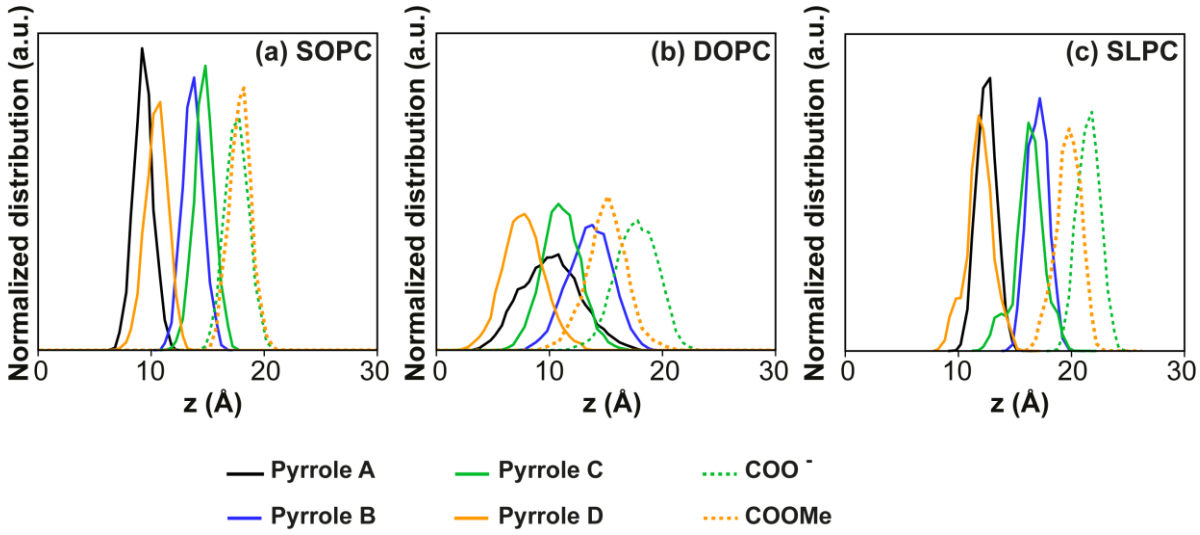

Figure S2.4. Distribution of pheophorbide a moiety positions along z-axis in (a) SOPC, (b) DOPC and (c) SLPC.

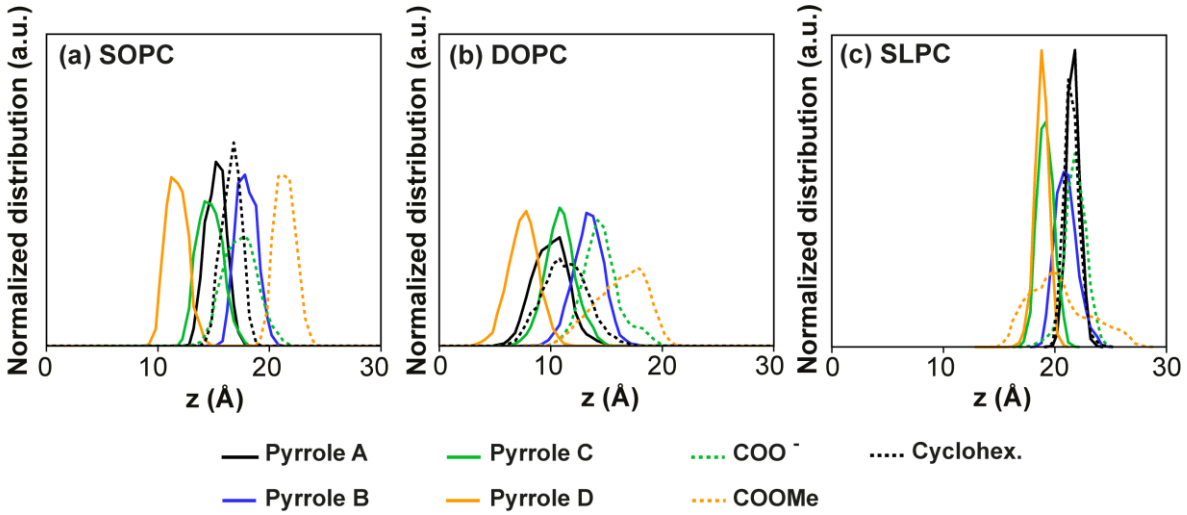

Figure S2.5. Distribution of verteporfin MAC moiety positions along z-axis in (a) SOPC, (b) DOPC and (c) SLPC.

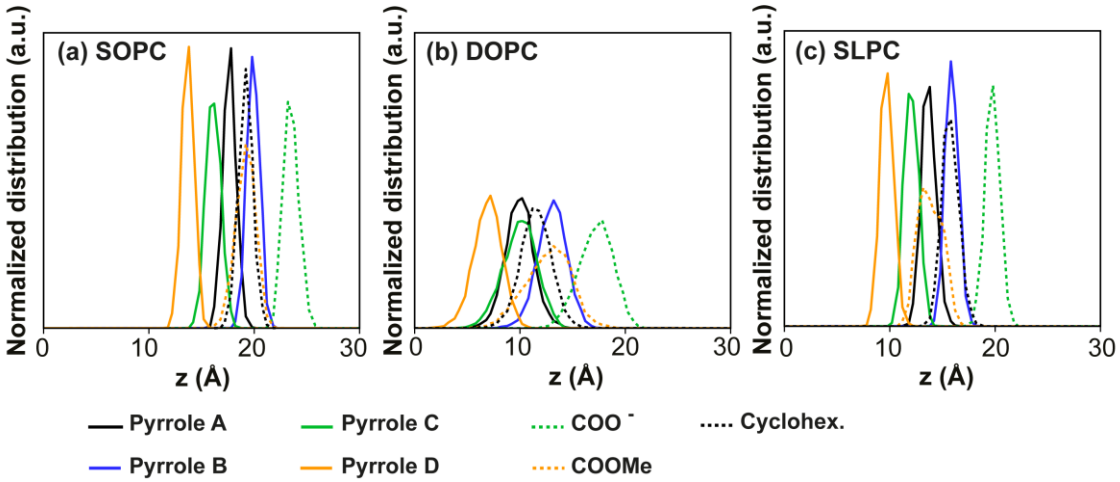

Figure S2.6. Distribution of verteporfin MAD moiety positions along z-axis in (a) SOPC, (b) DOPC and (c) SLPC.

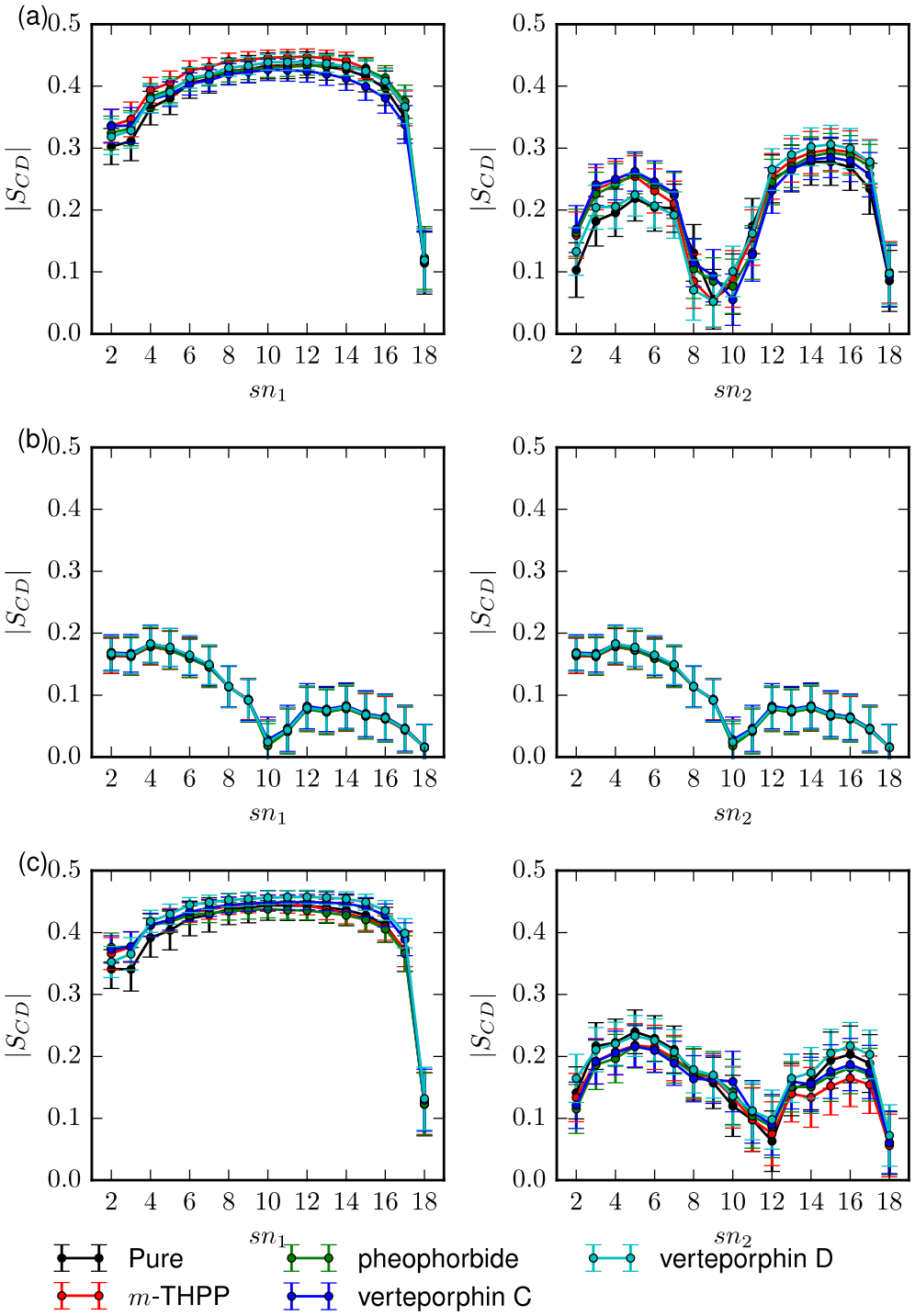

Figure S2.7. Calculated sn-1 lipid order profiles of (a) SOPC, (b) DOPC and (c) SLPC from MD simulations.

	SOPC		DOPC		SLPC	
	$<A>$	$\sigma_{<A>}$	$<A>$	$\sigma_{<A>}$	$<z>$	$\sigma_{<A>}$
Pure	57.9	0.9	68.4	1.5	61.6	1.2
m-THPP	55.2	0.6	68.8	1.6	60.7	0.7
Pheophorbide a	58.0	0.4	69.1	1.6	59.8	0.5
Verteporfin C	54.9	0.6	69.0	1.6	59.0	0.6
Verteporfin D	56.8	0.5	69.0	1.7	60.4	0.4

Table S2.1. Area per lipid ($<A>$, in Å²) and standard deviation ($\sigma_{<A>}$, in Å²) of *m*-THPP, pheophorbide a, verteporfin C and D in SOPC, DOPC and SLPC lipid bilayer membranes. The origin is defined to the center of the membrane.

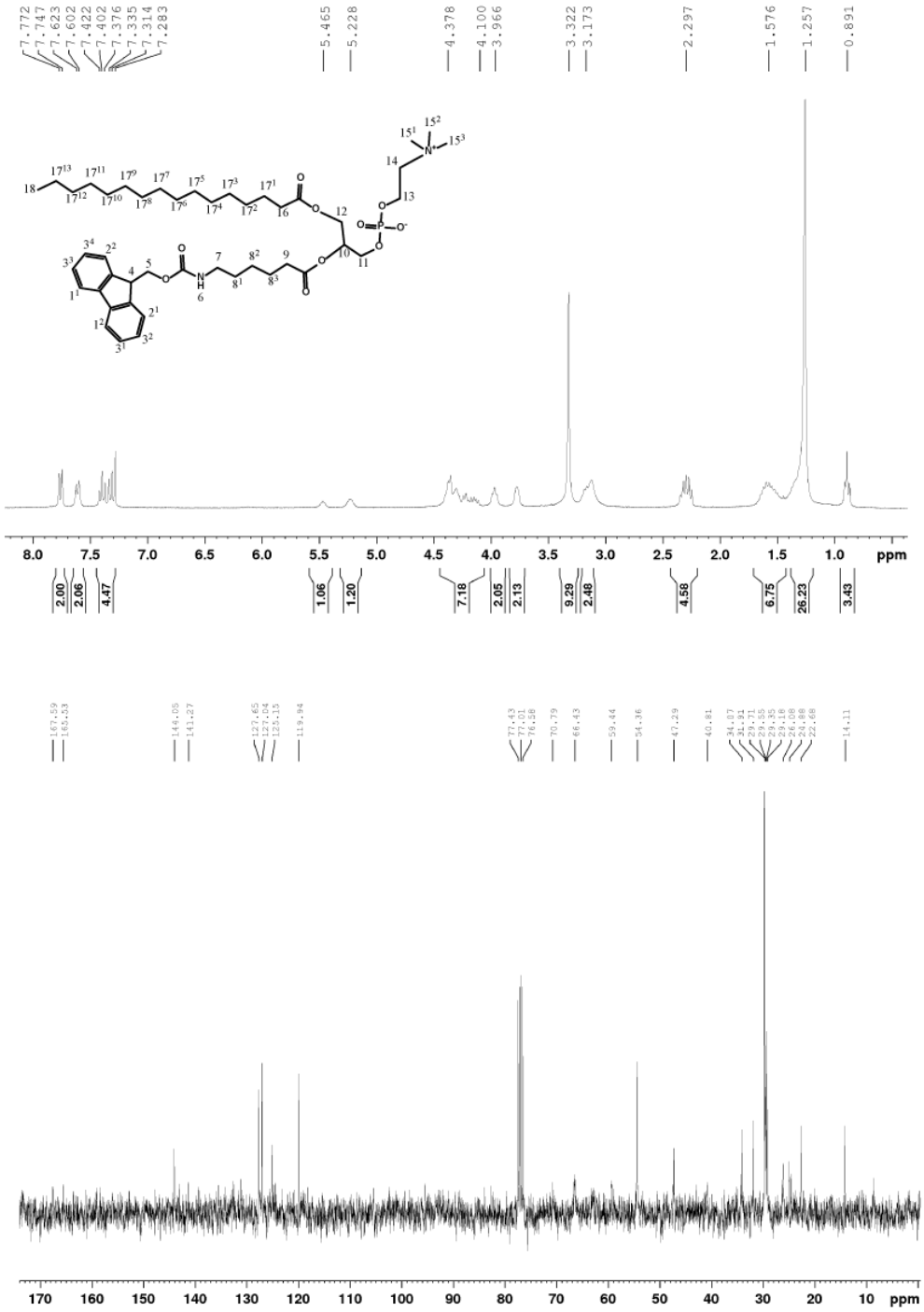

Figure S3.1. NMR characterization of compound 1
^{1}H NMR ($CDCl_3$, 300 MHz) δ (ppm) 7.76 (d, 2H, 1^1-H, 1^2-H, *J* = 7.5 Hz), 7.61 (d, 2H, 2^1-H, 2^2-H, *J* = 7.1 Hz), 7.42 (m, 4H, 3^1-3^4-H, *overlapped partially with CDCl$_3$*), 5.46 (br s, 1H, 6-N*H*), 5.23 (m, 1H, 10-H), 4.38-4.10 (br m, 7H, 4-H, 5-CH_2, 10-CH_2, 11-CH_2), 3.96 (m, 2H, 13-CH_2), 3.77 (br m, 2H, 14-CH_2), 3.32 (s, 9H, 15^1-15^3 3xCH_3), 3.17 (m, 2H, 7-CH_2), 2.29 (m, 4H, 9-CH_2, 16-CH_2), 1.58 (m, 6H, 8^1-CH_2, 8^3-CH_2, 17^1-CH_2), 1.26 (br s, 26H, 8^2-CH_3, 17^2-17^{13} 12xCH_3), 0.87 (t, 3H, 18-CH_3, *J* = 6.5 Hz); ^{13}C NMR ($CDCl_3$, 75 MHz) δ (ppm) 167.59, 165.52, 144.04, 141.26, 127.64, 127.03, 125.14, 119.93, 70.72, 66.33, 59.37,54.37,47.29, 40.81, 34.08, 31.91, 29.71 (br), 29.36 29.18, 26.11, 24.89, 22.68, 14.11

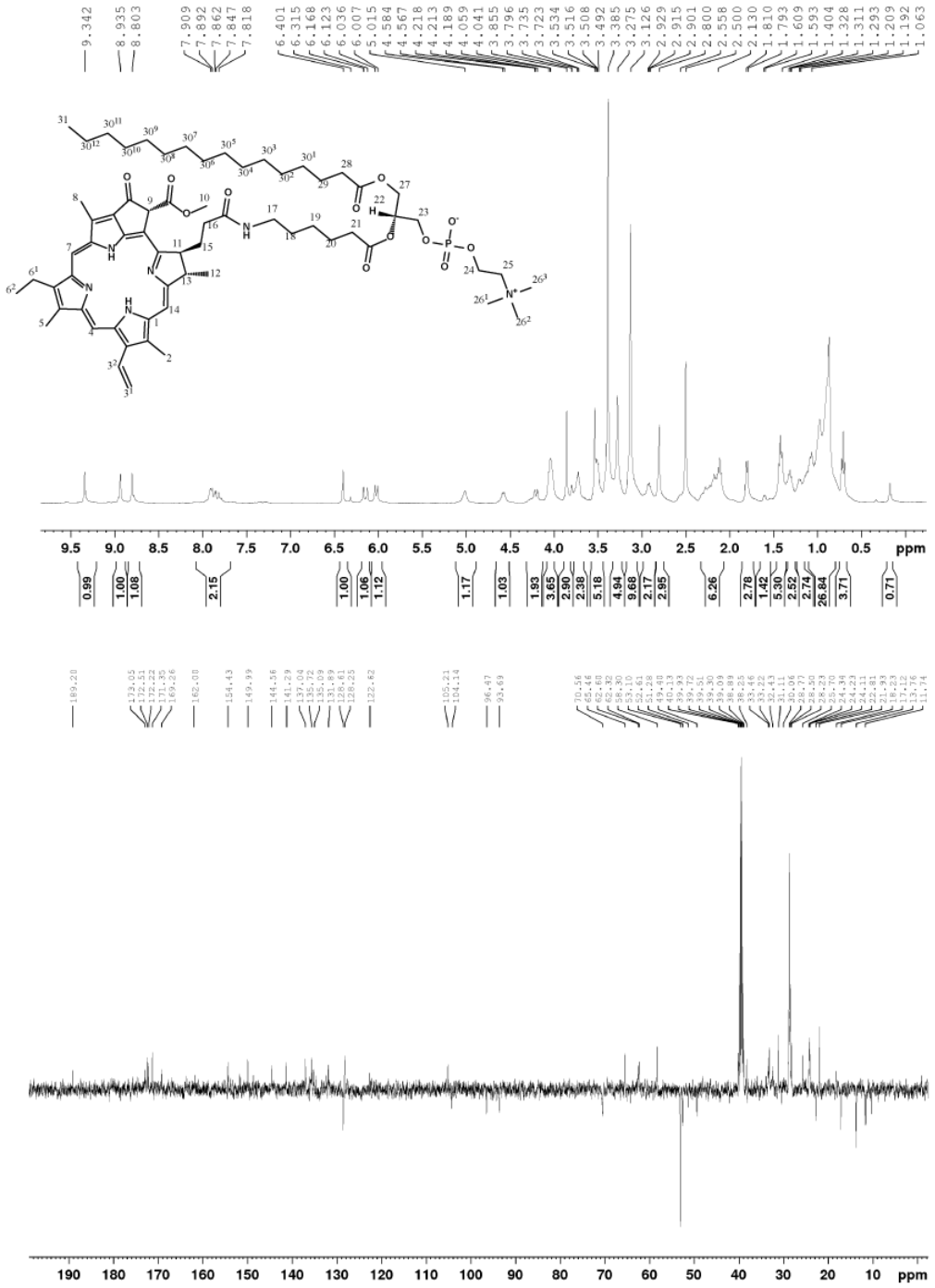

Figure S3.2. NMR characterization of Compound 2 (PhLPC).
^{1}H NMR (DMSO-d_6, 400MHz) δ (ppm) 9.34 (s, 1H, 7-H), 8.93 (s, 1H, 4-H), 8.80 (s, 1H, 14-H), 7.86 (m, 1H, 3^2-C*H*=CH_2), 6.40 (s, 1H, 9-H), 6.15 (m, 1H, cis 3^1-CH=C*H*H), 6.03 (bd, 1H, trans 3^2-CH=CH*H*, *J* = 11.5 Hz), 5.01 (b s, 1H, 22-H), 4.58 (d, 1H, 13-H, *J* = 6.9 Hz), 4.19 (d, 2H, 23-CH_2, *J* = 9.3 Hz), 4.05 (br m, 3H, 24-CH_2, 11-H), 3.86 (s, 3H, 10-CH_3), 3.72 (br m, 2H, 27-CH_2), 3.50 (m, 5H, 25-CH_2, 8-CH_3), 3.27 (br s, 5H, 6^1-CH_2, 2-CH_3), 3.13 (s, 9H, 26^1-26^3 3xCH_3), 2.91 (br m, 2H, 17-CH_2), 2.80 (s, 3H, 5-CH_3), 2.11 (br m, 6H, 15-CH_2, 21-CH_2, 28-CH_2), 1.81 (d, 3H, 12-CH_3, *J* = 6.9 Hz), 1.60 (m, 2H, 16-CH_2), 1.42 (m, 5H, 62-CH_3, 20-CH_2), 1.31 (m, 2H, 29-CH_2), 1.08 (m, 2H, 18-CH_2),1.06-0.85 (br s, 26H, 19-CH_2, 30^1-30^{12} 12xCH_2), 0.706 (t, 3H, 31-CH_3, *J* = 7.1 Hz), 0.17 (s, 1H, -N*H*); ^{13}C NMR (DMSO-d_6, 100MHz) δ (ppm) 189.18, 173.05, 172.52, 172.23, 171.36, 169.27, 161.90, 154.43, 150.00, 148.70, 144.57, 141.30, 137.05, 135.72, 135.10, 131.89, 128.62 (CH), 128.26, 122.80, 105.21, 104.20 (CH), 96.48 (CH), 93.70 (CH), 70.57 (CH), 65.47, 64.30, 62.60, 62.33, 58.30, 53.10 (3xCH3), 52.62 (CH3), 51.30 (CH), 49.41 (CH), 38.26, 33.22, 32.47, 31.12, 28.78, 28.51, 28.24, 25.71, 24.24, 24.10, 22.82 (CH3), 21.94, 18.31, 17.13 (CH3), 13.77 (CH3), 11.75 (CH3), 11.53 (CH3), 10.36 (CH3)

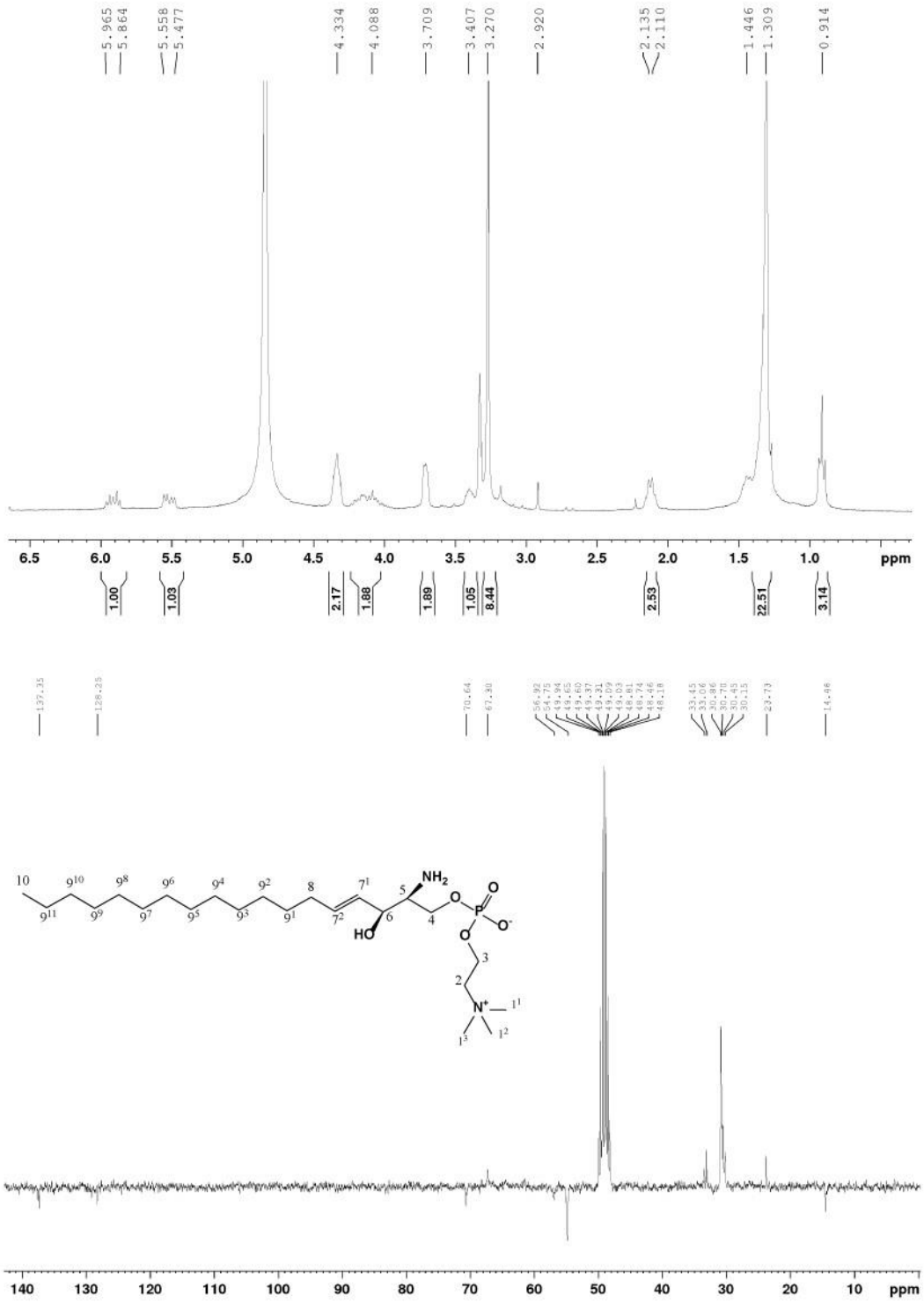

Figure S3.3. NMR characterization of Compound 3.
^{1}H NMR (MeOD, 300 MHz) δ (ppm) 5.86-5.96 (m, 1H, 7^{1}-C*H*), 5.51 (dd, 1H, 7^{2}-C*H*, *J* = 15.2, 6.6 Hz), 4.33 (m, 2H, 2-CH_2), 4.08 (br m, 3H, 4-CH_2, 6-H), 3.71 (br s, 2H, 3-CH_2), 3.40 (br s, 1H, 5-H), 3.27 (s, 9H, 1^{1}-1^{3}, 3xCH_3), 2.11 (m, 2H, 8-CH_2), 1.45 (br m, 2H, NH_2), 1.30 (br s, 22H, 9^{1}-9^{11} 11xCH_3) , 0.91 (t, 3H, 10-CH_3, *J* = 6.6 Hz); ^{13}C NMR (MeOD, 75 MHz) δ (ppm) 137.29 (CH), 128.25 (CH), 70.66 (CH), 67.31, 56.92 (CH), 54.79 (3xCH3), 33.45, 33.07, 30.80, 30.66, 30.46, 30.17, 23.74, 14.46 (CH3)

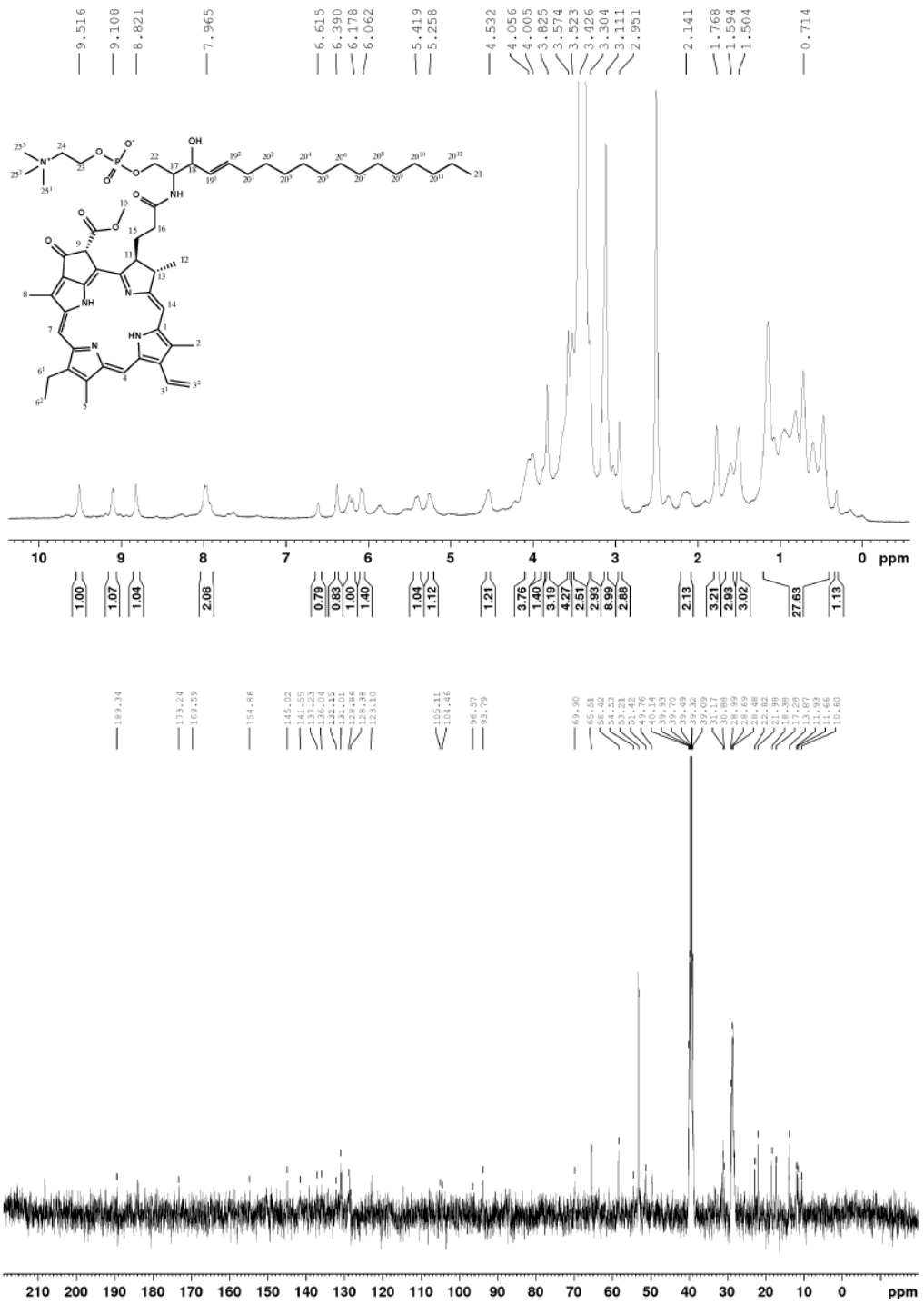

Figure S3.4. NMR characterization of Compound 4 (PhLSM).
^{1}H NMR (DMSO-d_6, 400 MHz) δ (ppm) 9.51 (s, 1H, 7-H), 9.11 (s, 1H, 4-H), 8.82 (s, 1H, 14-H), 7.96 (m, 1H, 3^1-C*H*=CH$_2$), 6.61 (s, 1H, -OH), 6.38 (s, 1H, 9-H), 6.18 (m, 1H, cis 3^2-CH=C*H*H, *J* = 18 Hz), 6.06 (m, 1H, trans 3^2-CH=CH*H*), 5.42 (br m, 1H, 19^2-H), 5.26 (br m, 1H, 19^1-H), 4.53 (br s, 1H, 13-H), 4.05-4.01 (br m, 3H, 23-CH_2, 11-H), 3.87 (br m, 1H, 18-H), 3.83 (s, 3H, 10-CH_3), 3.57 (s, 3H, 8-CH_3), 3.52 (s, 2H, 24-CH_2), 3.44-3.40 (br, m, 4H, 16-CH_2, 22CH_2, *overlapped partially with D$_2$O of DMSO-d$_6$*), 3.31 (s, 3H, 2-CH_3), 3.11 (s, 9H, 25^1-25^3, 3xC*H*3), 2.95 (s, 3H, 5-CH_3), 2.14 (br, m, 2H, 15-CH_2), 1.75 (s, 3H, 12-CH_3), 1.59-1.61 (br, m, 3H, 17-H, 6^1-CH_2), 1.50 (s, 3H, 6^2-CH_3), 1.20-0.50 (br, m, 27H, 21-CH_3, 20^1-20^{12} 12xCH_2), 0.30 (br s, 1H); ^{13}C NMR (DMSO-d_6, 100 MHz) δ (ppm) 189.34, 173.24, 169.59, 155.52, 154.57, 145.02, 141.55, 137.23, 136.04, 135.36, 132.07, 132.01, 131.03, 130.72, 128.80, 128.41, 123.09, 105.11, 104.46, 96.57, 93.79, 69.90, 65.51, 58.42, 54.53, 53.21, 52.66, 51.42, 49.76, 31.17, 30.88, 28.69, 22.82, 21.98, 21.84, 18.38, 17.28, 13.87, 11.93, 11.66, 10.60;

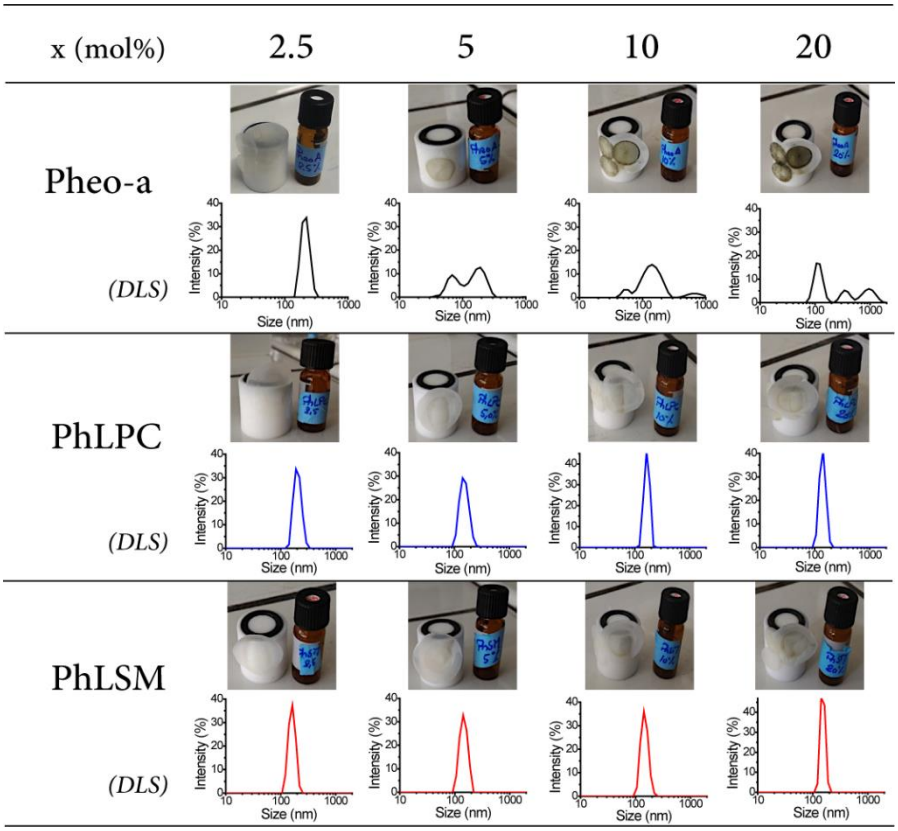

Figure S3.5. Dynamic light scattering profiles of PEGylated DSPC liposomes incorporating different molar percentage of photosensitizer. Pictures of the polycarbonate membrane retaining PSs after liposomes extrusion.

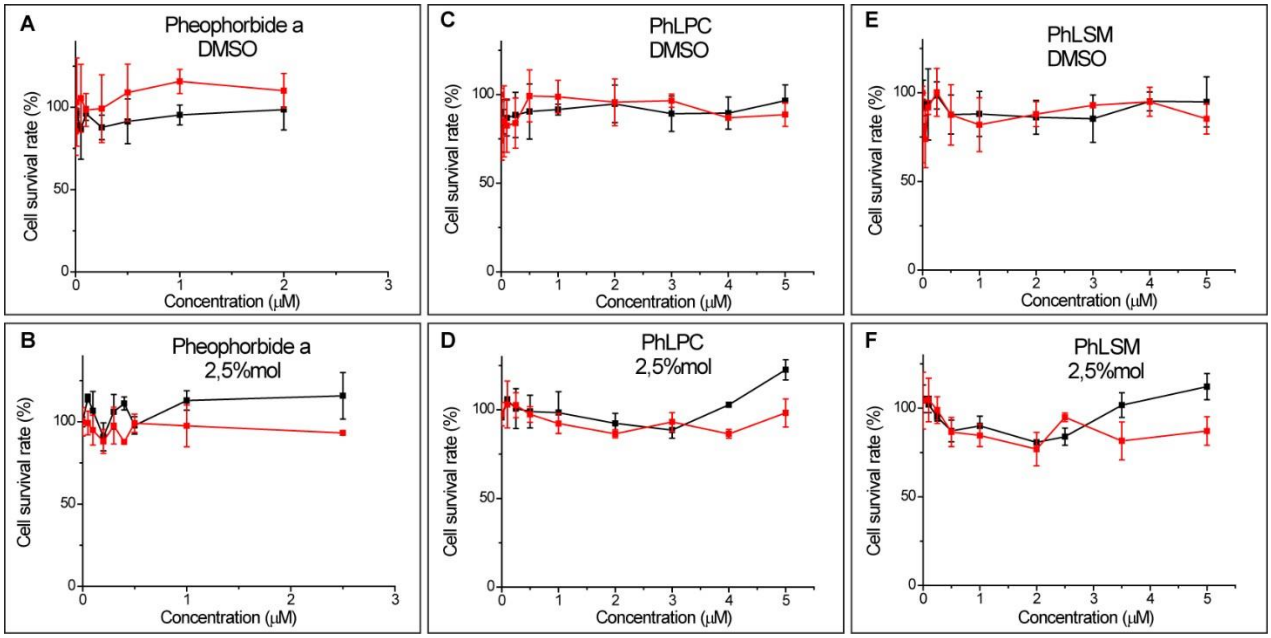

Figure S3.6. Dark cytotoxicity of free or incorporated PSs into PEGylated DSPC liposomes on HET-1A (black line) and Kyse-30 (red line). The error bars are the standard deviations (n = 3).

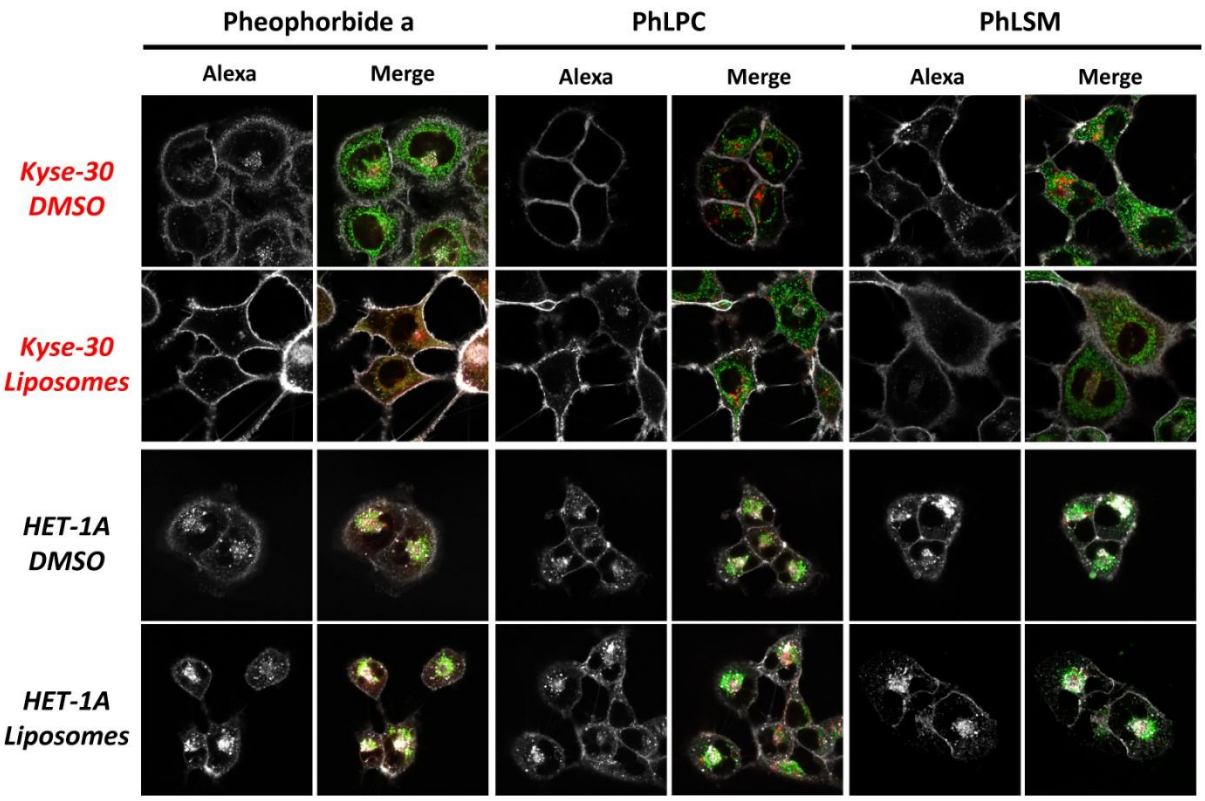

Figure S3.7. Confocal microscopy images of Kyse-30 cells and HET-1A treated with either free photosensitizers (red) dissolved in DMSO or incorporated into liposomes. The first column of each compound represents the membrane coloration with WGA Alexa Fluor 555. The second column for each compound corresponds to the merged images with those in the presence of Mitotracker (green) and PS (red).

Appendix III: Publication

Publication 1. Massiot, J.; Makky, A.; Di Meo, F.; Chapron, D.; Trouillas, P.; Rosilio, V. Impact of Lipid Composition and Photosensitizer Hydrophobicity on the Efficiency of Light-Triggered Liposomal Release. *Phys. Chem. Chem. Phys.* **2017**, *19* (18), 11460–11473

PCCP

PAPER

View Article Online
View Journal

Cite this: DOI: 10.1039/c7cp00983f

Impact of lipid composition and photosensitizer hydrophobicity on the efficiency of light-triggered liposomal release†

Julien Massiot,[a] Ali Makky,*[a] Florent Di Meo,*[b] David Chapron,[a] Patrick Trouillas[bc] and Véronique Rosilio[a]

Received 14th February 2017,
Accepted 31st March 2017

DOI: 10.1039/c7cp00983f

rsc.li/pccp

Photo-triggerable liposomes are considered nowadays as promising drug delivery devices due to their potential to release encapsulated drugs in a spatial and temporal manner. In this work, we have investigated the photopermeation efficiency of three photosensitizers (PSs), namely verteporfin, pheophorbide a and *m*-THPP when incorporated into liposomes with well-defined lipid compositions (SOPC, DOPC or SLPC). By changing the nature of phospholipids and PSs, the illumination of the studied systems was shown to significantly alter their lipid bilayer properties *via* the formation of lipid peroxides. The system efficiency depends on the PS/phospholipid association, and the ability of the PS to peroxidize acyl chains. Our results demonstrated the possible use of these three clinically approved (or under investigation) PSs as potential candidates for photo-triggerable liposome conception.

Introduction

Photo-triggered release of encapsulated drugs from liposomes is currently considered as a potential and interesting modality for drug delivery in a controlled manner.[1,2] Indeed, photosensitive liposomes are nanocarriers that can be activated upon illumination at a specific wavelength to release their cargo.[3,4] Several photo-triggering methods have been proposed for the conception of liposome-based nanomedicines, such as photopolymerization of membrane lipids,[3,5] photoisomerizable lipids,[6,7] photothermal techniques,[1,8] photooxidation of lipids[9] and/or photocleavage.[3,10,11] Using these approaches, light-responsive liposomes composed of biocompatible molecules, *i.e.*, phospholipids (PLs), possess efficient drug loading capacity, and are able to release their drug payload in a spatial, temporal, and dose controlled way.[1,9] Among the above-mentioned light triggered release modalities, photothermal and photooxidation methods appear to be the most advantageous ones, due to the use of some photoactive molecules that efficiently absorb in the near infrared region (NIR), known as the "phototherapeutic window".[1] Due to this absorption feature, these molecules allow deeper light penetration into tissues. In photo-oxidative liposomes, they can be embedded in a matrix constituted of PLs with monounsaturated or polyunsaturated fatty acyl chains.[12] Upon illumination, the photosensitive molecules generate reactive oxygen species (ROS), such as singlet oxygen ($^1O_2$), that oxidize the unsaturated chains of PLs. Lipid peroxidation provokes dramatic alterations of the PL molecular organization, the composition of the vesicle membrane and membrane permeability.[12] Indeed, the so-formed hydroperoxyl groups increase the hydrophilicity of the lipid chains originating from large free energy penalties. This results in conformational rearrangements[13] of the lipid chains to drive hydroperoxyl groups towards polar headgroups with an increase in area per lipid[14,15] like truncated PLs do with their carbonyl or carboxylic groups,[16–18] which in turn provokes an increase in membrane permeability.[12,19,20] Adding to the advantages of photo-oxidative liposomes in controlled drug release, the incorporation of a photosensitizer (PS) within the lipid bilayer may also produce a dual effect with the encapsulated drug *via* a photodynamic reaction.[21,22] Despite the potentiality of these drug delivery systems, most PSs used so far were either not clinically approved compounds,[11,19] new synthetic derivatives[19] or PS-coupled PLs;[1,9,23,24] moreover the systems were generally illuminated with high irradiance light sources (>100 mW cm^{-2}).[11,20] So far, a few studies, including molecular dynamic (MD) simulations, have highlighted the importance of the localization and orientation of PSs in lipid bilayers of liposomes in the efficiency of light-triggered drug delivery systems (see ref. 25–28). This theoretical approach elucidated the role of the PS charge state[26] or the presence of PEG (polyethylene glycol) inside lipid bilayers.[25] For instance,

[a] *Institut Galien Paris Sud, UMR 8612, Univ Paris-Sud, CNRS, Université Paris-Saclay, 5 rue J.B. Clément, F-92290 Châtenay-Malabry, France. E-mail: ali.makky@u-psud.fr*
[b] *INSERM UMR850, Univ. Limoges, 2 rue du Dr. Marcland, F-87025, Limoges, France. E-mail: florent.di-meo@unilim.fr*
[c] *Regional Centre for Advanced Technologies and Materials, Department of Physical Chemistry, Faculty of Science, Palacký University, Olomouc, Czech Republic*

† Electronic supplementary information (ESI) available. See DOI: 10.1039/c7cp00983f

hematorporphyrins were shown to reside in the phospholipid headgroup region of POPC in close contact with carbonyl groups, highlighting the importance of the charge state. By combining MD simulations with fluorescence quenching analysis, Dzieciuch *et al.*[25] reported that *p*-THPP partitioned in PEGylated liposomes in two preferred locations, either close to the center of the bilayer or wrapped within the PEG chains. Interestingly, liposomes made of coupled porphyrin–phospholipid were prepared, exhibiting new stable bilayers.[27]

With the aim of developing new drug delivery devices that overcome these limitations, three promising PSs were selected and used at a low molar percentage (2.5 mol%) to avoid both overestimation of release efficiency due to liposomal formulation instabilities,[1] and PS aggregation which may significantly alter singlet oxygen quantum yields.[29,30] *m*-THPP is a porphyrin derivative of a commercial chlorin, *m*-THPC, which is approved by the European Union for head and neck tumors under the name of Foscan®[31] (Fig. 1A–C). Verteporfin is a benzochlorin

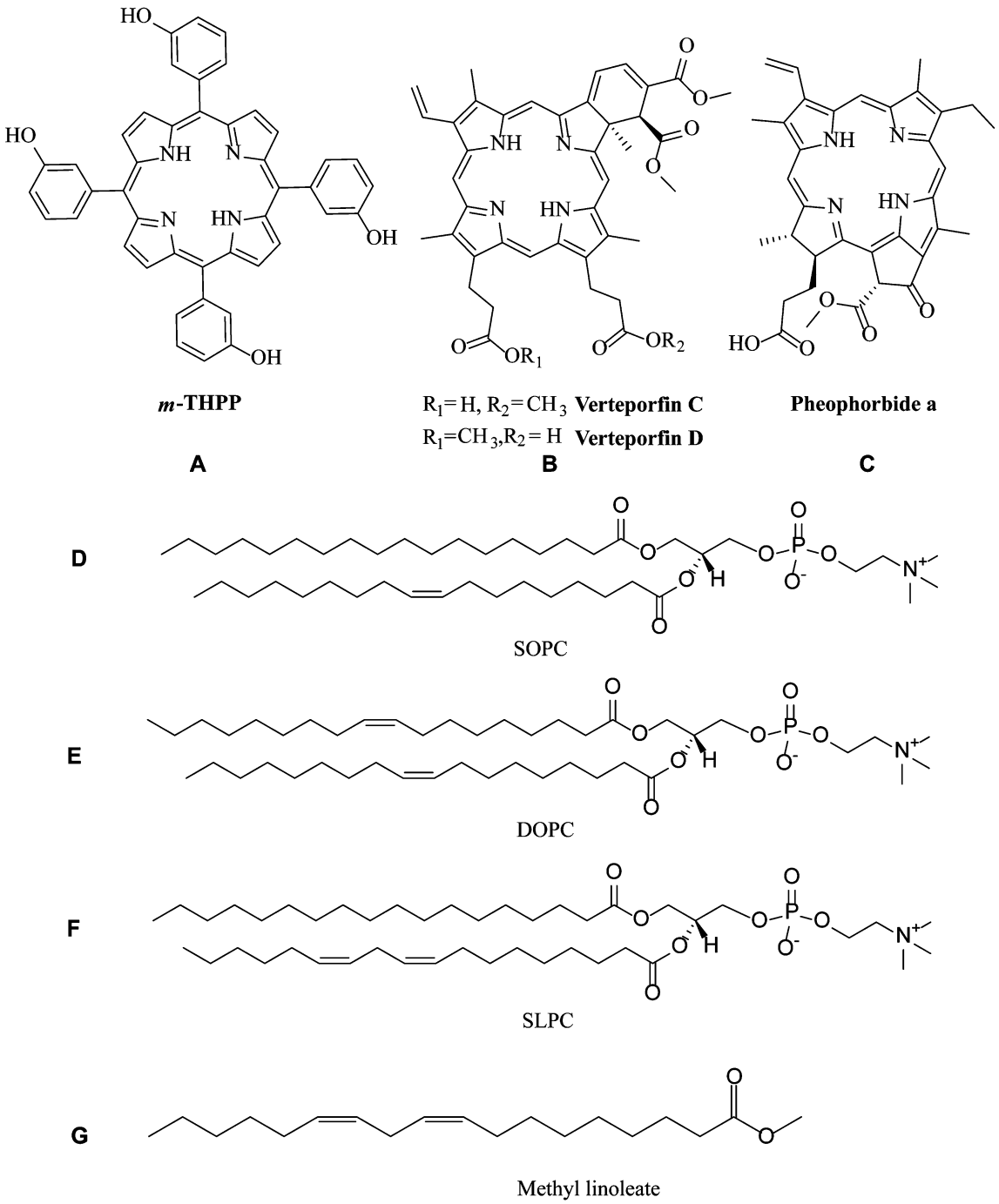

Fig. 1 Chemical structures of the photosensitizers (A–C), phospholipids and methyl linoleate (D–G).

derivative monoacid ring A (BPD-MA), which is composed of an equal amount of two regioisomers (C and D), each of which consist of a pair of enantiomers. Verteporfin is clinically approved by the Food and Drug Administration (FDA) as a liposomal formulation (trade name Visudyne®) for age-related macular degeneration (AMD),[32] and it exhibits efficient capacity for photo-triggered drug release from liposomes.[21] Pheophorbide a is a chlorophyll catabolite that has shown potential efficiency in photodynamic therapy (PDT) for the treatment of different cancers *in vitro*[33,34] causing lipid peroxidation in the mitochondrial membrane.[35]

The aim of this work was to investigate the efficiency of these three PSs in photo-induced membrane permeation at a low irradiance rate (*i.e.*, 2 mW cm^{-2}), which is usually used for *in vitro* PDT experiments.[36–38] We intended to establish the relationship between a well-defined lipid bilayer composition and the photo-induced drug release capacity of these PSs. Molecular dynamics (MD) simulations provided atomic rationalization of the insertion of the three PSs into bilayers with different compositions. This supported the understanding of photoreaction, photo-oxidation, and thermotropic effects.

Experimental

Chemicals

Verteporfin (≥94%, M_w = 718.79 g mol^{-1}), pheophorbide a (≥90%, M_w = 592.68 g mol^{-1}), methyl linoleate (≥99%, M_w = 294.47 g mol^{-1}), calcein (M_w = 622.53 g mol^{-1}), HEPES (99.5% pure, M_w = 238.31 g mol^{-1}), sodium chloride (NaCl, 99% pure, M_w = 58.44 g mol^{-1}), ammonium molybdate(VI) tetrahydrate (81–83%, M_w = 1235.86 g mol^{-1}), L-ascorbic acid (99%, M_w = 176.12 g mol^{-1}), 0.65 mM phosphorus standard solution and hydrogen peroxide (30 wt%) were purchased from Sigma (St. Louis, MI., USA). *m*-THPP was a gift from Dr Philippe Maillard (Institut Curie, France).[39]

1-Stearoyl-2-oleoyl-*sn-glycero*-3-phosphocholine (SOPC, M_w = 788.14 g mol^{-1}), 1,2-dioleoyl-*sn-glycero*-3-phosphocholine (DOPC, M_w = 786.11 g mol^{-1}) and 1-stearoyl-2-linoleoyl-*sn-glycero*-3-phosphocholine (SLPC, M_w = 786.11 g mol^{-1}) PLs were purchased from Avanti Polar Lipids (Alabaster, AL., USA). They were 99% pure and were used without any further purification. Chloroform, methanol, and tetrahydrofuran (99% pure) were analytical-grade reagents provided by Merck (Germany). The ultrapure water used in all experiments was produced by a Millipore Milli-Q® Direct 8 water purification system with a resistivity of 18.2 MΩ cm. The chemical structures of the studied PSs and PLs are shown in Fig. 1.

Light source

The light irradiation experiments were carried out by means of a homemade lamp composed of 4 Philips TL fluorescent tubes covered by a flat diffusing glass plate and fitted with an orange filter (λ ~ 520–680 nm with a λ_{max} = 590 nm) at a 2 J cm^{-2} fluence (Fig. S1, ESI†). The illumination duration (14 min) was kept constant for all experiments, and the samples were illuminated from the bottom of the glass vials (V = 5 mL, S = 5.5 cm^2).

Vesicle suspension preparation

Porphyrin-containing liposomes were prepared by the conventional thin lipid film hydration method[40] followed by vesicle suspension extrusion. In brief, PL/PS couples were solubilized in (9 : 1 v/v) chloroform : methanol mixtures at a 97.5/2.5 (mol%). After evaporation of the solvent under vacuum at 45 °C, the dry film was hydrated with 1 mL of either HEPES buffer (10 mM HEPES, 150 mM NaCl, pH 7.4, corresponding to ~285 mOsmol) or calcein solution (40 mM calcein, 10 mM HEPES, pH 7.4, ~285 mOsmol). The final lipid concentration was 10 mM. The osmotic pressure of the solutions was measured using a Loser osmometer (Camlab, Cambridge, UK). The mixture was then vortexed and extruded 19 times through a 200 nm pore-sized polycarbonate membrane, at room temperature. The hydrodynamic diameter was measured by dynamic light scattering (DLS). The PS incorporation percentage was determined by UV-visible absorption, after liposome disruption with a HEPES buffer/methanol/THF (0.2 : 0.8 : 1 mL) mixture. The PS content was controlled by measuring the absorbance at a specific wavelength (*m*-THPP: 417 nm, verteporfin: 689 nm, and pheophorbide a: 667 nm) using a CARY 100 Bio UV-visible spectrophotometer (Varian, USA). By comparison with standards at specific concentrations, the PS incorporation efficiency (*i.e.*, % of PS inserted into the liposome bilayer with regard to its initial amount in the chloroform–methanol solution) was determined by measuring the absorbance of each liposomal sample after rupture in a methanol/THF mixture. The molecular state of PSs in the liposome bilayer was investigated by UV-Vis spectroscopy. As deduced from the absorption spectra, the PSs did not aggregate when incorporated into the lipid matrices.

Dynamic light scattering (DLS) and zeta potential measurements

All DLS measurements were carried out on SOPC liposomes with a lipid concentration of 1 mM using a Zetasizer (Nano ZS90, Malvern). For the ζ-potential measurements, liposomes (without calcein) at a lipid concentration of 10 mM were prepared in 5 mM HEPES buffer with low ionic strength (5 mM NaCl) and diluted to 1 mM lipid in the same buffer just before measurements. All measurements were carried out at 25 °C.

Differential scanning calorimetry (DSC)

DSC measurements were carried out using a DSC Diamond Perkin-Elmer apparatus. To ensure that thermal equilibrium was reached, four successive heating/cooling scans were recorded between −10 °C and 15 °C at scan rates of 5 °C min^{-1} (for the first two cycles), 2 °C min^{-1} and 1 °C min^{-1} with an empty pan as a reference. Each scan was preceded by a 2 min isotherm recording at the initial temperature to allow the samples to set thermal equilibrium. The same thermal events were observed for all scans and all the observed transitions were reversible and reproducible. The samples (multilamellar suspensions) used for the DSC measurements were prepared by rehydration of either

pure SOPC thin films (5 mg) or SOPC–PS (97.5–2.5 mol%) with 45 μL of HEPES buffer. Analyses were performed in duplicate by placing the samples (~15 mg) in hermetically sealed aluminum pans. To monitor the effect of illumination on the PL thermal behavior, 50 μL of lamellar suspensions (5 mg of SOPC) were illuminated with orange light at a fluence of 2 J cm^{-2} for 14 min before starting the thermal measurements. The calibration was carried out with pure cyclohexane (>99.9% purity, 6.7 °C melting temperature).[41] Data were collected and processed using Pyris thermal analysis software (version 9.1). The PL transition onset temperatures (T_{on}) were determined from the intercept of the baseline with the tangent to the left side of the peak, while the offset temperatures were deduced from the extrapolation to zero heating rate from scans performed at 1 °C min^{-1}, 2 °C min^{-1} and 5 °C min^{-1}. Enthalpy variations (ΔH) were calculated by integrating the area under the transition peaks. The transition enthalpies were determined from the areas under the curve.

$$\Delta H = \int Cp \cdot \mathrm{d}T \quad (1)$$

Lipid oxidation monitoring by conjugated diene formation

The formation of conjugated dienes arising from the peroxidation of methyl linoleate (ML) following illumination was monitored by measuring the UV absorbance using a molar extinction coefficient of 27 000 M^{-1} cm^{-1} at 234 nm in ethanol.[42,43] In order to investigate the impact of the environment on the oxidation efficiency of the various PSs, the measurements were performed either in ethanol or in liposome suspensions with different ML concentrations. In ethanol solutions, ML at concentrations varying from 0 to 5 mM was dissolved in 5 mL of ethanol with 5 μM PS. In the experiments conducted in liposomes, 10, 20 or 30 mol% ML was added to the initial PL : PS mixture in chloroform : methanol (9 : 1; v/v). All samples were irradiated for 14 min at 2 J cm^{-2} (~2 mW cm^{-2}) and the absorption spectra were directly collected from 220 to 300 nm using a CARY 100 Bio UV-visible spectrophotometer. The increase in absorbance at 234 nm was evaluated by subtracting the spectrum of non-irradiated samples from that of irradiated ones.

The quantum yield of the formed conjugated dienes ($\Phi_{\text{conjugated dienes}}$) was determined according to the following equation:

$$\Phi_{\text{conjugated dienes}} = \frac{C_{\text{conjugated dienes}} \times V}{n_{\text{absorbed photons}} \times t} \quad (2)$$

where $C_{\text{conjugated dienes}}$ is the concentration of the conjugated dienes formed determined from the absorption spectra; V is the volume of the irradiated solution; $n_{\text{absorbed photons}}$ is the total number of absorbed photons per second; and t is the illumination duration.

$n_{\text{absorbed photons}}$ can be calculated according to Mojzisova *et al.*[12] as follows:

$$n_{\text{absorbed photons}} = \frac{s}{N_A} \sum_{\lambda} \frac{\mathrm{LI}_\lambda}{E_\lambda} \times \left(1 - 10^{-\mathrm{Abs}_\lambda}\right) \quad (3)$$

where s is the surface of the illuminated sample (because the sample container is much smaller than the lamp used); N_A is the Avogadro's number; LI_λ is the light irradiance (W m^{-2}) at each elemental wavelength; E_λ is the energy (joules) of one photon at the irradiation wavelength; and Abs_λ is the absorbance of the illuminated solution at each wavelength. For the determination of the LI_λ, the spectral irradiance of the lamp was measured using an Ocean Optics Red Tide UV-vis spectrophotometer. It is noteworthy that no photobleaching of PSs was observed in ethanol after 14 min of illumination, whereas for the liposome-embedded PSs there was a slight photobleaching, which did not exceed 5%. To correct the photobleaching of PSs in the calculation of $\Phi_{\text{conjugated dienes}}$ under liposome conditions, the absorption spectra of the different PL–PS liposomes were recorded before and after irradiation. The amount of photons absorbed was then calculated from the mean of the two spectra.

Calcein loading and release from liposomes

Calcein is a water soluble fluorescent probe which is self-quenched when confined in the inner aqueous core of liposomes.[44] Its release from the core of liposomes is accompanied by an increase in its fluorescence intensity due to its dilution in the buffer. To perform calcein release experiments, the extruded calcein-loaded liposomes were purified by ultracentrifugation, with two successive 1 hour cycles at 150 000*g* and at 4 °C, using a Beckman Coulter Optima™ LE-80K (Palo Alto, CA, USA) with a 70.1 – Ti rotor. The supernatant containing free calcein was carefully discarded and the pellet containing the liposomes was resuspended in HEPES buffer, to obtain a liposome suspension with about 10 mM lipid. The accurate lipid concentration was determined by the total phosphorus analysis.[45] In brief, liposome samples were treated with concentrated sulfuric acid at 220 °C for 25 min, followed by additional 30 min of heating after adding concentrated hydrogen peroxide. After cooling down, samples were diluted with deionized water, and a complex was formed by addition of 2.5% ammonium molybdate, immediately reduced by addition of 10% ascorbic acid. A blue colored complex was formed by heating this solution at 100 °C for 7 min, and the related absorbance was measured at 820 nm, once the solution had cooled down.

The calcein release experiments were performed on liposome suspensions diluted in HEPES buffer to 15 μM lipids. The estimation of calcein release was carried out by fluorescent spectroscopy using a Perkin-Elmer LS-50B computer controlled luminescence spectrophotometer (Massachusetts, USA) equipped with a red sensitive R6872 photomultiplier. The emission spectra were obtained before and after illumination, with excitation at $\lambda_{\text{excitation}}$ = 490 nm and emission measured at $\lambda_{\text{emission}}$ = 514 nm. The liposomes were then disrupted by addition of Triton X-100 at a final concentration of 1% (m/v), to entirely release the calcein content, with the release being calculated by using the following equation:

$$\%_{\text{calcein}} = \left(\frac{F - F_0}{F_{\text{det}} - F_0}\right) \times 100 \quad (4)$$

where F is the fluorescence intensity after liposome illumination at different times; F_0 is the initial fluorescence intensity; and F_{det} is the fluorescence intensity of calcein after rupture of

the liposomes with 1% of Triton X-100. Photobleaching of calcein ($\leq$10%) after illumination was taken into account in the % of released calcein. It should be noted that the kinetic profiles obtained in this work were normalized *versus* non-illuminated liposomes to take only the active release of calcein into account.

The time evolution of calcein release (%) for SOPC and DOPC vesicles was fitted with an exponential function:

$$\%_{\text{calcein}} = a + b \cdot e^{-b \cdot t} \quad (5)$$

The evolution of calcein release (%) as a function of time for SLPC formulations was fitted with a sigmoidal function:

$$\%_{\text{calcein}} = a' + \frac{b'}{1 + e^{(c'-t)/d'}} \quad (6)$$

where a' and b' are the coefficients at the base and the maximum of the sigmoidal curve; c' represents the critical time at which the % of released calcein reaches (base + max)/2; d' is the rise rate.

Force field (FF) parameters

For MD simulations, the force field (FF) parameters of the three PSs (*m*-THPP, verteporfin, pheophorbide a) were derived from GAFF[46] using the antechamber package.[47] Atomic charges were derived from RESP (restrained fit of electrostatic potential) based on calculations achieved within the density functional theory (DFT) formalism using the (IEFPCM)-B3LYP/cc-pVDZ method, in diethyl ether.[48] The DFT calculations and the atomic charge fitting were performed using the Gaussian 09, RevA[49] and RESP-v.III software programs,[50] respectively. The two regioisomers, C and D, of verteporfin (Fig. 1) were considered for MD simulations.

Lipid FFs available in the Amber16 package were used to describe the three PL types (DOPC, SLPC and SOPC). Namely, the lipid14[51] FF was used to describe DOPC, whereas the lipid11[52] and GAFFlipid[53] FFs were used to describe both SOPC and SLPC. The lipid11 FF is known to overestimate lipid order, therefore analyses of membrane structural properties must be considered with care, and structural analyses require further validation upon more accurate FFs. The ''three-point'' TIP3P water model[54] was used to describe water molecules.

Molecular dynamic (MD) simulations

Three pure DOPC, SLPC and SOPC bilayer membranes made of 72 lipids each were created using the membrane bilayer builder from the CHARMM-GUI server.[55] The membranes were solvated with a hydration number of 50 water molecules per one lipid molecule. Na^+ and Cl^- ions were added to match with the experimental conditions (*i.e.*, [NaCl] = 0.154 M). MD simulations were carried out using both the CPU and GPU codes available in Amber16.[56,57] Particle-Mesh Ewald (PME) MD simulations were first run on the pure DOPC, SOPC and SLPC bilayer membranes that were carefully prepared as follows: minimization of the water molecule system prior to the entire system minimization; slow thermalization of water molecules up to 100 K in the (*N*,*V*,*T*) ensemble for 200 ps; thermalization of the whole system to the final temperature (298.15 K) of the entire system for 500 ps (*N*,*P*,*T*); equilibration of the density of the system for 5 ns (*N*,*P*,*T*) MD simulations; and finally, the production of 400 ns MD simulation. PSs were inserted into equilibrated membranes, and the system was relaxed by a short minimization, so as to prevent any steric clash artifact; 400 ns MD simulations were then carried out. The total MD simulation time for the three PSs (considering the two regioisomers – C and D – of verteporfin) with the three lipid bilayer (DOPC, SLPC and SOPC) membranes was *ca.* 6 μs. The analyses were performed along the last 200 ns of the MD trajectories (series of snapshots of the molecular systems). This allowed obtaining a complete sampling of structural properties during 200 ns, after the equilibrium is reached (*i.e.*, within the first 200 ns of the MD simulation). PME MD simulations were carried out using the SHAKE algorithm and a 10 Å noncovalent interaction cut-off. The temperature was maintained using the Langevin dynamics with a collision frequency of 1 ps^{-1}. Anisotropic pressure scaling was used in which the pressure relaxation time was set at 1 ps. The analyses were carried out using the cpptraj software.[58]

The *z*-axis is defined as being perpendicular to the membrane surface. The depth of penetration of PSs was measured as the *z*-component of the vector originating at the center-of-mass (COM) of the lipid bilayer and pointing towards the PS COM. The orientation of PSs in the lipid bilayer membrane was assessed as the α-angle between the *z*-axis and the normal vector to the planar ring.

Entrapment is strongly correlated to the noncovalent interactions existing between PSs and lipid tails; the stronger the interaction energy E_{nc} between PSs and lipid tails, the higher the entrapment efficiency. PS–PL interactions were obtained from MD simulations by calculating noncovalent interaction energies (E_{nc}) between (i) PSs and PLs, as well as (ii) PSs and lipid tails of PLs only, with the lipid tails defined as the sn_1- and sn_2-chains. Both energy types were derived from the averaged sum of electrostatic and van der Waals energies per atom.

Results and discussion

Characterization of SOPC liposomes incorporating the three PSs

The characteristics of SOPC liposomes doped with PSs are summarized in Table 1.

The incorporation of various PSs into the SOPC lipid bilayers did not induce any significant change in their hydrodynamic radius compared to unloaded liposomes. Although, the ζ-potential of SOPC vesicles doped with *m*-THPP was also not significantly modified, both verteporfin and pheophorbide a led to more negative ζ-potential values. Apparently, these PSs were not deeply inserted in the bilayer leaflets. MD simulations agreed with these observations, showing that the distance of PS COM to the membrane center increased as follows *m*-THPP < pheophorbide a < verteporfin C/D (Table 1 and Fig. 2). *m*-THPP has a relatively hydrophobic nature, exhibiting an octanol/water partition coefficient log *P* value of 4.8 at neutral pH.[59,60] The tetrapyrrole ring of

Table 1 Hydrodynamic radius (nm), polydispersity index (PDI), ζ-potential (mV) of vesicle suspension and PS incorporation efficiency (%). The last column corresponds to the location of the PS COM with respect to the middle of the membrane (z = 0) ($\langle z \rangle$), as obtained from MD simulations. For verteporfin the two values are given for the two isoforms C and D, respectively

Composition	R (nm)	PDI	ζ-Potential (mV)	PS incorporation efficiency (%)	Distance from membrane center $\langle z \rangle$ (Å)
SOPC	106 ± 4	0.09 ± 0.02	−1.7 ± 0.1	—	—
SOPC–*m*-THPP	105 ± 3	0.09 ± 0.03	−3.8 ± 0.2	84.6 ± 4.4	9.6 ± 0.8
SOPC–verteporfin	98 ± 3	0.07 ± 0.04	−19.3 ± 0.6	68.0 ± 4.3	16.0 ± 0.9 18.0 ± 0.6
SOPC–pheophorbide a	103 ± 7	0.07 ± 0.01	−18.0 ± 0.7	75.1 ± 5.2	13.2 ± 0.8

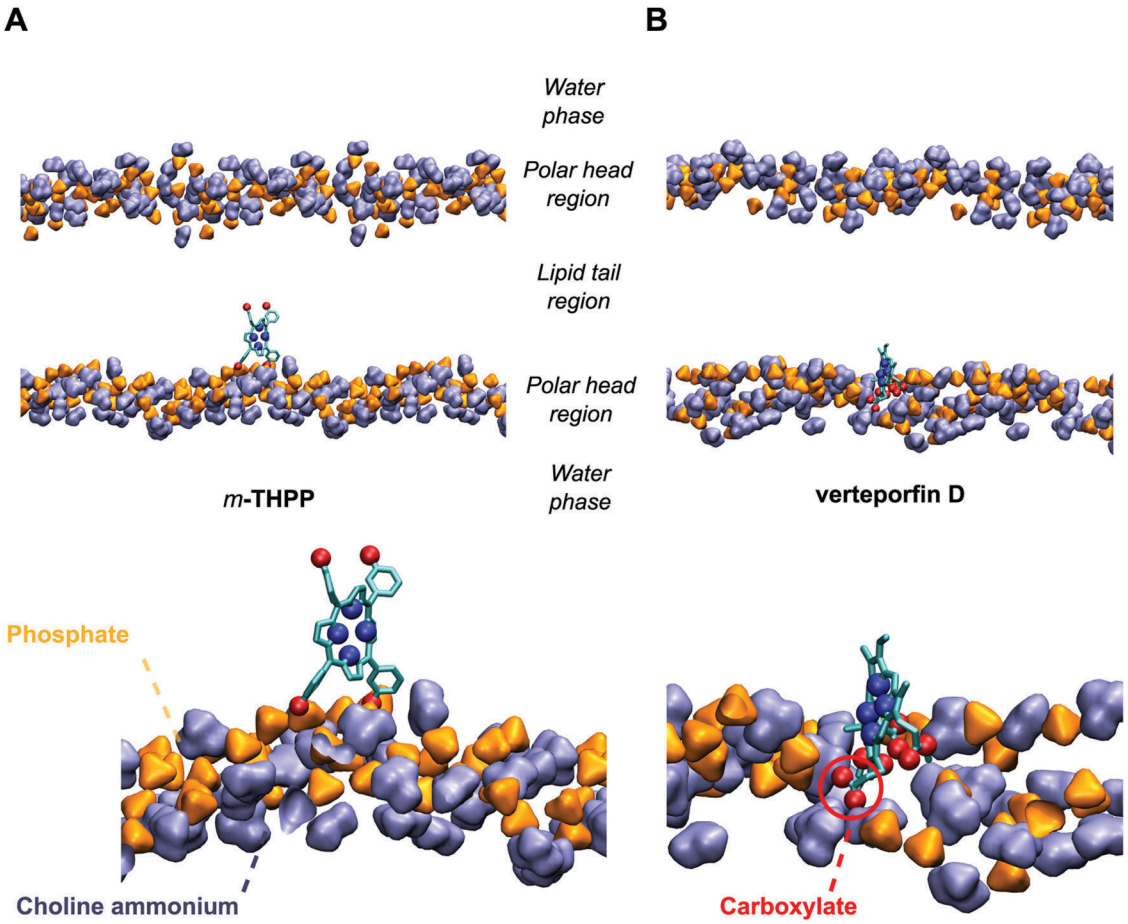

Fig. 2 Representative snapshots (top) and zoom (bottom) of (A) *m*-THPP and (B) verteporfin D interacting with the SOPC membrane. Phosphate and choline ammonium moieties are depicted in orange and ice blue, respectively. Hydrogen atoms, lipid tails and water molecules are omitted for the sake of readability.

this PS is embedded relatively deep in between the lipid tails, and adopts a perpendicular orientation with respect to the membrane surface (α-angle of *ca.* 90°, Fig. S2 in ESI†). In this case, van der Waals forces constitute the major contribution to E_{nc}, with a minor contribution of electrostatic interactions (Table 2). This agrees with previous fluorescence quenching experiments[61] showing relatively strong interactions of this compound with phospholipid tails. This location also agrees with the greater entrapment efficiency observed for *m*-THPP into SOPC bilayers (84.6 ± 4.4%), with respect to the other two PSs (Table 1).

Conversely, due to their negative charge, verteporfin and pheophorbide a appeared to be more anchored to the polar head region. For these two compounds, the electrostatic contribution to E_{nc} values was much greater than for *m*-THPP (Table 2). The carboxylate moieties of verteporfin and pheophorbide a interact with the ammonium moieties of PLs (Fig. 2), but also interestingly with water molecules. Due to the amphiphilic character of these two PSs, they are partially inserted in the bilayer, the tetrapyrrole ring being located in between the lipid chains (Fig. S3–S7, ESI†), adopting an orientation perpendicular to the membrane surface (α-angle of *ca.* 90°, Fig. S2, ESI†).

Table 2 Electrostatic (E_{elec}, J mol^{-1} atom^{-1}) and van der Waals (E_{vdW}, J mol^{-1} atom^{-1}) contributions and standard deviations ($\sigma_{\langle E_{elec}\rangle}$ and $\sigma_{\langle E_{vdW}\rangle}$, respectively, in J mol^{-1} atom^{-1}) to (A) PS-PLs and (B) PS-lipid tail E_{nc}

PS	E_{elec}	$\sigma_{\langle E_{elec}\rangle}$	E_{vdW}	$\sigma_{\langle E_{vdW}\rangle}$
A				
m-THPP	−55.6	8.4	−152.1	7.6
Pheophorbide a	−276.7	29.3	−143.6	9.2
Verteporfin C	−155.8	17.8	−165.5	8.2
Verteporfin D	−196.7	17.1	−167.3	8.0
B				
m-THPP	−3.4	2.0	−130.3	7.2
Pheophorbide a	−1.5	2.3	−117.2	8.6
Verteporfin C	1.7	1.7	−116.0	7.3
Verteporfin D	2.1	1.1	−98.0	7.1

In SOPC membranes, this orientation is particularly restrained due to the relatively high order of this bilayer. This less deep insertion of verteporfin and pheophorbide a compared to *m*-THPP in turn induced a larger loss of PS during liposome extrusion, as exemplified by the entrapment efficiencies compared to that of *m*-THPP (Table 1).

Impact of PS incorporation on the thermotropic behavior of phospholipid bilayers

To further investigate the incorporation of the different PSs into the lipid matrix and their ability to affect lipid bilayer properties, we have performed a calorimetric analysis on SOPC lamellar suspensions without and with PSs at 2.5 mol%. The obtained DSC thermograms are shown in Fig. 3.

The thermogram of pure SOPC exhibits a sharp endothermic peak at a T onset of ~6 °C with ΔH of 5.8 kcal mol^{-1}, which corresponds to the main transition of pure SOPC from the gel phase (L_β) to the liquid crystalline phase (L_α).[62] The incorporation of each PS dramatically alters the SOPC thermograms (Fig. 3B–D). Indeed, they all induced a decrease in the sharpness of the main transition peak and a shift toward lower transition temperatures, suggesting the destabilization of the PL intermolecular cooperativity.[63–66] This alteration depends on the PS chemical structure: *m*-THPP produced the strongest effect among the three PSs, inducing an intensive shift of the transition toward a (lower) T_{onset} at 1.1 °C.

The presence of two peaks rather than one in the case of *m*-THPP is attributed to its poor miscibility in the lipid bilayer at low temperature, leading to the formation of *m*-THPP-rich and -poor domains. The SOPC–pheophorbide a sample only leads to a limited T_{onset} shift; the homogenous and symmetric peak is characteristic of a good mixing with SOPC. The SOPC–verteporfin system is characterized by a broad and asymmetric peak with a T_{onset} of 3.7 °C indicating partial mixing of SOPC and verteporfin. This PS might act as a substitutional impurity.[67] Despite the significant perturbation of the SOPC thermogram in the presence of the three PSs, the overall phase

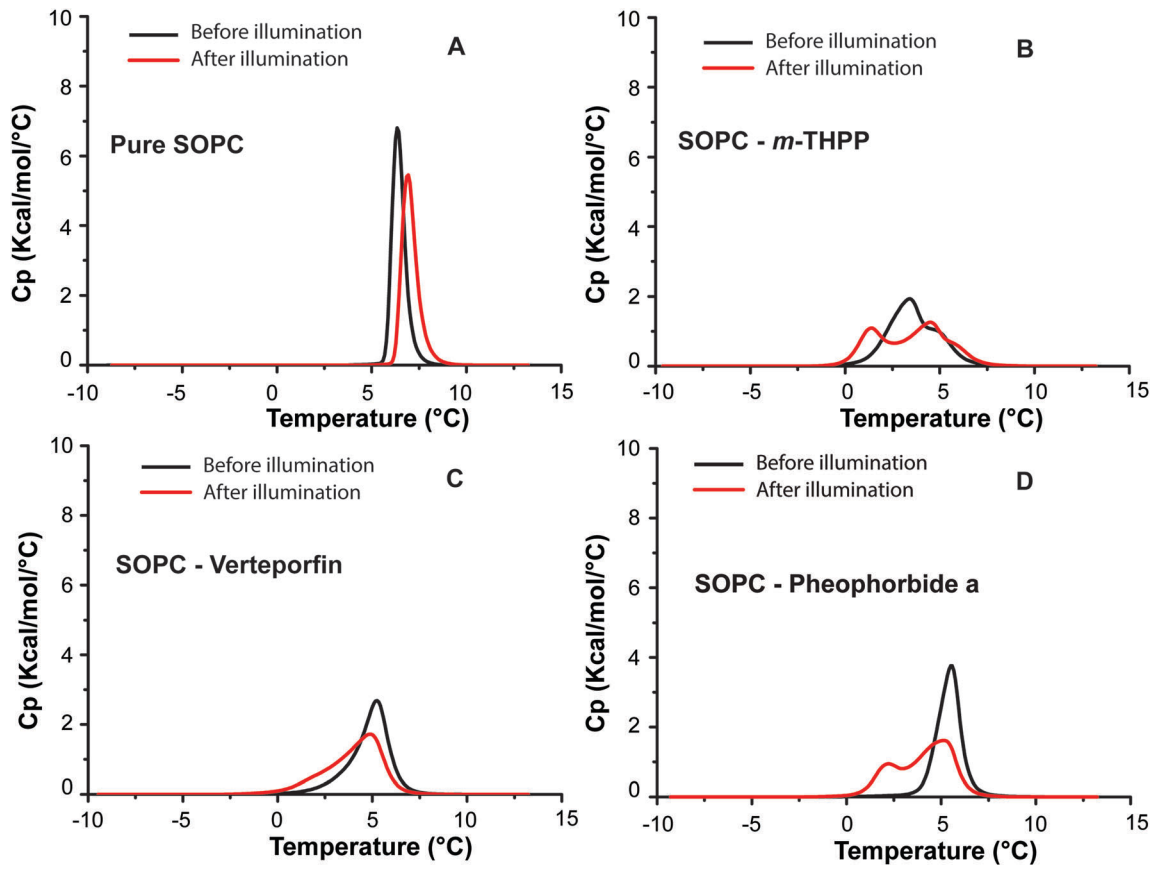

Fig. 3 DSC heating scans of pure SOPC liposomes, SOPC–*m*-THPP, SOPC–verteporfin and SOPC–pheophorbide a before and after illumination.

Table 3 T_{onset} temperatures, enthalpies of pure SOPC and SOPC doped with PSs before and after illumination

	Before illumination		After illumination	
Composition	T onset (°C)	ΔH (kcal mol^{-1})	T onset (°C)	ΔH (kcal mol^{-1})
SOPC	5.8	5.8	6.3	5.4
SOPC-*m*-THPP	1.1	5.7	0.12	5.4
SOPC–pheophorbide a	4.2	5.7	1.1	5.6
SOPC–verteporfin	3.7	5.7	1.6	5.4

transition enthalpy of the different systems remained almost constant (Table 3).

In order to assess the thermotropic phase behavior of SOPC–PS samples upon illumination, DSC scans were performed after illumination of SOPC lamellar suspensions for 14 min (see Fig. 3). After illumination of pure SOPC, its transition temperature was almost unchanged with a slight decrease in the transition enthalpy, which remained below 7%, suggesting that the pure PL bilayers remained almost intact. Conversely, upon illumination of SOPC–PS samples, the overall shape of the thermograms was dramatically affected with a significant shift of T_{onset} towards lower temperatures, and the appearance of a second peak for both *m*-THPP and pheophorbide a. For the SOPC–verteporfin sample, the peak was altered and became broader with the appearance of a shoulder at about 2 °C. These results indicate the formation of new phases upon the illumination of SOPC–PS systems, which may be related to the formation of new chemical species within the lipid bilayer. Interestingly, such a behavior was previously observed by Wallgren *et al.*[68] and one of us[18] with the incorporation of defined amounts (0 to 20 mol%) of oxidized PLs with either a carboxyl (1-palmitoyl-2-azelaoyl-*sn-glycero*-3-phosphocholine (PazePC)) or an aldehyde (1-palmitoyl-(9-oxononanoyl)-*sn-glycero*-3-phosphocholine (PoxnoPC)) group. This incorporation significantly altered the thermotropic phase behavior of DMPC[68] and SOPC[18] vesicles. Herein, *m*-THPP appeared to be the most efficient PS in creating new phases upon liposome illumination followed by pheophorbide a and verteporfin, respectively. Although the nature of the species formed upon photosensitization reaction cannot be predicted from the DSC thermograms, these species are most probably lipid hydroperoxides. Indeed, upon illumination at adequate wavelength, the PS absorbs radiation energy, creating its singlet excited state (^{1}PS*).[69] Porphyrin and chlorin ^{1}PS* are good candidates for intersystem crossing (ISC) processes, leading to the formation of a triplet state (^{3}PS*). ^{3}PS* then reacts *via* two different pathways – either electron/hydrogen transfer (type I reaction) or energy transfer (type II reaction) to triplet oxygen – producing free radicals or singlet oxygen, respectively.[69] The light-induced oxidation pathway highly depends on the solubility and concentration of molecular oxygen. Nevertheless, type II reaction is usually favored in lipid bilayers, as singlet oxygen has a longer half-life than in aqueous media.[70] The unsaturated alkyl chains of SOPC are substrates for singlet oxygen favoring the formation of lipid hydroperoxides.

Lipid peroxidation monitoring

ML is a fatty acid methyl ester that contains two unconjugated *cis* olefinic bonds (see Fig. 1). Upon their reaction with singlet oxygen, the latter is added to one of the C-atoms of the double bonds in a concerted and specific way known as ''ene addition'', forming *trans* allylic hydroperoxides,[71,72] with only 60% of them being conjugated.[71] Since conjugated dienes and hydroperoxides are simultaneously formed, the absorption measurement at 234 nm is considered as a relevant marker to quantify hydroperoxide formation.[12] The oxidation experiments of ML were performed in ethanolic solutions and on SOPC–PS liposome suspensions. The typical absorption spectra of the three PSs in ethanol (5×10^{-6} M) are presented in Fig. 4A.

As shown in Fig. 4B, the characteristic absorbance of conjugated diene formation at 234 nm increased as a function of ML concentration. For all studied PSs, in ethanol and in liposomes, the concentration of conjugated dienes linearly increased as a function of ML concentration (Fig. 4C and D), showing that peroxidation depends on substrate availability. From these linear plots, $\Phi_{\text{conjugated dienes}}$ were determined and plotted as a function of ML concentration (Fig. 4E and F).

Interestingly, the liposomes charged with PSs exhibited different ML peroxidation efficiencies compared to those measured in ethanol. The slopes of $\Phi_{\text{conjugated dienes}}$ *versus* PS concentration plots in liposomes (60.90, 39.25, and 21.56 M^{-1} for *m*-THPP, pheophorbide a and verteporfin, respectively) were at least two order of magnitude higher than those in ethanolic solutions (0.23, 0.17, and 0.17 M^{-1} for *m*-THPP, pheophorbide a and verteporfin, respectively). Similar results were obtained by Mojzisova *et al.*[12] who studied DOPC/ML liposomes incorporating different chlorin derivatives. This was attributed to the longer lifetime of singlet oxygen in lipid membranes than in ethanol solutions. Thus, a higher efficiency of singlet oxygen with ML unsaturation is expected in lipid membranes.[73] PS-induced oxidation efficiencies (Fig. 4E) were as follows: *m*-THPP > pheophorbide a > verteporfin, in agreement with DSC results (see Fig. 3 and Table 3). The different behavior observed with the three PSs could thus be explained by their confinement in the lipid bilayer and the production of singlet oxygen and/or free radicals directly in the vicinity of the unsaturated chains of both PL and ML. As discussed above, *m*-THPP is incorporated deeper inside the lipid bilayer than the other two PSs, which is related to their lipophilicity, as confirmed by our MD simulations and as previously showed by Engelmann *et al.*[74] Ehrenberg *et al.*[73] have also shown that the photodynamic efficacy of PSs is higher for those which can efficiently intercalate in between lipid tails, at a location where the excited state of a PS has higher probability to interact with dioxygen to generate singlet oxygen. In turn, singlet oxygen, generated in the hydrophobic interior, has a greater probability to react with unsaturated chains within the lipid matrix.

Photo-triggered release of calcein from liposomes

We demonstrated with the ML oxidation experiments that the peroxidation of unsaturated chains depends on substrate

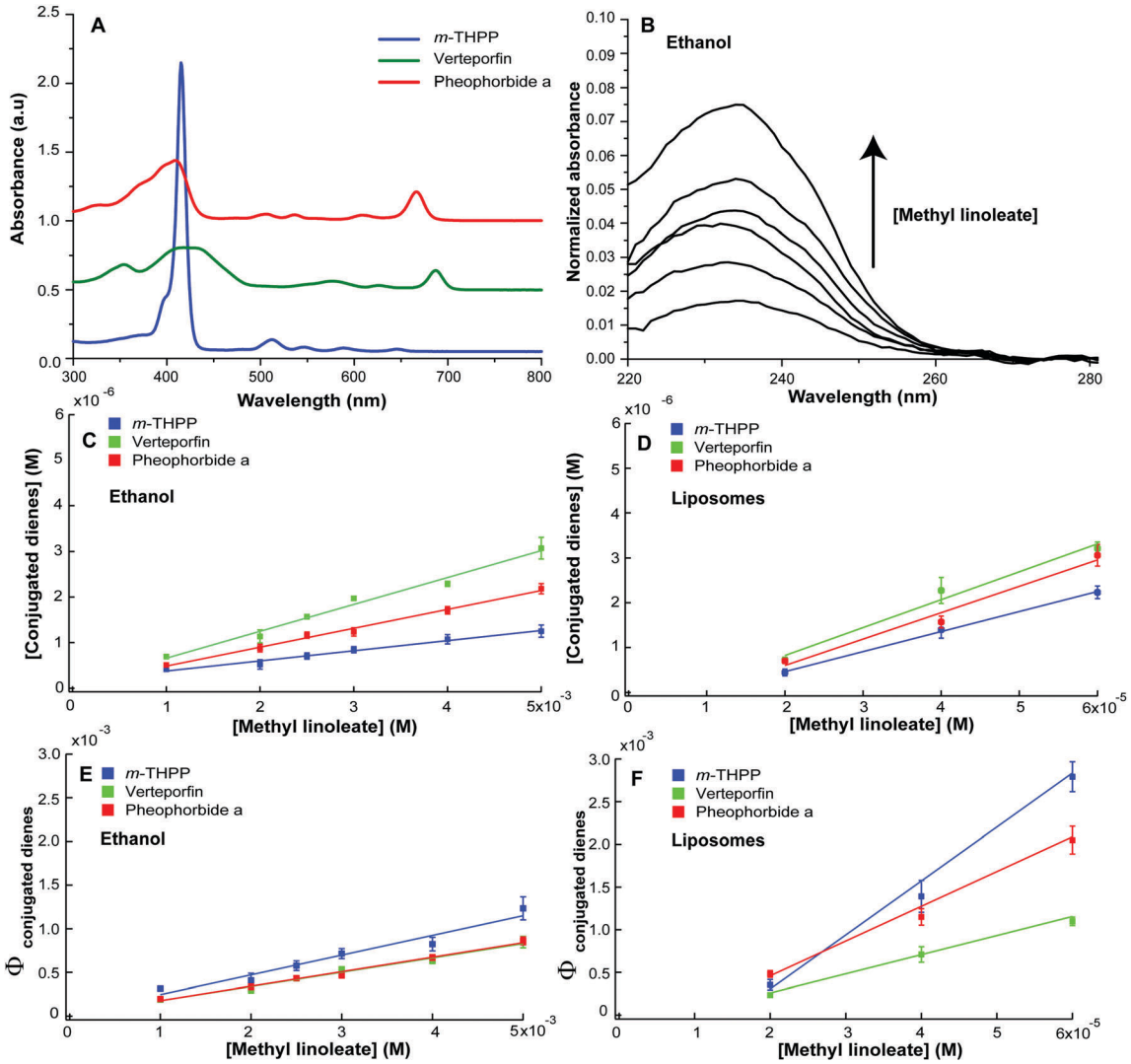

Fig. 4 ML peroxidation monitoring in ethanol and SOPC–PS liposomes at room temperature. (A) Absorption spectra of the three studied PSs at 5×10^{-6} M in ethanol. (B) Typical absorption spectra of the conjugated dienes formed in ethanol upon illumination of ML in the presence of verteporfin (5×10^{-6} M) for 14 min (2 J cm^{-2}). Concentrations and quantum yields of the formed conjugated dienes as a function of ML concentration in (C and E) ethanol and (D and F) liposomes at a PS concentration of 5×10^{-6} M.

availability (Fig. 4C–F). Peroxidation is a major driving factor for membrane permeation, which is required for photo-triggered release. To investigate the effect of phospholipid unsaturation chains on the permeation efficiency, liposomes made of various unsaturated phospholipids (*i.e.*, SOPC, DOPC and SLPC) were doped with the different PSs and calcein was encapsulated into their aqueous core. As for SOPC liposomes, the PS incorporation efficiency into DOPC and SLPC vesicles was the highest for *m*-THPP (Table S2, ESI†). The normalized kinetics release profiles upon illumination of PL–PS system are shown in Fig. 5. While no leakage of the dye was observed following illumination of pure phospholipid vesicles, significant calcein release occurred in PS-containing liposomes, which increased with time. As depicted in Fig. 5B–D, the leakage was incomplete for all three PSs and did not exceed 40% after 6 hours in the best case, but the lipid composition of liposomes appeared to play a crucial role in controlling the calcein release kinetics. Indeed, although for SOPC–PS and DOPC–PS vesicles the calcein leakage profiles increased exponentially with all PSs, SLPC–PS vesicles exhibited a slower release profile rate, which can be fitted by a sigmoidal function (Fig. 5B–D).

The system efficiency also seems to depend upon the PS/PL combination. Table 4 shows that for *m*-THPP, calcein photo-induced release was much more efficient for DOPC vesicles than for the SOPC or SLPC ones.

In addition, despite the low absorbance of the DOPC-*m*-THPP system in the region of the emission spectrum of the lamp (Fig. S1, ESI†), its illumination induced the highest calcein release after six hours compared to the other PL/PS combinations (Table 4). Conversely, for verteporfin and pheophorbide a, the photo-triggered calcein release appeared to be more efficient with SOPC and DOPC than with SLPC.

The difference in calcein release extent between the three PL/PS combinations may be related to the different permeation

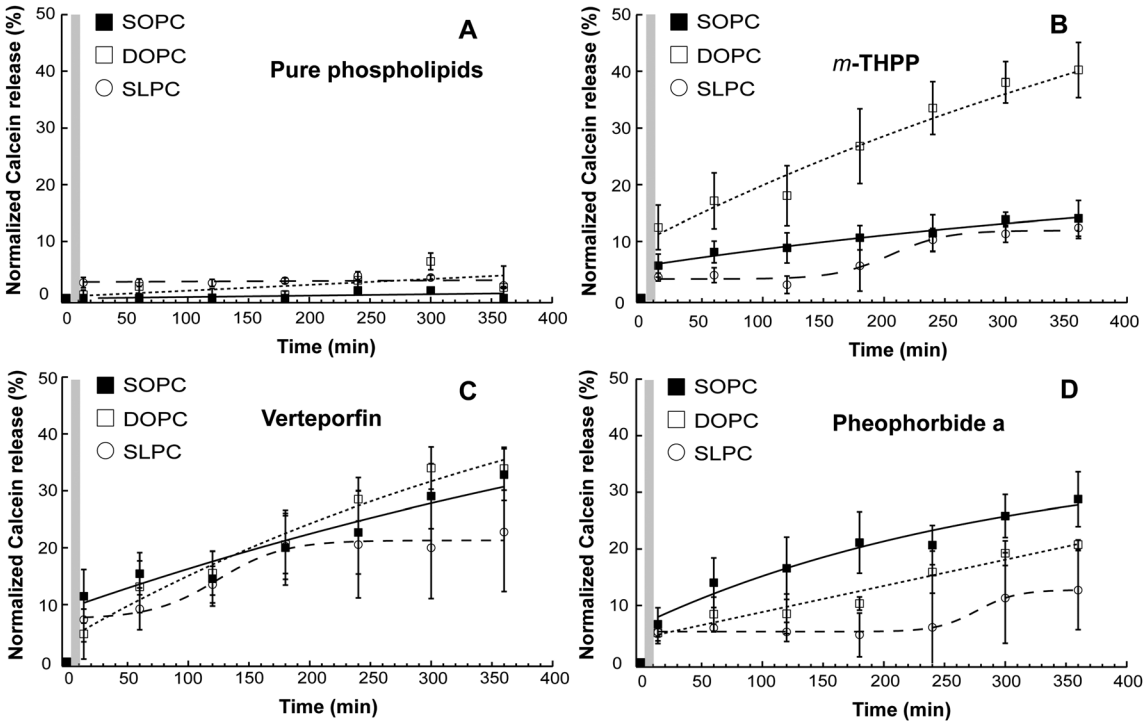

Fig. 5 Photo-triggered release of calcein as a function of time of (A) pure PLs, (B) PLs doped with *m*-THPP (C) PL–verteporfin and (D) PL–pheophorbide a. Solid black lines, dotted black lines and dashed black lines represent the fit of the calcein release from SOPC, DOPC and SLPC liposomes, respectively. The calcein release profiles were normalized by subtraction of the percentage of calcein released from non-illuminated samples. The data at 0 min in each graph correspond to the initial calcein release % before illumination. The gray vertical line corresponds to the duration of light exposure (14 min). The error bars are the standard deviations (n = 3). All measurements were performed at room temperature.

Table 4 Normalized calcein release (%) of different liposome/PS systems after 6 hours of illumination

Photosensitizer	SOPC	DOPC	SLPC
m-THPP	14.1 ± 3.1	40.2 ± 6.7	12.4 ± 1.9
Pheophorbide a	28.8 ± 4.8	20.8 ± 0.8	12.7 ± 6.8
Verteporfin	33.1 ± 6.1	33.8 ± 3.8	22.8 ± 10.5

mechanisms. In fact, membrane oxidation leads to the formation of lipid peroxides with different structures depending on the PL structure and the localization of the PS in the bilayer. PL peroxide derivatives may induce different effects on membrane properties varying from structure destabilization to liposome fusion. Hence, to gain a better insight into the mechanism of photo-triggered release, the size of the different liposomes was measured before and after illumination by DLS. Our results showed that neither the size nor the distribution of the vesicles changed even after 24 h of illumination (Table S2, ESI†), ruling out the fusion hypothesis. Thermal destabilization of the lipid bilayers was also considered. However, the illumination induced less than 2 °C increase in temperature of the liposome suspensions, and the lipids were all already in the liquid crystal phase. Furthermore, PS-unloaded vesicles illuminated under the same conditions (Fig. 5A) led to non-significant calcein release compared to those containing the PSs. Therefore, the mechanism of photo-induced calcein release could only be explained by the formation of a hydroperoxide group on the alkyl chain unsaturation, which altered the membrane structure. As *m*-THPP is deeply inserted in the lipid bilayers, the generated singlet oxygen has a higher potential to react with the alkyl chain unsaturation due to its longer diffusion path, compared to that produced by the other PSs in the proximity of polar headgroups where it is more quickly deactivated in the aqueous environment. The fact that the *m*-THPP/DOPC vesicles are more efficient than those with SOPC and SLPC could be explained by the formation of a hydroperoxide group on each alkyl chain, altering the phospholipid packing. A significant area expansion would lead to a higher membrane permeability compared to the SOPC and SLPC liposomes. Recently, Aoki *et al.*[75] have demonstrated, from surface pressure measurements combined with polarization-modulated infrared reflection absorption spectroscopy (PM-IRRAS), that the irradiation of a DOPC/erythrosin monolayer caused a significant relative surface area increase of *ca.* 19%.[75] Similarly, using a micropipette setup, Weber *et al.*[19] observed that the formation of PL hydroperoxides caused an increase in the excess area of GUVs of 15.6% and 19.1% for POPC and DOPC, respectively. Also, Luo *et al.*[9] demonstrated that the incorporation of DOPC into liposomes accelerated the light-triggered doxorubicin release from porphyrin–phospholipid (PoP) liposomes by one order of magnitude compared to DOPC-free liposomes. By mass spectrometry, they confirmed that the light-triggered drug release was related to DOPC oxidation and revealed the formation of three DOPC oxidized species.

The SLPC–PS liposomes exhibited the lowest release efficiency. Such behavior was also observed by Luo *et al.*[9] who attributed it to the lower probability of singlet oxygen accessing the unsaturated bonds present on the same chain. However, we found that the concentration of conjugated dienes formed in SLPC-*m*-THPP liposomes increased linearly as a function of

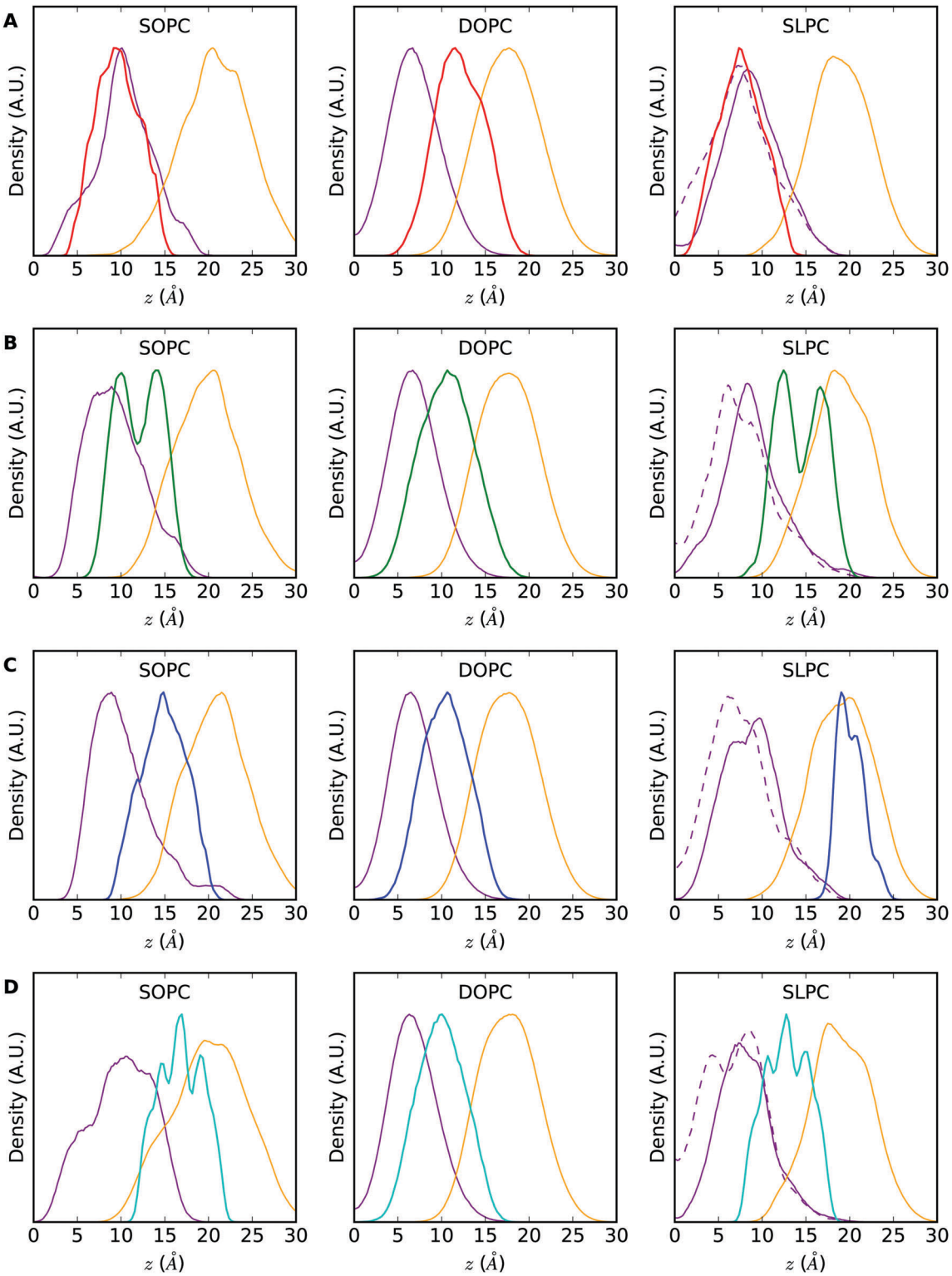

Fig. 6 Density of (A) *m*-THPP (red), (B) pheophorbide a (green), (C) verteporfin C (blue) and (D) verteporfin D (cyan) tetrapyrrole moieties along the *z*-axis in SOPC, DOPC and SLPC. C=C double bonds as well as high-density polar head region densities (*i.e.*, phosphatidylcholine moieties) are plotted in purple and orange, respectively. SLPC C_9=C_{10} and C_{12}=C_{13} are plotted in solid and dashed lines, respectively.

illumination duration (Fig. S10, ESI†). This demonstrates the ability of singlet oxygen to induce SLPC diene peroxidation. Therefore, the lower efficiency of membrane permeation observed for SLPC with respect to SOPC and DOPC could only be explained by the structure of the PL hydroperoxides formed. Indeed, Wong-Ekkabut *et al.*[13] investigated the effect of lipid peroxidation on the properties of PLPC (1-palmitoyl-2-linoleoyl-*sn-glycero*-3-phosphatidylcholine) lipid bilayers using MD simulations. They focused on the two main hydroperoxide products of linoleic acid: the 9-*trans*,*cis*-hydroperoxide linoleic acid (9-tc) and the 13-*trans*,*cis*-hydroperoxide linoleic acid (13-tc). According to their simulations,[13] both PL hydroperoxides at 11.1 mol% were unable to modify water permeability through PLPC bilayers. However, increasing the oxidized lipid fraction to 50 mol% in the membrane led to a higher water permeability compared to unoxidized PLPC, with an increase of two and one order of magnitude for 13-tc and 9-tc, respectively.[13] Their result suggests a relationship between water permeability of the bilayer and the position of the hydroperoxide group in the lipid bilayer, inducing a larger area expansion and a loss of lipid packing with 13-tc compared to 9-tc.[13]

Molecular insights into PS efficiency

PS efficiency in membranes depends on: (i) PS intrinsic parameters (*e.g.*, photophysical, excited- and ground-state conformational properties); (ii) molecular oxygen diffusion capacity, and (iii) the direct surrounding environment of the PS. The first two points are out of the scope of this work; here we evaluated the PS insertion/location in various lipid bilayers with different packing orders. *m*-THPP inserts significantly deeper than pheophorbide a and verteporfin into SOPC and SLPC bilayers (Table S1, ESI† and Fig. 6). A similar depth of penetration and orientation are observed for the three PSs respectively, in both SOPC and SLPC bilayers (Table S1 and Fig. S3–S7, ESI†). In contrast, in DOPC bilayers, the three PSs exhibit a similar depth of penetration (Table S1, ESI† and Fig. 6) likely owing to the higher fluidity of DOPC that allows higher diffusion motions.

DSC experiments have demonstrated that the presence of PSs in lipid bilayer membranes leads to structure destabilization. A thorough analysis of the characteristic orientation obtained, *e.g.*, with verteporfin D, highlighted disorganization of the membrane surface (Fig. 2). Also, in the more ordered (SOPC and SLPC) lipid bilayers, the structure destabilization was suggested by the asymmetric phosphatidylcholine distributions along the *z*-axis, in which the disturbance is on the side where PSs are located (Fig. 6). However, due to the small size of the membrane model used in the MD simulations, the structural destabilization could not be quantitatively evaluated neither by the calculated area per lipid nor by lipid order profiles (*i.e.*, no significant differences were observed in the presence of PSs, see Fig. S9 and Table S3, ESI†).

From ML peroxidation experiments, *m*-THPP appeared to be the most efficient PS in lipid peroxidation followed by pheophorbide a and verteporfin. This result agrees with their relative insertion depth in SOPC and SLPC bilayers. However, such observation was not necessarily correlated with calcein release experiments (Fig. 5), highlighting the role of the lipid environment as well as the nature of lipid peroxides produced.

It is worth noting that the tetrapyrrole planarity can be altered inside the lipid bilayers. This is known to dramatically affect photon absorption events and subsequently singlet oxygen generation. The planarity of pheophorbide a and verteporfin tetrapyrroles is more sensitive to the environment than *m*-THPP. The latter is indeed more π-conjugated and thus less flexible (Fig. S8, ESI†). DOPC offers more flexibility to the verteporfin and pheophorbide a central core leading to a broader distribution of tetrapyrrole dihedral angles. SOPC is more prone to disturb tetrapyrrole planarity owing to a slightly higher order with respect to SLPC. Lipid order is an important parameter since O_2-PS energy transfer occurs within the ^{3}PS state, in which the tetrapyrrole planarity is modified with respect to the PS ground state. The present MD simulations achieved with ground state geometries underlined the different impacts of the different lipid bilayers on tetrapyrrole planarity even though no straightforward trends can be dragged out. Such investigation would require the parameterization of triplet excited state PS force fields, which is out of the scope of the present study.

Conclusion

In conclusion, the present work highlights the possible use of three clinically approved (or under investigation) PSs in the conception of photo-triggerable liposomes. In particular, our results showed that the illumination significantly altered the lipid bilayer properties of the studied systems; the efficiency of membrane degradation and subsequently drug release depends on the PS/PL combination. Among other descriptors, the depth of PS incorporation into the lipid bilayer is a major contributor to the efficiency. *m*-THPP/DOPC appeared to be the most efficient system, where the photo-triggered release of the cargo reached approximately 40% six hours after illumination at a low light fluence. Such photo-triggered release would be even more efficient with encapsulated drugs having a smaller molecular weight than calcein (*i.e.*, doxorubicin) and with a light source of high irradiance. Adding to its efficiency in photo-permeation drug release, *m*-THPP (or its derivative *m*-THPC which has a stronger absorption coefficient at 652 nm) incorporated into DOPC liposomes would represent a promising photo-triggerable system with potential dual activity (chemo- and photodynamic therapy) against relevant cancer tumors.

Acknowledgements

The authors thank Dr Ali Tfayli (Lips(Sys)^2, Groupe de Chimie Analytique de Paris-Sud, FKA EA4041, Châtenay-Malabry, France) for his technical assistance with the spectroradiometer for the lamp fluence measurement. JM is thankful to the French Ministry of Research for the financial support of his PhD thesis. FDM and PT thank CALI (CAlcul en LImousin) for computing facilities.

Notes and references

1 J. F. Lovell, C. S. Jin, E. Huynh, H. Jin, C. Kim, J. L. Rubinstein, W. C. Chan, W. Cao, L. V. Wang and G. Zheng, *Nat. Mater.*, 2011, **10**, 324–332.
2 A. Puri, *Pharmaceutics*, 2013, **6**, 1–25.
3 P. Shum, J. M. Kim and D. H. Thompson, *Adv. Drug Delivery Rev.*, 2001, **53**, 273–284.
4 S. J. Leung and M. Romanowski, *Theranostics*, 2012, **2**, 1020–1036.
5 B. Bondurant, A. Mueller and D. F. O'Brien, *Biochim. Biophys. Acta*, 2001, **1511**, 113–122.
6 R. H. Bisby, C. Mead and C. G. Morgan, *Biochem. Biophys. Res. Commun.*, 2000, **276**, 169–173.
7 R. H. Bisby, C. Mead and C. G. Morgan, *Photochem. Photobiol.*, 2000, **72**, 57–61.
8 T. Lajunen, L. S. Kontturi, L. Viitala, M. Manna, O. Cramariuc, T. Rog, A. Bunker, T. Laaksonen, T. Viitala, L. Murtomaki and A. Urtti, *Mol. Pharmaceutics*, 2016, **13**, 2095–2107.
9 D. Luo, N. Li, K. A. Carter, C. Lin, J. Geng, S. Shao, W. C. Huang, Y. Qin, G. E. Atilla-Gokcumen and J. F. Lovell, *Small*, 2016, **12**, 3039–3047.
10 D. H. Thompson, J. Shin, J. Boomer and J. M. Kim, *Methods Enzymol.*, 2004, **387**, 153–168.
11 D. H. Thompson, O. V. Gerasimov, J. J. Wheeler, Y. Rui and V. C. Anderson, *Biochim. Biophys. Acta*, 1996, **1279**, 25–34.
12 H. Mojzisova, S. Bonneau, P. Maillard, K. Berg and D. Brault, *Photochem. Photobiol. Sci.*, 2009, **8**, 778–787.
13 J. Wong-Ekkabut, Z. T. Xu, W. Triampo, I. M. Tang, D. P. Tieleman and L. Monticelli, *Biophys. J.*, 2007, **93**, 4225–4236.
14 O. Mertins, I. O. L. Bacellar, F. Thalmann, C. M. Marques, M. S. Baptista and R. Itri, *Biophys. J.*, 2014, **106**, 162–171.
15 J. Heuvingh and S. Bonneau, *Biophys. J.*, 2009, **97**, 2904–2912.
16 K. Sabatini, J.-P. Mattila, F. M. Megli and P. K. J. Kinnunen, *Biophys. J.*, 2006, **90**, 4488–4499.
17 A. Korytowski, W. Abuillan, A. Makky, O. Konovalov and M. Tanaka, *J. Phys. Chem. B*, 2015, **119**, 9787–9794.
18 A. Makky and M. Tanaka, *J. Phys. Chem. B*, 2015, **119**, 5857–5863.
19 G. Weber, T. Charitat, M. S. Baptista, A. F. Uchoa, C. Pavani, H. C. Junqueira, Y. Guo, V. A. Baulin, R. Itri, C. M. Marques and A. P. Schroder, *Soft Matter*, 2014, **10**, 4241–4247.
20 A. Pashkovskaya, E. Kotova, Y. Zorlu, F. Dumoulin, V. Ahsen, I. Agapov and Y. Antonenko, *Langmuir*, 2010, **26**, 5726–5733.
21 B. Q. Spring, R. B. Sears, L. Z. Zheng, Z. M. Mai, R. Watanabe, M. E. Sherwood, D. A. Schoenfeld, B. W. Pogue, S. P. Pereira, E. Villa and T. Hasan, *Nat. Nanotechnol.*, 2016, **11**, 378–387.
22 P. C. Peng, R. L. Hong, Y. J. Tsai, P. T. Li, T. Tsai and C. T. Chen, *Lasers Surg. Med.*, 2015, **47**, 77–87.
23 K. A. Riske, T. P. Sudbrack, N. L. Archilha, A. F. Uchoa, A. P. Schroder, C. M. Marques, M. S. Baptista and R. Itri, *Biophys. J.*, 2009, **97**, 1362–1370.
24 E. Huynh, J. F. Lovell, R. Fobel and G. Zheng, *Small*, 2014, **10**, 1184–1193.
25 M. Dzieciuch, S. Rissanen, N. Szydlowska, A. Bunker, M. Kumorek, D. Jamroz, I. Vattulainen, M. Nowakowska, T. Rog and M. Kepczynski, *J. Phys. Chem. B*, 2015, **119**, 6646–6657.
26 M. Stepniewski, M. Kepczynski, D. Jamroz, M. Nowakowska, S. Rissanen, I. Vattulainen and T. Rog, *J. Phys. Chem. B*, 2012, **116**, 4889–4897.
27 K. A. Carter, S. Shao, M. I. Hoopes, D. Luo, B. Ahsan, V. M. Grigoryants, W. Song, H. Huang, G. Zhang, R. K. Pandey, J. Geng, B. A. Pfeifer, C. P. Scholes, J. Ortega, M. Karttunen and J. F. Lovell, *Nat. Commun.*, 2014, **5**, 3546.
28 R. M. Cordeiro, *Biochim. Biophys. Acta*, 2015, **1850**, 1786–1794.
29 C. Tanielian and G. Heinrich, *Photochem. Photobiol.*, 1995, **61**, 131–135.
30 P. B. Merkel and D. R. Kearns, *J. Am. Chem. Soc.*, 1972, **94**, 1029–1030.
31 M. O. Senge and J. C. Brandt, *Photochem. Photobiol.*, 2011, **87**, 1240–1296.
32 U. Schmidt-Erfurth and T. Hasan, *Surv. Ophthalmol.*, 2000, **45**, 195–214.
33 M. Cho, G. M. Park, S. N. Kim, T. Amna, S. Lee and W. S. Shin, *J. Microbiol. Biotechnol.*, 2014, **24**, 346–353.
34 P. H. Baudelet, A. L. Gagez, J. B. Berard, C. Juin, N. Bridiau, R. Kaas, V. Thiery, J. P. Cadoret and L. Picot, *Mar. Drugs*, 2013, **11**, 4390–4406.
35 V. Rapozzi, M. Miculan and L. E. Xodo, *Cancer Biol. Ther.*, 2009, **8**, 1318–1327.
36 B. A. Hartl, H. Hirschberg, L. Marcu and S. R. Cherry, *Biomed. Opt. Express*, 2015, **6**, 770–779.
37 A. Makky, K. Daghildjian, J. P. Michel, P. Maillard and V. Rosilio, *Biochim. Biophys. Acta*, 2012, **1818**, 2831–2838.
38 J. Hempstead, D. P. Jones, A. Ziouche, G. M. Cramer, I. Rizvi, S. Arnason, T. Hasan and J. P. Celli, *Sci. Rep.*, 2015, 5.
39 D. Oulmi, P. Maillard, J.-L. Guerquin-Kern, C. Huel and M. Momenteau, *J. Org. Chem.*, 1995, **60**, 1554–1564.
40 A. D. Bangham, M. M. Standish and J. C. Watkins, *J. Mol. Biol.*, 1965, **13**, 238–252.
41 D. M. Price, *J. Therm. Anal.*, 1995, **45**, 1285–1296.
42 H. W. Chan and G. Levett, *Lipids*, 1977, **12**, 99–104.
43 W. A. Pryor and L. Castle, *Methods Enzymol.*, 1984, **105**, 293–299.
44 B. Maherani, E. Arab-Tehrany, A. Kheirolomoom, D. Geny and M. Linder, *Biochimie*, 2013, **95**, 2018–2033.
45 P. S. Chen, T. Y. Toribara and H. Warner, *Anal. Chem.*, 1956, **28**, 1756–1758.
46 J. Wang, R. M. Wolf, J. W. Caldwell, P. A. Kollman and D. A. Case, *J. Comput. Chem.*, 2004, **25**, 1157–1174.
47 J. Wang, W. Wang, P. A. Kollman and D. A. Case, *J. Mol. Graphics Modell.*, 2006, **25**, 247–260.
48 Y. Duan, C. Wu, S. Chowdhury, M. C. Lee, G. Xiong, W. Zhang, R. Yang, P. Cieplak, R. Luo, T. Lee, J. Caldwell, J. Wang and P. Kollman, *J. Comput. Chem.*, 2003, **24**, 1999–2012.
49 M. J. Frisch, G. W. Trucks, H. B. Schlegel, G. E. Scuseria, M. A. Robb, J. R. Cheeseman, G. Scalmani, V. Barone,

B. Mennucci, G. A. Petersson, H. Nakatsuji, M. Caricato, X. Li, H. P. Hratchian, A. F. Izmaylov, J. Bloino, G. Zheng, J. L. Sonnenberg, M. Hada, M. Ehara, K. Toyota, R. Fukuda, J. Hasegawa, M. Ishida, T. Nakajima, Y. Honda, O. Kitao, H. Nakai, T. Vreven, J. A. Montgomery, J. E. Peralta, F. Ogliaro, M. Bearpark, J. J. Heyd, E. Brothers, K. N. Kudin, V. N. Staroverov, R. Kobayashi, J. Normand, K. Raghavachari, A. Rendell, J. C. Burant, S. S. Iyengar, J. Tomasi, M. Cossi, N. Rega, J. M. Millam, M. Klene, J. E. Knox, J. B. Cross, V. Bakken, C. Adamo, J. Jaramillo, R. Gomperts, R. E. Stratmann, O. Yazyev, A. J. Austin, R. Cammi, C. Pomelli, J. W. Ochterski, R. L. Martin, K. Morokuma, V. G. Zakrzewski, G. A. Voth, P. Salvador, J. J. Dannenberg, S. Dapprich, A. D. Daniels, Ö. Farkas, J. B. Foresman, J. V. Ortiz, J. Cioslowski and D. J. Fox, *Gaussian 09, Revision A*, Wallingford CT, 2009.

50 F. Y. Dupradeau, A. Pigache, T. Zaffran, C. Savineau, R. Lelong, N. Grivel, D. Lelong, W. Rosanski and P. Cieplak, *Phys. Chem. Chem. Phys.*, 2010, **12**, 7821–7839.

51 C. J. Dickson, B. D. Madej, Å. A. Skjevik, R. M. Betz, K. Teigen, I. R. Gould and R. C. Walker, *J. Chem. Theory Comput.*, 2014, **10**, 865–879.

52 Å. A. Skjevik, B. D. Madej, R. C. Walker and K. Teigen, *J. Phys. Chem. B*, 2012, **116**, 11124–11136.

53 C. J. Dickson, L. Rosso, R. M. Betz, R. C. Walker and I. R. Gould, *Soft Matter*, 2012, **8**, 9617–9627.

54 D. J. Price and C. L. Brooks, 3rd, *J. Chem. Phys.*, 2004, **121**, 10096–10103.

55 S. Jo, T. Kim, V. G. Iyer and W. Im, *J. Comput. Chem.*, 2008, **29**, 1859–1865.

56 R. Salomon-Ferrer, D. A. Case and R. C. Walker, *Wiley Interdiscip. Rev.: Comput. Mol. Sci.*, 2013, **3**, 198–210.

57 D. A. Case, R. M. Betz, W. Botello-Smith, D. S. Cerutti, T. E. Cheatham III, T. A. Darden, R. E. Duke, T. J. Giese, H. Gohlke, A. W. Goetz, N. Homeyer, S. Izadi, P. Janowski, J. Kaus, A. Kovalenko, T. S. Lee, S. LeGrand, P. Li, C. Lin, T. Luchko, R. Luo, B. Madej, D. Mermelstein, K. M. Merz, G. Monard, H. Nguyen, H. T. Nguyen, I. Omelyan, A. Onufriev, D. R. Roe, A. Roitberg, C. Sagui, C. L. Simmerling, J. Swails, R. C. Walker, J. Wang, R. M. Wolf, X. Wu, L. Xiao, D. M. York and P. A. Kollman, *AMBER 2016*, University of California, San Francisco, 2016.

58 D. R. Roe and T. E. Cheatham, *J. Chem. Theory Comput.*, 2013, **9**, 3084–3095.

59 M. C. Desroches, A. Kasselouri, M. Meyniel, P. Fontaine, M. Goldmann, P. Prognon, P. Maillard and V. Rosilio, *Langmuir*, 2004, **20**, 11698–11705.

60 B. Cunderlikova, O. Kaalhus, R. Cunderlik, A. Mateasik, J. Moan and M. Kongshaug, *Photochem. Photobiol.*, 2004, **79**, 242–247.

61 H. Ibrahim, A. Kasselouri, C. You, P. Maillard, V. Rosilio, R. Pansu and P. Prognon, *J. Photochem. Photobiol., A*, 2011, **217**, 10–21.

62 C. Vilcheze, T. P. McMullen, R. N. McElhaney and R. Bittman, *Biochim. Biophys. Acta*, 1996, **1279**, 235–242.

63 M. Manrique-Moreno, P. Garidel, M. Suwalsky, J. Howe and K. Brandenburg, *Biochim. Biophys. Acta*, 2009, **1788**, 1296–1303.

64 M. Manrique-Moreno, M. Suwalsky, F. Villena and P. Garidel, *Biophys. Chem.*, 2010, **147**, 53–58.

65 M. Manrique-Moreno, F. Villena, C. P. Sotomayor, A. M. Edwards, M. A. Munoz, P. Garidel and M. Suwalsky, *Biochim. Biophys. Acta*, 2011, **1808**, 2656–2664.

66 M. Tanaka, A. Jutila and P. K. J. Kinnunen, *J. Phys. Chem. B*, 1998, **102**, 5358–5362.

67 G. Cevc, *Phospholipids Handbook*, CRC Press, New York, 1993.

68 M. Wallgren, L. Beranova, Q. D. Pham, K. Linh, M. Lidman, J. Procek, K. Cyprych, P. K. Kinnunen, M. Hof and G. Grobner, *Faraday Discuss.*, 2013, **161**, 499–513; discussion 563–489.

69 *Photodynamic Therapy from Theory to Application*, ed. M. H. Abdel-Kader, Springer-Verlag, Berlin, Heidelberg, 2014.

70 D. B. Min and J. M. Boff, *Compr. Rev. Food Sci. Food Saf.*, 2002, **1**, 58–72.

71 E. N. Frankel, *Prog. Lipid Res.*, 1980, **19**, 1–22.

72 W. E. Neff and E. N. Frankel, *Lipids*, 1980, **15**, 587–590.

73 B. Ehrenberg, J. L. Anderson and C. S. Foote, *Photochem. Photobiol.*, 1998, **68**, 135–140.

74 F. M. Engelmann, S. V. O. Rocha, H. E. Toma, K. Araki and M. S. Baptista, *Int. J. Pharm.*, 2007, **329**, 12–18.

75 P. H. B. Aoki, L. F. C. Morato, F. J. Pavinatto, T. M. Nobre, C. J. L. Constantino and O. N. Oliveira, *Langmuir*, 2016, **32**, 3766–3773.

Titre : Conception de nanomédicaments photostimulables à base de lipides et porphyrines ou de conjugués lipide-porphyrine pour la libération contrôlée de substances actives

Mots clés : lipide, porphyrine, conjugué, libération, lumière, liposome

Résumé : L'objectif des travaux de cette thèse était de développer un système de délivrance stimulus-sensible innovant. Basé sur des vésicules lipidiques, il permet la libération d'une substance anti-cancéreuse hydrophile encapsulée dans leur cœur aqueux, sous l'effet de la lumière. Des porphyrines, incorporées dans leur bicouche, permettent, une fois illuminées, de générer de l'oxygène singulet qui oxyde les chaînes acyl insaturées des phospholipides. Cela induit une augmentation de la perméabilité des liposomes et permet la libération de leur cargo. Nous avons, dans un premier temps, effectué une sélection de phospholipides et de porphyrines permettant de construire le système. Les résultats expérimentaux ont pu être corrélés à une étude de simulation de dynamique moléculaire. L'ensemble a mis en exergue l'importance de la profondeur d'insertion de la porphyrine dans la bicouche lipidique et de sa proximité avec la double-liaison des phospholipides. Mais il a aussi montré les limites de ce système. Nous avons alors développé deux nouvelles molécules dérivées de phospholipides naturels auxquels a été couplée la pheophorbide a. Malgré leur possible autoassemblage sous la forme de vésicules, ces derniers n'étaient pas stables et s'agrégeaient rapidement. Nous avons donc associé ces conjugués à des lipides classiques (DSPC, cholestérol) et analysé les propriétés des mélanges obtenus. Les propriétés photothermiques des systèmes conçus ont été confirmées, capables d'induire une élévation en température de 14°C. La chaleur générée, responsable d'une plus grande fluidité de la bicouche lipidique, a permis de favoriser la libération du cargo. Enfin, les deux conjugués synthétisés ont montré eux-mêmes une activité phototoxique (PDT), additionnée d'une sélectivité vis-à-vis de cellules du cancer de l'œsophage. Ces nouvelles molécules offrent donc de nombreuses opportunités pour le développement de systèmes multimodaux, bio-inspirés et biodégradables, pour la délivrance d'un médicament sous l'effet de la lumière.

Title: Design of photoactivatable drug delivery systems made of lipids and porphyrins or lipid-porphyrin conjugates for the controlled release of active pharmaceutical ingredients

Keywords: lipid, porphyrin, conjugate, release, light, liposome

Abstract: The aim of this work was to develop an innovative stimulus-responsive delivery system. Based on lipid vesicles, it allows the controlled release, by light, of a hydrophilic anti-cancer substance encapsulated in their aqueous core. Once illuminated, porphyrin molecules inserted into the lipidic bilayer, generate singlet oxygen which oxidizes the unsaturated acyl chains of the phospholipids. This induces an increase in the permeability of the liposomes and the release of their cargo. We first made a selection of phospholipids and porphyrins to build the system. Our experimental study could be correlated with results of molecular dynamics simulations. The whole work highlighted the importance of the depth of insertion of porphyrin into the lipid bilayer and its proximity to the double bond of phospholipids. But it also showed the limits of this system. We then developed two new molecules derived from natural phospholipids, to which pheophorbide a was coupled. The conjugates were able to form self-assembled vesicles but were unstable and quickly aggregated. We therefore associated these conjugates with classical lipids (DSPC, cholesterol) and analyzed the properties of these mixtures. We highlighted photothermal properties of the designed systems, capable of inducing a temperature rise of 14 °C. The generation of heat, responsible for a greater fluidity of the lipid bilayer, subsequently promoted the encapsulated cargo release. Finally, the two synthesized conjugates showed a phototoxic activity (PDT), with selectivity towards esophageal cancer cells. These new molecules therefore offer many opportunities for the development of multimodal, bio-inspired and biodegradable systems, for the delivery of a drug under the effect of light.

Université Paris-Saclay
Espace Technologique / Immeuble Discovery
Route de l'Orme aux Merisiers RD 128 / 91190 Saint-Aubin, France